Atomic-Scale and Three-Dimensional Transmission Electron Microscopy of Nanoparticle Morphology

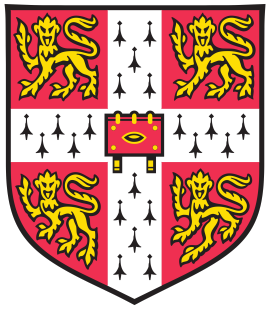

Rowan Kendall Leary

University of Cambridge

Department of Materials Science and Metallurgy

Peterhouse

Submitted for the degree of Doctor of Philosophy

June 2014

Abstract

Atomic-Scale and Three-Dimensional Transmission Electron Microscopy of Nanoparticle Morphology

Rowan Kendall Leary

The burgeoning field of nanotechnology motivates comprehensive elucidation of nanoscale materials. This thesis addresses transmission electron microscope characterisation of nanoparticle morphology, concerning specifically the crystallographic status of novel intermetallic $GaPd_2$ nanocatalysts and advancement of electron tomographic methods for high-fidelity three-dimensional analysis.

Going beyond preceding analyses, high-resolution annular dark-field imaging is used to verify successful nano-sizing of the intermetallic compound $GaPd_2$. It also reveals catalytically significant and crystallographically intriguing deviations from the bulk crystal structure. So-called 'non-crystallographic' five-fold twinned nanoparticles are observed, adding a new perspective in the long standing debate over how such morphologies may be achieved.

The morphological complexity of the $GaPd_2$ nanocatalysts, and many cognate nanoparticle systems, demands fully three-dimensional analysis. It is illustrated how image processing techniques applied to electron tomography reconstructions can facilitate more facile and objective quantitative analysis ('nano-metrology'). However, the fidelity of the analysis is limited ultimately by artefacts in the tomographic reconstruction.

Compressed sensing, a new sampling theory, asserts that many signals can be recovered from far fewer measurements than traditional theories dictate are necessary. Compressed sensing is applied here to electron tomographic reconstruction, and is shown to yield far higher fidelity reconstructions than conventional algorithms. Reconstruction from extremely limited data, more robust quantitative analysis and novel three-dimensional imaging are demonstrated, including the first three-dimensional imaging of localised surface plasmon resonances. Many aspects of transmission electron microscopy characterisation may be enhanced using a compressed sensing approach.

Acknowledgments

Teamwork is the most enjoyable part of this type of research. Although this thesis summarises my own contributions to atomic-scale and 3D characterisation of nanoparticles in the transmission electron microscope, many aspects have been a team effort.

Always encouraging, I am especially grateful to Professor Paul Midgley. Providing guidance, but encouraging exploration with freedom, ambition and fun, I could not imagine a better mentor or role model. I have worked especially closely on the intricacies of electron tomography with Daniel Holland and Zineb Saghi, to whom I am indebted. Sir John Meurig Thomas has broadened by horizons, especially regarding materials chemistry.

For their role in managing the practicalities of the TEMs, in particular the Titan, I am grateful to Graham Sharp and Jon Barnard. I thank Alex Eggeman for his computational support of our research group. I am also grateful to all of our collaborators, and thank in particular Francisco de la Peña, Olivia Nicoletti and Cate Ducati, as well as Marc Amrbrüster and his co-workers. I also thank Rik Brydson and colleagues for their ongoing encouragement, and for inviting me back to the University of Leeds each year to lecture on electron tomography at the Royal Microscopical Society Electron Microscopy School.

This work, and thoughts of future work, would not be possible without my family. I thank my mum, dad and brother especially for their continuing support.

Declaration

This dissertation is submitted to the University of Cambridge in partial fulfilment of the degree of Doctor of Philosophy. It is an account of the research I have undertaken in the Department of Materials Science and Metallurgy at the University of Cambridge between October 2010 and April 2014, under the supervision of Prof. P. A. Midgley.

The work described is original and a result of my own work, except where clearly stated to the contrary. This dissertation does not exceed the word limit set by the Degree Committee for the Faculty of Physics and Chemistry, and no part of it has already been, or is currently being, submitted for any other degree, diploma, or other qualification, at any other university.

Specific collaborators whose contribution is cited are from the Department of Materials Science and Metallurgy, University of Cambridge, unless stated otherwise.

Peer reviewed journal publications

R. Leary, F. de la Peña, J.S. Barnard, Y. Luo, M. Armbrüster, J.M. Thomas, and P.A. Midgley. Revealing the Atomic Structure of Intermetallic $GaPd_2$ Nanocatalysts by using Aberration-Corrected Scanning Transmission Electron Microscopy. *ChemCatChem,* 5(9): 2599-2609, 2013.

R. Leary, Z. Saghi, P.A. Midgley, and D.J. Holland. Compressed sensing electron tomography. *Ultramicroscopy,* 131: 70-91, 2013.

O. Nicoletti, F. de la Peña, **R.K. Leary,** D.J. Holland, C. Ducati, and P.A. Midgley. Three-dimensional imaging of localized surface plasmon resonances of metal nanoparticles. *Nature,* 502(7469): 80-84, 2013.

J.M. Thomas, C. Ducati, **R. Leary,** and P.A. Midgley. Some turning points in the chemical electron microscopic study of heterogeneous catalysts. *ChemCatChem,* 5(9): 2560-2579, 2013.

J.M. Thomas, **R. Leary,** P.A. Midgley and D.J. Holland. A new approach to the investigation of nanoparticles: electron tomography with compressed sensing. *Journal of Colloid and Interface Science,* 392: 7-14, 2013.

J.M. Thomas, P.A. Midgley, C. Ducati, and **R.K. Leary.** Nanoscale electron tomography and atomic scale high-resolution electron microscopy of nanoparticles and nanoclusters: A short survey. *Progress in Natural Science: Materials International,* 23(3): 222-234, 2013.

R. Leary, P.A. Midgley, and J.M. Thomas. Recent advances in the application of electron tomography to Materials Chemistry. *Accounts of Chemical Research,* 45(10): 1782-1791, 2012.

R. Leary, Z. Saghi, M. Armbrüster, M., G. Wowsnick, R. Schlögl, J.M. Thomas, and P.A. Midgley. Quantitative high-angle annular dark-field scanning transmission electron microscope (HAADF-STEM) tomography and high-resolution electron microscopy of unsupported intermetallic $GaPd_2$ catalysts. *The Journal of Physical Chemistry C,* 116(24): 13343-13352, 2012.

Z. Saghi, D.J. Holland, **R. Leary,** A. Falqui, G. Bertoni, A.J. Sederman, L.F. Gladden, and P.A. Midgley. Three-dimensional morphology of iron oxide nanoparticles with reactive concave surfaces. A compressed sensing-electron tomography (CS-ET) approach. *Nano Letters,* 11(11): 4666-4673, 2011.

Peer reviewed conference proceedings

R. Leary, Z. Saghi, P.A. Midgley, and D.J. Holland. Compressed Sensing Electron Tomography: Theory and Applications. *Microscopy and Microanalysis,* 19(SupplementS2): 546-547, 2013.

R. Leary, Z. Saghi, P.A. Midgley, and D.J. Holland. Compressed Sensing Reconstruction of Smooth Signals in Electron Tomography. *Microscopy and Microanalysis,* 19(SupplementS2): 568-569, 2013.

R.K. Leary, F. de la Peña, J.S. Barnard, M. Walls, Y. Luo, M. Armbrüster, J.M. Thomas, and P.A. Midgley. Nano-sized intermetallics: unraveling intricacies of $GaPd_2$ catalysts using aberration-corrected STEM. *Microscopy and Microanalysis,* 19(SupplementS2): 1696-1697, 2013.

R. Leary, F. de la Peña, J.S. Barnard, M. Walls, Y. Luo, M. Armbrüster, J.M. Thomas, and P.A. Midgley. Intermetallic $GaPd_2$ nanocatalysts revealed using aberration-corrected scanning transmission electron microscopy. *11*$^{\text{th}}$ *European Congress on Catalysis - EuropaCat-XI*, Lyon, France, 1^{st}-6^{th} September, 2013.

R. Leary, Z. Saghi, A. Falqui, G. Bertoni, M. Armbrüster, G. Wowsnick, R. Schlögl, J.M. Thomas, P.A. Midgley, and D.J. Holland. Exploiting sparsity at the nanoscale: a compressed sensing approach to electron tomography. *15*$^{\text{th}}$ *European Microscopy Congress,* Manchester Central, UK, 16^{th}-21^{st} September, 2012.

R. Leary, Z. Saghi, Z. M. Armbrüster, G. Wowsnick, R. Schlögl, J.M. Thomas, and P.A. Midgley. Structural intricacies of unsupported intermetallic Ga-Pd catalyst nanoparticles studied by high resolution and three-dimensional electron microscopy. *15*$^{\text{th}}$ *European Microscopy Congress,* Manchester Central, UK, 16^{th}-21^{st} September, 2012.

F. de la Peña, O. Nicoletti, **R.K. Leary,** P.A. Midgley, and C. Ducati. Mapping substrate-induced hybridised surface plasmon resonances of a silver nanocube using machine learning methods. *15*$^{\text{th}}$ *European Microscopy Congress,* Manchester Central, UK, 16^{th}-21^{st} September, 2012.

O. Nicoletti, **R.K. Leary,** F. de la Peña, D.J. Holland, C. Ducati, and P.A. Midgley. Three-dimensional imaging of localized surface plasmon resonances of metal nanoparticles. *15*$^{\text{th}}$ *European Microscopy Congress,* Manchester Central, UK, 16^{th}-21^{st} September, 2012.

R. Leary, Z. Saghi, Z. M. Armbrüster, R. Schlögl, J.M. Thomas, and P. Midgley. Quantitative HAADF-STEM tomography of unsupported intermetallic Ga-Pd catalysts. *Journal of Physics: Conference Series,* 371(1): 012024, 2012.

P.A. Midgley, Z.Saghi, J. Hindson, **R. Leary,** D. Holland, A. Sederman, L. Gladden, V. Schmidt, and N. Greenham. Recent developments in quantitative electron tomography. *Microscopy and Microanalysis,* 17(SupplementS2): 932-933, 2011.

Conference presentations

R. Leary, Z. Saghi, P.A. Midgley, and D.J. Holland. Compressed Sensing Electron Tomography: Theory and Applications. *Microscopy and Microanalysis,* Indianapolis, IN, USA. 4^{th}-8^{th} August, 2013.

R. Leary, Z. Saghi, P.A. Midgley, and D.J. Holland. Compressed Sensing Reconstruction of Smooth Signals in Electron Tomography. *Microscopy and Microanalysis,* Indianapolis, IN, USA. 4^{th}-8^{th} August, 2013.

R.K. Leary, F. de la Peña, J.S. Barnard, M. Walls, Y. Luo, M. Armbrüster, J.M. Thomas, and P.A. Midgley. Nano-sized intermetallics: unraveling intricacies of $GaPd_2$ catalysts using aberration-corrected STEM. *Microscopy and Microanalysis,* Indianapolis, IN, USA. 4^{th}-8^{th} August, 2013.

R. Leary, F. de la Peña, J.S. Barnard, M. Walls, Y. Luo, M. Armbrüster, J.M. Thomas, and P.A. Midgley. Intermetallic $GaPd_2$ nanocatalysts revealed using aberration-corrected scanning transmission electron microscopy. *11^{th} European Congress on Catalysis - EuropaCat-XI*, Lyon, France, 1^{st}-6^{th} September, 2013.

R. Leary, Z. Saghi, A. Falqui, G. Bertoni, M. Armbrüster, G. Wowsnick, R. Schlögl, J.M. Thomas, P.A. Midgley, and D.J. Holland. Exploiting sparsity at the nanoscale: a compressed sensing approach to electron tomography. *15^{th} European Microscopy Congress,* Manchester Central, UK, 16^{th}-21^{st} September, 2012.

R. Leary, Z. Saghi, Z. M. Armbrüster, G. Wowsnick, R. Schlögl, J.M. Thomas, and P.A. Midgley. Structural intricacies of unsupported intermetallic Ga-Pd catalyst nanoparticles studied by high resolution and three-dimensional electron microscopy. *15^{th} European Microscopy Congress,* Manchester Central, UK, 16^{th}-21^{st} September, 2012.

R.K. Leary, Z. Saghi, A.J. Sederman, J.M. Thomas, L.F., Gladden, M. Armbrüster, R. Schlögl, P.A. Midgley, and D.J. Holland. Compressed sensing electron tomography for 3D nanometrological studies of complex nanoparticle catalyst systems. *2^{nd} International Symposium on Advanced Electron Microscopy for Catalysis and Energy Storage Materials,* Fritz Haber Institute of the Max Planck Society, Germany, 5^{th}-8^{th} February, 2012.

R.K. Leary, Z. Saghi, M. Armbrüster, R. Schlögl, J.M. Thomas, and P.A. Midgley. HAADF-STEM tomography of unsupported intermetallic Ga-Pd catalysts. *Canadian Centre for Electron Microscopy Summer School,* McMaster University, Canada, 13^{th}-17^{th} June, 2011.

R.K. Leary, Z. Saghi, M. Armbrüster, R. Schlögl, J.M. Thomas, and P.A. Midgley. Quantitative HAADF-STEM tomography of unsupported intermetallic Ga-Pd catalysts. *Electron Microscopy and Analysis Group Conference,* University of Birmingham, UK, 6^{th}-9^{th} September, 2011.

Other presentations

R. Leary. Principles and practice of electron tomography. *Royal Microscopical Society Electron Microscopy School,* University of Leeds, UK, 2011, 2012, 2013 & 2014.

R. Leary. Compressed sensing in electron microscopy. *Guest lecture in the series: Contemporary Sampling Techniques and Compressed Sensing (A.C. Hansen and B. Roman)*, Department of Applied Mathematics and Theoretical Physics, University of Cambridge, UK. 27$^{\text{th}}$ February, 2014.

R. Leary, Z. Saghi, P.A. Midgley, and D.J. Holland. Compressed sensing electron tomography: a promising approach for quantitative 3D nano-metrology. *Quantitative Interpretation of TEM Image and Diffraction Data; one day meeting dedicated to Professor Mike Whelan FRS in Celebration of his 80*$^{\text{th}}$ *Birthday,* University of Oxford, UK. 20$^{\text{th}}$ July, 2012.

Nomenclature

AC Aberration-Corrected
ADF Annular Dark-Field
AIR Algebraic Iterative Reconstruction
BF Bright-Field
CS Compressed Sensing (or Compressive Sampling)
DCT Discrete Cosine Transform
DWT Discrete Wavelet Transform
EELS Electron Energy-Loss Spectroscopy
ET Electron Tomography
FCC Face-Centred Cubic
LSPR Localised Surface Plasmon Resonance
MRI Magnetic Resonance Imaging
NMF Non-negative Matrix Factorisation
NUFFT Non-Uniform Fast Fourier Transform
PSF Point Spread Function
SIRT Simultaneous Iterative Reconstruction Technique
SPM Single Particle Microscopy
SNR Signal-to-Noise Ratio
(S)TEM (Scanning) Transmission Electron Microscope/Microscopy
TV Total Variation
WBP Weighted Back-Projection
XRD X-Ray Diffraction
Z atomic number
$[uvw]$ lattice direction
$\langle uvw \rangle$ family of crystallographically equivalent lattice directions
(hkl) lattice plane
$\{hkl\}$ family of crystallographically equivalent lattice planes

Contents

Chapter 1

Introduction

1.1 The role and expectations of transmission electron microscopy

The need for materials characterisation is pervasive throughout scientific academic research, as well as in industrial and commercial contexts. This is especially so in the field of nanotechnology, where the aim is to achieve novel properties through precise control of nano- or atomic-scale structure. It is now well-recognised, for example, that by determining the chemically conducive nano- and/or atomic-scale morphologies, it becomes possible to design new and improved catalysts - the societal significance of which should not be underestimated, as the adept materials chemist will readily assert (e.g. [1]). New catalysts, often of increasing sophistication, must in turn be scrutinised, propagating demand for characterisation. Knowledge-based development in this way is clearly potent not just in catalytic contexts, but across many areas of nanotechnology.

Capable of providing nano- and atomic-scale imaging and spectroscopy, transmission electron microscopy (TEM) is extensively utilised to characterise nanostructured materials, nanoparticles and catalysts especially. While TEM is often one of many requisite methods in the repertoire of characterisation techniques, the ability to examine internal and surface features at high spatial resolution can contribute a number of unique and essential forms of information (Figure 1.1). Size, shape, spatial distribution, local composition, crystal structure and many other significant properties of nanoparticles, such as plasmonic response, can be probed directly on a nanoparticle-by-nanoparticle basis using TEM, permitting in-depth analysis.

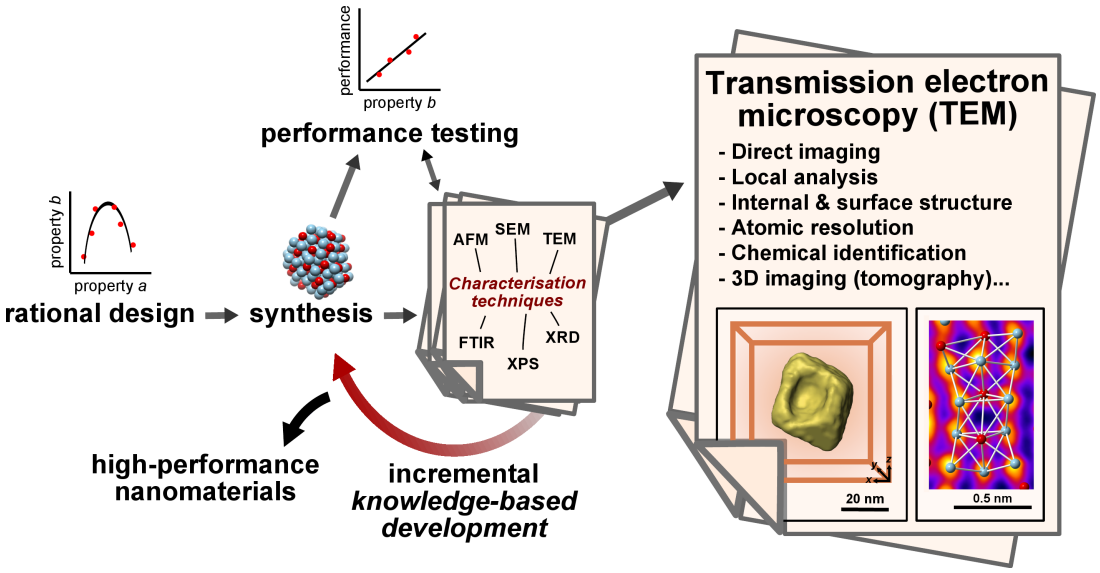

FIGURE 1.1: Scheme of nanotechnology research and specific contributions of TEM. Thorough characterisation, usually harnessing a number of techniques, facilitates *knowledge-based development*.

Moreover, there have been significant recent advances in TEM characterisation capabilities. Correction of electron optical aberrations [2–5], primarily, has improved spatial resolution as well as a number of other significant parameters pertaining to high-quality TEM imaging and spectroscopy [6–8]. Intricate structural and chemical features may now be studied with unprecedented rigour, often with vivid atomic-scale detail. There is eminent scope for advanced TEM to contribute to materials characterisation where other techniques, or standard TEM practices, may struggle.

Perennially though, TEM methods must also be advanced further to meet demand for increasingly comprehensive and sophisticated information. Especially, the three-dimensional (3D) complexity of many nanoscale materials warrants a fully 3D analysis. However, a standard TEM image typically constitutes only a 2D projection of the 3D structure, meaning that 3D information may be lost or 'hidden'. It is recognised patently by the TEM community that, although yielding a great many insights, electron tomography (ET) in particular [9, 10], established methods for 3D analysis using TEM leave much to be desired. There is a pressing demand for 3D TEM analysis that is of higher fidelity, quantitative and capable of addressing a range of important materials, structures or properties that cannot currently be analysed.

1.2 Topics addressed

The overarching theme of this thesis is the elucidation of nanoparticle morphology via advanced TEM, including crystallography and 3D structure. There are two distinct but overlapping topics:

- application of state-of-the-art TEM to obtain detailed insights into novel intermetallic Ga-Pd nanocatalysts;
- development of advanced ET techniques for 3D TEM.

1.2.1 Unravelling intricacies of intermetallic Ga-Pd nanocatalysts

Established recently in a series of foundational studies, a promising new class of selective hydrogenation catalysts has emerged based on intermetallic Ga-Pd compounds [11]. However, although the catalytic efficacy of bulk and nanoparticulate Ga-Pd intermetallic compounds has been demonstrated, aspects determining the observed catalytic behaviour require further elucidation, most fundamentally the precise structural and chemical state of the intermetallic compound in the nano-sized form. Several studies had already been performed in this vein, primarily using non-spatially resolved techniques and documenting a challenging task due to many closely related phases and inability to view structural intricacies directly.

Described herein, advanced TEM has been used to elucidate the nature of unsupported Ga-Pd catalysts in nanoparticulate form, $GaPd_2$ in particular. Primarily, the specific advantages offered by annular dark-field imaging in aberration-corrected scanning TEM have been exploited, with electron energy-loss spectroscopy, energy dispersive X-ray spectroscopy, conventional TEM and ET providing supporting information.

The analysis confirms and provides further insight into a number of key aspects raised in preceding work, including not only the verification of the intermetallic state in nano-sized form (through direct chemically sensitive imaging of the intermetallic structure) but also the nature of the deviations from the 'ideal' bulk crystal structure, such as decomposition of the intermetallic surface in an oxidising environment. Further effects related to nano-sizing of the intermetallic compound, hitherto relatively unexplored, that are of catalytic significance and crystallographic intrigue, such as the nanoparticle morphologies

and nanocrystalline defects, are reported and discussed, including the occurrence of five-fold twinned nanoparticles.

1.2.2 Advancing ET for high-fidelity, quantitative & novel 3D imaging

ET is by far the most widely practised method to garner 3D information from TEM. In essence, it involves recording an angular series of 2D TEM projections, which are input to computational algorithms to reconstruct a 3D image. However, despite yielding a great many insights in both the physical [9] and life sciences [12], frailties can be readily identified in current ET practices.

Remarkably, despite their potentially rich 3D information content, ET reconstructions are often treated only qualitatively, or else have been subject to time-consuming and user-dependent manual procedures to delineate objects. Fast and robust methods are needed for analysing ET reconstructions quantitatively, striving for routine and reliable 'nano-metrology'. A key, indeed necessary, step to achieve this is the application of image processing techniques to segment ET reconstructions.

Here, a semi-automated image processing routine for the segmentation of densely-packed nanoparticles is described, and applied specifically to the Ga-Pd nanocatalysts. The segmentation results are also critically assessed, showing that the fidelity of the segmentation and quantitative analysis is limited primarily by the artefacts in the reconstruction. The study also therefore takes significance in demonstrating clearly that, as a prerequisite to robust quantitative 'nano-metrology' via ET, and in general for high-fidelity analysis, there is a need to improve the ET reconstruction itself.

The primary factor limiting the fidelity of ET reconstructions is paucity of data; specifically the limited number and angular range of the projections that can be acquired practically for input to tomographic reconstruction. In light of the (presently) insurmountable practical restrictions, there is a pressing need to develop improved reconstruction algorithms capable of yielding high-fidelity reconstructions from the limited data.

It is well-recognised that the reconstruction process in ET is challenging [13]. However, the widely adopted reconstruction algorithms in ET, which date back to the 1970s or earlier [14–16], do only little to address the challenges. To remedy this situation, prior knowledge about the specimen can be introduced during the reconstruction process. Significant new opportunities are offered in this regard by the recently developed mathematical theory of 'compressed sensing' [17, 18]. The

prior knowledge harnessed in compressed sensing is relatively liberal and widely applicable, based on principles of transform sparsity used in image compression, yet can be extremely powerful for the recovery of undersampled signals.

The latter chapters of this thesis establish the application of compressed sensing to ET reconstruction. The key underlying principles are distilled to provide an accessible but comprehensive overview sufficient for the ET practitioner. This is an important aspect, as much of the compressed sensing literature, at the present time, can be dense in mathematical content and sometimes challenging to digest. The efficacy of compressed sensing based ET is then critically evaluated, showing considerable performance enhancements over conventional reconstruction algorithms. High-fidelity reconstruction is possible, even from very few projections, facilitating more facile and higher fidelity segmentation and quantitative analysis (including re-visiting the Ga-Pd catalysts), and the door is opened to new ET investigations.

1.3 Thesis structure

The thesis is structured to progress from materials insights using current advanced TEM capabilities, through to ET technique development to provide new capabilities.

Giving background to the TEM techniques used, the relevant principles, capabilities and recent advances in TEM, scanning TEM and aberration correction in particular, are reviewed in chapter 2.

Chapter 3 addresses the materials insights into the Ga-Pd catalysts. Relevant background to the Ga-Pd nanocatalysts is given, followed by results from the aberration-corrected scanning TEM analysis and arising discussion. One particularly intriguing finding in chapter 3, the observation of five-fold twinned nanoparticles, provides a novel context in which to consider these long perplexing 'non-crystallographic' morphologies, which is pursued in chapter 4.

Chapters 5-8 deal primarily with ET technique development. The principles, practices and scope for development of ET are reviewed in detail in chapter 5. Chapter 6 provides a link between the first and second halves of the thesis, describing the segmentation routine devised to study the Ga-Pd nanocatalysts in 3D. The results clearly act as a motivator (amongst others) for the development of improved ET reconstruction via compressed sensing. In chapter 7, the salient aspects of compressed sensing theory are described, and specifically their applicability to ET. In chapter 8, the compressed sensing approach to ET is

evaluated in a number of case studies; firstly, a proof-of-principle investigation, then a series of systematic investigations. Finally, compressed sensing based ET is used to enable the first 3D reconstruction of localised surface plasmon resonances, from a very limited data set.

Each chapter finishes with discussion and/or conclusions regarding the particular topic(s) addressed. A set of more global conclusions and areas for future work are given in chapter 9.

Chapter 2

Transmission electron microscopy

The primary TEM techniques used in this thesis and rationale behind their selection are outlined in this chapter. These comprise firstly annular dark-field scanning TEM, and specifically aberration-corrected annular dark-field scanning TEM for high-resolution chemically sensitive imaging. Spectroscopic TEM techniques, harnessed more sparingly in the work herein, are also briefly covered, as are electron beam induced damage and contamination.

2.1 Conventional TEM or scanning TEM?

Stemming from the various electron beam-specimen interactions (Figure 2.1), the modern TEM permits a variety of signals to be recorded, judicious choice of which should be made according to the information sought. Influencing the choice may be the ability to readily interpret the signal, whether the signal can be recorded with sufficient signal-to-noise-ratio (SNR), and/or suitability for post-processing procedures that retrieve information not available directly (such as 3D reconstruction via ET).

Fundamentally, the two primary modes of TEM operation must be considered, namely (i) conventional TEM (CTEM) with parallel illumination, in which usually the bright-field (BF) signal is used (Figure 2.2a); and (ii) scanning TEM (STEM) with a focused electron probe, in which usually the annular dark-field (ADF) signal is used (Figure 2.2b).[1]

The choice between CTEM or STEM for the investigation of nanoparticle morphology is now well-versed in the literature, from which it can be ascertained

[1] These two imaging modes are related by the principle of reciprocity (see e.g. [20, chapter 2]), meaning that equivalent information could, in theory, be obtained in either mode of operation. Practical electron optical configurations, however, mean that it is distinctly advantageous, in most cases, to concentrate on the favoured signal for each mode of operation.

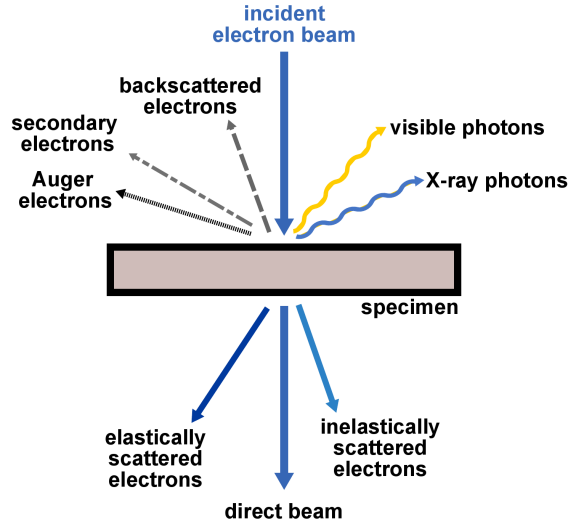

FIGURE 2.1: Principal signals of interest generated by an incident electron beam. Adapted from [19].

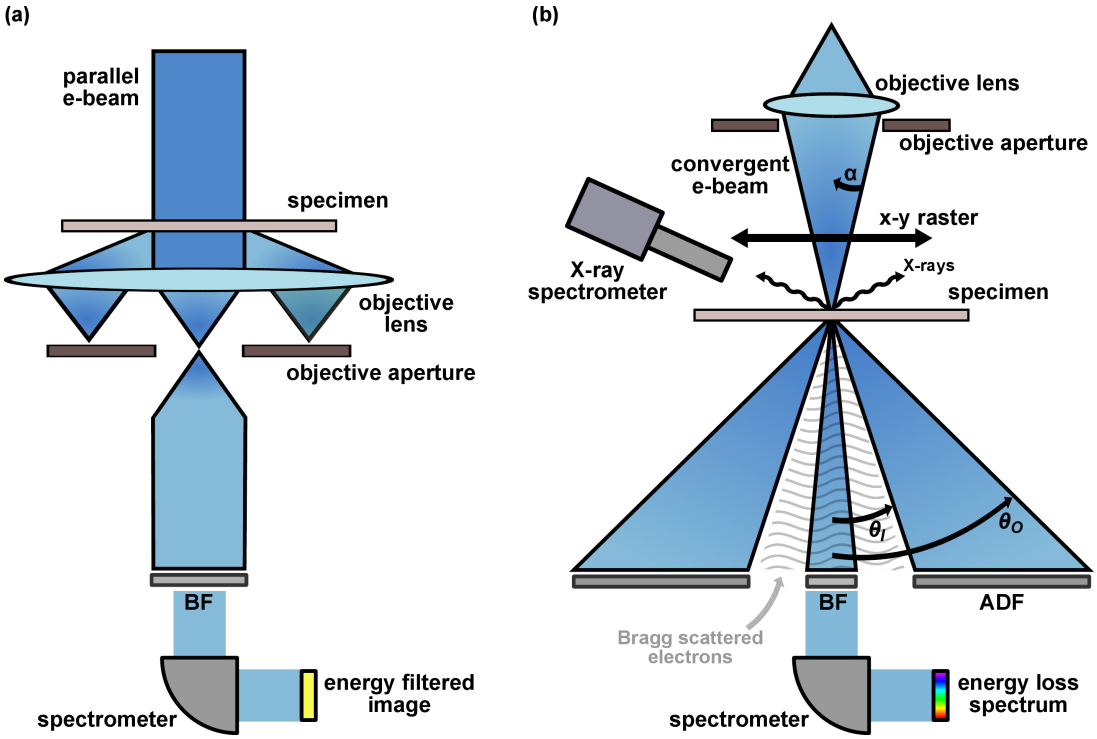

FIGURE 2.2: Essential aspects of (a) BF-CTEM and (b) STEM. In (b) α is the electron beam semi-convergence angle. θ_I and θ_O are the inner and outer ADF detection angles, respectively.

that while numerous insights into nanoparticle morphology have been made (e.g. [21]), and continue to be made (e.g. [22–25]), using CTEM, STEM has become increasingly popular. Recent books dedicated to STEM [20, 26] and numerous reviews [7, 13, 27–35] (citing just a selection) recount this rising interest. Overwhelmingly, it is clear that a major reason for the popularity of STEM is the ADF imaging mode, which can often provide both intuitive and high-fidelity analysis due to its 'direct interpretability.' Combined with simultaneously acquired point-by-point spectroscopic signals, it is widely recognised that STEM can be extremely powerful for the elucidation of nanoparticle morphology, heavy metal nanoparticles (including many nanocatalysts) on low atomic number support materials especially, including both high-resolution [30, 31, 33, 35, 36], [20, chapter 13], and 3D imaging via ET [9, 13, 32, 37–43], [44, chapter 12], [20, chapter 8].

Although BF-CTEM has been used for several decades, the images are not always straightforward to interpret for several reasons [19, 45]. In BF-CTEM, the image intensity, generally, does not show a monotonic dependence on the specimen thickness, depending strongly and in an involved manner on defocus. As such, contrast reversals in the image can occur through the specimen thickness or as a result of small changes in the electron optical conditions. By their nature, BF-CTEM images typically yield only weak chemical sensitivity - a considerable drawback when seeking to investigate complex multi-element nanoparticles and when seeking to resolve fine-scale features against the contrast generated from the specimen support. For strongly scattering crystalline specimens, further complications in BF-CTEM can be introduced due to strong Fresnel contrast and domination of the image by diffraction contrast (Bragg scattering). These signals carry a wealth of information that is of interest in certain contexts, such as diffraction contrast imaging of planar defects and strain fields [19, chapters 25 and 26], but in other contexts they can preclude a general facile interpretation that a monotonically varying signal endows. Significant image complications, so-called 'delocalisation', may also arise at high resolution due to lens aberrations.

Aberration-corrected (AC) optics (see section 2.4) and the use of 'negative spherical aberration imaging' (see Urban et al. in [8]) can permit compensation of aberrations and allow more readily interpretable BF-CTEM images to be formed, potentially improving spatial and chemical resolution; so too can computational procedures applied *a posteriori* to a series of images, so-called 'exit-wave reconstruction' [46] - see [22, 24, 25, 47] for examples in the context of nanoparticle morphology. However, direct information on chemical composition

is still lacking.

Contrary to BF-CTEM, images from ADF-STEM typically show atomic number sensitivity, monotonic variation in intensity with specimen thickness and insensitivity to defocus. In view of these benefits, the foundations of which are described below, the work in this thesis has primarily involved the use of ADF-STEM in preference to BF-CTEM.

2.2 Annular dark-field scanning transmission electron microscopy

Figure 2.2b summarises the principal aspects of STEM. A focused electron beam is moved point-by-point across the specimen and the signal generated at each point is recorded. BF images are typically formed using an axial detector, while the most widely used ADF signal is obtained via an annular detector positioned to integrate the signal from electrons scattered to relatively high (ca. 40-200 mrad) angles. Recent monographs by Nellist (respective chapters in [20, 26, 48]) as well as earlier publications by Nellist and Pennycook such as [27, 28] provide detailed coverage of the principles of STEM imaging.

The motivation for collecting an ADF signal is that at high detection angle, and with a large angular integration range, coherent contributions to the image from Bragg-scattered beams are negated. With the detected signal then dominated by Rutherford-like and thermal diffuse scattering, the scattering detected from each atom can be considered as transversely incoherent. The signal intensity should then vary monotonically with the thickness of the specimen and the atomic number Z of the constituent atoms, approaching a Z^2 relationship. The actual Z exponent lies somewhere in the region of $Z^{1.3-2}$, depending (primarily) on the inner detection angle θ_I [49, 50]. Unlike the phase contrast transfer function of BF-CTEM, the optical transfer function of ADF-STEM does not oscillate rapidly with changing spatial frequency or defocus. It is these characteristics that endow 'direct interpretability' and high contrast.

It was realised in the early development of STEM in the 1970s (see Pennycook's historical review in chapter 1 of [20]) that high contrast chemically sensitive atomic resolution images can be obtained of heavy metal nanoparticles, clusters or even single atoms on low-Z support materials. These are characteristics fulfilled by many supported nanoparticulate catalyst systems, and also in general by loose heavy metal nanoparticles deposited on low-Z TEM sample support grids. Two demonstrative examples are shown in Figure 2.3. Similarly, it

was shown that chemically sensitive images of crystalline lattices can be obtained. In 2001, it was shown by Midgley, Weyland and co-workers [51, 52] that the characteristics of ADF-STEM also make it a particularly successful imaging mode for 3D imaging of strongly scattering crystalline specimens via ET.

Different angular ranges of the ADF signal can be identified, usually comprising low- (LAADF), medium- (MAADF) and high-angle (HAADF) [50]. In this thesis 'ADF' is used generally to refer to images collected at sufficiently high angle and over sufficiently large angular ranges that they can be considered as showing largely incoherent Z-contrast.[2] The direct interpretability of the ADF signal means that a qualitative interpretation, without recourse to image simulation, suffices for many materials investigations. This is indeed the extent of the analysis for the high-resolution analysis of the Ga-Pd catalysts in this thesis.

However, ADF-STEM is not immune to potential difficulties that can lead to complications in interpretation, especially if seeking to analyse the intensity quantitatively. It is often pointed out that for crystalline specimens, the intensity of the image may be modified due to strong Bloch wave channelling when the crystal is near zone-axis orientation, which tends to concentrate the beam intensity onto atomic columns [55]. Primarily, this can increase the high angle scattering, and thereby the intensity in the image. Especially in high-resolution imaging, it can manifest clearly as a non-linear dependence of image intensity on thickness (number of atoms in a column), necessitating careful analysis in quantitative investigations [56]. In general though, this effect tends to occur only at a small numbers of crystal orientations, is more uniform across a crystal and is less pronounced relative to diffraction contrast in BF-CTEM.

In spite of such challenges, there is steadily growing attention being given to quantitative interpretation of the ADF intensity, with particularly sought-after aims being high-resolution atomic column-by-atomic column [56, 57] or atom-by-atom [49, 56] compositional analysis, and determination of the number of atoms in a nanoparticle [58] or atomic column [59, 60]. Often, these approaches are being pursued as a means of 3D structure determination, and are discussed in

[2] As noted by Treacy [50], despite the prevalent use of the term 'HAADF' in the literature many studies do not use a sufficiently large collection angle to be classed, strictly, as HAADF. Using a slightly lower collection angle can improve signal intensity, often with sufficient preservation of incoherence and Z-contrast. As detailed in [53], an inner detection angle θ_I of around three times the objective aperture radius typically suffices for incoherent imaging; or as suggested by Howie [54], consideration of thermal diffuse scattering dominating suggests $\theta_I \geq \lambda/d_{thermal}$, where λ is the electron wavelength and $d_{thermal}$ the amplitude of atomic thermal vibration, yielding $\theta_I \gtrsim 40$ mrad for many specimens at 200-300 kV.

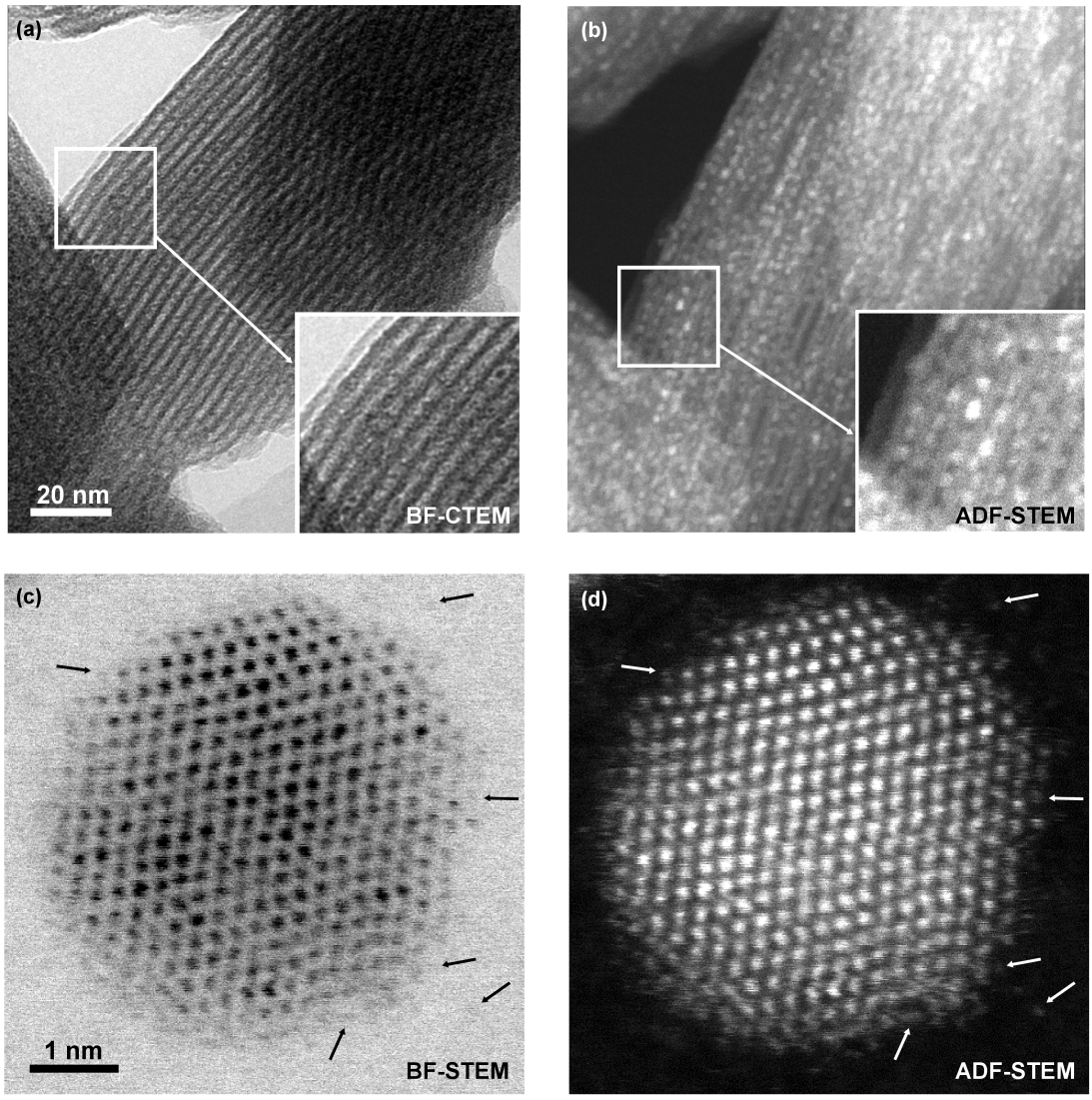

FIGURE 2.3: Illustrative examples of the efficacy of ADF-STEM for the study of small metallic nanoparticle heterogeneous catalysts. (a, b) Concerning the visibility of supported nanoparticles at relatively low resolution, the Pt-Ru nanoparticles supported on mesoporous silica are almost invisible in the phase-contrast BF-CTEM image (a), but clearly stand out against the lower atomic number support in a ADF-STEM image (b), owing to the atomic number contrast inherent in the imaging mode. A similar situation occurs at high resolution as shown in (c) and (d), which are simultaneously acquired BF- and ADF-STEM images of a Ga-Pd nanocatalyst. At the periphery of nanoparticle, the atomic columns may contain only a few atoms, yet these may still be visualised in an ADF image (d), as may isolated atoms on the low atomic number amorphous silicon support (examples are indicated by the arrows). In the BF-STEM image (c), the arrows at the same positions show that the phase-contrast image formation mechanism has not rendered these visible. (a, b) Reproduced from [29].

that respect in section 5.4.

Recent developments have been made, by several groups, including placing ADF-STEM images on a calibrated intensity scale to permit direct comparison to simulation [56, 59, 61, 62]. These methods have required careful determination of a number of imaging parameters, although progress is being made towards methods robust against hard-to-estimate parameters [56]. A complementary method, applicable at high resolution, is to construct a histogram of atomic column intensities and to delineate clusters of intensities in the histogram as integer atom counts in the column. This route has been pursued extensively by van Aert and co-workers, using a model-based approach with statistical parameter estimation theory to aid analysis of atomic column intensities and assignment of atom counts [57, 60, 63–66].

2.3 Spectroscopy in TEM

To complement the BF/DF imaging modes in TEM, spectroscopic signals may be recorded. The most established of these are energy dispersive X-ray spectroscopy (EDXS) and electron energy-loss spectroscopy (EELS). The energy of the X-rays emitted from the specimen when probed by the electron beam, or energy lost by electrons that have been inelastically scattered as they pass through the specimen, are characteristic of the constituent atoms. These techniques are therefore used for elemental identification and, under favourable circumstances, for quantification. EELS can often provide information on more intricate properties such as bonding states, surrounding atomic environment and plasmonic response.

EDXS is most commonly implemented using a Si semiconductor detector on one side on the microscope column. The restricted detector geometry can make obtaining sufficient X-ray counts from thin TEM specimens challenging. Recently though, large solid angle silicon drift detectors have become available for TEM [67]. Although not used in this thesis, the scope for more routine EDXS tomography is of relevance to the ET development in chapters 5-8.

EELS involves the collection and energy-resolved analysis of the forward scattered beam, which is usually achieved using a post-column spectrometer, and can be further sub-divided into energy-filtered TEM (EF-TEM) and STEM-EELS. In STEM-EELS, EEL spectra spanning a selected but relatively broad energy-loss range are acquired point-by-point, whereas in EF-TEM an image is formed in parallel using electrons in a specific energy-loss window. A considerable

strength of STEM-EELS is that the ADF signal can be acquired simultaneously, and this is also the case for STEM-EDXS.

EDXS and EELS are covered comprehensively by, amongst others, Williams and Carter [19] and Egerton [68], and recent developments are addressed in [20, 26]. Advances in spectroscopic TEM hardware exploited in this thesis are: AC optics, covered in the next section; a high-brightness field-emission gun ('X-FEG') electron source, enabling higher probe current for a given probe size [69]; beam monochromation, improving energy resolution in EELS [70]; and a fast (Gatan GIF Quantum) EEL spectrometer, reducing STEM-EELS acquisition time.

The post-processing of data obtainable from the EDXS and EELS signals is also advancing through the development of sophisticated software for noise reduction and information extraction. Particularly, methods falling under the umbrella terms of 'multivariate analysis' or 'blind source separation' such as principal component analysis (PCA) and independent component analysis (ICA) have shown considerable success [71, and references therein]. They offer an automated means of identifying significant components in the data using minimal prior knowledge, which can be especially useful in the case of low SNR or overlapping spectral features. Another variant of such methods, 'non-negative matrix factorization' (NMF) [72, 73], is applied to STEM-EELS data for the first time in chapters 3 and 8. Briefly, NMF performs an approximate factorisation of a positive matrix into (usually) two positive matrices, with the non-negativity constraint making the obtained matrices generally easier to analyse. Valuably, spatially resolved STEM-EELS data can be decomposed into (i) the spectral components and (ii) the corresponding spatial distribution maps, with the positivity constraint precluding unphysical negative spectral components.[3]

Due to more limited signal count rates in comparison to the BF and ADF signals, EDX or EELS signals are often recorded at selected points or as line-scans. However, with hardware advances yielding higher count rates and/or post-processing enabling noisy data to be treated effectively, 2D point-wise recording in STEM, to form a 'spectrum-image' [74], is becoming feasible more frequently (reviewed by Colliex, Kociak et al. in [8, 20]). Using microscopes optimised for spectroscopic performance, STEM-SI can yield several novel forms of information from nanoparticulate specimens, including information pertaining to the morphology of localised surface plasmon resonance, which is exploited in

[3]The application of NMF was carried out in close collaboration with (chapter 3), or exclusively by (chapter 8), Dr Francisco de la Peña.

this thesis in chapter 8. However it is important to point out that, in many cases, application of spectroscopic techniques to nanoparticulate specimens can be very challenging owing to the weak signal obtainable from the small particle before radiation damage or carbonaceous contamination (detailed below in section 2.5) limits the acquisition. As such, it is often the ADF-STEM signal that is more efficacious for high-resolution compositional analysis of small nanoparticles.

2.4 TEM in the aberration-corrected era

Major improvements in electron optics took place at the turn of the century for both CTEM [2] and STEM [3–5]. The partial correction of spherical aberration limiting the performance of electron lenses has facilitated a step change in capabilities. A great many materials insights have been realised in recent years that were previously unobtainable.

Electron lenses are notoriously poor, suffering from 'aberrations'. Figure 2.4b illustrates how spherical aberration degrades lens performance by focusing rays passing through the periphery of the lens to a different point than those passing through the centre. Practically, this deficiency can now be corrected using a series of multipole lenses.

Although the poor performance of electron lenses had been highlighted by Scherzer in 1936 [75], and many attempts at aberration correction had been made since that time, it was not until availability of the required computational power, efficient algorithms, precision in component fabrication and stability of electrical components that AC optics yielded performance improvements in practice. First generation AC optics have addressed the major limiting aberration, third-order spherical aberration. In a more select number of microscopes, correction of

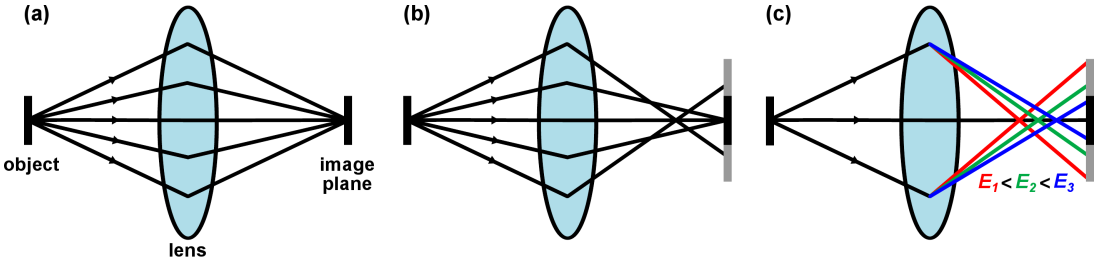

FIGURE 2.4: A perfect lens and the major electron optical aberrations. (a) A perfect lens focuses a point source to a single point in the image. (b) Spherical aberration: electrons passing through the periphery of the lens are focused more strongly than those passing through the centre. (c) Chromatic aberration: electrons of different wavelength (or equivalently, different energy E) are focused differently.

spherical aberration to fifth order has been implemented, leaving, in many cases, chromatic aberration correction (Figure 2.4c) as the next-step [76], which is currently an active (although niche) research area.

The new capabilities and opportunities with AC optics were reviewed comprehensively at a Royal Society Discussion in 2009 [8] and in a dedicated volume of Advances in Imaging and Electron Physics [6]. Details of AC optics can also be found in [20, 26, 48, 76, 77], and reviews of enabled materials insights are numerous, e.g. [6–8, 20, 30, 31, 35]. The salient capabilities of AC-STEM of relevance to this thesis are summarised below.

Firstly, by virtue of the ability to use a larger probe forming aperture (and therefore convergence semi-angle α, see Figure 2.2b), it is possible to form a smaller probe (Figure 2.5), improving lateral resolution in imaging. The resolution improvement follows intuitively from the incoherent imaging model: the STEM image is approximately a convolution of the probe intensity profile with the object function. The latter is sharply peaked at atomic sites, and so the resolution is essentially determined by the probe size. A probe size of ca. 1 Å is now commonplace, and sub-0.5 Å resolution can be achieved using resolution-optimised microscopes and amenable specimens [78]. Figure 2.6 charts the rise in resolving power as high-resolution microscopy has progressed from light to electron optics to AC electron optics.

While a discussion of AC optics will almost invariably begin by emphasising resolving power, the advantages extend well beyond point-to-point resolution. The sharper probe can enable much clearer imaging of nanoparticle shape, defects, surface structures such as steps, kinks and adatoms and few/single-atom species, as highlighted in the pioneering study of Batson et al. [79]. Further, the smaller full-width half maximum and reduced tails of an AC probe can reduce the contribution of the probe to neighbouring atomic columns, yielding stronger chemical contrast between columns of different composition.

Particularly advantageous is the increased probe current permitted by the larger objective aperture, enabling shorter acquisition times and higher SNRs. The ‘quality’ of atomic resolution imaging (see for example Figure 1-34 in [20]) and spectroscopy [80] have been raised due to the better counting statistics and reduced sample drift.

Another significant opportunity is the ability to work at lower accelerating voltages yet still achieve atomic resolution (reviewed in [20, chapter 15]). This can allow reduction of knock-on damage, which is the primary source of damage for many inorganic nanoparticles (see section 2.5).

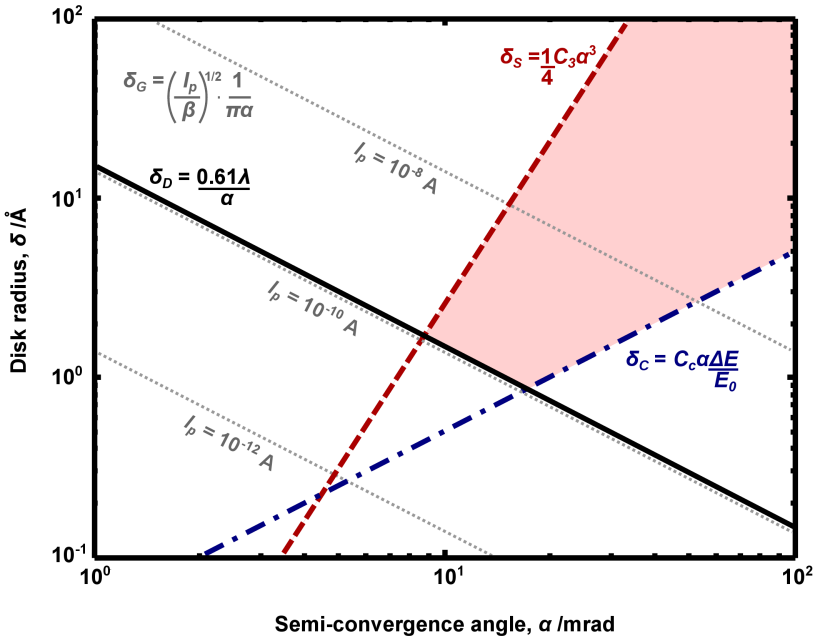

FIGURE 2.5: Contributions to STEM probe size based on a geometric model, and indication of the parameter space (shaded in pink) opened up by (third-order C_3) spherical aberration correction. The error disks due to diffraction δ_D , spherical aberration δ_S, chromatic aberration δ_C and effective source diameter δ_G (shown for three different probe currents I_p) are dependent on the illumination semi-convergence angle α. The spherical and chromatic aberration coefficients C_3 and $C_C = 1$ mm. The electron source has a brightness $\beta = 5\text{x}10^{12}$, an energy width of $\Delta E = 1$ eV and the beam energy $E_0 = 200$ keV, yielding an electron wavelength $\lambda = 2.5$ pm. After refs. [19, 26, 77].

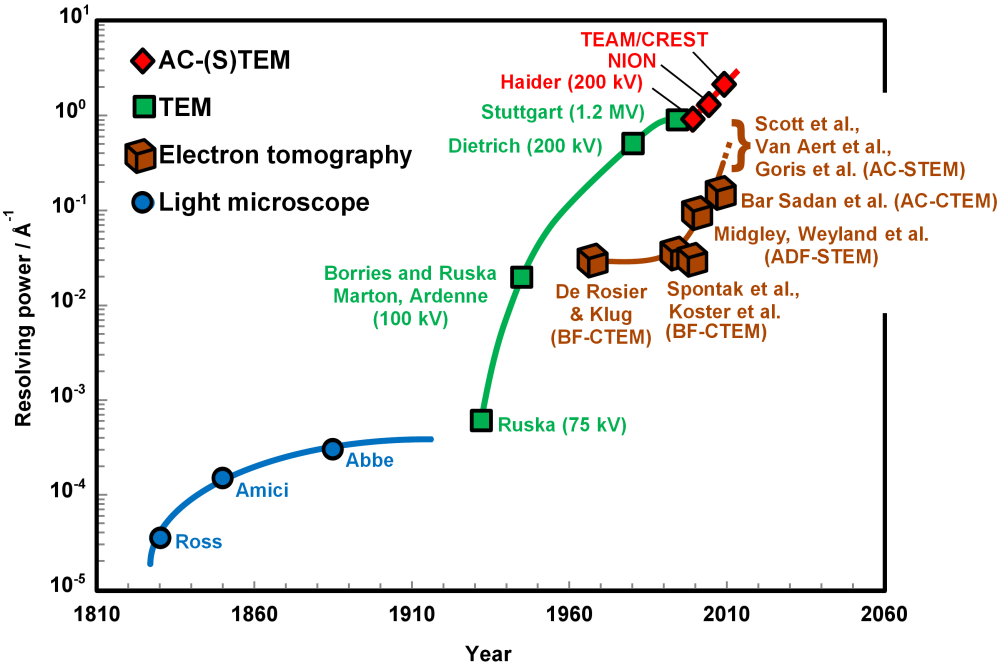

FIGURE 2.6: Resolving power of light and transmission electron microscopy techniques over time. Adapted from H.H. Rose [6, chapter 1].

A lesser mentioned benefit is improved phase contrast imaging using BF-STEM. This is due to the increased probe currents and the ability to increase the collector aperture whilst maintaining coherent conditions (see Pennycook et al. in [8]). Although the ADF-STEM signal is still frequently the most valuable, and the imaging conditions may be optimised for the ADF image, the BF-STEM signal can be recorded simultaneously. Potentially important and complementary information may be revealed in the BF-STEM image, making it good practice to record both.

Finally, the ability to widen the objective aperture also reduces the depth-of-field Δz, varying as $\Delta z \approx \lambda/\alpha^2$ (more rapidly than lateral resolution, $\Delta(x, y) = \lambda/\alpha$), where λ is the electron wavelength. While this can hamper conventional approaches to imaging of thick specimens by rendering large portions of the image out of focus, it can alternatively be used to obtain 3D information by 'optically sectioning' the specimen (discussed in section 5.4).

2.5 Beam-induced damage & contamination

While yielding the valuable signals that form the basis of TEM analysis, the electron beam-specimen interactions (Figure 2.1) can act to alter the specimen to a non-negligible degree. Beam-induced excitation is sometimes harnessed in 'dynamic' studies (e.g. [64]). The goal more often though, is to obtain a representative 'native-state' analysis of the specimen, motivating careful protocols to minimise beam-induced changes. The most significant damage mechanisms, identified by Egerton et al. [81], are: displacement damage, sputtering, heating, electrostatic charging, ionization damage (radiolysis) and hydrocarbon contamination.

Enabled by AC-optics, low beam energy operation has recently fallen *in vogue*, offering the potential to reduce atom displacement or sputtering. Concurrently though, reduced beam energy leads to an increase in the inelastic cross section, increasing ionisation damage and heating effects. In cases where these effects dominate, the tolerable electron dose becomes critical, which may relate to the total dose and/or dose rate.[4] Potential beam damage must be traded against higher SNRs as dose increases.

Hydrocarbon contamination occurs due to polymerisation of mobile hydrocarbons (which may come from the specimen itself) by incoming or outgoing

[4]It is worth remarking that the increased probe currents available with AC-optics may actually have raised the prevalence, or at least the pertinence, of dose related damage.

electrons. Therefore, as it builds up, contamination insidiously obscures the very region being examined. Despite improvements in microscope vacuum, the use of an *in situ* 'cold finger' onto which contaminants may deposit and knowledge of the need for clean specimens, contamination remains a frequent problem in TEM.

Regardless of the particular damage or contamination mechanism, it is clear that lower electron beam exposure will result in less beam-induced modification. This is especially critical in ET, where multiple images need to be acquired, and faithful tomographic reconstruction is reliant on the premise that the specimen does not change form during collection of the image series. Hence there is strong motivation to develop methods that reduce the necessary electron dose, as addressed in chapters 7 and 8.

2.6 Conclusions

ADF-STEM can provide directly interpretable imaging and chemically sensitive analysis, making it well-suited to the intuitive investigation of nanoparticle morphology. Enhanced by AC optics, it is possible to analyse with clarity all species and structural features down to atomic-scale intricacies, including atomic column chemical composition and inter- and intra-particle heterogeneities. Such direct analysis has the potential to reveal crystallographic morphology of bimetallic nanocatalysts such as the Ga-Pd nanocatalysts addressed in this thesis, and also to permit high-fidelity 3D morphological analysis via ET. Recent advances in spectroscopy can offer valuable complementary information to ADF-STEM and offer new opportunities in spectroscopic ET. Beam damage and contamination remain as prevalent problems in TEM, creating pressing need for methods that can reduce electron beam exposure.

Chapter 3

Revealing the atomic structure of $GaPd_2$ nanocatalysts

This chapter addresses the study of 'nano-sized' intermetallic Ga-Pd catalysts using AC-STEM. It begins with an introduction to the rational design underlying the Ga-Pd catalysts. This is followed by discussion of intricacies that may arise on nanostructuring, a review of previous characterisation efforts, and identification of gaps in knowledge to which TEM analysis can contribute. Results from ADF imaging and EELS are presented, and the observed manifestation of the intermetallic compound in the nano-sized catalysts is discussed from a crystallographic and catalytic perspective. The central aspect addressed is the extent to which the rationally selected intermetallic structure is attained in the nanoparticles. This relates not simply to success of the synthesis process, but also to effects that may lead to features distinct from the 'ideal' bulk crystal structure, especially those related to 'nano-sizing'. These include surface segregation, nanoparticle shape and nanostructural defects. The results shown in this chapter have been published in [82].

3.1 Introduction

3.1.1 Rational design of catalytic morphology

The role of solid heterogeneous catalysts is to mediate desired interactions of reactants, with the critical chemical processes taking place usually on, or in close vicinity to, the catalyst surface [1]. The atomic-scale surface (and possibly near-surface) features of the catalyst must adsorb reactants, direct adsorbate interactions along the desired reaction pathway and enable facile dissociation

of products. Moreover, any unwanted reactions must be discriminated against, i.e. the catalyst must be selective. Structural, compositional and electronic properties of the surface are known to play crucial roles in choreographing these processes [1, 11, 83–89]. Armed with such knowledge, it becomes possible to embark upon *rational catalyst design*. In the rational design approach, particular materials systems and morphologies are selected or developed to meet the desired surface properties. Such practices, rather than haphazard trial-and-error searches, form the bedrock of much efficacious (nano)catalysis research, and are the basis of this chapter.

3.1.2 Intermetallic compounds as well-defined catalysts

Intermetallic compounds, as defined by Schlögl and co-workers [90], are materials that possess an - at least partially - ordered crystal structure that differs from those of the constituent elements. They are single phase and, in contrast to a random 'alloy', offer uniformity of structure (Figure 3.1).[1] Correspondingly, in pursuit of well-defined active sites, they have been identified as promising catalytic materials [90]. In addition, their distinct crystal structure can result in a strongly altered electronic structure [11, 87, and references therein], influenced by the often covalent interactions between the atoms; hence conferring the ability to tailor, or at least select, this critical property too. Intermetallic compounds therefore offer a tantalising opportunity to pursue rational catalyst design, in which the use of well-defined systems can enable detailed relation of the structure and properties of the intermetallic compound to catalytic performance.

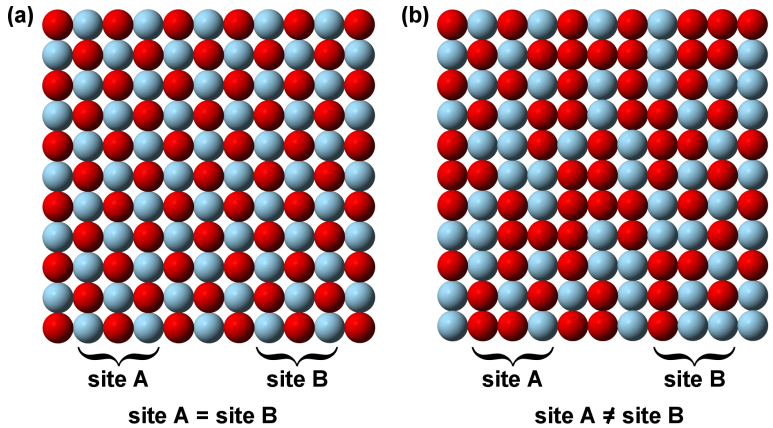

FIGURE 3.1: The chemically ordered structure of an intermetallic compound (a) in comparison to a random alloy (b). The former offers consistent surface sites.

[1] Some authors do not make this important distinction.

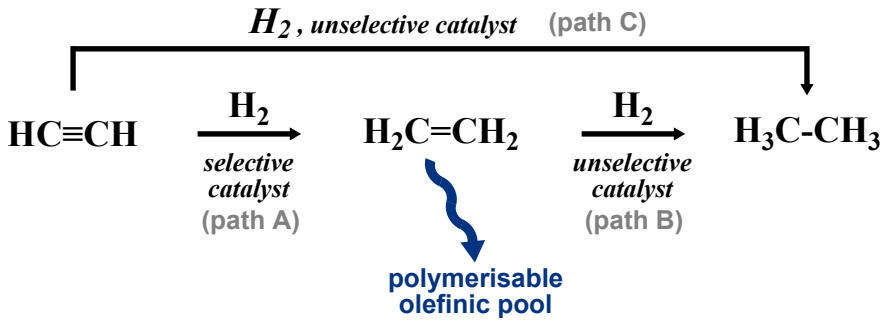

FIGURE 3.2: Selective and unselective hydrogenation of acetylene. Partial hydrogenation of acetylene to ethylene (path A) is desired, while the full hydrogenation (paths B or C) is undesired. In a general context, a selective hydrogenation catalyst must facilitate the hydrogenation of a C≡C bond to a C=C bond, but not hydrogenate as far as a C−C bond.

3.1.3 Intermetallic Ga-Pd catalysts

In a series of studies, stemming from ca. 2007 [90], it has been established that intermetallic Ga-Pd compounds constitute a promising new class of catalyst. Predominantly, they have been targeted for effecting selective hydrogenation[2] of acetylene (C_2H_2) [11]. This reaction is of considerable importance for removal of acetylenic impurities in polyethylene production (which amounts to ca. 50 Megatons per year), and is quite elegant in that the impurities may be profitably converted into part of the ethylene (C_2H_4) pool that is polymerizable (path A in Figure 3.2) [83, 91]. The catalyst must be 'selective' in that the full hydrogenation (paths B or C in Figure 3.2) to ethane (C_2H_6) must be avoided. Beside other polymerisation reactions, such as polypropylene and polystyrene production, selective hydrogenation is also of central importance in a number of fine and intermediate chemical syntheses, including agrochemicals, pharmaceuticals, vitamins, flavours and fragrances [91, 92].

Accordingly, significant attention has been devoted to the development of catalysts for effecting selective hydrogenation reactions, with the aim to achieve simultaneous high *selectivity*, *activity* and *stability* [83, 84, 87, 88, 91, 92]. Entailing a firm - although often intricate - example of the importance of structure-property relationships, it has indeed been evident that these characteristics may be imparted via geometric and electronic effects - through judicious control of the catalyst's composition, crystal structure, size and shape - making possible the rational design of high performance catalytic systems.

Monometallic Pd is highly active for hydrogenation reactions. However, the Pd catalysts typically suffer from poor selectivity and deactivation. While numerous interpretations of the Pd catalytic mechanism can be found in the

[2]Sometimes referred to as 'semi-hydrogenation'.

literature, the salient point to note is that rational design and the control of activity and selectivity is challenging due to the significant roles of Pd hydrides and a Pd-C phase formed in *in situ* during particular reaction conditions [87].

To improve selective hydrogenation performance, the concept of 'active site isolation' has been pursued, such as in Ag-Pd alloys [93]. In those systems the beneficial effect can be interpreted in terms of a dilution of Pd, reducing the size of homoatomic Pd ensembles, which minimises the unwanted reactions that require larger active sites than the partial hydrogenation [84]. Alternatively, Nørskov and co-workers have interpreted the beneficial effect based on electronic modification [85]. Alloying can shift the d-band away from the Fermi level, which may endow selectivity by lowering the energy barrier of desorption of the ethylene intermediate compared to the energy barrier to further hydrogenation. In any case, however, these solid solution type alloys are prone to segregation of Pd to larger active sites, resulting in diminishing selectivity [93, 94].

Seeking to overcome these problems, the well-ordered crystal structures and covalent bonding in Ga-Pd intermetallic compounds have been identified as offering precise active site isolation and modification of electronic structure [11, 85, 90]. Under the proviso that this intrinsic catalytically efficacious structure is stable under reaction conditions, they are a clear example of rational catalyst design. Catalytic testing concerning the selective hydrogenation of acetylene shows that they can indeed yield superior performance to the conventional monometallic Pd or Ag-Pd alloy catalysts [11]. Further, in addition to selective hydrogenation reactions, Ga-Pd systems have also received considerable interest with regards to application in several other important processes, such as methanol synthesis and methanol steam reforming [95–104].

3.1.4 Unraveling complexities of 'nano-sized' Ga-Pd catalysts

In foundational studies, the use of model systems, specifically single-phase unsupported Ga-Pd compounds in bulk or powdered form, has enabled detailed analysis of the unique structural and electronic properties of the intermetallic compounds, and the relation of these properties to catalytic performance [90, 105–110]. With the aim of achieving systems that may be applicable industrially, attention is now also being given to the development of high-performance nanoparticulate Ga-Pd catalysts [11, 97, 102, 111–115].

The transition from bulk to nanoparticulate form is a pivotal step in the development of the Ga-Pd catalysts. Nano-sizing can have many consequences

for mono- and multi-metallic systems and properties quite distinct from the bulk may arise [21, 116–118], with catalytic implications [119] - it is indeed precisely because unique properties frequently arise in nanoscale systems that the field of nanotechnology (including nanocatalysis) is flourishing!

Although the catalytic efficacy of bulk and nanoparticulate Ga-Pd intermetallic compounds has been demonstrated, anomalous behaviour has been observed. Therefore aspects determining the observed catalytic behaviour require further elucidation, most fundamentally the precise structural and chemical state of the intermetallic compound in the nanoparticulate form. Several studies have already been performed [11, 97, 102, 111–115], employing techniques such as X-ray diffraction (XRD), X-ray absorption spectroscopy (XAS), Fourier transform infrared (FTIR) spectroscopy and X-ray photoelectron spectroscopy (XPS), while spatially resolved analyses such as provided by TEM (although there are some notable exceptions) have played only a supporting role.

In the investigations reported in this thesis, the specific advantages offered by TEM have been used to address hitherto challenging or relatively unexplored aspects of the Ga-Pd catalysts in nanoparticulate form. The main topics addressed may be divided into:

- Confirmation of phase in nano-sized form
- Compositional segregation and surface stability
- Size, shape and nanostructural defects

3.1.4.1 Confirmation of phase in nano-sized form

A significant difficulty noted in previous investigations is that the Ga-Pd phase diagram (Figure 3.3) [120], reveals a number of possible phases, many of which have similar crystal structures. This makes unambiguous verification of the phase in nanoparticulate form extremely challenging using conventional techniques such as XRD, or even BF-CTEM. It is shown here that it is possible to alleviate this ambiguity through atomic-scale chemically sensitive imaging, using ADF imaging in AC-STEM. This is achieved by identifying individual nanoparticles oriented such that the electron beam is parallel to particular crystal zone axes where the image of the structure is unique to the phase of interest, $GaPd_2$. Shown in Figure 3.4, $GaPd_2$ has an orthorhombic Co_2Si-type [121] crystal structure; specifically *Pnma* (No. 62), a = 5.4829(8) Å, b = 4.0560(4) Å, c = 7.7863(8) Å [122].

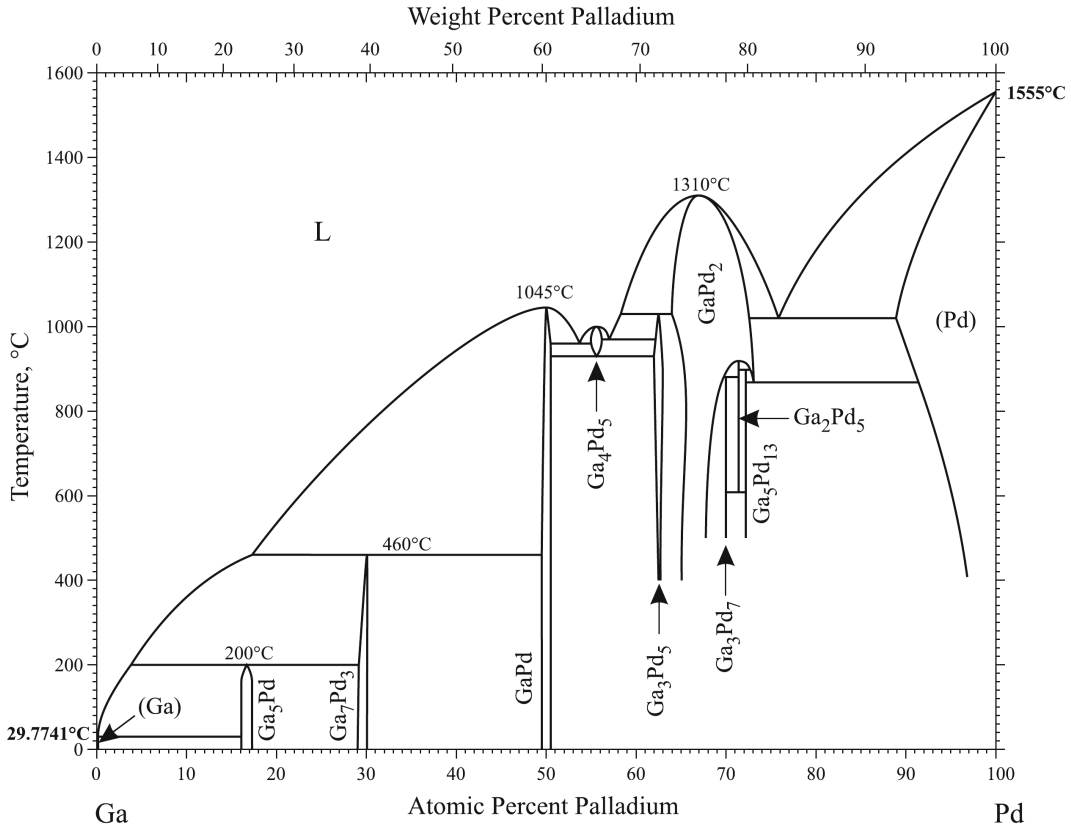

FIGURE 3.3: Ga-Pd phase diagram. Reproduced from [120].

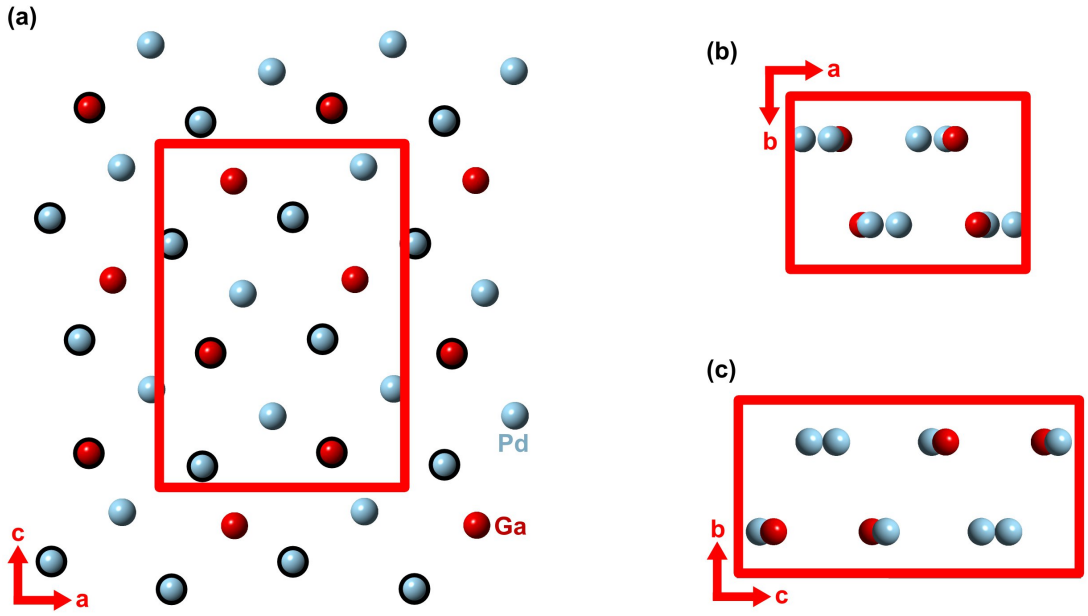

FIGURE 3.4: Crystal structure of $GaPd_2$ viewed down the (a) [010], (b) [001] and (c) [100] zone axes, with Pd atoms in blue and Ga atoms in red. In (a) atoms outlined in bold are located at $y = \frac{1}{4}$, the others at $y = \frac{3}{4}$.

3.1.4.2 Compositional segregation and surface stability

The high proportion of surface atoms in nanoparticles gives added importance to the nature of the surface (and near-surface) structure and its stability, which may not be the same as for the 'bulk' form of the compound. It is well-known that peculiar mixing patterns can be rife in nano-sized particles; Figure 3.5, taken from Ferrando et al.'s thorough review of nanoalloys [117], depicts just some of the compositional mixing/segregation possibilities in bimetallic nanoparticles. When a support material and other species, such as surface adsorbates, are considered, the possibilities for deviation from the 'model' structure clearly become even greater.

It has indeed already been observed that while the bulk structure of Ga-Pd compounds is stable in an oxidising environment, a decomposition of the surface may occur, resulting in partial coverage by Ga_xO_y species [97, 100, 102, 103, 105–108, 112, 113]. Owing to the potentially significant catalytic implications of such surface modifications, particularly for nanoparticulate Ga-Pd catalysts, the occurrence and nature of the decomposition has received considerable attention, including specific investigation with regard to nanoparticles of $GaPd_2$.

Haghofer et al. [97, 113], in particular, have investigated the surface stability of Ga_xO_y-supported $GaPd_2$ nanoparticles exposed to oxidising conditions similar to those involved in this work, using a combination of XRD, FTIR spectroscopy of CO absorption and XAS. They concluded that the resultant state of the nanoparticles was one in which Ga segregated to the near-surface regions and formed oxidic islands on the surface of the nanoparticles, leaving behind a surface layer that consisted of regions of $GaPd_2$, Ga-depleted intermetallic and metallic Pd, while the core was still $GaPd_2$. Their proposed model is shown in Figure 3.6.

The combination of bulk and surface sensitive techniques used by Haghofer et al. [97, 113] enabled powerful insights and confidence in their nanostructural model, but it is readily appreciated that direct imaging has the potential to yield complementary information. While a segregated over-layer can be seen in BF-CTEM images presented in some publications, these lack the required chemical

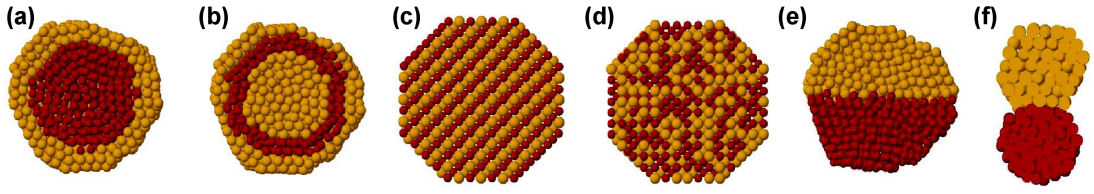

FIGURE 3.5: Some possible mixing patterns in bimetallic nanoparticles: (a) core-shell, (b) three-shell, (c) ordered, (d) random, (e, f) sub-cluster segregated. Reproduced from [117]

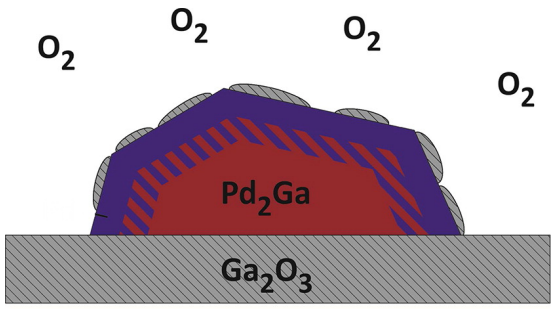

FIGURE 3.6: Structural model proposed by Haghofer et al. [113] for the state of $GaPd_2$ nanoparticles (supported on Ga_2O_3) following exposure to O_2. The red/purple hatched region indicates a zone of Ga depleted intermetallic compound between the $GaPd_2$ core (red) and a largely Pd-like surface (purple) decorated with Ga oxides (grey).

sensitivity. Chemically sensitive ADF imaging and spatially resolved EELS in AC-STEM, however, are shown here to be apt for this task.

3.1.4.3 Size, shape and nanostructural defects

Markedly lacking in most previous studies of the Ga-Pd system, yet potentially of high importance, is thorough consideration of nanoparticle size, shape and structural defects. The interplay between (nano)particle size/shape and catalytic reaction mechanisms is generally termed 'structure sensitivity'. Although the concept of structure sensitivity is by no means new ([123–125] are often cited as pioneering studies), it is now expressly articulated that thorough and precise investigations into nanoparticle structure and relation to catalytic structure sensitivity can play an essential part in realising and improving rationally designed nanocatalysts [88, 126–131]. These aspects have been identified as significant in selective hydrogenation by monometallic Pd [88, 127], yet have received relatively little attention with regards to Ga-Pd catalysts (understandable in light of their novelty). Direct imaging using AC-STEM offers the opportunity to begin to address this aspect by identifying the nanoparticle morphologies present.

Fundamentally, it is necessary to identify the basic size, shape and crystallographic morphologies of the nanoparticles. Thereafter, it is desirable to retrieve as much information as possible about the nature of the terminating atomic planes bounding the nanoparticle. Further, nanoparticles, by their nature, introduce additional structural features compared to a planar bulk terminated surface: low coordinated corner atoms (at the junctions between surface lattice planes), steps, kinks, adatoms or surface irregularities due to nanocrystalline defects. While the use of bulk surfaces with different terminating planes or with

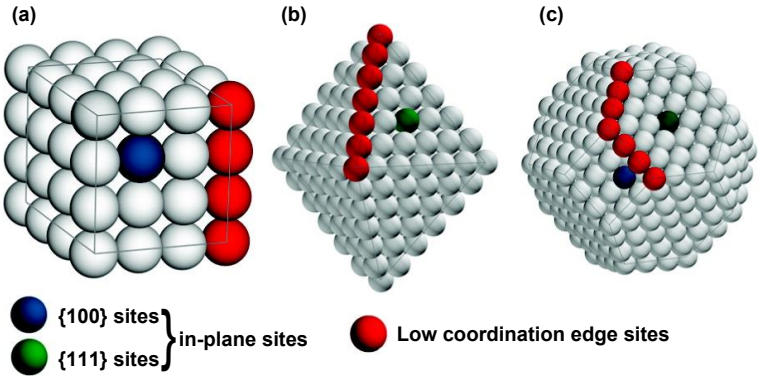

FIGURE 3.7: Identification of different surface sites endowed by FCC nanoparticle morphology in the (a) cube, (b) octahedron and (c) truncated octahedron. In-plane atoms constitute one class of site, and can be further identified as {100} or {111} plane atoms. Low coordinated atoms at edges or corners provide a different atomic environment. Adapted from [127].

defects such as steps and kinks can enable some structure-property correlations of such features [132], such idealised samples still lack the overall complexity of a genuine nanoparticulate system; a discrepancy known as the 'materials gap'. Hence, thorough characterisation of the real nanocatalyst is vital.

Metals and alloys that in principle possess a face centred cubic (FCC) crystal structure - by far the most widely studied to date and shown hereinafter to be relevant to the present study - are found typically to exhibit structures corresponding to truncation on {100} and {111} planes, forming octahedral, truncated octahedral, cuboctahedral and cubic morphologies depending on the ratio of {100} to {111} surface areas [21, 116]. In these (defect free) morphologies, primarily three distinct environments can be identified, as shown in Figure 3.7: {111} plane atoms, {100} plane atoms and low coordinated edge/corner atoms.

These have been variously implicated as endowing differing activity, selectivity and stability in selective hydrogenation reactions depending on the particular nanocatalyst and reaction of interest. It is worth reiterating that unravelling of size and shape effects in the case of selective acetylene hydrogenation by Pd is markedly complicated by the role of dynamic phases formed *in situ*, which in turn can be structure sensitive [133]; as discussed in [88, 126, 134].

Other, more complex, nanocrystalline morphologies may also be derived from an FCC lattice such as the rhombic dodecahedron, or those with significant higher index faceting, most often endowing rounded morphologies. Figure 3.8 shows the principal defect free morphologies considered by Barnard in recent theoretical modelling of Pd nanocatalysts [135]. Also common are nanoparticles with defects, such as the single twinned truncated octahedron, examples of which are shown in Figure 3.9. Multiple parallel twinning is also possible, often termed

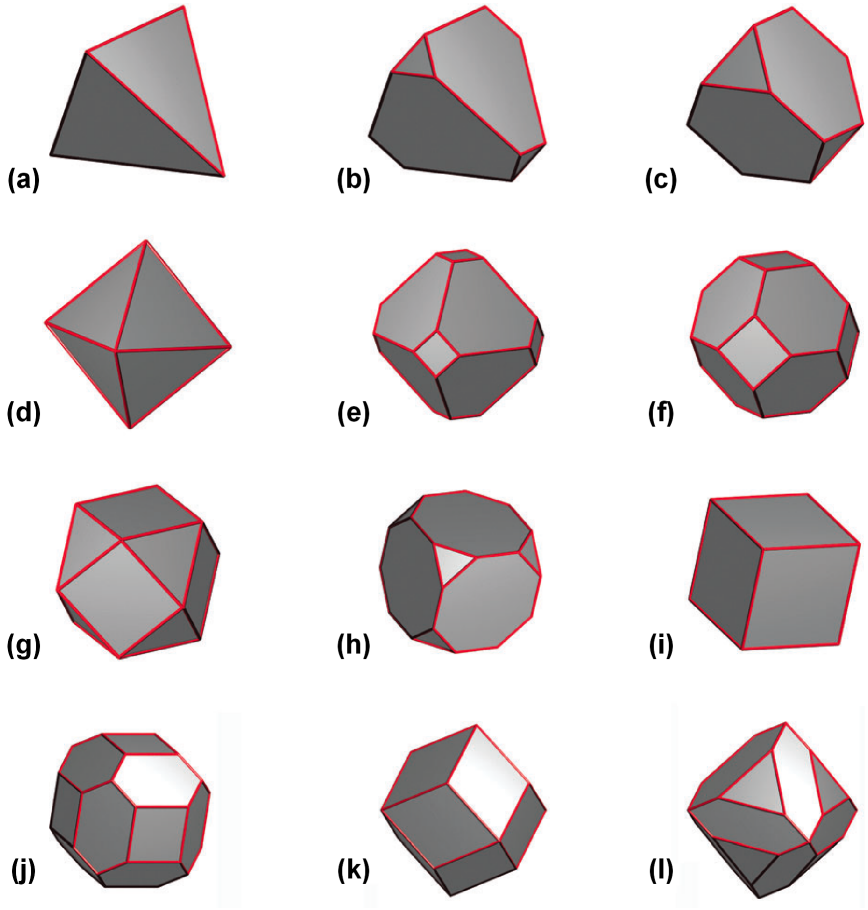

FIGURE 3.8: Defect-free FCC nanoparticle morphologies. The first four shapes [(a) regular tetrahedron, (b) minimally-truncated tetrahedron, (c) truncated tetrahedron, and (d) octahedron] are entirely enclosed by {111} facets, whereas the following shapes [(e) minimally-truncated octahedron, (f) truncated octahedron, (g) cuboctahedron and (h) truncated cube] are enclosed by an increasingly large fraction of {100} facets, until the cube (i) which is entirely enclosed by {100} facets. The final shapes [(j) cubo-rhombic dodecahedron, (k) rhombic dodecahedron, and (l) octo-rhombic dodecahedron] are based on the rhombic dodecahedron, enclosed by a combination of {100} and {110} facets, entirely with {110} facets, and a combination of {111} and {110} facets, respectively. Reproduced from [135].

'lamellar' twinning.

In addition to the nanocrystalline morphologies, it is found frequently that 'non-crystallographic' five-fold twinned decahedral and icosahedral morphologies may arise, examples of which are shown in Figure 3.10. These occur primarily, though not exclusively, in smaller (<10 nm) nanoparticles, where surface energy contributions are significant. For these morphologies, an ideal FCC lattice would not entirely fill space, meaning that some form of lattice distortion is required [21, 116, 118, 136, 137]; a topic pursued in detail in chapter 4.

Naturally, in more complex morphologies, there is greater diversity of active sites. In a bimetallic system, the potential diversity is raised further, as both structurally and chemically different terminating planes may arise.

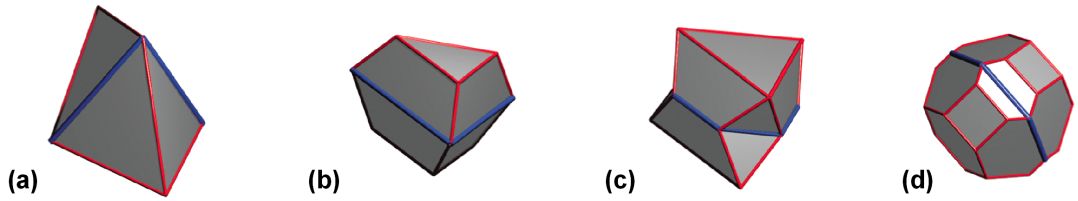

FIGURE 3.9: Twinned FCC nanoparticle morphologies: (a) tetrahedral bipyramid, (b) truncated tetrahedral bipyramid, (c) symmetrically twinned octahedron, (d) symmetrically twinned truncated octahedron. Twin boundaries are highlighted in blue (regular edges appear in red). Reproduced from [135].

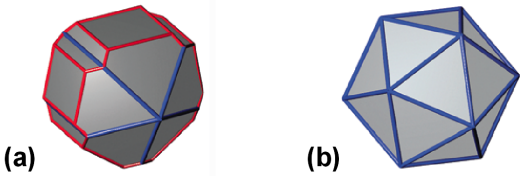

FIGURE 3.10: Multiply twinned ('non-crystallographic') nanoparticle morphologies: (a) Marks decahedron, and (b) Mackay icosahedron. Twin boundaries are highlighted in blue (regular edges appear in red). Reproduced from [135].

Furthermore, the potential significance of nanostructural defects, such as twins, lattice distortion or other surface irregularities should not be underestimated. For example, it has been proposed recently, with the aid of AC-CTEM, that ornate atomic-scale defects, comprising Cu steps decorated with Zn atoms that are stabilised by bulk defects and surface species, constitute the active site in $Cu/ZnO/Al_2O_3$ catalysts employed in the methanol synthesis reaction [95]. Alternatively, as recently shown in the AC-CTEM work of Walsh et al. [25], the induced lattice strain in five-fold twinned nanoparticles, in their case in decahedral Au nanocatalysts for CO oxidation, can have immediate catalytic implications.

The prevalence of certain terminating lattice planes, and of crystalline or non-crystallographic nanoparticle morphologies, relates to surface, strain, twinning and compositional segregation energies, with the prevailing structures often dependent on both thermodynamic and kinetic effects [21, 116–118, 138]. Synthesis processes, observation conditions and the intrinsic properties of the particular materials system may all be highly influential.

Lastly, despite the desire, in many cases, to control precisely nanoparticle morphology, it is also frequently the case that nanoparticle populations comprise many irregular morphologies. These may arise, for example, from irregular growth processes or subsequent particle coalescence, especially when the synthesis process is challenging.

While theoretical modelling of nanoparticle morphology, such as the 'Wulff construction' and its variants (reviewed recently in [138]) or first principles atomistic simulations such as Barnard's [135] should play a part in the development of Ga-Pd nanocatalysts, empirical characterisation is also vital. For the Ga-Pd catalysts studied here, many fundamental factors that may be influential in practice are yet to be identified clearly. To contribute to the present level of knowledge, the further, grounding, empirical characterisation addressed here is befitting.

3.2 Methods

3.2.1 Nanoparticle synthesis

The Ga-Pd nanoparticles studied here were synthesised by co-reduction of ionic precursors, followed by an additional annealing step.[3] Figure 3.11 summarises the synthesis; a comprehensive description has been given by Armbrüster et al. [111]. The co-reduction leads initially to the formation of Pd nanoparticles, followed by Pd-mediated reduction of Ga^{3+} on their surfaces, requiring annealing to obtain single-phase products. Either single-phase GaPd or $GaPd_2$ (as indicated by XRD) can been produced according to the specific synthesis parameters. The latter is studied here in (nominally) unsupported form, seeking to avoid additional affects of a particular support material.[4] The synthesis distinctly avoids the use of surfactants that would block or modify the intrinsic nanoparticle surface. A consequence however, combined with the absence of a support material, is that significant particle agglomeration is inevitable.

3.2.2 AC-STEM imaging

AC-STEM was performed on an FEI Titan Cubed 80-300 (S)TEM equipped with an X-FEG source, Wien-type monochromator (not used in this investigation) and CESCOR probe aberration corrector (CEOS GmbH). Ga-Pd nanoparticle samples were deposited as a dry powder or from a methanol suspension, onto standard holey C film Cu mesh support grids (Agar Scientific) or 5 nm thick Si

[3]The nanoparticles studied here as well as in chapters 3, 6 and 8 were synthesised by Mr Gregor Wowsnick, Ms Yuan Luo and Dr Marc Armbrüster (Max-Planck-Institut für Chemische Physik fester Stoffe, Nöthnitzer Str. 40, 01187 Dresden, Germany).

[4]This investigation is still therefore, to a considerable extent, a 'foundational' or 'model' study, seeking to explore the intrinsic properties of the nano-sized intermetallic compound, rather than a fully industrially applicable system.

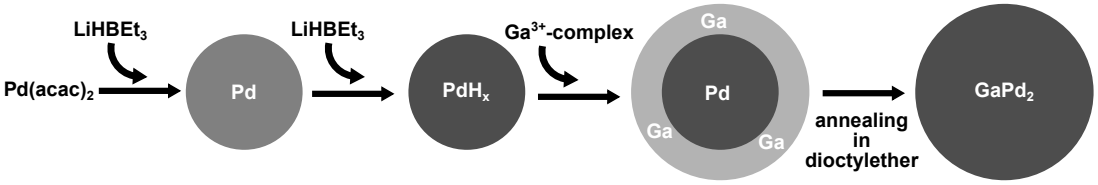

FIGURE 3.11: Proposed mechanism for the two-step synthesis of $GaPd_2$ [111]. The co-reduction of ionic metal precursors (acac = acetylacetonate) with Superhydride ($LiHBEt_3$ in tetrahydrofuran) leads initially to the formation of Pd nanoparticles, followed by a Pd-mediated reduction of Ga^{3+} on their surface. Subsequent annealing in dioctylether at high temperature is required to form single phase $GaPd_2$.

membranes (TEMwindows, SiMPore Inc.). ADF imaging was performed at 80 or 300 kV, with a probe semi-convergence angle of 15 or 22 mrad and an ADF detector inner angle of 40 mrad. A beam current of ∼60 pA and per-pixel dwell times of ∼10 μs (resulting in a typical electron dose of ∼10^6-10^7 electrons per nm^2) were found to yield the most satisfactory ADF images of both the smaller and larger nanoparticles, including imaging of the surface/near-surface regions. These were judged to be parameters that provided, in most cases, adequate SNR yet sufficiently negated beam induced modification of the nanoparticles to enable a representative first-pass image to be acquired.

3.2.3 Image processing

The Fourier transforms shown in Figures 3.14-3.16 were obtained after first applying a Hanning window to the image. These can be thought of as analogous to the diffraction pattern that would be produced from the imaged region, and therefore, with reference to a simulated diffraction pattern, be used to aid structure identification. The low-pass Fourier filtering of the ADF images in Figures 3.14-3.16, applied for noise reduction, was achieved using a 2^{nd} order Butterworth filter [139] with a nominal cut-off of 0.1 nm.

3.2.4 AC-STEM-EELS

AC-STEM-EELS was performed[5] on the same FEI Titan used for the high-resolution imaging, with a probe semi-convergence angle of 22 mrad. Spectra were recorded using a Gatan 865 Tridiem spectrometer and a collection semi-angle of 52 mrad. To minimise potential electron beam-induced modification of the nanoparticles, the EELS was performed at 80 kV with low beam currents and small dwell times, at the expense of reduced spatial resolution and SNR. EELS

[5]STEM-EELS acquisition was carried out in close collaboration with Dr Jon Barnard.

line scans were recorded for the energy-loss ranges 210-620 eV and 910-1320 eV; the former incorporating the Pd $M_{4,5}$-edge at 335 eV, the Pd M_3-edge at 531 eV, the Pd M_2-edge at 559 eV and the O K-edge at 532 eV (as well as the C K-edge at 284 eV), and the latter the Ga $L_{2,3}$-edge at 1115 eV and Ga L_1-edge at 1298 eV [68, 140].

The intensity of the EELS signal corresponding to Pd at each point in the line scans was obtained by the curve fitting method [141, 142]. The overlap of the Pd M_3- and Pd M_2-edges and O K edge preclude the quantification of the O EELS signal using conventional methods. However, as noted in section 2.3, it has been shown that blind source separation methods offer the potential to achieve a decomposition of the EELS signal into components that correspond to the different species in the sample, even in the case of severely overlapping spectral features [71, and references therein]. In this work NMF [72, 73] was used to decompose the EELS signal into significant components, obtaining the spatial distribution of the different chemical species across the 1D line scans. The EELS analysis[6] was performed using Hyperspy, [71][7] which harnesses a projected gradient method for NMF [143, 144].

3.2.5 Crystal structure analysis

Crystal structure parameters used for the identification of Ga-Pd phases were taken from the following references: $GaPd_2$ [122], Ga_5Pd_{13} [145], Ga_2Pd_5 [146], Ga_3Pd_7 [147], Ga_3Pd_5 [148], Ga_4Pd_5 [146], GaPd [149], Ga_7Pd_3 [146], Ga_5Pd [150]. Structural models and simulated diffraction patterns were generated using CrystalMaker and SingleCrystal (CrystalMaker Software Ltd.).

3.3 Results and discussion

3.3.1 Overview

Figures 3.12a and 3.12b show simultaneously acquired ADF- and BF-STEM images, recorded at relatively low magnification to provide a representative overview of the sizes and morphologies of the unsupported Ga-Pd nanoparticles. The dense packing (which, as noted in section 3.2.1 is expected due to the absence of additional stabilisers [111]), and the overlap of the nanoparticles when viewed in projection, prohibits a quantitative estimate of the nanoparticle size

[6] EELS analysis was carried out in close working collaboration with Dr Francisco de la Peña.
[7] Hyperspectral Data Analysis Toolbox. Available At: http://Hyperspy.Org/.

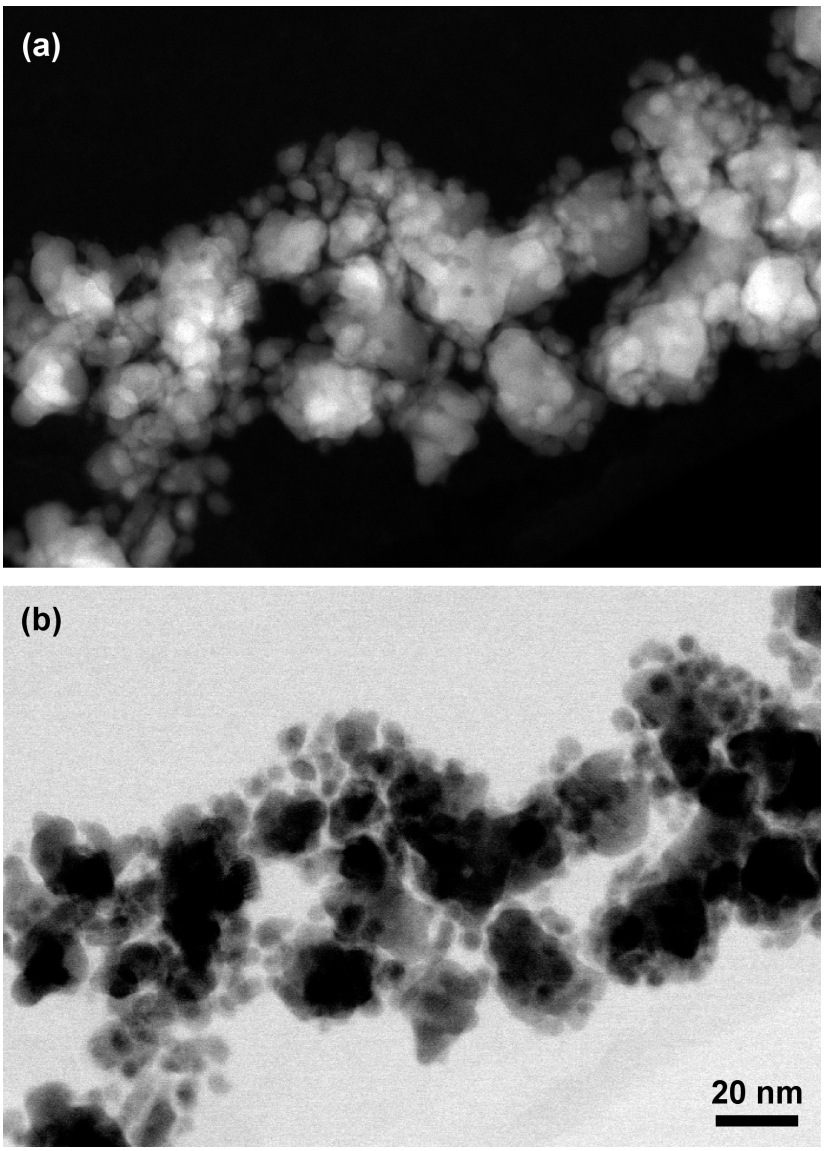

FIGURE 3.12: Simultaneously acquired low magnification ADF (a) and BF (b) STEM images of the Ga-Pd nanoparticles.

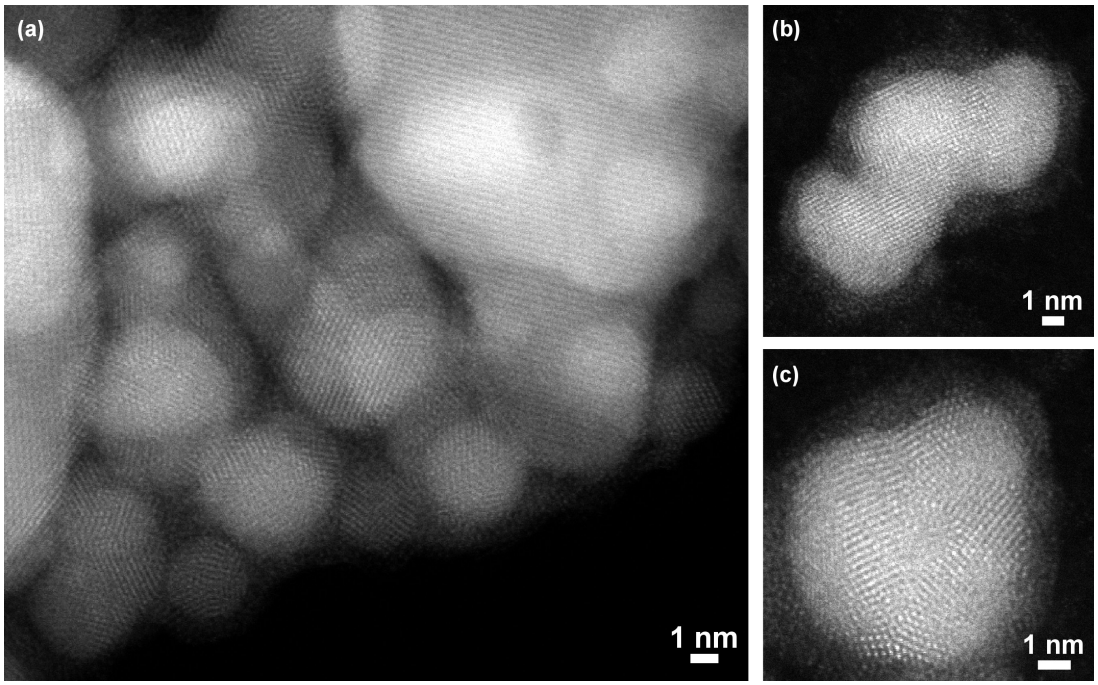

FIGURE 3.13: ADF-STEM images illustrating the sizes and morphologies of the Ga-Pd nanoparticles. (a) Small (<10 nm) and larger single crystalline nanoparticles. (b, c) Examples of polycrystalline nanoparticles resulting from the coalescence of multiple nanoparticles.

and shape distributions based on 2D images. This motivated the 3D ET study described in chapter 6, where the size distribution is shown to be strongly peaked in the sub-10 nm range. Polydispersity within the population is also revealed by ET, with the size distribution extending to ca. 30 nm equivalent diameter, and comprising a diverse range of nanoparticle morphologies. This is consistent with the AC-STEM studies, which show that the larger nanoparticles may be single crystalline or polycrystalline. Irregular shapes, exemplified in Figure 3.13, arise primarily due to the agglomeration or coalescence of multiple smaller nanoparticles, although polycrystalline growth is also likely to be responsible. Also evident in Figure 3.13 is a disordered over-layer that surrounds much of the nanoparticles. Consistent with the previously observed surface decomposition (cf. Figure 3.6), this was seen to be present on the majority of nanoparticles and is addressed in section 3.3.3.

3.3.2 Confirmation of phase in nano-sized form

Although both ADF and BF images are shown in Figure 3.12, the latter is included only for completeness. It was shown in ref. [82] to illustrate to the reader unfamiliar with STEM that ADF and BF signals can be acquired simultaneously. As expected from the discussion in chapter 2, the direct interpretability of ADF

images in terms of the projected atomic structure of the sample has proven far more powerful in this investigation; in particular the atomic number '*Z*-contrast' enabling distinction between atomic columns consisting of Ga or Pd. This is shown clearly in Figures 3.14-3.16, in which ADF-STEM has been used to identify the intermetallic $GaPd_2$ structure in nanoparticles oriented suitably with respect to the electron beam.

Figure 3.14a shows an ADF image of a number of nanoparticles, in which a nanoparticle in the lower right hand side is oriented favourably, enabling atomically-resolved images of the crystal structure to be recorded. Figure 3.14b is a subsequent (unprocessed) image recorded at higher magnification from the boxed region (ai) in Figure 3.14a. The left hand portion of the image is disturbed by an underlying nanoparticle at a different orientation, but the right hand side clearly shows the chemically ordered structure of $GaPd_2$ viewed parallel to the [010] zone axis. This is confirmed in Figure 3.14c by the agreement between a simulated diffraction pattern for [010] $GaPd_2$ and a Fourier transform of the image in Figure 3.14b. Figure 3.14d shows the same region as Figure 3.14b following a low-pass Fourier filtering operation to reduce noise in the image, over which the [010] projection of part of the $GaPd_2$ structure has been placed, further reinforcing the match.

Although $GaPd_2$ possesses an orthorhombic crystal structure [122] (the unit cell is shown in red in Figure 3.14d), there is a close relationship between the structure and a distorted FCC lattice [146, 147], which is most clear in the [010] projection. This is illustrated in Figure 3.14d, where two 'FCC-like' units are outlined by dashed black lines. This is an important theme brought out by the direct imaging, and is addressed again in this chapter and in chapter 4.

The [010] zone axis of $GaPd_2$ is also particularly distinctive because it is one of relatively few zone axes in $GaPd_2$ in which the projected columns are well-spaced and consist exclusively of well-aligned Ga (shown in red) or Pd (shown in blue) atoms. Significantly, this particular ordering of Ga and Pd columns is found only in $GaPd_2$. As described in chapter 2, the ADF imaging mode is sensitive to the projected thickness and constituent atoms of the sample, therefore for a small area, over which the thickness of the sample is approximately constant, the relative intensities of the atomic columns in the ADF image can be used to infer their chemical composition. This is shown in Figure 3.14e for a selected region (di) from Figure 3.14d, containing two 'FCC-like' units. The unprocessed (ei) and low-pass filtered (eii) images are shown in false colour to emphasise the atomic number contrast between the columns of atoms, which as shown by overlaying

the structural model in (eiii) are in agreement with those of $GaPd_2$; the columns consisting of the lower atomic number Ga ($Z = 31$) having a lower intensity in the image than those of Pd ($Z = 46$). Although there are other Ga-Pd phases that possess very similar crystal structures that also bear resemblance to a distorted FCC-lattice [145–147], the clear correspondence to the orthorhombic symmetry and lattice spacings of $GaPd_2$, coupled with the direct verification of the distinct chemical ordering shown in Figure 3.14e enables a confident identification as $GaPd_2$.

As a second example, Figure 3.15 shows an ADF image of a $GaPd_2$ nanoparticle oriented close to the [311] zone axis. The atomic model for [311] $GaPd_2$ is shown inset in (ai), confirming the direct interpretability of the image (a), where the positions of atomic columns correspond to high image intensity. The identity and orientation of the nanoparticle is further confirmed in Figure 3.15b by the agreement between the simulated diffraction pattern for [311] $GaPd_2$ and the Fourier transform of the image in Figure 3.15a. Although in this case, the alignment of the Ga or Pd atoms in the atomic columns is less distinct compared to that in the [010] projection, and the sampling (pixel size) is coarser in Figure 3.15a compared to Figure 3.14b, it is still possible to resolve detail of the atomic columns and their chemical nature.

A selected region (aii) from Figure 3.15a is shown in Figure 3.15c, over which the nanoparticle is of sufficiently constant thickness to facilitate relative analysis of the atomic column intensities. By comparing the unprocessed (ci) or low-pass filtered (cii) images with the [311] projection of the $GaPd_2$ structure, which is overlaid in (ciii), it is evident that the image once again reflects the chemical ordering present in $GaPd_2$. Although at this zone axis the atoms are not precisely in alignment down the atomic columns, it is sufficiently clear that the brighter columns in the image correspond to those that consist exclusively of the higher atomic number Pd atoms (an example of which is outlined in white in each image), compared to columns on either side, of lower intensity in the image, that consist of a mixture of Ga and Pd (examples of which are outlined in black).

For a third example, Figure 3.16 shows an ADF image of a nanoparticle that can be assigned to the [120] zone axis of $GaPd_2$. As seen clearly in the inset structural model, the distinct characteristic of the intermetallic crystal structure in this orientation is the undulating (or 'wavy') nature of the lattice planes. Although the ADF image (a) and its associated Fourier transform (b) cannot be unambiguously assigned to $GaPd_2$ in preference to some other Ga-Pd phases, it nevertheless shows the intermetallic state.

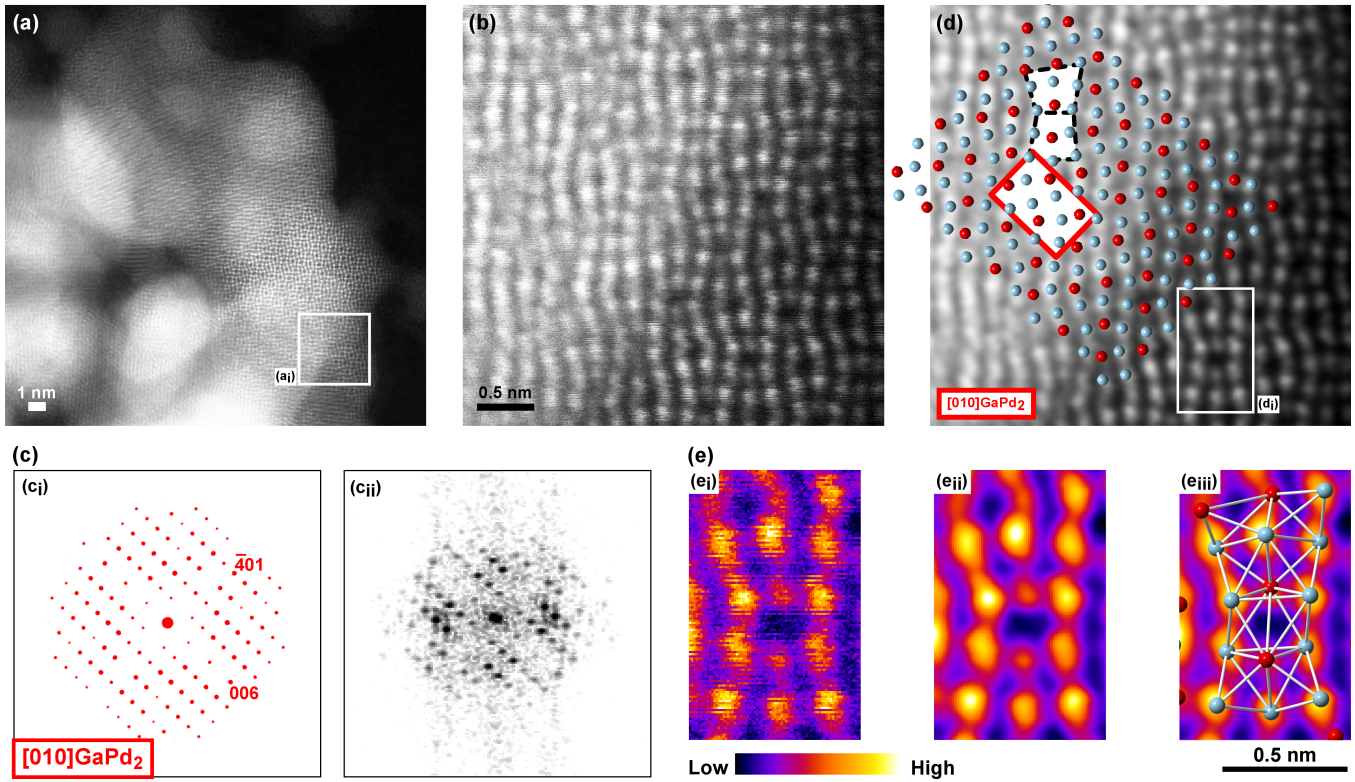

FIGURE 3.14: Identification of nanoparticulate $GaPd_2$ via the [010] zone axis. (a) Atomically resolved ADF image showing a collection of nanoparticles, in which the nanoparticle in the lower right hand side is oriented close to the [010] zone axis. (b) Subsequently recorded higher magnification ADF image of the region (ai) indicated in (a). (c) Confirmation of [010] $GaPd_2$ via comparison of the simulated diffraction pattern (ci) and the Fourier transform (cii, shown with inverted contrast) of the image in (b). (d) The region shown in (b) after low-pass Fourier filtering. The structure of $GaPd_2$ in [010] projection is overlaid with Ga atoms shown in red and Pd atoms in blue. The orthorhombic unit cell is outlined in red, and two 'FCC-like' units are outlined by dashed black lines to emphasise the close relationship of the structure to an FCC lattice. (e) A selected region (di) from (b) and (d) over which the thickness of the nanoparticle is sufficiently constant to enable a relative comparison of the intensities of the atomic columns in the image. (ei) is from the unprocessed image (b) and (eii) from the low-pass Fourier filtered image (d). A portion of the $GaPd_2$ structure in [010] projection (containing two 'FCC-like' units with nearest neighbour bonds shown) is overlaid in (eiii), confirming that the lower intensity atomic columns in the image correspond to those in the [010] projection of the $GaPd_2$ structure that exclusively contain Ga, and likewise the higher intensity columns in the image match with those in the [010] projection that exclusively contain Pd.

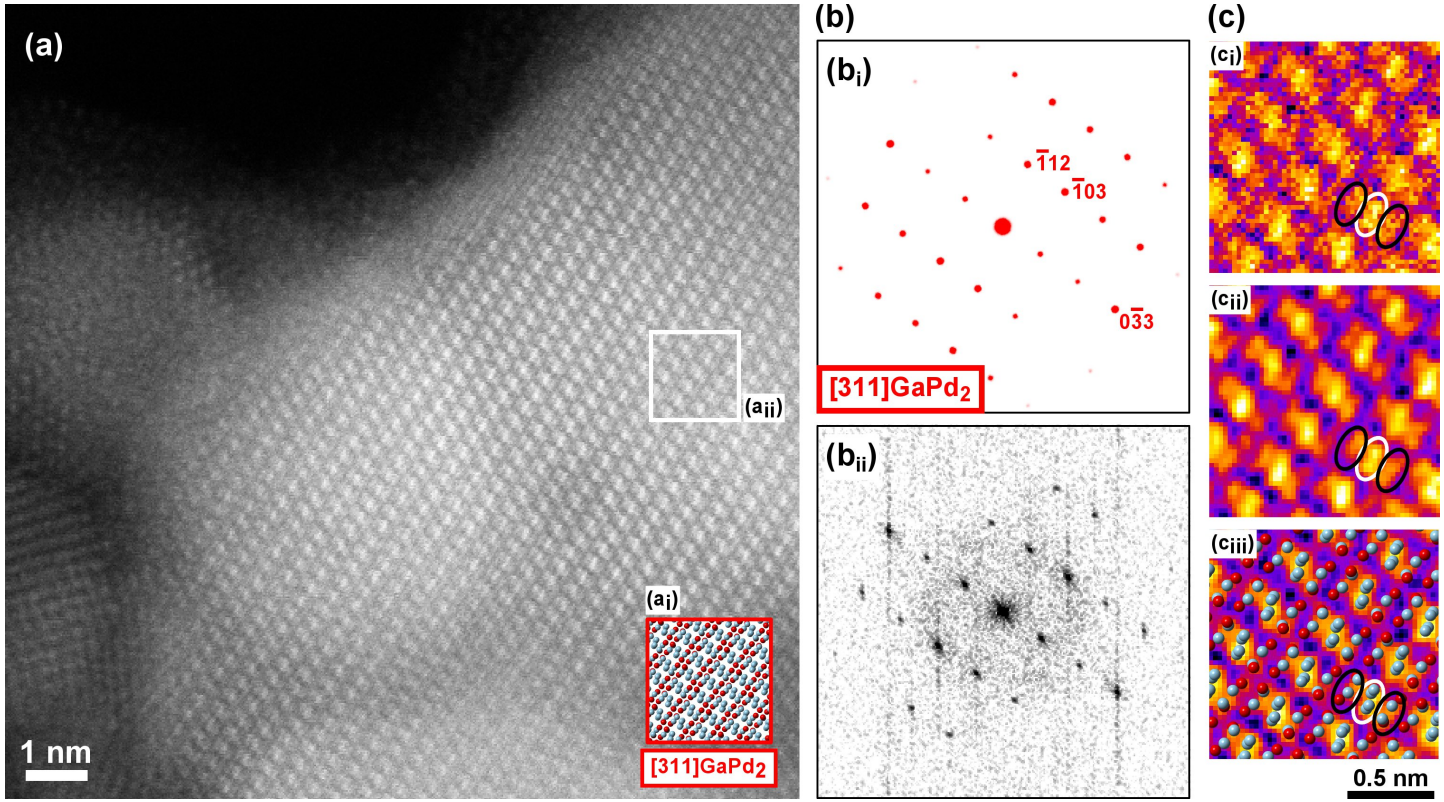

FIGURE 3.15: Identification of nanoparticulate $GaPd_2$ via the [311] zone axis. (a) Atomically resolved ADF image showing a $GaPd_2$ nanoparticle oriented close to the [311] zone axis. The structural model of $GaPd_2$ in [311] projection is inset in (ai), where Ga atoms are shown in red and Pd atoms in blue. (b) Further confirmation of [311] $GaPd_2$ via comparison of the simulated diffraction pattern (bi) and the Fourier transform (bii, shown with inverted contrast) of the image in (a). (c) A selected region (aii) from (a) over which the thickness of the nanoparticle is sufficiently constant to enable a relative comparison of the intensities of the atomic columns in the image. (ci) is from the unprocessed image (a), and (cii) has been low-pass Fourier filtered. (ciii) The $GaPd_2$ structure in [311] projection is overlaid on the selected region, confirming that the higher intensity atomic columns in the image match with those in the $GaPd_2$ structure that exclusively contain Pd, an example of which is outlined in white in each image, and that columns of lower intensity in the image match with those in the structural model that consist of a mixture of Ga and Pd, examples of which are outlined in black in each image. The colour map assigned to the images in (c) is the same as used in Figure 3.14e.

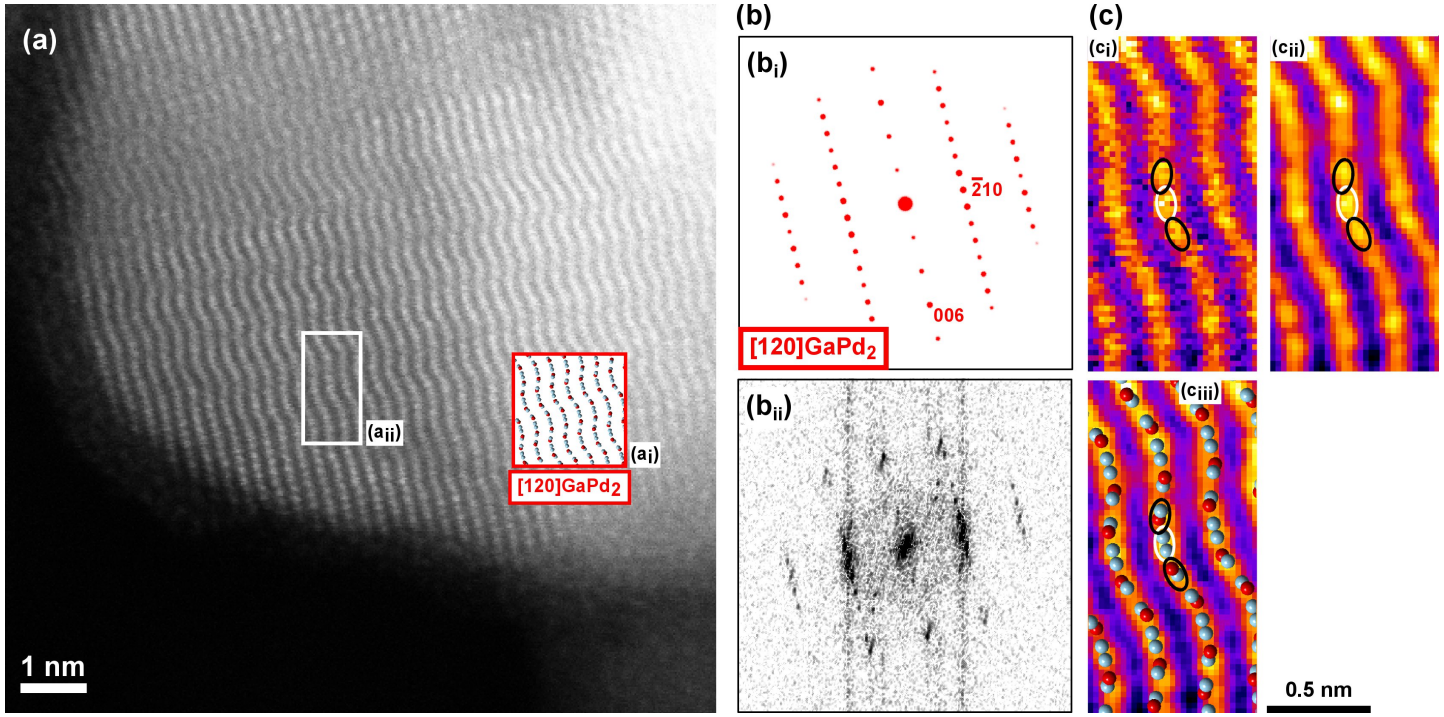

FIGURE 3.16: Identification of a nanoparticle that can be assigned to the [120] $GaPd_2$ zone axis, also exhibiting interior and near-surface deviations from the ideal bulk crystalline structure. (a) Atomically resolved ADF image showing the crystal structure of a nanoparticle that is consistent with $GaPd_2$ viewed close to the [120] zone axis. The structural model of $GaPd_2$ in [120] projection is inset in (ai), where Ga atoms are shown in red and Pd atoms in blue. (b) Comparison of the [120] $GaPd_2$ simulated diffraction pattern (bi) and the Fourier transform (bii, shown with inverted contrast) of the image in (a), showing a general match, but some deviations due to the lattice distortions visible in the image in (a). (c) A selected region (aii) from (a), over which the thickness of the nanoparticle is sufficiently constant to enable a relative comparison of the intensities of the atomic columns in the image. (ci) is from the unprocessed image (a), and (cii) has been low-pass Fourier filtered. (ciii) The $GaPd_2$ structure in [120] projection overlaid on the selected region, showing that the atomic columns in the image (regions of localised intensity maxima along the lattice planes) can be correlated with the different atomic columns in the $GaPd_2$ structure. One type consists of Pd, an example of which is outlined in white in each image, and the other on either side consists of a mixture of Ga and Pd, examples of which are outlined in black in each image. The contrast that could arise in the image due to the compositional differences of the atomic columns is reduced by the effects of the different spatial arrangements of the atoms within the columns, and possibly also due to a slight tilt off the exact zone axis. The colour map assigned to the images in (c) is the same as used in Figure 3.14e.

In [120] projection, the chemical ordering of the $GaPd_2$ structure is less easy to discern compared to the [010] or [311] zone axis images. The atomic number (Z) contrast is reduced somewhat by the effects of the spatial distribution of the atoms on the intensity of the atomic columns in the image. Still, as shown in (c), it is possible to correlate the different atomic columns in the image with those in the $GaPd_2$ structure; one type consisting of Pd (an example of which is outlined in white in each image) and the other on either side that consists of a mixture of Ga and Pd (examples of which are outlined in black).

Additionally however, Figure 3.16 also clearly shows deviations from the ideal intermetallic structure, both in the interior of the nanoparticle in terms of a distortion of the undulating nature of the lattice planes from the ideal shown in the structural model (ai), and at the near-surface regions, where the lattice planes are seen to 'relax' to a straighter form. This 'relaxation' could be the result of structural and/or chemical effects. Structurally, it is well-known that the distribution of strain in the interior and surface regions of nanoparticles may be different, and in particular that lattice relaxation and reconstruction can occur at the surface [21, 116, 118]. In the present case, the structural deviations in the interior regions may also be influenced by adjoining (sintered or agglomerated) nanoparticles visible in the upper and right hand regions of the image. Concerning the near-surface regions, there is reason to believe that chemical segregation effects may also be playing a role.

3.3.3 Compositional segregation and surface stability

The spatially resolved analysis into segregation effects, using ADF imaging and EELS is summarised in Figures 3.17 and 3.18, and is consistent with the model proposed by Haghofer et al. [97, 113]. Figures 3.17a-c show ADF images of the surface and near surface regions from selected areas of the nanoparticles shown in Figures 3.14-3.16, respectively, with a colour map chosen to enhance the visibility of the disordered over-layer decorating the surface. An illustrative example showing the over-layer on smaller nanoparticles is shown in Figure 3.17d. These images were all acquired as the first high-magnification/slow scan image acquisition over the region of interest. Upon continued exposure to the electron beam, the over-layer was observed to be mobile, forming more ordered crystalline arrays that in general appear to form an interface coherent with the crystalline surface planes of the 'core' of the nanoparticles.

The fact that the over-layer is readily visible using the ADF imaging mode is evidence of the presence of high Z (strongly scattering) atomic species, consistent

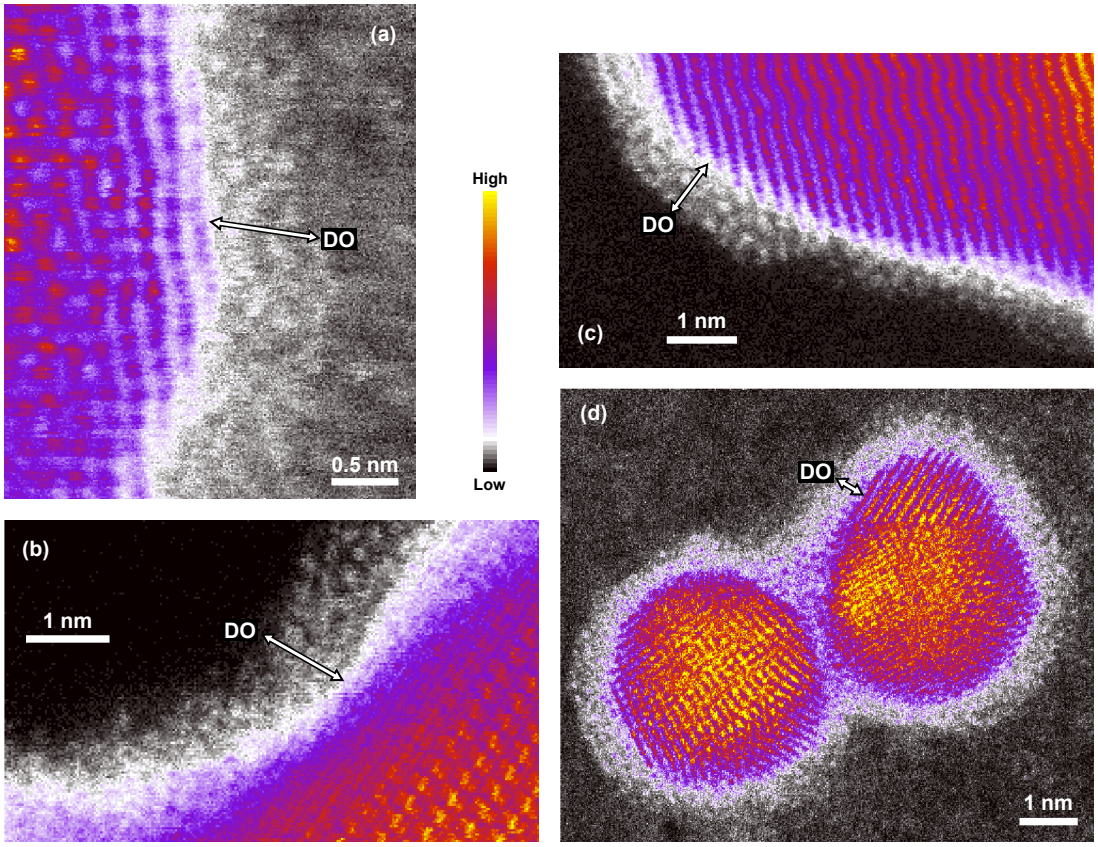

FIGURE 3.17: ADF images of the surface regions of the Ga-Pd nanoparticles, shown in false colour to emphasise the disordered over-layer (DO) decorating the surfaces. (a-c) Surface regions from nanoparticles shown in Figures 3.14-3.16, respectively. (d) Representative example of the over-layer on smaller nanoparticles.

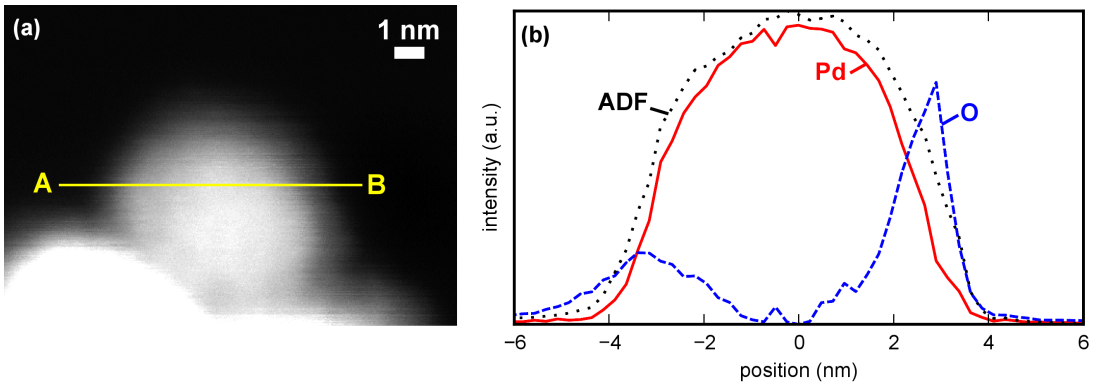

FIGURE 3.18: AC-STEM EELS analysis of an individual nanoparticle, in the energy range incorporating the relevant Pd and O edges. (a) Position of a 1D EELS line scan (A to B) across the nanoparticle. (b) Corresponding profiles for Pd (obtained by curve fitting, solid red line) and O (obtained by NMF, dashed blue line), along with the simultaneously acquired ADF signal (dotted black line), showing that Pd is present in the 'core' of the nanoparticle, while O is only present at the periphery of the nanoparticle.

with the presence of Ga. According to the synthesis process (section 3.2.1, [111]) for the nanoparticles studied here, surface Ga could also result from incompletion of the synthesis reaction that involves Ga diffusion into an initially monometallic Pd core. However, the evident formation of the intermetallic compound, as exemplified in Figures 3.14-3.16, and previous characterisation [111] of the successful reaction product following the same synthesis process, suggests that subsequent segregation effects are likely.

Seeking to further confirm the chemical identity of the over-layer, AC-STEM EELS line scans were recorded across isolated nanoparticles. The extent of the present analysis is limited by the low SNR of the data and the small number of spectra acquired, but the results are nonetheless immediately informative.

An NMF decomposition of the spectra in the range 210 to 620 eV into three components was found to model the dataset with sufficient accuracy. The first two components could be directly identified as corresponding to Pd and O, respectively. Figure 3.18 shows the spatial distribution of the O component across one isolated nanoparticle, clearly in agreement with the presence of an oxidic over-layer surrounding a Pd-containing core. The third component could not be unequivocally identified due to the limited SNR, although is likely to correspond to Pd in a different chemical state/environment. Similarly, although the application of NMF to the EELS line profiles recorded in the energy range incorporating the Ga $L_{2,3}$ and L_1 edges suggested the presence of more than one significant component, indicating the presence of Ga in more than one chemical state/environment, the low SNR of the spectra prohibited reliable identification of the status and spatial distribution of these components.[8]

The ADF images of Figure 3.17 support the notion that the over-layer may form predominantly as 'islands,' rather than completely covering the nanoparticle surface, therefore leaving exposed regions of the inner metallic/intermetallic core; although recalling previous studies [97, 100, 102, 103, 105–108, 112, 113] (and the more recent studies of Wowsnick et al. [151, 152], discussed specifically in section 3.3.5) the amount may be variable, dependent on the support material, pre-treatment history and oxidative conditions. Additionally, the images corroborate the existence of different surface/near-surface states. In Figure 3.17a it can be seen that the 'distorted-FCC' structure of the $GaPd_2$ nanoparticle in [010] orientation persists to the very edge of the nanoparticle. The over-layer in this case is relatively less developed compared to those in

[8]The individual components yielded by NMF are not shown here as the interpretation requires exposition beyond the confines of this thesis. The interested reader is referred to the references in section 2.3.

Figures 3.17b and c; evident as the ADF image intensity corresponding to the over-layer is lower and only slightly greater than that resulting from the thin (in this case 5 nm Si) support film. In Figures 3.17b and c, where the over-layer is more extensive, a degradation of the intermetallic structure towards the surface is more evident, particularly so in Figure 3.17c where the undulation of the lattice planes subsides, leaving straight planes with more distinct atomic columns near the surface.

In this regard it is worth noting that in contrast to many intermetallic compounds (including the line compounds in the Ga-Pd system) that exhibit quite pronounced stoichiometry, the $GaPd_2$ phase (which should more strictly be referred to as Co_2Si-type [121] $Ga_{1-x}Pd_{2+x}$) can exist over a relatively broad compositional range [147, 148]. Hence it is possible to see how for small amounts of segregation of Ga to surface oxides, it may be possible to retain the Co_2Si-type structure.

On the other hand, as noted by Wannek and Harbrecht [147], only small shifts of the atom positions in $GaPd_2$ (of less than 50 picometres) are required to transform the $GaPd_2$ crystal structure into one of an undistorted, mainly ordered 'FCC-like' arrangement; a phenomenon that was indeed increasingly approached in progressively Pd rich (Ga poor) $Ga_{1-x}Pd_{2+x}$ phases. Hence it is plausible to suggest that a significant driving force in the observed relaxation of the intermetallic structure may be related to the segregation of Ga to the surface, and that the relaxed structure may be a Pd rich ordered FCC-like manifestation of the intermetallic, akin to a mainly ordered Ga_xPd_{1-x} solid solution.

For more extensive Ga segregation, a Ga_xPd_{1-x} solid solution in which little chemical ordering persists could predominate, or, in the extreme, the 'relaxed' structure could indeed correspond to FCC metallic Pd. However, it is plausible to suggest that a random alloy Ga_xPd_{1-x} solid solution at the surface is unlikely, given that the solubility of Ga in Pd is <3 at% at ambient temperature [120]. The EELS line scans did not reveal regions devoid of Ga, which suggests the absence of large regions of metallic Pd, although the recording of more and higher quality EELS (or EDXS) data is necessary to verify this with certainty. Accordingly, this would suggest that, for the nanoparticles studied here, an ordered structure is most likely at the surface, be it in the Co_2Si-type structure, or a 'relaxed' but ordered 'FCC-like' manifestation of the intermetallic compound. Finally, although segregated Ga should have a higher affinity to form surface oxides, the presence of Pd oxides should not be discounted.

3.3.4 Size, shape and nanostructural defects

As established in section 3.1.4.3, it is important to consider the morphologies observed here for the Ga-Pd nanoparticles, which may lead to a predisposition to certain surface structures, or other properties of the nanoparticles that are distinct from the bulk. As they form a greater proportion of the population, and the larger Ga-Pd nanoparticles found are typically complex agglomerates displaying irregular morphologies, the focus here is on the small nanoparticles in the sub-10 nm range. Moreover, this is precisely the size regime in which cross-over between bulk-like, nanocrystalline and non-crystallographic structures becomes significant [21, 116–118]. An illustrative summary of the observed distinct crystallographic structures and morphologies is shown in Figure 3.19.

Given that the vast majority of nanoparticles are formed from systems that possess an FCC crystal structure and the aforementioned close relationship of the $GaPd_2$ structure (and other Ga-Pd intermetallic crystal structures) to an FCC lattice, it is convenient, for the analysis presented here, to describe the observed structures in terms of pseudo-equivalent crystallographic zone axes and lattice planes of an FCC system. Moreover, it becomes appropriate when considering the potential relaxation of the intermetallic towards an 'FCC-like' structure.[9]

Firstly, examples can be found in the small nanoparticles, such as those shown in Figures 3.19a and b, where, although the crystalline structures cannot be unambiguously assigned to those of the phase $GaPd_2$ specifically, there is evident persistence of the intermetallic state. Comparable to Figure 3.14 where the 'distorted-FCC' structure of $GaPd_2$ was seen in a relatively larger nanoparticle, Figure 3.19a shows a smaller nanoparticle where such a 'distorted-FCC' structure characteristic of the intermetallic is visible; although there is clear deviation from this structure in some regions of the nanoparticle. The second example, shown in Figure 3.19b, exhibits undulating lattice planes characteristic of the intermetallic compound, analogous to those seen in Figure 3.16.

A number of zone axes of $GaPd_2$ are less easily distinguishable from those of other Ga-Pd phases or an undistorted FCC lattice, but are significant in characterising the morphologies observed in the small nanoparticles. Although this conundrum makes a precise and unambiguous determination of the structural and chemical nature of the surface terminations in many of the nanoparticles challenging (although the topic is well-worthy of future attention by AC-TEM and other techniques), it is nevertheless informative to report the observed morphologies and nanocrystalline features at a more qualitative level.

[9] This concept of crystal structural pseudo-equivalence is addressed thoroughly in chapter 4.

While many nanoparticles seem to exhibit a near spherical appearance due to their particular orientation with respect to the electron beam or partial rounding of surface facets, there are also rather distinct morphologies frequently seen. These span the range of single crystal and twinned nanocrystalline and the non-crystallographic morphologies identified in section 3.1.4.3, posing intriguing questions from both a crystallographic and catalytic perspective.

Figures 3.19c and d show truncated octahedral Ga-Pd nanoparticles observed close to a pseudo-$\langle 110 \rangle_{FCC}$ zone axis, exhibiting relatively well-defined pseudo-$\{111\}_{FCC}$ and pseudo-$\{100\}_{FCC}$ terminating planes. Potential implications of the low co-ordination of atoms occupying positions at abrupt boundaries between nanoparticle surface planes were alluded to in section 3.1.4.3, and clearly, as revealed here, may be pertinent to Ga-Pd catalysts. The abundance of such low coordinated surface sites was also identified in the work of Shao et al. [115] on carbon nanotube supported $GaPd_2$ nanoparticles.

Additional low coordinated surface sites are created by the presence of re-entrant facets observed in the nanoparticles, an example of which is shown in Figure 3.19e. This, and further factors that may influence surface and sub-surface catalytic processes are highlighted in Figure 3.20. For completeness, the disordered over-layer cannot go without mention again (labelled DO on Figure 3.20). Also significant is a twin-boundary (labelled TB) permeating the nanoparticle and leading to perturbation of the surface, particularly in the region indicated by the curly brace. The effect of such defects on the nanocrystalline structure is clear, and correspondingly should be expected to affect catalytic processes, possibly profoundly so - see again the study of Behrens et al. [95] as a pertinent example.

The occurrence of decahedral and icosahedral (five-fold twinned) morphologies in the Ga-Pd nanoparticles (see Figures 3.19f-j) adds a further intricacy that should be considered in elucidating physico-chemical behaviour. Such morphologies inherently yield differing atomic environments as compared to crystalline nanoparticles, indeed the formation of such structures is usually necessarily accompanied by a distortion of the crystalline lattice. It is well-known (and has been the subject of much debate and controversy [21, 116, 118, 136, 137]) that in FCC systems, a distortion of the FCC lattice is required to fill space in these morphologies. Potential catalytic implications were already cited in section 3.1.4.3. The extent to which the intermetallic $GaPd_2$ structure may be maintained in such morphologies poses an intriguing puzzle and is analysed further in chapter 4.

FIGURE 3.19: ADF images revealing the nanocrystalline status of small (sub-10 nm) Ga-Pd nanoparticles. (a, b) Evidence of nanocrystalline structure characteristic of Ga-Pd in the intermetallic state: (a) 'distorted-FCC' and (b) 'undulating' lattice structures. (c) A well-faceted single crystalline truncated octahedral nanoparticle viewed down a pseudo-$\langle 110 \rangle_{\mathrm{FCC}}$ zone axis. (d) Smaller truncated octahedral nanoparticle, also clearly showing the disordered over-layer. (e) Twinned truncated octahedral nanoparticle exhibiting pseudo-$\{111\}_{\mathrm{FCC}}$ re-entrant facets and surface defects; see Figure 3.20 for further details. (f, g) Decahedral nanoparticles viewed close to the five-fold symmetry axis. (h-j) Icosahedral nanoparticles viewed close to (h) three-fold, (i) two-fold and (j) five-fold symmetry axes. Scale bars: 1 nm.

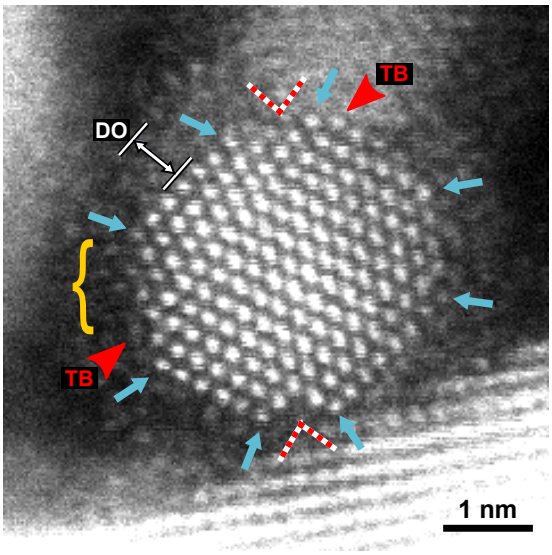

FIGURE 3.20: The complex surface structure of a twinned Ga-Pd nanoparticle. Features of the structure that are distinct from a pristine bulk terminated surface, with potential implications for catalytic processes, include re-entrant faceting (indicated by dashed V's), a high proportion of low coordinated atoms at the junctions between neighbouring surface planes (indicated by blue arrows) and perturbation of the surface (in the region enclosed by the curly bracket) due to the emergence of a twin boundary (TB, indicated by arrowheads). Also visible is the disordered over-layer (DO) of variable thickness surrounding most of the nanoparticle.

3.3.5 Assessing rational catalyst design aspirations

By revealing directly the 'distorted' FCC-like structure and chemical ordering of Ga and Pd, the AC-STEM analysis has shown firmly that the salient features of the rationally designed intermetallic catalyst can be achieved in nanoparticulate form. However, it has also given insight into how the intermetallic compound may manifest differently in practice, and specifically at the nanoscale.

A novel result of the AC-STEM imaging is that it has highlighted a particular need to consider morphological factors related specifically to nano-sizing. Each of the observed nanoscale morphologies/defects differs in the extent to which they may preserve the 'bulk' intermetallic structure. The crossover between bulk-like crystalline, nanocrystalline and non-crystallographic structures requires further attention if Ga-Pd nanoparticle catalyst systems are to be as well defined as bulk model systems. Dominating above nanoscale crystallography, however, is the evident instability of the $GaPd_2$ surface under an oxidative environment. This is clearly a major deviation from the rationally selected pristine intermetallic surface.

While the surface decomposition may be particularly severe for nanoparticulate $GaPd_2$, drawing together findings in the literature, it has also become clear that the surface of $GaPd_2$ in general (i.e. including the surface of bulk

specimens) can be unstable, even under mildly oxidative conditions. The frailty of the $GaPd_2$ surface has recently been charted comprehensively by Wowsnick et al. [151, 152], in a series of systematic studies exposing bulk metallographic, milled and powdered $GaPd_2$ to different environmental conditions. Their proposed structural models closely resemble the model of Haghofer et al. [113] and the AC-STEM analysis shown here, and show further evidence of the dynamic nature of the surface and susceptibility to oxidation. Their study also confirms a strong dependence of the degree/nature of decomposition or reformation on particular conditions. Especially worrying is the finding that the decomposition, under certain conditions, can yield significant regions of monometallic Pd. They conclude that a pure intermetallic surface is only obtained under highly reducing atmospheres. This clearly restricts the reaction conditions under which $GaPd_2$ catalysts can be used in their rationally designed form.

Thus, while model systems protected from oxidising environments would indeed be expected to show high selectivity and long term stability in the selective hydrogenation of acetylene, those exposed to oxidising conditions prior to, or during, reaction on the other hand would be expected to show a changing catalytic response due to *in situ* decomposition or reformation of the surface. In some cases, such as liquid-phase hydrogenation, the oxophilicity of Ga may preclude practical application [152].

Considering previously reported [111] catalytic evaluation of bulk and nanoparticulate $GaPd_2$, some connections can be attempted between the observed catalytic activity, selectivity and stability and the nanostructural states revealed here. Intuitively, nano-sizing leads to a much higher activity per unit mass, which can be related readily to the substantial increase in surface area. Conversely, the activity per unit surface area was found to be significantly (an order of magnitude) higher, and the selectivity marginally (ca. 13 %) higher, for bulk $GaPd_2$. This could be interpreted by considering the structural differences observed, wherein not all of the nano-sized catalysts fully possess the 'ideal' intermetallic structure of the bulk catalyst, especially in the catalytically most important surface regions. However, the nanostructural aspects, such as the 'FCC-like' relaxation of the intermetallic structure or non-crystallographic structures, may be dominated by the surface decomposition/reformation. Stronger coverage with Ga_xO_y could explain the lower surface specific activity of the nanoparticulate material compared to that of bulk $GaPd_2$. This is plausible in light of the high surface-area-to-volume ratio of nanoparticles and the extensive segregation observed here. Further work, however, would be necessary to identify

different decomposition in the nanoparticle surface and to attribute this to nano-sizing, as opposed to environmental or pre-treatment effects. Moreover, the nanostructural states observed here may not be the same as those under reaction conditions.

Overall, the conclusion can be made that the rationally designed $GaPd_2$ catalysts can, largely, be realised under favourable conditions, but the robust practical applicability that was hoped for is perhaps not achievable. That being said, even though a pristine nano-sizing of the bulk intermetallic structure may be the most rational route to high-performance Ga-Pd nanocatalysts, different structures in the nanoparticles could still be active and selective. For example, islands of Ga_xO_y could impart active site isolation and therefore selectivity to exposed surface regions that they surround; even to regions of metallic Pd, if they were sufficiently small. Similarly, the distinct nanocrystalline or 'non-crystallographic' structures adopted by many of the sub-10 nm nanoparticles may also still yield isolated Pd active sites if they retain a chemically ordered structure. However, if these catalytic morphologies are dynamic, the goal of a pre-selected catalytically efficacious, practically applicable, selective hydrogenation structure remains elusive.

This study provides a clear illustration of a 'materials gap' and a 'pressure gap' between model and real systems; a conclusion also made by Wowsnick, Armbrüster and co-workers [151, 152]. This is not to say, however, that such a knowledge-based approach, progressing from model to real systems, is not efficacious - far from it - but that some lessons have been learned regarding rational design. The conclusions of Wowsnick, Armbrüster and co-workers [151, 152] and co-workers are fitting in this aspect as well: it is not sufficient simply to identify candidate materials based on electronic properties or crystal structure. Chemical dynamics and instabilities need to be considered as well. The results here also show that additional nano-sizing effects need to be considered, relating primarily to nanoscale morphologies and consequent differing manifestations of crystal structure (and most likely electronic structure too).

Evidently, nanostructuring can result in additional intricacies that require further unravelling in order to obtain understanding and control of Ga-Pd nanocatalysts comparable to that achieved for the bulk systems. With greater control over the nanoparticle morphologies, or perhaps via theoretical modelling, or identification of most efficacious terminating planes via bulk specimens, it may become possible to identify the most catalytically efficacious nanoscale morphologies. However, given the dynamic and easily disturbed nature of the

surface, one questions whether this is a readily achievable or profitable task, as the well-defined intermetallic surface could be easily (possibly irreversibly) decomposed during preparation, before or during characterisation, or during real reaction conditions. Ga-Pd systems may still yield superior catalysts in a number of applications, but it seems, similar to the case of monometallic Pd, it may often be the phases formed *in situ* that are of interest.

3.3.6 Future work

This study has considered (nominally) unsupported nanoparticles (the nanoparticles being deposited on thin C or Si substrates post-synthesis to enable TEM analysis). While this analysis is valuable for characterising the intrinsic nature of the nanoparticulate Ga-Pd compounds, AC-TEM should also contribute significantly to the analysis of Ga-Pd nanoparticles supported on high surface area solids (as already shown by Shao et al. [115]).

Dynamic studies using powerful, but non-spatially resolved, techniques have yielded valuable information regarding the modifications occurring in Ga-Pd nanoparticles during synthesis and under reaction conditions [11, 90, 96, 97, 99, 102, 104–107, 111–113, 115]. Significant further insight may be achievable by the application of *in-situ* AC-TEM [153], to provide dynamic atomic-scale analysis under synthesis- and application-relevant conditions.

Optimised STEM-EELS or STEM-EDXS mapping may also be insightful regarding the surface (or interior [152]) decomposition, although clearly care must be taken to ensure that the analysis conditions are relevant.

3.4 Conclusions

AC-STEM has shown directly the distinct structure and chemical ordering of the intermetallic phase $GaPd_2$ in nano-sized particles. It has also revealed deviations from the 'ideal' bulk structure, including atomic-scale intricacies and a partial decomposition of the surface and near-surface regions of the nanoparticles following exposure to ambient (oxidative) conditions. The high (frequently) atomic resolution and directly interpretable imaging has proven invaluable for exploring intricacies of the challenging but fascinating (nano)-Ga-Pd system. Building on previous studies, the analysis verifies the successful 'nano-sizing' of Ga-Pd intermetallic compounds, but also provides important insight into how Ga-Pd nanocatalysts may differ from bulk or model systems.

The manifestation of the distinctive intermetallic compound in nano-sized form is crystallographically intriguing, comprising both nanocrystalline 'FCC-like' and so-called 'non-crystallographic' five-fold twinned structures. The latter in particular is pursued in chapter 4.

There are many aspects still to be elucidated concerning the propensity of the bulk intermetallic structure towards different manifestations in nano-sized forms, including the exact role that the deviations from the bulk may play in catalytic processes and the extent to which they can be controlled to obtain only those nanostructures that may be catalytically most active and selective under reaction conditions. The insights provided here should be a significant contribution to the earlier suggested [90] incremental knowledge-based development, obtaining understanding from the bottom up.

Chapter 4

Five-fold twinned $GaPd_2$ nanoparticles

Five-fold twinned nanoparticles are common in nominally FCC crystal systems, yet an FCC lattice does not fill space in such morphologies. The nature of the required distortion has been a subject of long-standing debate. Similarly, the occurrence of five-fold twinned Ga-Pd nanoparticles is intriguing. It was shown in chapter 3, by AC-STEM, that the Ga-Pd nanoparticles specifically comprise the intermetallic compound $GaPd_2$. The manner in which five-fold twinned structures could be accommodated in the distinctive orthorhombic crystal structure of this intermetallic compound provides novel perspectives for analysing nanoscale five-fold twinning.

This chapter provides a crystallographic analysis, considering the intermetallic $GaPd_2$ (orthorhombic, Co_2Si-type) structure as closely related to an FCC lattice. 'Building blocks' of the orthorhombic structure could be arranged in different crystallographic orientations with respect to five-fold twinning, leading to consideration of different solid angle deficiencies and the symmetry or pseudo-symmetry characteristics of candidate twin planes. Possible arrangements of $GaPd_2$ building blocks in this crystallographic puzzle are presented, along with discussion of the structures actually manifesting in practice.

4.1 Introduction

The occurrence of five-fold twinned (also referred to as 'multiply twinned') nanoparticles has posed an intriguing puzzle for decades [21, 116, 136, 137, 154]. Well-known to arise frequently in nanoparticles of important metals such as Au, Ag, Pt and Pd that usually possess an FCC crystal structure, competing

models have been proposed regarding the necessary distortion of the crystalline lattice to fill space in the five-fold geometry; and the subject continues to receive considerable attention [23, 25, 155–158].[1]

Five-fold twinning is practically achievable in many materials with twinning angles of ca. $2\pi/5$ and in which the twin boundary energy is not too large - see Hofmeister's review [154] for an extensive tabulated survey. Indeed, five-fold twinning has been observed in many bulk materials, including intermetallic compounds. However, at the nanoscale, mechanisms underlying the five-fold twinning can be considerably different.

In nanoscale materials systems, finite size effects are significant in determining morphology [21, 116–118, 136, 137, 154]. Crystal structures that do not seem to fit the five-fold twinned morphologies may undergo structural transitions. Rather than nanocrystalline analogues of the bulk structure, the so-called 'non-crystallographic' five-fold twinned morphologies may prevail. It is well-known that such morphologies are stabilised, primarily, because the strain due to lattice distortion and twinning is offset by reduction of surface energy. However, despite much effort, many intricacies of five-fold twinned nanoparticles are still not well-understood, including the precise nature of the structural distortion.

There have been many studies of monometallic five-fold twinned nanoparticles. Seeking new properties, multicomponent five-fold twinned nanoparticles have attracted increasing attention [117]; for example (citing TEM studies), Pt-Pd [36], Au-Ag [159], Au-Fe [160], Au-Pd [161] and Au-Cu [161]. While most studies have considered random alloys of the solid solution type, or segregated systems such as core-shell morphologies, there has also been a more select number of investigations involving five-fold twinning in nano-sized intermetallic compounds. For example, concerning Au-Pd [162], Au-Cu [163], Fe-Pd [164] and Co-Pt [165] intermetallic compounds; and in particular Fe-Pt, where there have been detailed TEM studies and consideration of the geometry of five-fold twinning (see e.g. [158, 165, 166, and references therein]).

Five-fold twinning in multicomponent nanoparticles can be considerably more complex than in monometallic systems, and better understanding of a number of important parameters is required. The effects of alloying, chemically ordered structures, order/disorder transitions, chemical segregation or other structural/chemical particulars in multicomponent five-fold twinned nanoparticles are relatively poorly understood.

[1] A closely related topic is that of quasicrystals, which display 'forbidden' five-fold and ten-fold symmetry. Although quasicrystals and five-fold twinned structures have often been found to co-exist, they are quite distinct - as can be readily seen in a TEM image.

The (nominally) well-defined, chemically ordered and often distinctive structures of intermetallic compounds can offer novel contexts in which to study five-fold twinning. The topic of this chapter, nanoscale five-fold twinning in the Ga-Pd system and the particular structure of $GaPd_2$, offers an intriguing, although challenging and intricate, scenario. Further to those in chapter 3 (Figure 3.19), exemplar ADF-STEM images of decahedral and icosahedral nanoparticles from the Ga-Pd samples are shown in Figure 4.1. The occurrence of these Ga-Pd decahedra and icosahedra was noted, but not further explored, in refs. [82, 167]. The aim of this chapter is to establish the crystallographic basis for interpreting these nanoparticles and their specific morphologies, under the assumption that they are composed from the crystal structure of the intermetallic compound $GaPd_2$. The actual structures manifesting in practice are also discussed with reference to the AC-STEM images.

4.1.1 Decahedral & icosahedral structures

The basis for interpreting five-fold twinned geometries begins with considering the packing of tetrahedral 'subunits' around a five-fold axis, as shown schematically in Figures 4.2a and c, respectively, for Bagley's [168] decahedron (the pentagonal dipyramid) and Mackay's [169] (regular) icosahedron. Each tetrahedron has an edge coinciding with a five-fold axis and the boundaries between tetrahedra constitute twin planes.[2] The decahedron is composed of five tetrahedra packed together with D_{5h} point group symmetry, and 20 tetrahedra arranged with I_h symmetry form the icosahedron. In the decahedron, each tetrahedron forms two twin interfaces, compared to three in the icosahedron.

The tetrahedra in the decahedron and icosahedron are irregular. If on the other hand, one were to attempt to form these five-fold structures from the regular tetrahedra of an FCC lattice, a solid angle deficiency results (Figures 4.2b and d). This inability to fill space is sometimes termed 'packing frustration'. Specifically, in FCC systems the relevant twin boundaries are formed by the $\{111\}_{FCC}$ family of planes. With an angle of 70.53° between $\{111\}_{FCC}$ twin planes, there is an angular deficiency of 7.35° around a five-fold arrangement of such tetrahedra, as shown for the decahedron in Figure 4.3. Necessarily therefore, some form of distortion of an FCC lattice is required to achieve space filling [21, 23, 25, 136, 137, 155–157].

[2]Fundamental concepts of twinning are covered in many textbooks such as Hammond's introductory crystallography text [170]. More rigorous crystallographic description can be found in, e.g. [171–173].

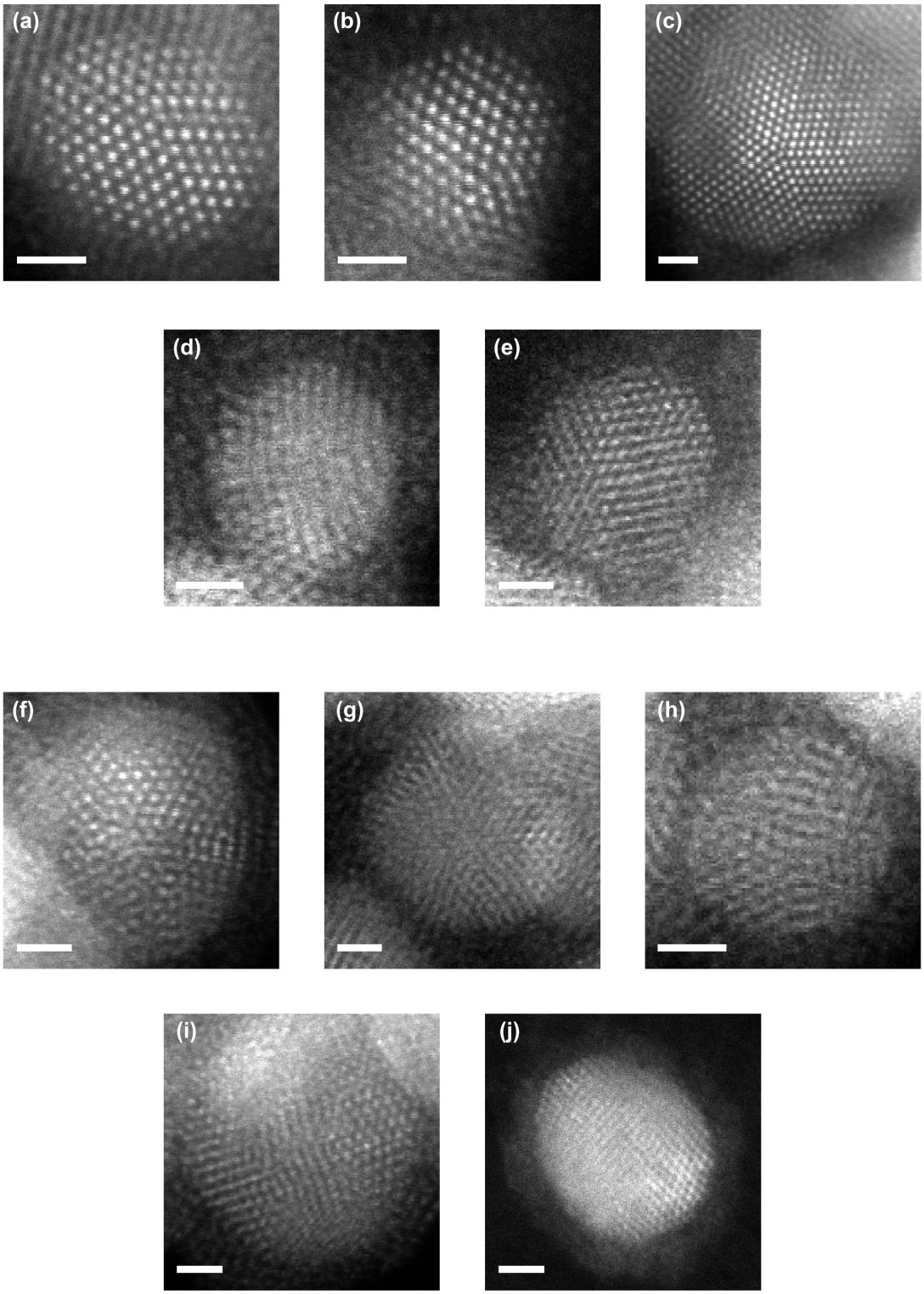

FIGURE 4.1: Five-fold twinned morphologies arising in the nanoparticulate Ga-Pd system. (a-e) Decahedral and (f-j) icosahedral nanoparticles, viewed at or close to respective symmetry axes: (a-c) five-fold, (d) between five/two-fold, (e) two-fold, (f) five-fold, (g) three-fold, (h) between five/three-fold, and (i, j) two-fold. Scale bars: 1 nm.

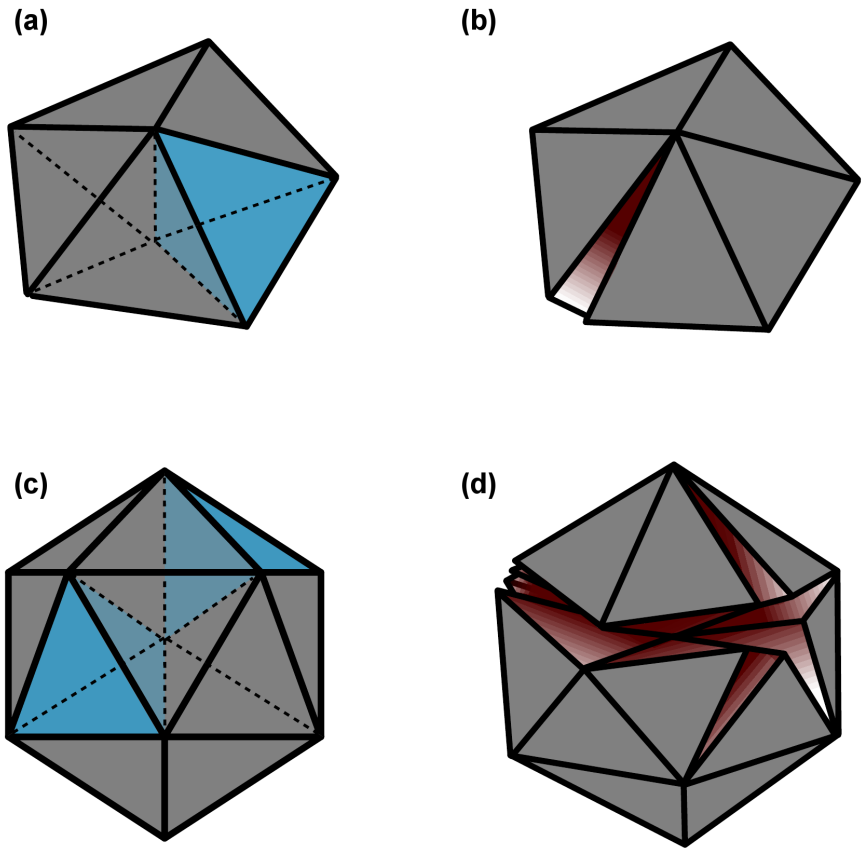

FIGURE 4.2: Geometry of five-fold twinned particles. The decahedron (a) or icosahedron (c) can be considered as composed of irregular tetrahedra. A single tetrahedron of the decahedron is shaded in blue in (a) and two tetrahedra of the icosahedron are shaded in (c). Boundaries between neighbouring tetrahedra constitute twin planes. By contrast, the packing of regular tetrahedra around a five-fold axis results in a solid-angle deficiency. Hence, using regular tetrahedra, space filling cannot be achieved for either the decahedron (b) or icosahedron (d).

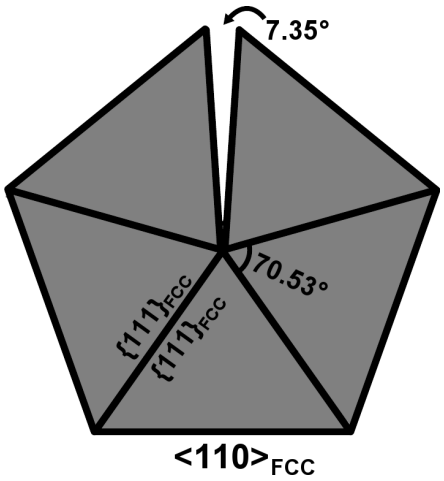

FIGURE 4.3: The decahedron in terms of FCC tetrahedra. The decahedron is viewed down its five-fold axis, and each tetrahedron is viewed down a $\langle 110 \rangle_{\mathrm{FCC}}$ direction. The twin boundaries between neighbouring tetrahedra are formed by the $\{111\}_{\mathrm{FCC}}$ family of planes. With an angle of 70.53° between $\{111\}_{\mathrm{FCC}}$ twin planes, there is an angular deficiency of 7.35°.

Competing models have been proposed and variously invoked regarding the nature of this distortion; saliently involving strain, lattice modification and/or introduction of defects. Detailed accounts of the saga have been written by Marks [21], Hofmeister [137] and Gryaznov et al. [136]. More recently, Johnson et al. [23] as well as Mayoral et al. [118] have given notable succinct summaries.

In general, defects such as dislocations and stacking faults are common in larger five-fold twinned nanoparticles (see examples in [21, 136, 174]). In the smaller size regimes, typical of the nanoparticles in this chapter, five-fold twinned nanoparticles may be essentially free of point defects, and usually require strain, or lattice modification, of the nominal 'bulk' crystal structure.

On one hand, although neither the decahedron or icosahedron have true translational symmetry, they could be considered as twinned crystals where each (distorted) tetrahedron has a body-centred orthorhombic (BCO) or rhombohedral crystal structure, respectively, as shown in Figures 4.4 and 4.5 [168, 169, 175]. Early TEM analysis was presented advocating such structures [176, 177].

Also backed by empirical TEM observations [179], but contrary to such homogeneous lattice modification (or other homogeneous lattice strain analysis such as Ino's [180]), an inhomogeneous argument was put forward [174, 181]. Illustrated in Figures 4.6a and b (taken from de Wit's paper of 1972) a 'star disclination'[3] at a five-fold axis suffices to resolve the solid angle deficiency via inhomogeneous strain [181]. Hence a single disclination at the five-fold axis is required for the decahedron, while for the icosahedron it is necessary to introduce six disclinations (Figures 4.6c and d). The disclination approach yields a much smaller strain energy density compared to homogeneous strain models, and suggests compression towards the centre and tensile strain at the periphery of the five-fold twinned particle [174].

In another model, based on empirical observations of decahedral In and Pb nanoparticles, coexistence of subunits with FCC structure and others with a body-centred tetragonal (BCT) structure was proposed [183, 184].

Other stress relief mechanisms in five-fold twinned nanoparticles may include:

- Shape modification by external facet truncation, such the 'Ino decahedron' [180] or 'Marks decahedron' [185]. The Ino decahedron possesses truncations on $\{001\}_{FCC}$ facets, and the Marks decahedron also contains re-entrant $\{111\}_{FCC}$ facets at the twin boundaries (see again Figure 3.10a).

[3]Disclinations are defects similar to dislocations, but differ in that they are usually related to symmetries of rotation rather than translation in a crystalline lattice. See, for example, Gryaznov et al. [136] or Romanov & Kolesnikova [182] for general reviews.

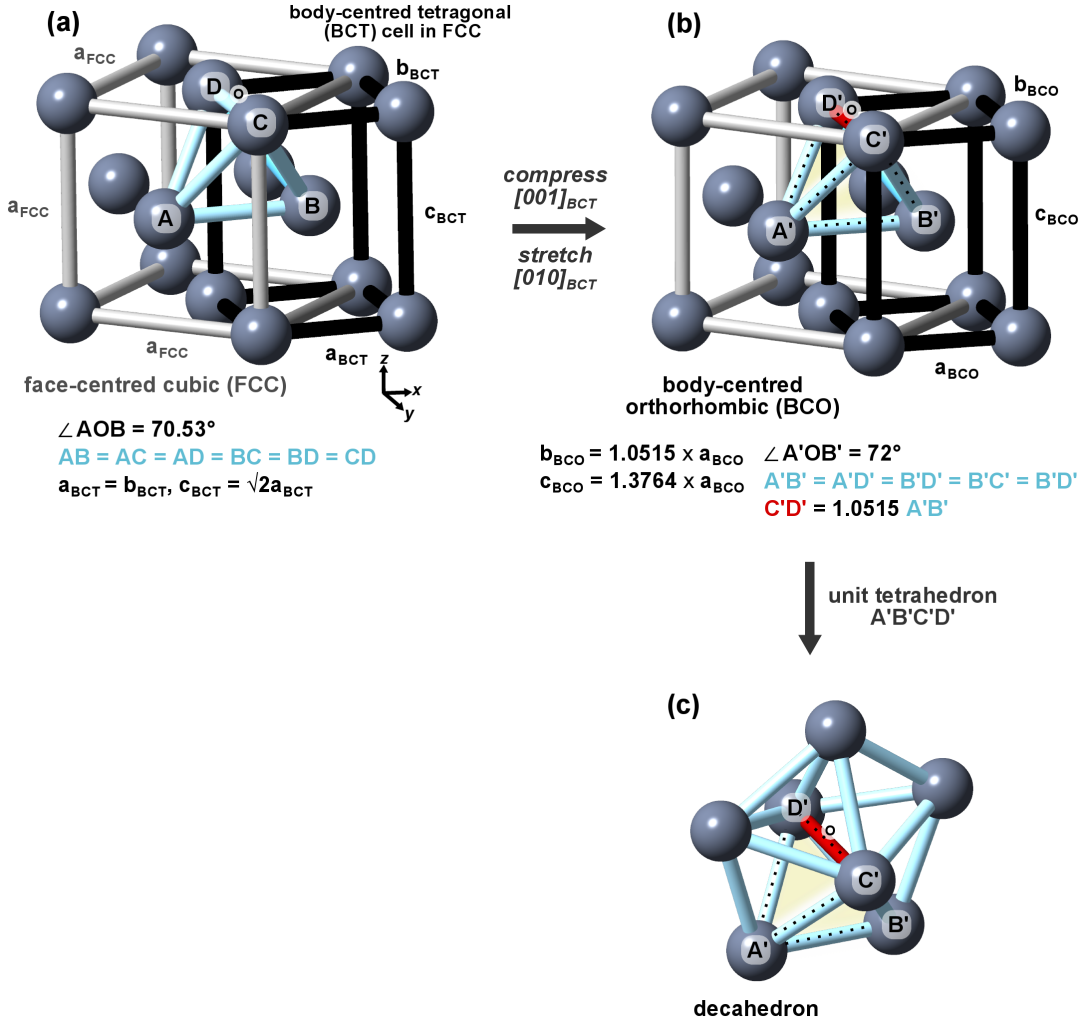

FIGURE 4.4: Relations between FCC and BCO crystal structures and the decahedron. (a) FCC cell with regular tetrahedron ABCD (outlined in light blue). A BCT cell contained within the FCC lattice is outlined in black, but with the indicated dimensions, the lattice has FCC characteristics. (b, c) The decahedron (c) can be considered as comprising of the same tetrahedron A′B′C′D′ (delineated by black dotted lines and shaded in yellow) as contained in a BCO lattice with the dimensions shown in (b). The BCO cell in (b) can be derived from the BCT cell in (a) via a biaxial stress. Edges of the unit tetrahedron are colour-coded, in red or light blue, according to their relative dimensions. (The BCO cell defined in this figure corresponds to a decahedron of minimal surface area, i.e. the close-packing is preserved [168]. Some authors also give the geometry of a decahedron of minimum volume [136, 178], for which the BCO cell dimensions are $a = 1.0181b, c = 1.4013b$.)

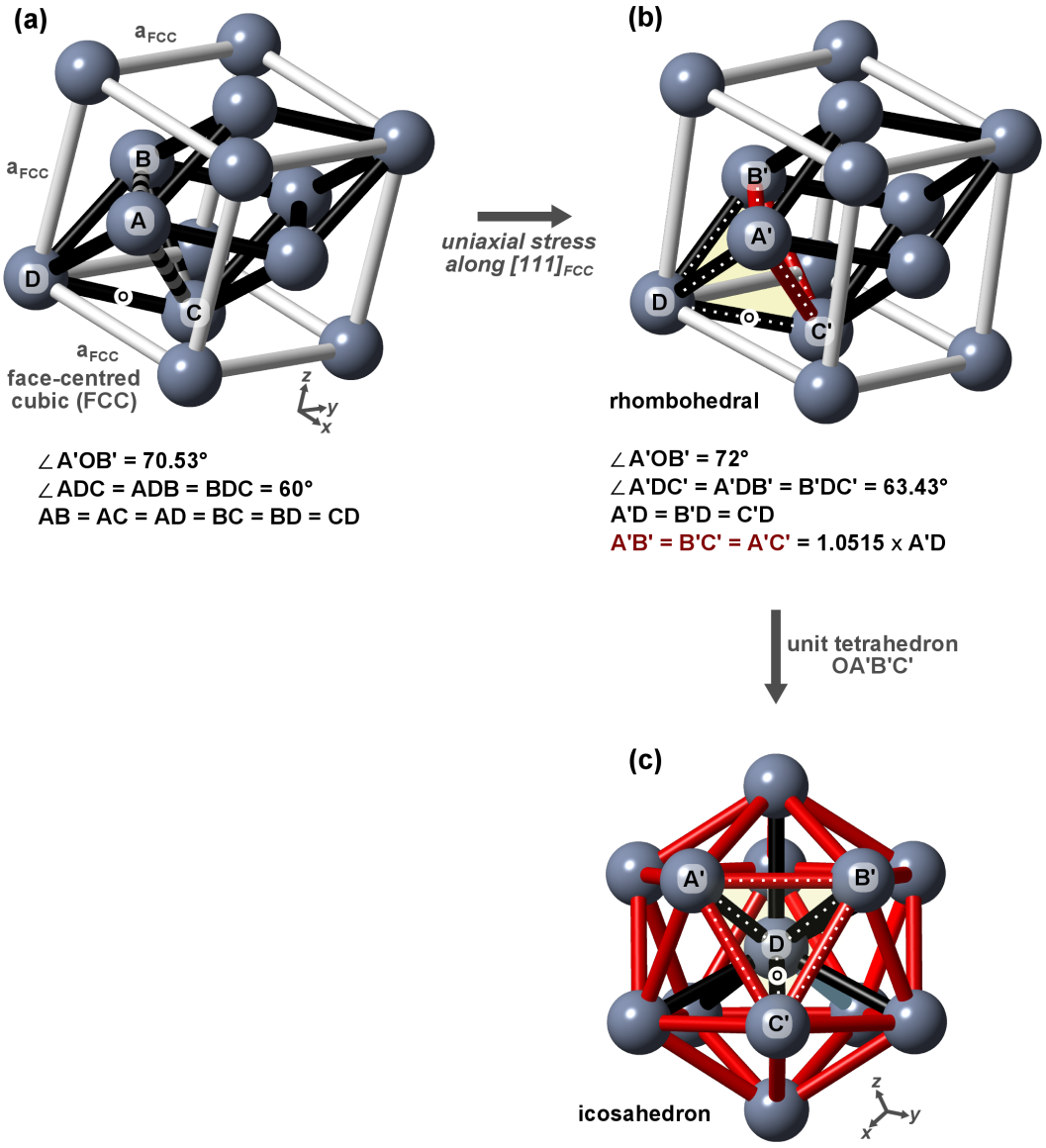

FIGURE 4.5: Relations between FCC and rhombohedral crystal structures and the icosahedron. (a) FCC cell with regular tetrahedron ABCD (outlined by solid black or black/grey stripes). A rhombohedral cell contained within the FCC lattice is outlined in solid black, but with the indicated dimensions, the lattice has FCC characteristics. (b, c) The icosahedron (c) can be considered as comprising of the same tetrahedron $A'B'C'D'$ (delineated by white dotted lines and shaded in yellow) as contained in a rhombohedral lattice with the dimensions shown in (b). The rhombohedral cell in (b) can be derived from that in (a) via a uniaxial stress. Edges of the unit tetrahedron in (b) and (c) are colour-coded, in red or black, according to their relative dimensions.

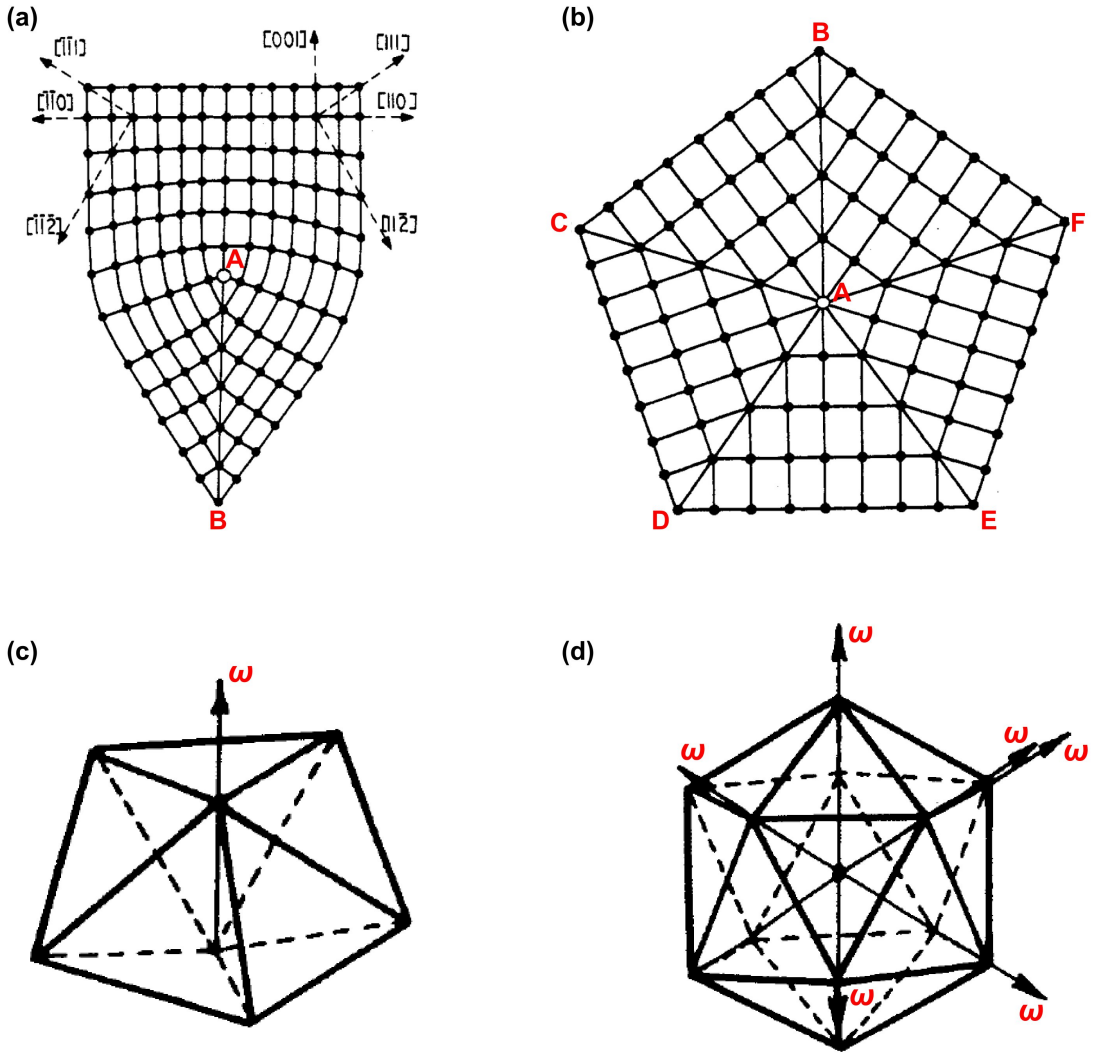

FIGURE 4.6: Disclination model for (a, b) FCC crystals, and (c, d) five-fold twinned nanoparticles. (a) Illustrates the concept for a positive partial wedge disclination at A, of strength $\omega = 70.53°$. The plane of the paper is $(1\bar{1}0)$ and the twin boundary AB has been formed by bringing together the $(11\bar{1})$ and $(\bar{1}\bar{1}\bar{1})$ planes. (b) The star disclination that accommodates five-fold twinning is a positive partial wedge disclination at A, of strength $\omega = 7.35°$. (The elastic distortion in (b) is so small that it is barely visible in the schematic). (c, d) Disclinations in the decahedron and icosahedron. (a, b) Reproduced from [181], (c, d) from [136].

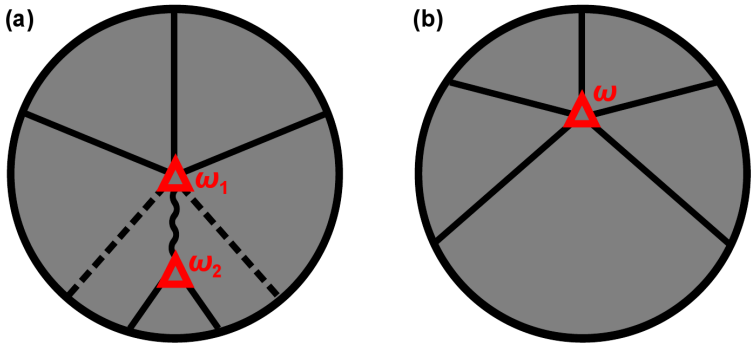

FIGURE 4.7: Schematic illustration of elastic stress relation mechanisms in five-fold twinned nanoparticles. (a) Splitting of the five-fold axis into two partial disclinations ω_1 and ω_2. (b) Displacement of the five-fold axis from the centre. Redrawn from [136].

- Surface modification, such as steps, kinks or non-regular surface lattice distortion; e.g. [186, 187].

- Modification of the five-fold axis, such as splitting into two or more disclinations, or displacement off-centre (Figure 4.7) [136]. The latter can be rationalised based on elastic strain energy considerations wherein, modelling the decahedron as a cylinder with disclination of strength ω shifted away from the centre, the strain energy is [188]:

$$E_s = \frac{G\omega^2}{16\pi(1-\nu)} r^2 \left[1 - \left(\frac{x}{r}\right)^2\right]^2, \tag{4.1}$$

  where G is the shear modulus, ν Poisson's ratio and x is the displacement of the disclination from the centre of a cylinder of radius r.

More case specific factors that can stabilise five-fold twinned nanoparticles include alloying, chemical ordering or segregation, surface adsorbates and the substrate. Alloying in particular can be a significant stabiliser, and chemical ordering or segregation have often been cited as being intimately linked to strain reduction (e.g. [158, 160–162, 166]). 'Magic compositions' may exist that stabilise certain morphologies [117].

Icosahedra are near-spherical and enclosed entirely by close-packed planes, but are inherently highly strained. They are therefore, in general, favoured in the smallest sized particles. Since the strain energy in five-fold twinned nanoparticles is proportional to their volume, nanocrystalline structures should predominate at large particle sizes. At intermediate sizes the (truncated) decahedron, which is strained but achieves better optimisation of surface energy than nanocrystalline structures, may become the preferred structure. However, it is well-known

that the structural cross-over can vary significantly depending on the particular materials system, history and environmental effects [21, 116–118, 138].

TEM has been the stalwart technique in the empirical study of five-fold twinned nanoparticles, using techniques such as weak-beam dark-field imaging, diffraction and BF-CTEM. More recently, the benefits of ADF-STEM have been exploited (e.g. [36, 58, 82, 187, 189]), as well as those of AC-optics in both AC-CTEM and AC-STEM (e.g. [23, 25, 36, 58, 82, 155–159, 165, 187, 189]). In particular, harnessing AC-CTEM Johnson et al. [23] carried out geometric phase analysis of strain in a decahedral Au nanoparticle, concluding that, in addition to the presence of a disclination, elastic anisotropy plays a critical role, and shear strain is present at the twin boundaries. Walsh et al. [25, 157] have also presented quantitative AC-CTEM studies of decahedral Au nanoparticles finding, in agreement with elasticity theory [174], considerable lattice parameter expansion at the surface. Following a custom method for strain analysis, they found that the strain is coherent across the twin interfaces. Sun et al. [156] observed that a BCT phase exists in decahedral Ag nanoparticles, which is stabilised by a highly strained core and less strained periphery. More recently, Chen et al. [155] have used ADF-STEM ET to visualise, in 3D, atomic steps at the twin boundaries and the 3D core structure of edge and screw dislocations in a decahedral Pt nanoparticle. Very recently also, Li et al. [158] have studied chemically ordered FePt decahedra using both AC-STEM and AC-CTEM (some notable earlier TEM studies of five-fold twinned FePt nanoparticles are also cited therein). They found significant surface segregation of Pt and evidence of inhomogeneous strain in terms of random spatial distribution of lattice parameter variation, which they attributed to the competition between the Pt segregation and Fe/Pt ordering. Although segregation effects have frequently been concluded as significant in five-fold twinned FePt nanoparticles (especially in FePt icosahedra), TEM analysis such as Li et al.'s shows firmly that the distinct chemical ordering of the $L1_0$ structure can be substantially preserved, including chemical ordering across the twin interfaces.

Many other investigations seeking to explain five-fold twinned nanoparticle morphologies continue to be published (too numerous to cite here). There is now a general consensus that most five-fold twinned nanoparticles possess a significant degree of inhomogeneous strain. In certain cases though, where the crystal structure of a particular material is conducive to five-fold twinned morphologies, there is the possibility for the strain or structural distortion to be smaller (see examples cited in Hofmeister's review [154]). The main conclusion from reviewing

the literature is that there is an ongoing need to better understand the various phenomena that may stabilise five-fold twinned nanoparticles, especially in novel materials systems and where the precise morphologies are directly related to targeted properties.

4.2 Five-fold twinning in $GaPd_2$

The Co_2Si-type structure of $GaPd_2$ has been described in various different manners [147, 190, and references therein]. Seeking to interpret the five-fold twinned $GaPd_2$ nanoparticles it is informative to recall (section 3.3.3) that the $GaPd_2$ structure [122] can be interpreted as a 'distorted' FCC-like lattice [146, 147]. As described by Wannek and Harbrecht [147] the structure can be viewed as resulting from an orthorhombic distortion and small shifts of the atom positions (<50 picometres) of an FCC unit cell, where also the specific chemical ordering of Ga and Pd yields a Co_2Si-type [121] structure. Pursuing this FCC-like relationship seems apt considering the prevalence of five-fold twinning in FCC systems, and the close resemblance shown directly in chapter 3 between many of the Ga-Pd nanoparticles and FCC nanoparticle morphologies.

4.2.1 Pseudo-equivalent relationship between $GaPd_2$ and FCC crystal structures

Figure 4.8 shows explicitly the close relationship between the orthorhombic $GaPd_2$ structure and an FCC lattice, from which it can be seen that the following equation can be used to convert FCC zone axes $[u\ v\ w]_{\mathrm{FCC}}$ into the pseudo-equivalent directions $[u'\ v'\ w']_{\mathrm{GaPd_2}}$ in the $GaPd_2$ unit cell:

$$\begin{bmatrix} u' \\ v' \\ w' \end{bmatrix}_{\mathrm{GaPd_2}} \approx \begin{pmatrix} 0 & \bar{\frac{1}{2}} & \frac{1}{2} \\ 1 & 0 & 0 \\ 0 & \frac{1}{3} & \frac{1}{3} \end{pmatrix} \begin{bmatrix} u \\ v \\ w \end{bmatrix}_{\mathrm{FCC}} \tag{4.2}$$

Similarly, FCC planes $(h\ k\ l)_{\mathrm{FCC}}$ are related to those in the $GaPd_2$ structure $(h\ k\ l)_{\mathrm{GaPd_2}}$ by:

$$\begin{pmatrix} h' & k' & l' \end{pmatrix}_{\mathrm{GaPd_2}} \approx \begin{pmatrix} h & k & l \end{pmatrix}_{\mathrm{FCC}} \begin{pmatrix} 0 & 1 & 0 \\ \bar{1} & 0 & 1\frac{1}{2} \\ 1 & 0 & 1\frac{1}{2} \end{pmatrix} \tag{4.3}$$

The reverse relationships may be obtained by using the inverse of the transformation matrix. In this regard, the $GaPd_2$ structure could be regarded as a superstructure of FCC-like cells, with $1 \times \langle 110 \rangle_{FCC}$ in the $[100]_{GaPd_2}$ direction, $1 \times \langle 100 \rangle_{FCC}$ in the $[010]_{GaPd_2}$ direction and $1\frac{1}{2} \times \langle 110 \rangle_{FCC}$ in the $[001]_{GaPd_2}$ direction.[4] The most important FCC crystallographic directions and lattice planes involved in five-fold twinning, and their pseudo-equivalents in $GaPd_2$, are given in Tables 4.1 and 4.2.

TABLE 4.1: Pseudo-equivalent zone axes of the FCC and $GaPd_2$ crystal structures.

$[uvw]_{FCC}$	$[u'v'w']_{GaPd_2}$
[100]	[010]
[010]	[$\bar{3}$02]
[001]	[302]
[110]	[$\bar{3}$62]
[101]	[362]
[011]	[001]
[10$\bar{1}$]	[$\bar{3}$6$\bar{2}$]
[1$\bar{1}$0]	[36$\bar{2}$]
[01$\bar{1}$]	[$\bar{1}$00]
[111]	[032]
[11$\bar{1}$]	[$\bar{1}$10]
[1$\bar{1}$1]	[110]
[$\bar{1}$11]	[0$\bar{3}$2]

TABLE 4.2: Pseudo-equivalent lattice planes of the FCC and $GaPd_2$ crystal structures.

$(hkl)_{FCC}$	$(h'k'l')_{GaPd_2}$
(200)	(020)
(020)	($\bar{2}$03)
(002)	(203)
(220)	($\bar{2}$23)
(202)	(223)
(022)	(006)
(20$\bar{2}$)	($\bar{2}$2$\bar{3}$)
(2$\bar{2}$0)	(22$\bar{3}$)
(02$\bar{2}$)	($\bar{4}$00)
(111)	(013)
($\bar{1}\bar{1}$1)	(2$\bar{1}$0)
($\bar{1}$1$\bar{1}$)	($\bar{2}\bar{1}$0)
(1$\bar{1}\bar{1}$)	(01$\bar{3}$)

4.2.2 Five-fold twinning in FCC & 'pseudo-FCC' $GaPd_2$

Most significantly, the orthorhombic distortion in $GaPd_2$ can be viewed as yielding an asymmetric subunit involved in FCC-like five-fold twinning. Similar to the orthorhombic distortion that yields the BCO structure of the tetrahedra in a space filling decahedron (Figure 4.4), orthorhombic distortion of an FCC structure according to the unit cell dimensions of $GaPd_2$ is shown explicitly in Figure 4.9. In this case, the distortion yields an irregular tetrahedron with three different edge lengths and the three different dihedral angles; i.e. three different

[4] In addition, the crystallographic 'group-subgroup relations' [191] between an FCC Ga-Pd solid solution and the $GaPd_2$ phase could be considered, but doing so is not necessary for the analysis here.

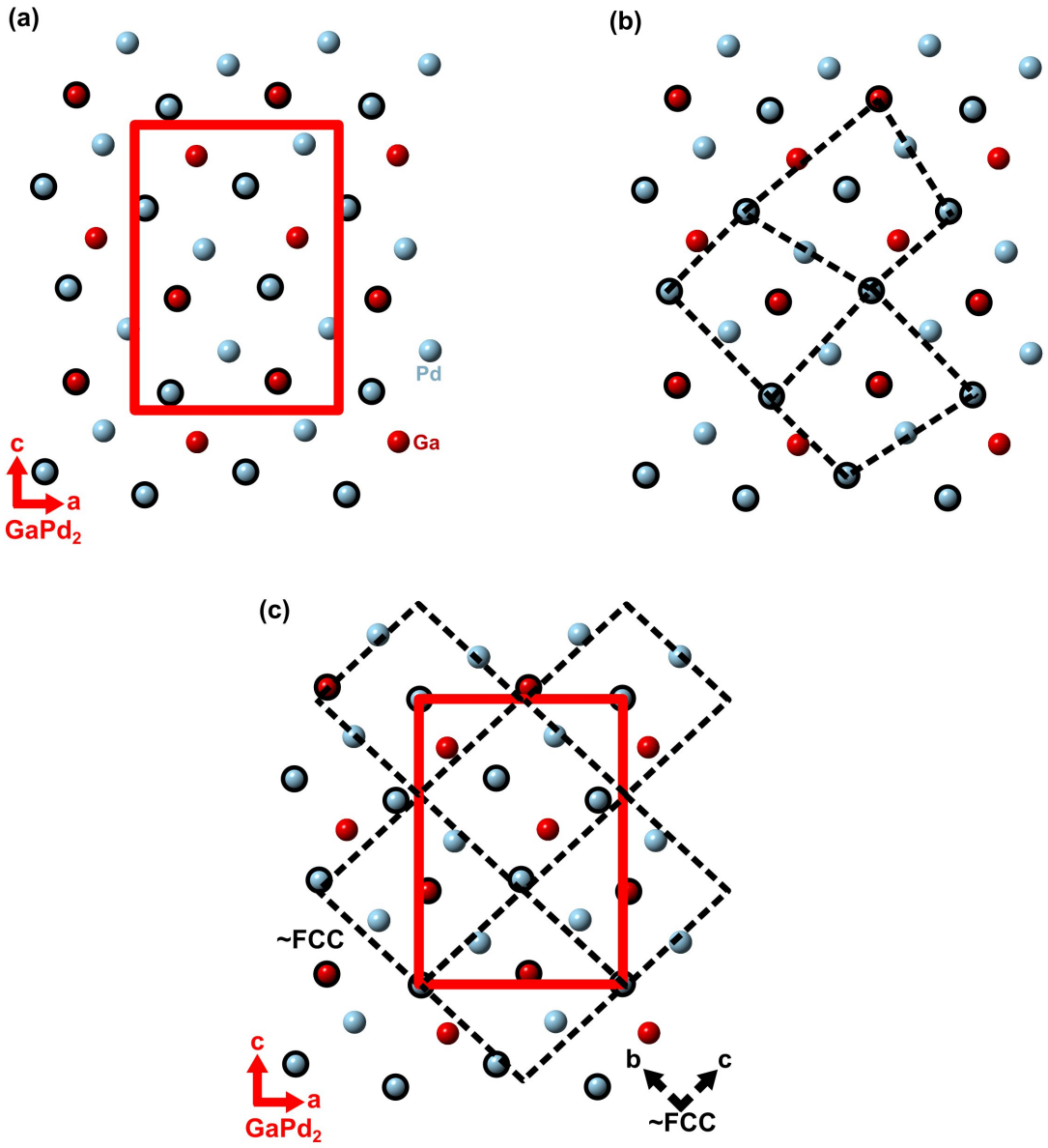

FIGURE 4.8: $GaPd_2$ in terms of an 'FCC-like' structure. (a) $GaPd_2$ structure shown with the unit cell (outlined in red) in the conventional position, reflecting the full space group symmetry. (b) Within the $GaPd_2$ lattice there are substructures resembling FCC unit cells. In (b) individual substructures, each resembling an FCC unit cell, are delineated by dashed black lines between atom positions. This aids initial visualisation of the FCC-like characteristics, but these are not analysed *per se*; rather the full $GaPd_2$ structure is considered. (c) Shifting the $GaPd_2$ unit cell position shows the topological relationship between the orthorhombic $GaPd_2$ structure (outlined in red) and an FCC-like lattice (outlined by dashed black lines), where $[010]_{GaPd_2} \approx [100]_{FCC}$, $[\bar{\frac{1}{2}}0\frac{1}{3}]_{GaPd_2} \approx [010]_{FCC}$, $[\frac{1}{2}0\frac{1}{3}]_{GaPd_2} \approx [001]_{FCC}$. Atoms outlined in bold are located at $y = \frac{1}{4}$, the others at $y = \frac{3}{4}$.

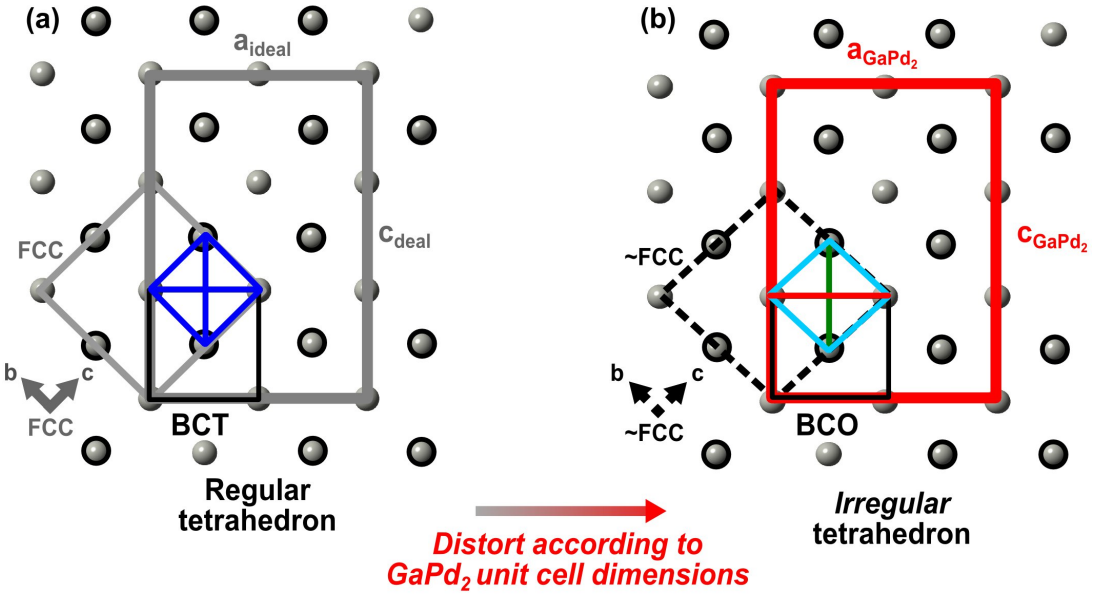

FIGURE 4.9: (a) An FCC lattice can be set in *Pnma* coordinates, with an orthorhombic cell in which $a_{\text{ideal}} = 2a_{\text{FCC}}/\sqrt{2}, b_{\text{ideal}} = a_{\text{FCC}}, c_{\text{ideal}} = 3a_{\text{FCC}}/\sqrt{2}$. As in Figure 4.4a, a BCT cell can be defined within the FCC lattice. (b) Altering the dimensions of the orthorhombic cell to those of $GaPd_2$ distorts the FCC structure, yielding a BCO cell (cf. Figure 4.4b), with unit tetrahedron and corresponding angles between the twin planes of the tetrahedron determined by the dimensions of the distortion. The edge lengths of this tetrahedron, viewed down the [100], [001] or one of the [362]-type directions of the distorted orthorhombic cell (shown in red, green and blue respectively), are 2.74 Å, 2.60 Å and 2.77 Å, and the dihedral angles are 65.23°, 68.11° and 72.43°, respectively.

possible twinning angles, which are 65.23°, 68.11° and 72.43°.[5] Reiterating, these possible twinning angles in $GaPd_2$ compare to a (nominal) twinning angle of 70.53° in the regular tetrahedra of an FCC lattice, and to a twinning angle of 72° in the space filling irregular tetrahedra of an ideal decahedron or icosahedron (Figures 4.3-4.5).

Moving from FCC to an orthorhombic 'FCC-like' structure also results in a reduction in symmetry in the crystallographic planes that would constitute the five-fold twin boundaries. As shown in Figure 4.10, the six-fold symmetry of the $\{111\}_{\text{FCC}}$-type lattice planes is reduced to only two-fold and 'pseudo-six-fold' symmetry in the pseudo-equivalent $(2\bar{1}0)$, $(\bar{2}\bar{1}0)$, (013) and $(01\bar{3})$ $GaPd_2$ planes. Likewise, the family of equivalent $\langle 110\rangle_{\text{FCC}}$ directions that would lie parallel to the five-fold axis is reduced to the pseudo-equivalent set [100], [001], [362], $[\bar{3}62]$,

[5]Concerning the full Co_2Si-type structure of $GaPd_2$ as being FCC-like (cf. Figure 4.8), the salient aspects beyond the BCO cell depicted in Figure 4.9 are the specific chemical ordering of Ga and Pd, the small displacements of the atoms from the 'ideal' FCC positions, and therein that the structure contains more than one FCC-like unit cell. Considering just a BCO distortion yielded by the $GaPd_2$ unit cell dimensions suffices for most aspects involved in a first approximation analysis of five-fold twinning in $GaPd_2$, but it is useful to keep in mind the full Co_2Si-type structure (*Pnma* symmetry).

$[\bar{3}6\bar{2}]$ and $[36\bar{2}]$ in $GaPd_2$.[6]

Hence the $GaPd_2$ structure should be oriented at a [100] or [001], or a [362], $[\bar{3}62]$, $[\bar{3}6\bar{2}]$ or $[36\bar{2}]$ direction, and then truncated on the appropriate $(2\bar{1}0)$, $(\bar{2}\bar{1}0)$, (013) or $(01\bar{3})$ planes. Placing the resulting structural units around a five-fold axis enables analysis of the solid angle deficiency and twin plane compatibility in five-fold twinned $GaPd_2$ nanoparticles (akin to arranging the regular tetrahedra contained in an FCC lattice or the irregular tetrahedra of BCO or rhombohedral crystal structures that exactly fulfil decahedral or icosahedral morphologies). In the following analysis of a $GaPd_2$ decahedron, each subunit is colour-coded according to its crystallographic orientation: red = [100]; green = [001]; blue = [362], $[\bar{3}62]$, $[\bar{3}6\bar{2}]$ or $[36\bar{2}]$.

4.2.3 $GaPd_2$ decahedron

4.2.3.1 Crystallographic model

Pursuing a purely geometrical analysis, there are different possible combinations of the $GaPd_2$ subunits to form five-fold twinned nanoparticles; or in other words there is a crystallographic puzzle to be solved. Some possible combinations for the conceptually simpler decahedron are illustrated schematically in Figure 4.11.[7]

Considering Figures 4.11a and b, it is evident that structures in which the $GaPd_2$ subunits are oriented such that all [100] or all [001] directions are parallel to the five-fold axis are unlikely, as these would result in large angular deficiencies. Those in which all $GaPd_2$ subunits have a [362]-type direction parallel to the five-fold axis (Figure 4.11c), or in which four $GaPd_2$ subunits have a [362]-type direction parallel to the five-fold axis and the remaining $GaPd_2$ subunit is in [001] orientation (Figure 4.11d) seem more plausible; the angular discrepancies in these cases being -2.16° or 2.16°, respectively.

The lower symmetry of the $\{111\}_{FCC}$-like twinning planes in $GaPd_2$ suggests the possibility of twin and 'pseudo-twin' boundaries, as dictated by their two-fold and pseudo-six-fold symmetry.[8] Neighbouring subunits at the same type of orientation and adjoining one another with the same (013)-type or with (210)-type planes could, in principle, due to the two-fold symmetry of these planes, form a perfectly coherent twin boundary. The two twinned subunits

[6]Similar reductions of symmetry are apparent in comparing an FCC structure to the BCO or rhombohedral crystal structures (Figures 4.4 and 4.5) that exactly fulfil the decahedral and icosahedral morphologies [175].

[7]For simplicity differing characteristic edge lengths of the $GaPd_2$ subunits are neglected in Figures 4.11 and 4.12.

[8]Similar concepts of pseudo-twin boundaries were postulated in refs. [183, 184].

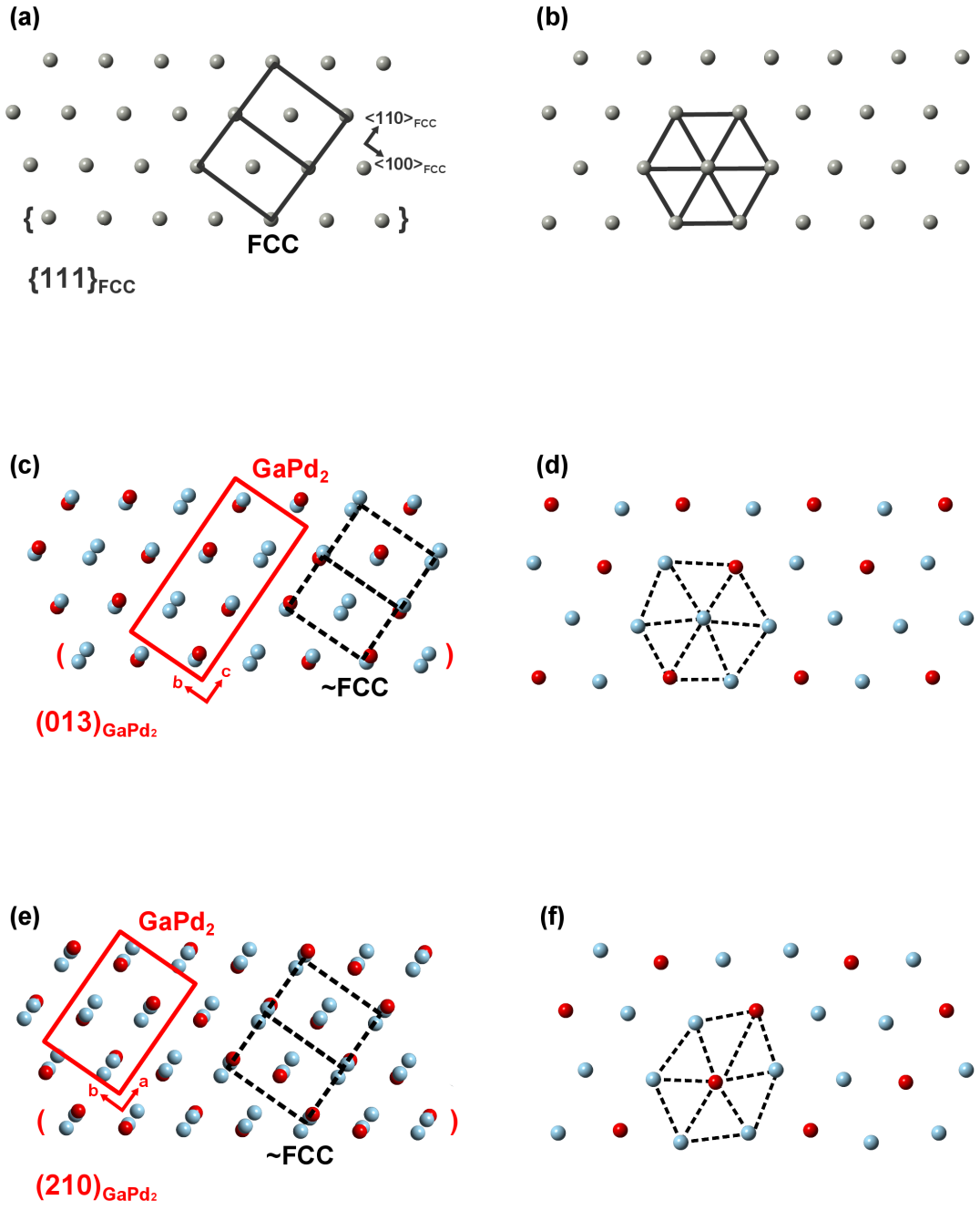

FIGURE 4.10: (a, b) Close-packed $\{111\}_{FCC}$ lattice planes, and (c-f) analogous pseudo-close-packed (210) and (013) planes in $GaPd_2$. (a, c , e) Views parallel to these planes showing four (pseudo)-close-packed layers, stacked in the vertical direction. The unit cell or pseudo-unit cell are shown in solid or dashed lines, respectively. (b, d, f) Corresponding views normal to the planes, in which six-fold (b) and pseudo-six-fold (d, f) motifs are indicated by solid and dashed lines respectively.

are simply regarded as inverted with respect to one another, such as being viewed, respectively, down [100] and [$\bar{1}$00] directions (Figure 4.12a). A subtle 'frustration', however, occurs when trying to pack five subunits in this way, as seen in Figures 4.11a and b where, inevitably, two neighbouring subunits must be at the same orientation, such as two neighbouring subunits in [100] orientation. This means that that a coherent twin boundary is not readily[9] formed, as illustrated in Figure 4.12b. Owing to the FCC-like pseudo-symmetry though, there may be an approximate match up of atoms. Such pseudo-twin boundaries are denoted by light blue dotted lines.

Pseudo-twin boundaries with incoherent (or 'mismatched') atomic positions would also result from neighbouring subunits being placed together such that different $\{111\}_{FCC}$-like planes of $GaPd_2$ face one another, as illustrated in Figure 4.12c, and denoted by dot-dashed yellow lines.

In another case, if the neighbouring subunits adjoin one another with the same type of plane, but each subunit is at one of the different $\langle 110\rangle_{FCC}$-like orientations, such as an [001] oriented subunit adjoining a [362]-type subunit, the twin planes would be rotated by ca. 60° (i.e. the angle between [001] and [362]) with respect to one another in the plane of the twin boundary. Once again, as there is only pseudo-six fold symmetry in the twin planes, there would only be an approximate match of atoms across the twin interface at such boundaries (Figure 4.12c). These pseudo-twin boundaries are denoted by dashed pink lines.

Referring again to the possible combinations of five $GaPd_2$ subunits exemplified in Figure 4.11, there is always a degree of packing frustration, resulting in one or more of the pseudo-twin boundaries.

4.2.3.2 Empirical observations from ADF-STEM

Undoubtedly there is complex interplay of many factors that act to stabilise the novel Ga-Pd decahedra and icosahedra - far more intricate than the analysis presented here. Nonetheless, the crystallographic analysis is informative as it indicates that the 'bulk' intermetallic $GaPd_2$ structure, interpreted in terms of an FCC-like lattice, does not intrinsically fulfil five-fold twinned geometries. Therefore, as with FCC systems, it is likely that some extent of structural distortion is required with respect to the bulk crystal structure. The ADF-STEM analysis can provide some valuable insight into the structures of the Ga-Pd decahedra occurring in practice.

[9] In a more general context, these planes could, of course, be brought into coherency by the appropriate symmetry operation (i.e. according by the *Pnma* symmetry).

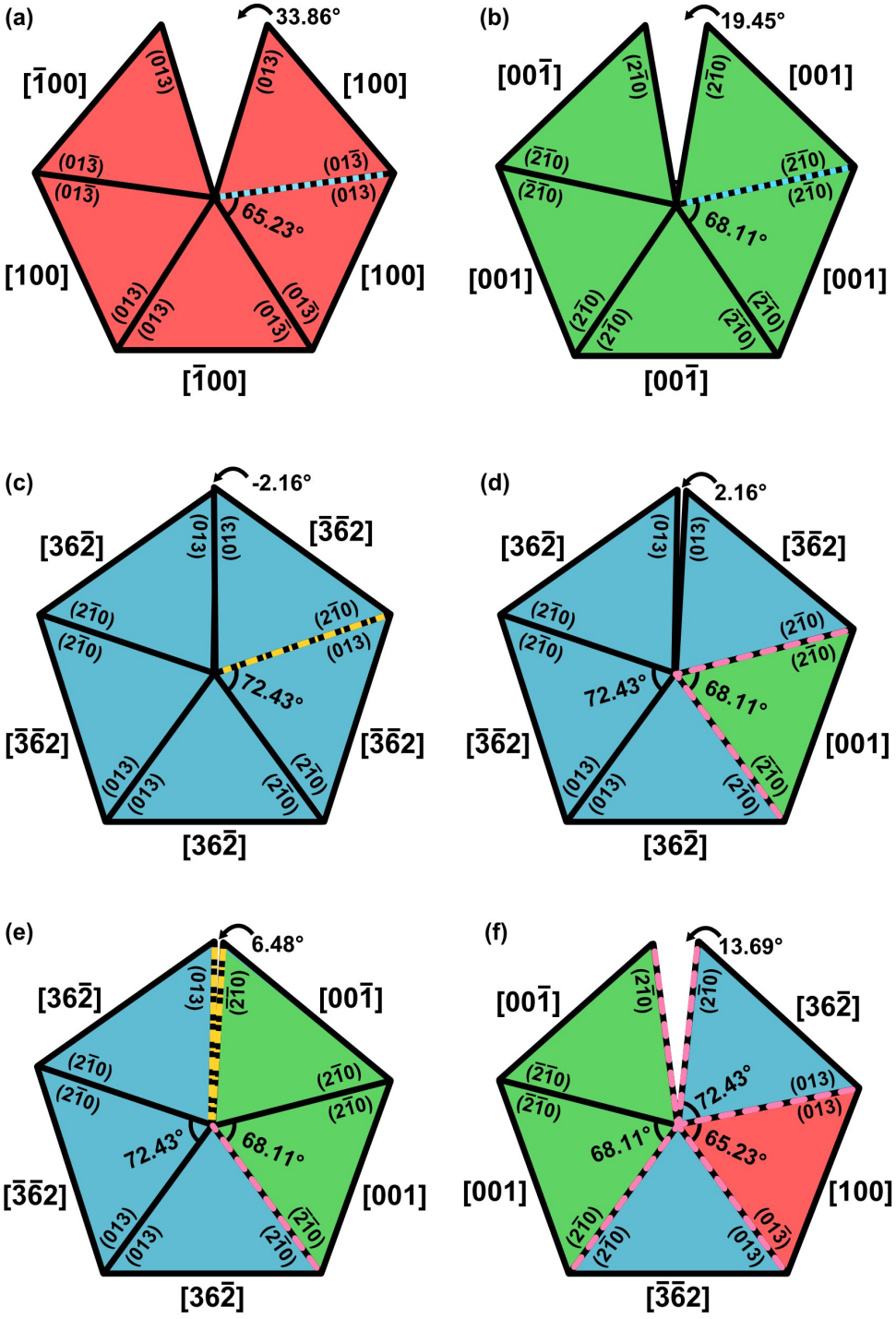

FIGURE 4.11: Example crystallographic structures for a decahedron in which each subunit possess the intermetallic $GaPd_2$ structure. Each subunit may be oriented with its [100], [001] or a [362]-type direction parallel to the five-fold axis (the subunits are colour-coded in red, green and blue, respectively, for each of these orientations). The crystallographic planes interfacing the (nominal) twin boundaries are labelled in round brackets. See Figure 4.12 for description of the twin boundaries.

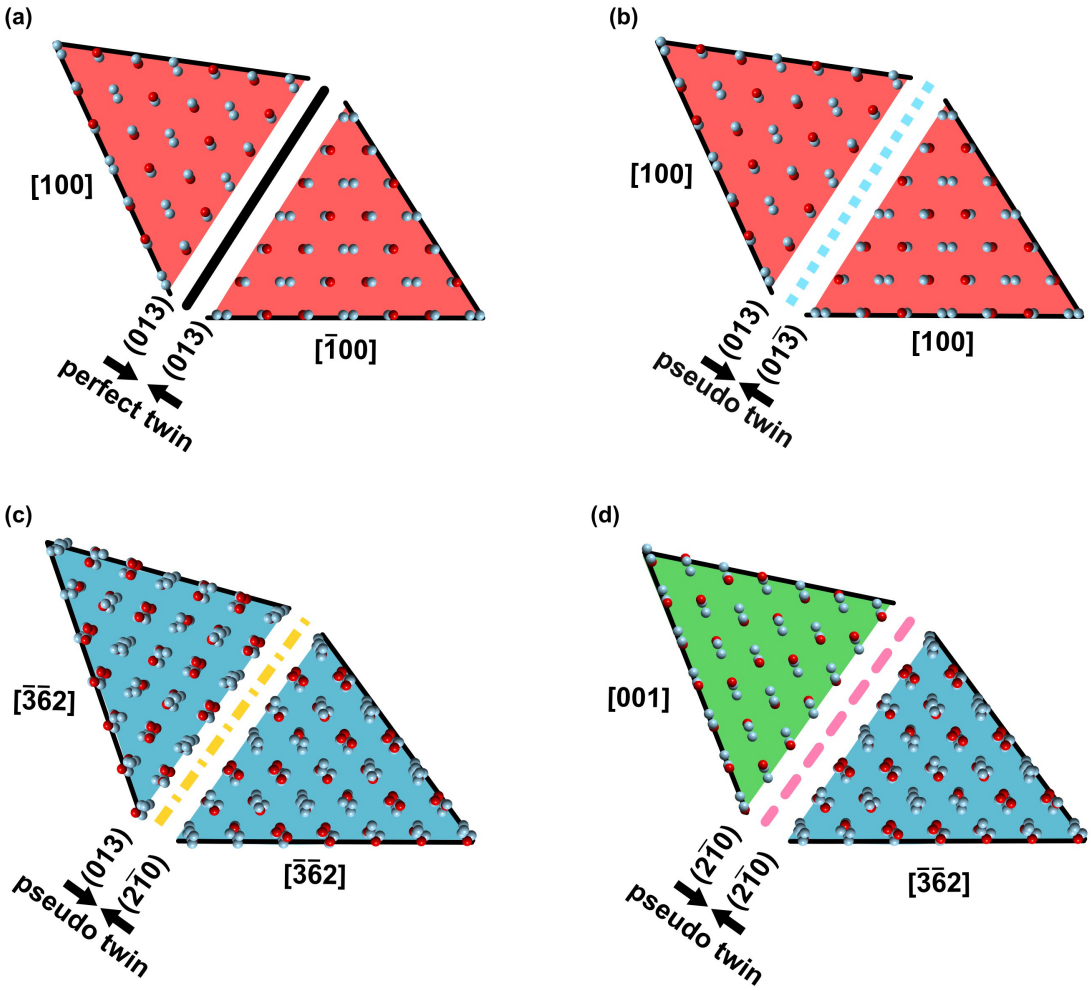

FIGURE 4.12: Schematic illustrations of possible $\{111\}_{FCC}$-like twins and 'pseudo-twins' between $GaPd_2$ subunits. (a) Neighbouring subunits can form a perfect (fully coherent) twin if they are viewed down the same type of crystallographic direction, but reversed in sign with respect to one another; exemplified here for [100] and [$\bar{1}$00] oriented subunits, this brings the (013) planes of each subunit together, the two-fold symmetry in these planes permitting a match-up of atoms. (b) Subunits brought together at the same orientation, exemplified for two [100] subunits, do not immediately, in this five-fold twinning context, form a perfect twin boundary as the different planes are brought together; in this case (013) and (01$\bar{3}$). This yields only a pseudo-match up of atoms, endowed by the FCC-like pseudo-symmetry. (c) Bringing subunits together such that different $\{111\}_{FCC}$-like planes in $GaPd_2$ face each other yields another type of pseudo-twin. (d) Bringing together two subunits at different crystallographic orientations also yields a pseudo-twin, as the twin planes are rotated by ca. 60° with respect to one another in the plane of the twin interface. The colour-coding and dotted/dash-dotted/dashed lines used in (b-d) to indicate the different types of pseudo-twin interface is the same as used in Figure 4.11.

Significant atomic-scale features of decahedra are typically rendered most visible when they are viewed down their five-fold axis. This avoids overlap of the subunits, and provides a view parallel to the plane of the twin boundaries. Noteworthy features of the decahedra shown in Figures 4.1a-c and Figure 3.19f (from chapter 3) are highlighted specifically in Figure 4.13. The use of ADF imaging and AC-STEM in this investigation offers scope for some immediate, intuitive, interpretation of the atomic-scale features of the decahedra (a considerable advantage compared to the majority of TEM studies of five-fold twinned nanoparticles, which have traditionally used BF-CTEM for high-resolution imaging). However, owing to the complexity of the $GaPd_2$ structure, the dense-packing or overlap of the nanoparticles, and the partial decomposition of their surface, as well as the deficiencies of the acquired images (all of which are discussed below), only very tentative interpretation is attempted here.

Firstly, if five-fold twinning resembling the idealised models were to occur, it is likely that 'pseudo-twin' boundaries would possess a perturbed structure. Some suggestions of irregular twin boundaries are apparent in the ADF-STEM images in Figure 4.13; particularly at the boundaries indicated by red arrows (and denoted dashed red lines in the accompanying schematics). Careful consideration is required, however, to differentiate genuine lattice distortion from image artefacts.

In the case of Figure 4.13a, the twin boundaries indicated by the red arrows show markedly different contrast compared to neighbouring lattice planes, which could be interpreted as reflecting structural disturbance at those boundaries. Strong caution must be taken in interpreting this effect though, considering the disposition of the decahedron with respect to the lattice planes of an underlying nanoparticle. More generally, it is important to bear in mind that, in addition to possible complication of the image contrast, the other nanoparticles visible in Figures 4.13a, b, e and f may also be influential in determining the nature of the decahedral morphologies, especially where they are intimately touching, partially coalesced with or acting like a substrate to the decahedra.

Also warranting discussion are the twin boundaries indicated by wavy red arrows in Figure 4.13e and Figure 4.13f, which show deviation from linearity. Similarly, some other lattice planes, particularly those of subunit 5 in Figure 4.13e, show a degree of curvature. While these are enticing observations, given the discussions of lattice strain in this chapter, it is important to differentiate genuine lattice distortion in this manner from image distortion due to the nature of STEM imaging [192]; for example, as caused by sample

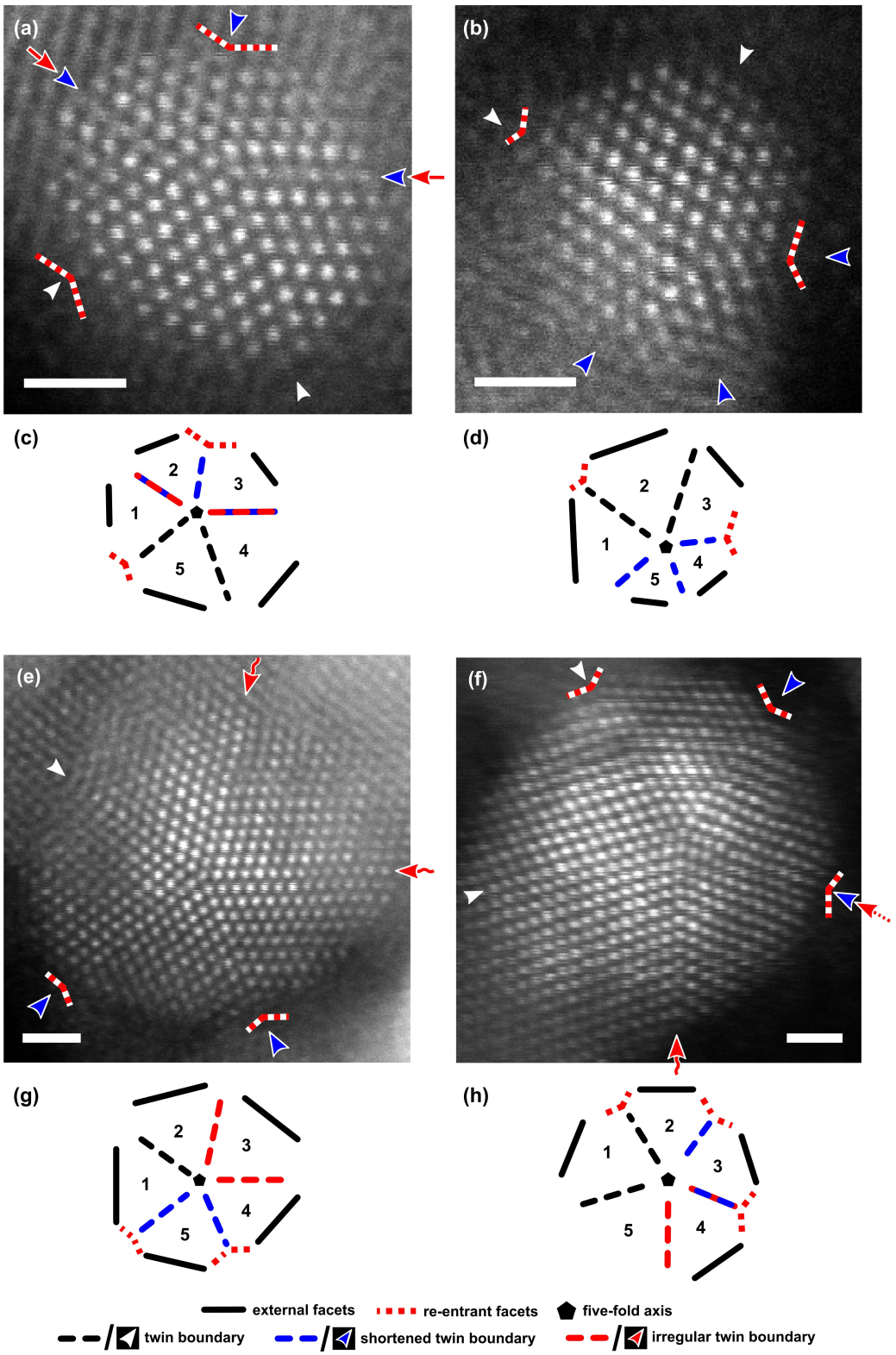

FIGURE 4.13: Significant features of decahedral Ga-Pd nanoparticles viewed down their five-fold (pseudo-$\langle 110 \rangle_{FCC}$) axes. (a, b, e, f) ADF-STEM images; (c, d, g, h) corresponding schematics highlighting key features. See text for description. Scale bars: 1 nm.

drift during the point-by-point serial image acquisition. In the context of five-fold twinning, making this distinction can be decidedly challenging, but the apparent non-linearities of the twin boundaries indicated by wavy red arrows bear typical characteristics of STEM imaging distortion, and are most probably artefactual. On the other hand, images acquired prior (at lower magnification), and subsequent, to Figure 4.13e also show some curvature or 'warping' of the lattice planes in subunit 5, potentially supporting the notion of a genuine element to this distortion. A similar degree of lattice plane curvature is also hinted at in Figure 3 of ref. [167]. However, more sophisticated image acquisition and/or analysis is required to reliably interpret this apparent distortion (see later discussion, section 4.3).

Of potential significance also is that the twin boundary indicated by a dotted red arrow in Figure 4.13f exhibits some buckling of the atomic columns, and that a number of the other lattice planes in subunits 3 and 4 (above and below this twin boundary) exhibit similar irregularities. This may be indicative of considerable structural complications in and/or between these subunits. The relatively undistorted nature of many of the other twin boundaries in Figures 4.13a, b, e and f (indicated by white arrowheads or dashed black lines) suggests that they may be more similar to the 'perfect' twin boundaries discussed, that the $GaPd_2$ structure has 'relaxed', or that significant structural/compositional deviations have occurred (e.g. the decahedra could in fact be closer to FCC monometallic Pd if there has been significant segregation of Ga). However, only tentative conclusions can be made from these 2D projection images, which may not render visible important structural features [155]. Influence of the electron beam, potentially causing or negating buckled atomic columns, should also be kept in mind.

As a second major point, it is justifiable to speculate, on the basis of the crystallographic model and experimental images, that $GaPd_2$ decahedra may have a heightened predisposition to displace the five-fold axis off-centre. Perhaps most significantly, shifting the five-fold axis in the direction of any pseudo-twin boundaries would reduce the boundary size. Such shortened twin boundaries, due to the eccentricity of the five-fold axes, are marked by blue arrowheads or dashed blues lines in Figure 4.13, where Figure 4.13b has the most strongly eccentric five-fold axis. Another example of a highly eccentric five-fold axis can be found in Figure 3 of ref. [167]. The position of the five-fold axis is indicated in each schematic, although is notably ambiguous in Figure 4.13a and b due to the distorted structures of the decahedra.

Such eccentric disposition of the subunits could also be a consequence of the mismatches between the pseudo-equivalent FCC-like lattice parameters along the different candidate crystallographic directions of $GaPd_2$. Although a well-known stabilising mechanism in FCC systems [136], an off-centre position of the five-fold axis has been observed in a significant proportion of the Ga-Pd decahedra. It should be born in mind though that these speculative correlations between the basic model and empirical observations may well be oversimplifications, given that the analysis here neglects many other influential factors. In general, such shifting of the five-fold axis indicates that considerable elastic stress has developed in the nanoparticles.

Thirdly, although quite subtle, the decahedra show slight re-entrant faceting of the $\{111\}_{FCC}$-like planes at the twin boundaries; indicated by red-white dotted lines at the periphery of the decahedra in Figure 4.13. This leads to Marks-like decahedral morphologies [185] (cf. Figure 3.10a). Such re-entrant facets are often necessary to stabilise the decahedral morphology [185], and hence are common in conventional FCC systems. Nonetheless (again neglecting other influential factors), it is plausible at least to speculate that re-entrant faceting, since it reduces the size of a twin boundary, could be more prevalent at the less favourable twin boundaries in $GaPd_2$ decahedra.

4.2.3.3 First approximation model

Seeking a speculative model from the simple geometric analysis presented and the empirical observations, it was noted previously that the candidate structures in Figures 4.11a and b are highly improbable due to their very large solid angle deficiencies. Similarly, Figure 4.11f seems unlikely due to its large solid angle deficiency and the high number of pseudo-twin boundaries. In Figure 4.11e there are fewer pseudo-boundaries, and solid angle deficiency is approximately half that of Figure 4.11f (and comparable to that in conventional FCC systems). However, the solid angle deficiency is still large compared to Figures 4.11c and d. Figures 4.11c and d seem to be most conducive to preserving the intermetallic $GaPd_2$ structure in a decahedron, and are taken here as the candidate structures.

Modifying Figures 4.11c and d to include the discussed re-entrant faceting at the pseudo-twin boundaries, as well as an eccentric position of the five-fold axis that also reduces the length of the pseudo-twin boundaries, yields Figures 4.14a and b as basic models. These models are at least partially consistent with the empirically observed Ga-Pd decahedra.

Figures 4.14a and b have been drawn as space-filling structures, implying that

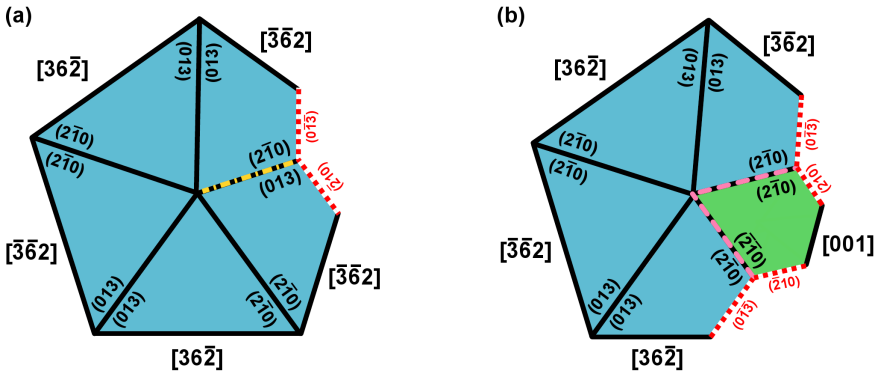

FIGURE 4.14: Basic structural models based on the crystallography of $GaPd_2$ and the experimentally observed Ga-Pd decahedral morphologies. (a) and (b) correspond to modified structures of Figures 4.11c and d, respectively, in which an eccentric position of the five-fold axis reduces the length of the pseudo-twin boundaries (dot-dashed yellow or dashed pink lines), and the length of these boundaries is also reduced by $\{111\}_{FCC}$-like re-entrant facets (red-white dotted lines).

a crystallographic distortion is present to resolve the solid angle discrepancies of -2.16° or 2.16°, respectively, present in Figures 4.11c and d. Interestingly, with angular discrepancies of opposing sign, the distortions and the resultant strain state of these two decahedra would be subtly different, such as corresponding to a negative or positive wedge disclination of magnitude 2.16°, or a respective shear strain of ±3.8 %. A further subtle consideration not explicitly shown in the schematics of Figures 4.11 is the dimensional mismatch between subunits, including along the five-fold axis of the decahedron (i.e. into the plane of the paper). Significantly in this regard, Figure 4.11d contains four [362]-type segments and one [001] segment, which, in addition to two pseudo-twin boundaries with neighbouring segments, will be mismatched with all of the [362]-type segments at the five-fold axis. Figure 4.11c on the other hand, consists entirely of [362]-type segments, and there is also only one pseudo-twin boundary. Accordingly, it is reasonable to suggest Figure 4.14a as the favoured model morphology.

4.3 Discussion

The purely crystallographic analysis and basic interpretation of AC-STEM images in this chapter provide a fundamental first step toward interpreting five-fold twinning in $GaPd_2$ and, more generally, in the Ga-Pd system. In practice, the five-fold twinned (and nanocrystalline) morphologies are dictated by complex interplay between many parameters that have not been considered explicitly here. These include surface energies, the substrate, surface adsorbates, synthesis

conditions (i.e. kinetics) and energies involved in formation of the ordered intermetallic compound $GaPd_2$ or other ordered/disordered atomic structures. Moreover, the energetics of twinning relationships and lattice strain should be analysed more rigorously; ideally quantitatively.

Perhaps most significant is the inherent instability of the $GaPd_2$ surface under oxidising conditions, as was addressed in chapter 3. The resultant chemical segregation will almost certainly be strongly linked to the adoption of particular morphologies. As noted in section 4.1.1, segregation effects have often been cited as being highly influential in five-fold twinned morphologies. The ADF-STEM images (Figures 4.1 and 3.19) indeed show that the segregated Ga_xO_y overlayer is present on the five-fold twinned nanoparticles. Accordingly, recalling also that the studied Ga-Pd nanoparticles are derived from a monometallic FCC Pd 'parent' (see again the synthesis process in section 3.2.1) a number of possibilities could be mooted regarding the development of the five-fold twinned structures: (i) an initial five-fold twinned Pd nanoparticle; (ii) five-fold twinning upon formation of $GaPd_2$ or some other Ga-Pd phase; or (iii) upon subsequent segregation of Ga.

Distortion or 'relaxation' of the crystal structure in the nano-sized $GaPd_2$ intermetallic compound was also discussed previously in chapter 3 (section 3.3.3). There it was suggested that at near-surface regions, the structure potentially 'relaxed' towards FCC characteristics, with the relaxation conceivably being mediated by the segregation of Ga to surface oxides. In a similar manner, it is plausible to see how the structure could 'relax' to accommodate the five-fold twinned structures. Caution should be noted though in making inferences about the five-fold twinning based on characteristics of the nanocrystalline particles. Although the intermetallic $GaPd_2$ structure, or the 'relaxed' structure, was revealed in nanocrystalline Ga-Pd particles in chapter 3 (even in light of partial Ga segregation), the five-fold twinned nanoparticles could be considerably different. Much more challenging to characterise, the precise atomic structure and composition of the five-fold twinned Ga-Pd nanoparticles has not been so clearly revealed. As was noted in chapter 3 (section 3.3.3) it is reasonable to presume that a Ga-Pd solid solution is unlikely, therefore suggesting chemically ordered and/or segregated compositions. While chemical ordering and the ideal $GaPd_2$ structure has been assumed for the crystallographic analysis in this chapter, the possibility of major structural or chemical deviations cannot be ruled out based on the present analysis. At the extreme, extensive segregation of Ga could even have left near monometallic Pd five-fold twinned nanoparticles.

The aforementioned recent studies concerning Ag, Au, Pt and FePt nanoparticles [23, 25, 155–158, 187] used state-of-the-art TEM to carry out sophisticated analyses, such as 3D reconstruction at atomic resolution, or quantitative analysis of strain. Here, some basic insights have been obtained from the experimental images, but the scope of the analysis is more limited. Further to the limitations already discussed, the disordered Ga_xO_y over-layer means that pristine imaging of the atomic columns in the small nanoparticles is not possible. The quality of the images is also limited by the beam sensitivity of the small particles and mobility of the segregated over-layer. Hence quantitative image analysis has not been feasible. Similarly, EELS or EDXS analysis that might reveal any compositional segregation in the five-fold twinned nanoparticles is challenging. However, valuable analysis may be possible for some of the larger (decahedral) nanoparticles, and/or with optimised acquisition such as using a fast EEL spectrometer or large solid-angle EDX detector(s).

As well as the experimental challenges, it should also be emphasised that firm identification of the $GaPd_2$ structure in the five-fold twinned nanoparticles is challenging in principle. Firstly, there is very close resemblance to an FCC structure along important crystal zone axes, such as the five-fold orientation ($\langle 110 \rangle_{FCC}$-like). This is in contrast to decahedral FePt nanoparticles, where the chemical ordering in the $L1_0$-type structure can be clearly revealed down the five-fold axis [158]. Secondly, subunits often overlap in atomic resolution images of five-fold twinned nanoparticles. Both of these factors complicate identification of distinctive zone axes, as was feasible for single crystalline domains in chapter 3 (Figures 3.14-3.16). Slightly differing TEM images would be expected for each of the [001], [100] and [362]-type directions in $GaPd_2$, but the subtle differences may well be rendered negligible in the small particles, and further so by lattice relaxation/distortion. The effects of electron beam channelling (discussed in section 2.2) on the intensities of the atomic columns in the ADF images also makes identification of subtle differences in atomic column chemical composition challenging, especially if further compounded by strain effects and underlying nanoparticles. Although there are some marked regional differences in atomic column contrast in Figures 4.13d and e, this was found to change between successive images, with small changes in particle tilt and/or can be attributed to the effects of underlying particles, suggesting that it is not due to substantial compositional variation. Nonetheless, further insights into chemical ordering may be achievable via high-resolution AC-STEM, particularly if careful sample preparation can minimise particle overlap and the extent of the Ga_xO_y over-layer.

Image simulation could also aid interpretation of complicated images, as has often been used for FCC systems and, for example, has recently been insightful in the study of ordered FePt nanoparticles [158].

The correction of STEM image distortions that have affected this investigation is, in general, an active area of research (e.g. ref. [192]). However, specific consideration of the STEM artefacts with respect to imaging of five-fold twinned nanoparticles may be important, both during acquisition and in post-processing. Particularly, acquiring multiple STEM images in which for each image the fast scan direction is altered could reduce doubt over false lattice distortion, and allow fairer comparison between the lattice structure in each of the subunits. Consideration of the optimum scanning direction with respect to the twin boundaries, certain lattice planes or key directions of strain may also be important. An alternative approach is joint CTEM/STEM analysis (such as performed by Li et al. [158]), combining the direct interpretability of ADF-STEM and the absence of scanning distortions in CTEM.

To address the surface segregation effects, the use of *in situ* TEM [153] to view structural changes under various atmospheres or temperature regimes could prove especially illuminating, as has been performed, for example, for Au nanoparticles [157, 193]. This chapter and chapter 3 also invite theoretical modelling of Ga-Pd nanoparticles. Finally, gathering population statistics of the different nanocrystalline or five-fold twinned Ga-Pd morphologies yielded by particular synthesis routes or present under certain conditions would enable assessment of the prevalence, and therefore the practical significance, of the five-fold twinning.

4.4 Conclusions

Having considered various arrangements in the crystallographic puzzle, the intermetallic $GaPd_2$ crystal structure, interpreted from an 'FCC-like' perspective, does not fit perfectly the geometry of five-fold twinned nanoparticles, necessitating at least some lattice distortion to form such morphologies. AC-STEM has given initial insight into the atomic-scale structure of the five-fold twinned Ga-Pd nanoparticles occurring in practice, showing hallmarks of structural strain/distortion, as well as significant chemical segregation. The precise atomic structure of the five-fold twinned Ga-Pd nanoparticles though remains to be determined. Evidently, multicomponent systems and/or those in which the structural geometry deviates from the conventional FCC setting can

add both opportunity and complexity for unravelling five-fold twinning.

In the context of knowledge-based development and rational catalyst design, this chapter reinforces the notion (from chapter 3) that the crossover between assumed bulk crystalline structures and non-crystallographic five-fold twinned structures requires further attention in the exploitation of nano-sized intermetallic compounds. As an intriguing area that may not only provide materials systems with hitherto unobtainable properties, but also shed light on many aspects of nanoparticle structure and stability, further investigation of novel nano-sized intermetallic compounds should prove a productive area of research from both an experimental and theoretical standpoint.

Chapter 5

Electron tomography: foundations, contemporary methods & opportunities

In this chapter the principles, established practices and limiting factors in electron tomography (ET) are reviewed, along with state-of-the-art methods, opportunities and aspirations. The drive for robust quantitative analysis is identified, which motivates the move towards robust image processing based segmentation described in chapter 6. The limited number of measurements (tilt-series images) that can be acquired practically and the inability of conventional reconstruction algorithms to yield satisfactory results from such undersampled data are identified as primary factors hampering ET. This leads towards the theory and investigations in chapters 7 and 8, where new compressed sensing approaches for ET reconstruction are described and demonstrated.

5.1 Introduction

While not stated explicitly in chapter 2, it must always be borne in mind that a standard TEM image is, at best, only a 2D projection of a 3D object. It is the goal of 3D TEM methods to retrieve the 3D information, using one or more 2D images.

The first example of 3D reconstruction using TEM came from DeRosier and Klug [194] in which, harnessing prior knowledge of the helical symmetry of the object, they obtained a 3D reconstruction of the tail of the T4 bacteriophage from a single 2D image. They also outlined the principles of reconstructing arbitrarily shaped 3D objects from a series of 2D TEM images; or more specifically, TEM

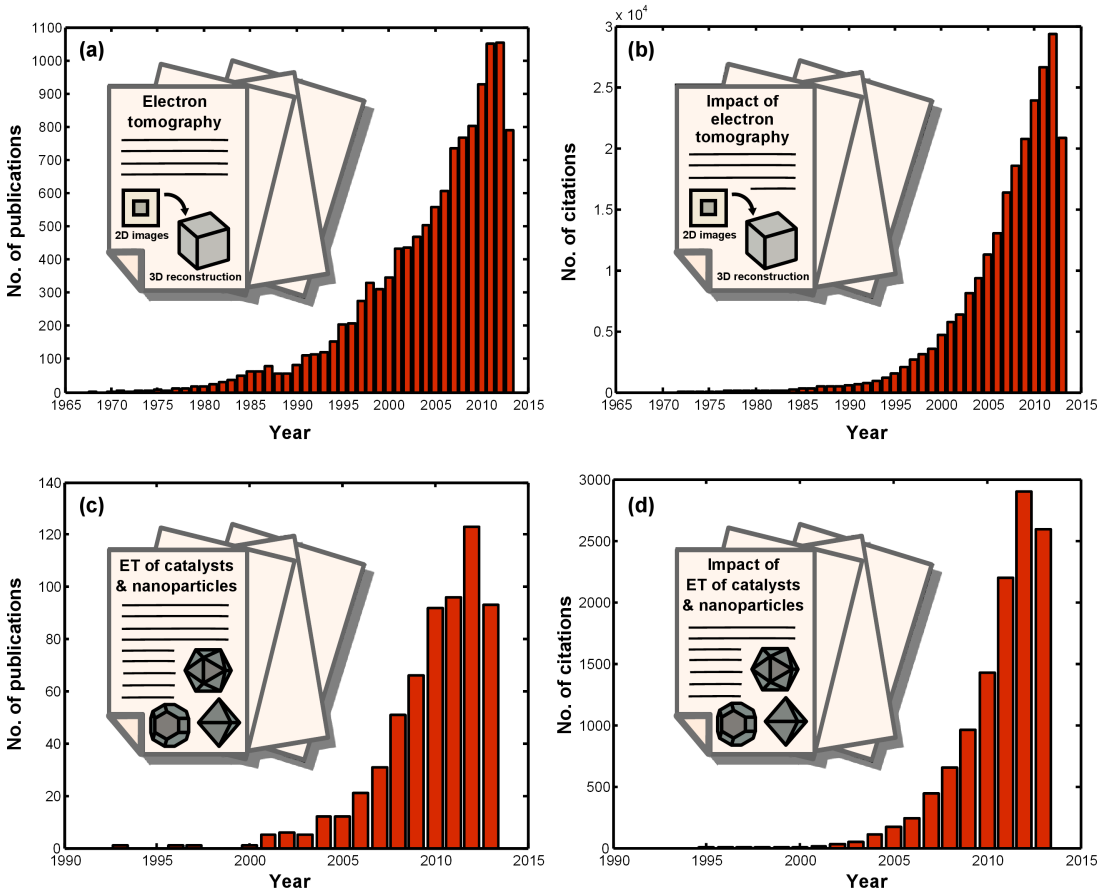

FIGURE 5.1: Annual number of publications retrieved by the search terms (a) 'electron tomography', and (c) 'electron tomography AND (nanoparticle* OR catalyst*)'; (b, d) respective annual numbers of citations of these publications. Source: ISI Web of Knowledge, search date October 2013.

'projections'. Along with two other seminal papers from the same year [195, 196], this is generally seen as the starting point of ET.

ET is now widely practised and has significant research impact, as may be inferred from Figures 5.1a and b. It is (arguably) the most widely applicable and successful method of 3D analysis in TEM to date. Alternative 3D TEM imaging modes are reviewed at the end of this chapter in section 5.4.

This chapter focuses on ET in the physical sciences, but reference is made to methods or application in the biological sciences when appropriate. Indeed, ET progressed originally in the biological sciences using BF-CTEM [197]. Since the introduction of alternative imaging modes by Midgley, Weyland and co-workers [13, 51, 52] it has become popular in the physical sciences as well [9]. Supported heavy metal nanoparticles, including nanocatalysts, have been some of the systems most studied by ET, as Figures 5.1c and d illustrate.

It is important to emphasise, however, that ET is now being used to

address a range of different nanoparticulate and nanoscale materials. These have been reviewed by a number of different authors. Some reviews have focused on specific applications where ET has been particularly valuable, such as heterogeneous catalysts [37], mesoporous solids [198], polymers [199–201], solar cells [202], semiconductors [203] and dislocation structures [204]. Many other reviews cover a broad range of applications from across the materials science context [13, 38, 39, 41, 42, 205–208], [44, chapters 11 & 12], [20, chapter 8]. Correspondingly, the range of structures and properties studied by ET is diversifying; for example, ranging from features with homogeneous composition and sharply defined boundaries, such as many nanoparticle systems [209–211], to those that may display smoothly varying properties such as plasmons [212, 213], electrostatic potentials [214, 215] or compositional gradients [216, 217]; or specimens with convex [218, 219] or concave [220] boundaries; or primarily spherical [221, 222], hexagonal [219] or elongated [221] morphologies.

A number of recent reviews covering state-of-the-art methods and applications can be found in a special issue of Current Opinion in Solid State and Materials Science [223]. Specifically, these address computational methods [224], high-resolution ET [225], ET of soft materials [201], holographic ET [214] and ET of catalysts [43]. Midgley and Saghi [223] also highlight the growing importance of multi-dimensional ET signal modes, such as STEM-EELS and STEM-EDXS.

5.2 Foundations of tomography

5.2.1 Essence of tomography

Although the literal meaning of the term ‘tomography’ refers to the visualisation of slices, transmission tomography, such as TEM tomography (referred to here as ET) or X-ray tomography, can be considered as a method of reconstructing the interior of an object from a set of projections through its structure. In essence, this form of tomography is achieved by recording an angular series of projections, usually about a single tilt axis. The ensemble of images is then used to form a reconstruction, or ‘tomogram’, via some operation that can essentially be seen as an inversion of the original projection process.

5.2.2 Mathematical foundations

The mathematical framework for tomography originates from a seminal paper by Radon in 1917 [226], which defined the 'Radon transform'. As highlighted by Bracewell in 1956 [227], tomography is also underpinned by the more widely known Fourier transform. The foundational principles of tomography stemming from these transforms are now well-established, and further coverage beyond that given here can be found in [10, 228–235], [44, chapter 2].

Although tomography is typically referred to as a 3D reconstruction method, the most common single axis geometry permits the reconstruction process to be addressed in terms of a series of, in principle, independent 2D reconstructions. In general this is both algorithmically and computationally easier, and is used for the descriptions provided here. A possible disadvantage of slice-by-slice 2D reconstruction of a 3D volume is that it may be difficult to fully exploit 3D prior knowledge during the reconstruction process, in which case 'fully 3D' reconstruction may be desirable.

5.2.2.1 The Radon transform

The Radon transform $\mathcal{R}$ describes directly the projection process, mapping a function f by line integrals along all possible lines L. With increment ds along L, the transformation may be defined as:[1]

$$\breve{f}(l,\theta) = \mathcal{R}f = \int_L f(x,z)ds, \tag{5.1}$$

the geometry of which is illustrated in Figure 5.2. The function f is defined here on the 2D real space co-ordinates (x,z) and the Radon transform converts the data into 'Radon space' (l,θ), frequently referred to as a 'sinogram', where l is the line perpendicular to the projection direction and θ is the angle of projection (Figure 5.3).

In principle, the real space structure of the object $f(x,z)$, can be recovered from the Radon domain $\breve{f}(l,\theta)$ by an inversion of the Radon transform. Since the empirical sampling of an object by a projection is equivalent to a discrete sampling of the Radon integral, the goal in tomography is then to acquire a sufficient number of projections so that the sampling of Radon space is sufficient such that an inverse transform, or some other means of reconstruction, can yield an adequate approximation of the object.

[1] Comprehensive coverage of the Radon transform can be found in the text by Deans [228]. Here, one of the most intuitive definitions is given, following the notation from [13].

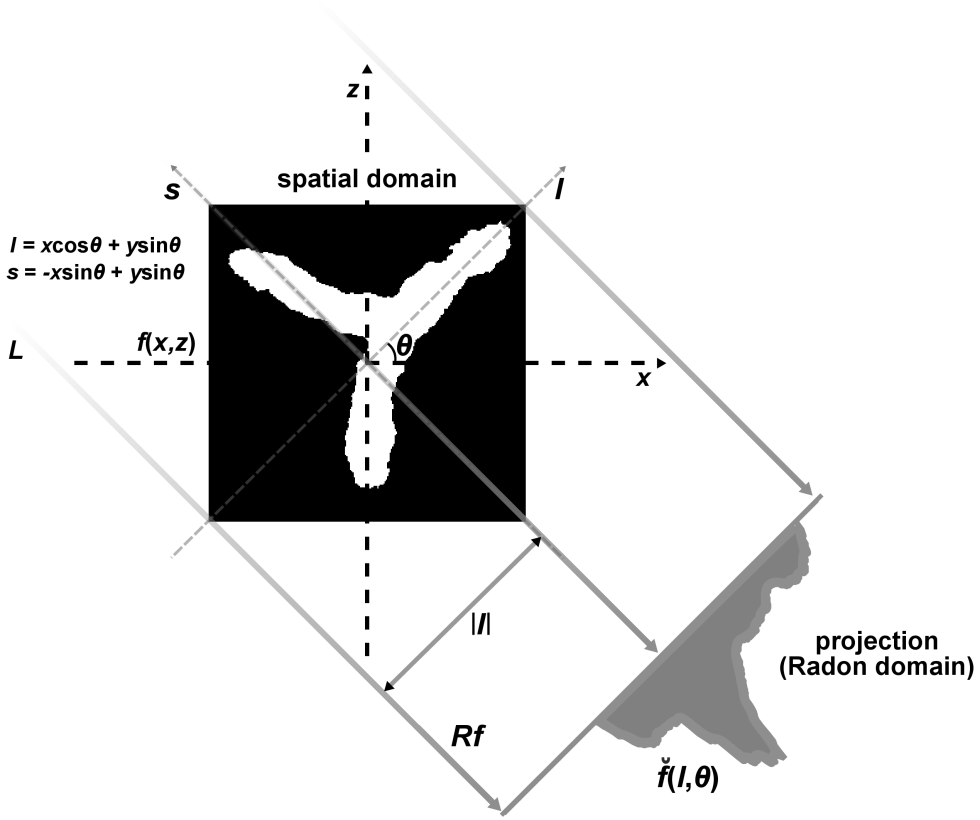

FIGURE 5.2: Geometry of the Radon transform.

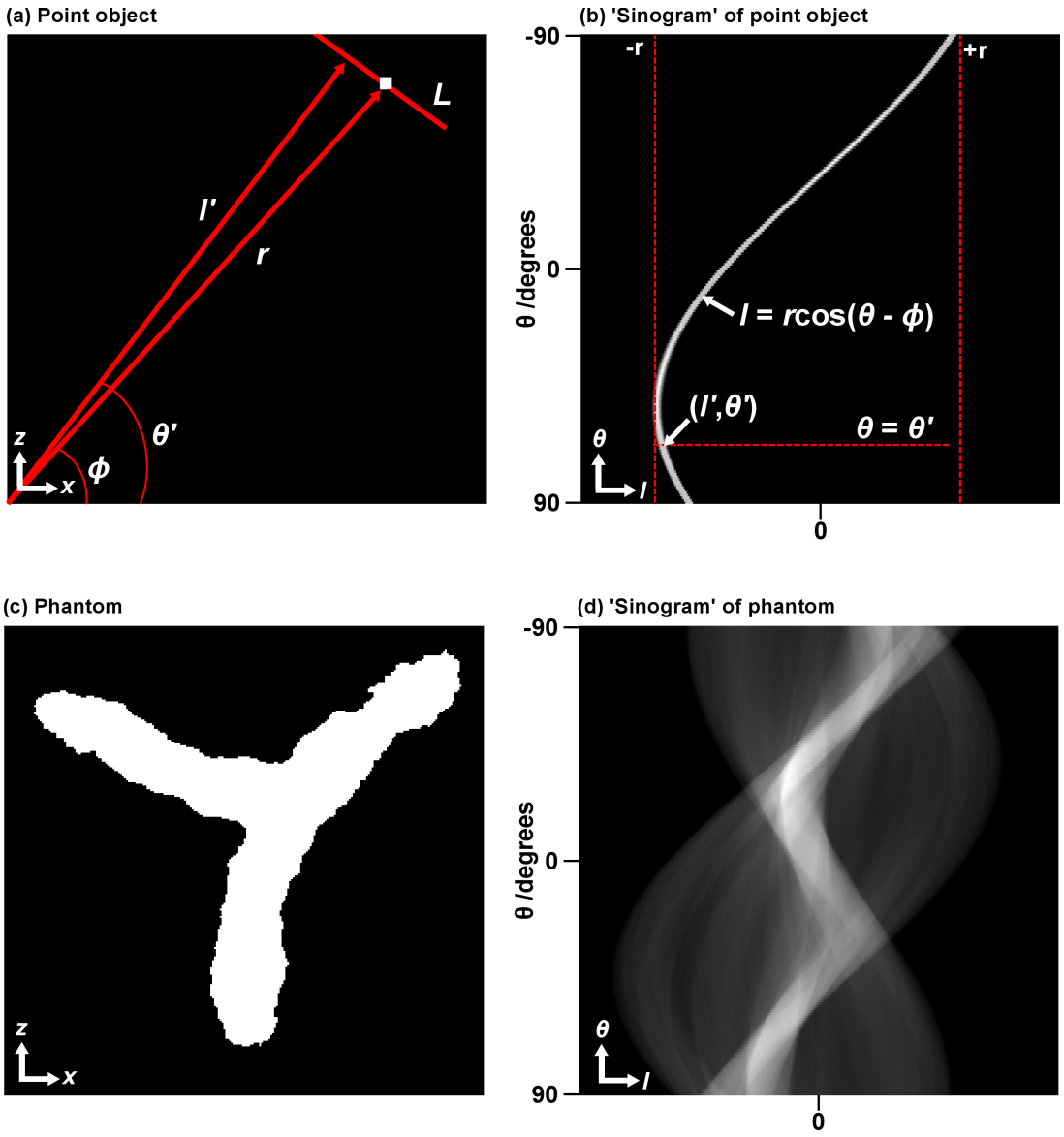

FIGURE 5.3: The relationship between real space (a, c) and Radon space (b, d). Using polar co-ordinates (r, ϕ), related to Cartesian co-ordinates by $r = \sqrt{x^2 + z^2}$ and $\phi = \tan^{-1}(z/x)$, a point object in real space $(x = r\cos\phi, z = r\sin\phi)$ is a line in Radon space (l, θ) linked by $l = r\cos(\theta - \phi)$.

5.2.2.2 The Fourier transform

Closely related to the Radon transform is the Fourier transform, which for the general case of an N-dimensional function f, may be written as:

$$\tilde{f}(\mathbf{k}) = \mathcal{F}_N f = \int_{-\infty}^{\infty} f(\mathbf{x}) e^{-2\pi i \mathbf{k}\cdot\mathbf{x}} d\mathbf{x}, \tag{5.2}$$

where $\mathbf{x} = x_1, x_2, ..., x_N$ are the co-ordinates in real space, and $\mathbf{k} = k_1, k_2, ..., k_N$ the corresponding co-ordinates in Fourier space. In words, the Fourier transform provides an alternative means of representing a function by decomposing it into (spatial) frequency components. Amongst many applications, one use of this decomposition was already made in chapter 3 for analysing the characteristic periodicity in images of crystalline lattices. There is significance and practical application in the tomographic imaging context too, which is embodied in the 'Fourier slice theorem'.

5.2.2.3 The Fourier slice theorem

The work of Bracewell [227] highlighted the important relationship between projections formed via the Radon transform and the Fourier representation of an object, which has become known as the 'Fourier slice theorem'. The theorem states that:[2] *the Fourier transform of the projection of a function, at a given angle, is equivalent to a central section, at that angle, through the Fourier transform of the function.* Figure 5.4 illustrates the theorem for 1D projections of a 2D object; an analogous relationship applies to 2D projections of an object and central sections in its 3D Fourier space.

The Fourier slice theorem further aids the understanding of tomographic reconstruction and the consequences of finite sampling: acquiring projections at different angles is equivalent to sampling sections of the object's Fourier space over the range of frequencies in each central section. However, most objects will not be fully described by the frequencies in one section, or even a few sections, meaning that many projections at different angles are required to sample Fourier space sufficiently such that, in principle, it would be possible to obtain a satisfactory description of the object in real space by direct inversion of the sampled Fourier space.

The relationships between real, Radon and Fourier space are shown explicitly in Figure 5.5. From Figure 5.5 and the foregoing discussion, it is apparent

[2]See e.g. Kak and Slaney [229] for a concise derivation, or Deans [228] for a comprehensive description.

that the tomographic reconstruction process can be approached via either a real space based 'back-projection' route, or a Fourier inversion route. The practicalities of ET however, reviewed hereinafter, mean that either approach is rarely straightforward to achieve.

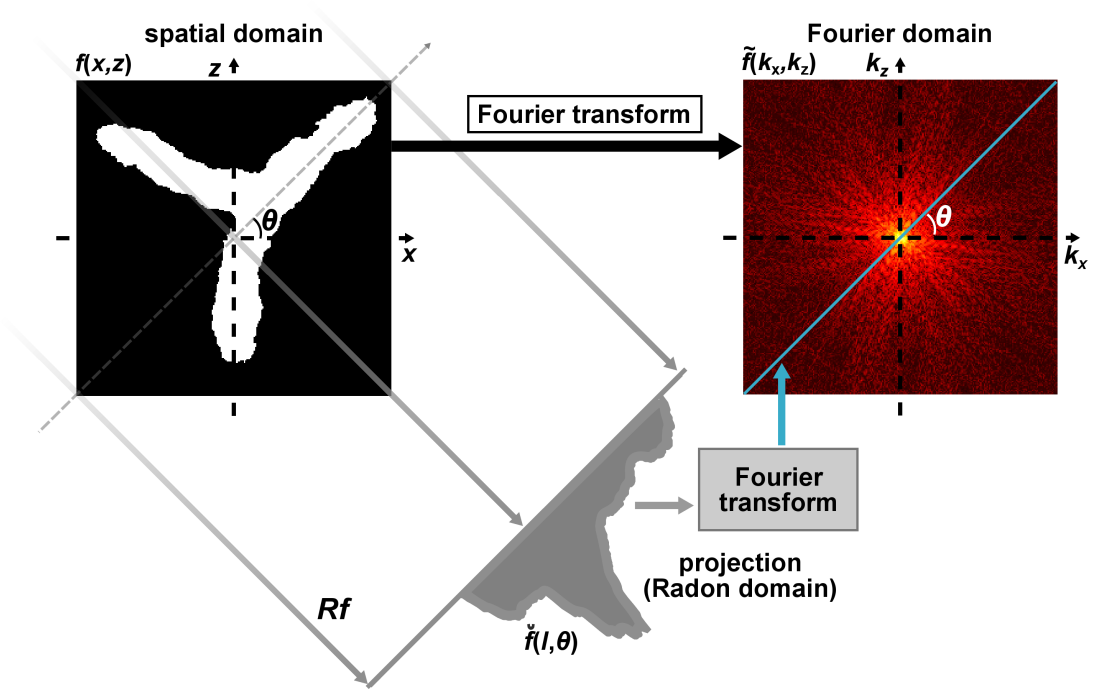

FIGURE 5.4: Schematic illustration of the Fourier slice theorem.

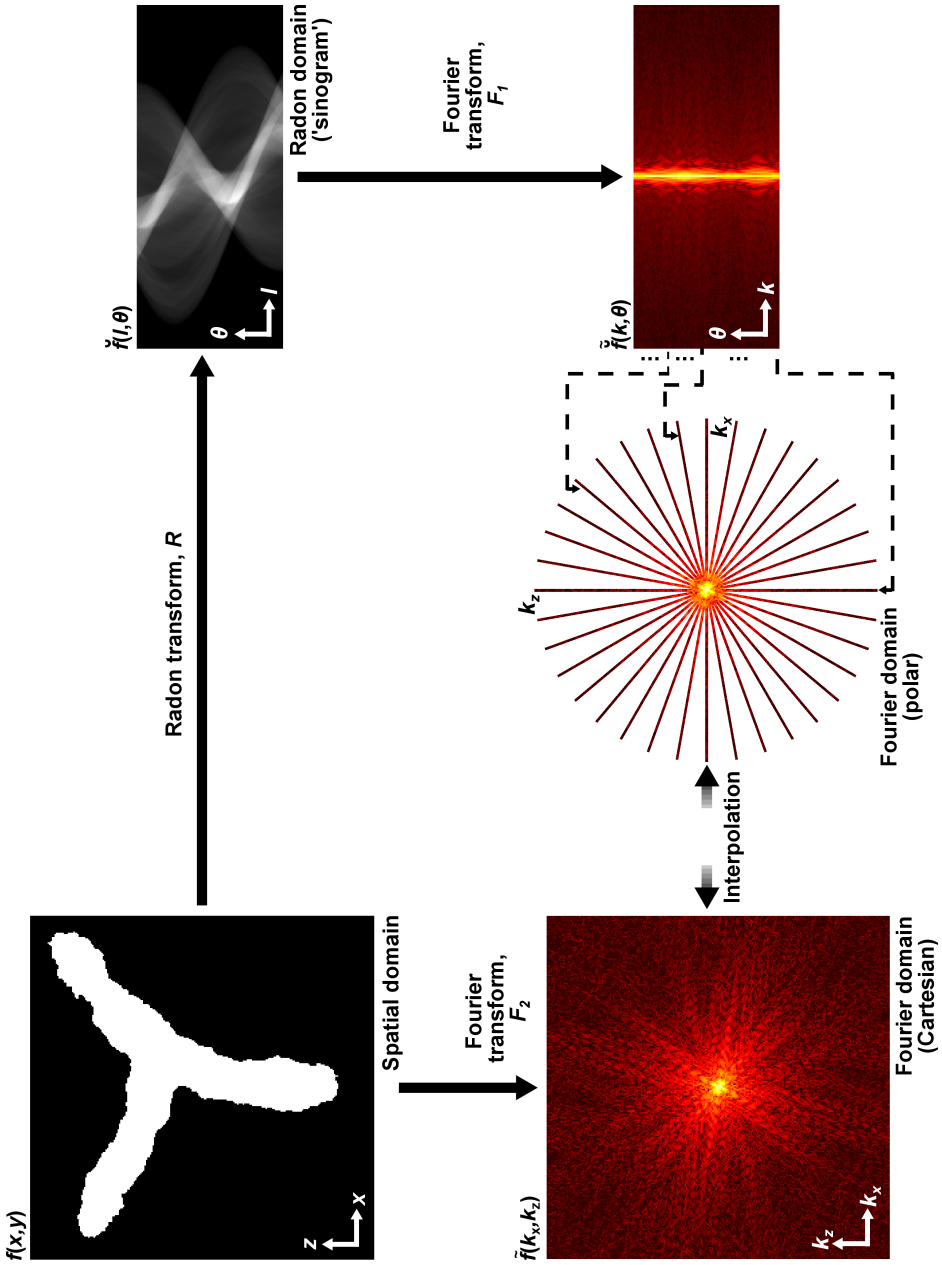

FIGURE 5.5: The relations between real, Fourier and Radon space.

5.3 Principles & Practice of ET

An ET investigation consists of a number of distinct but inter-related stages, summarised in Figure 5.6. With the exception of sample preparation, which is referred to only in specific cases, these are reviewed sequentially in the following sections. Noteworthy reviews of foundational ET practices in the physical sciences can be found in [13, 38, 41, 42, 205, 207], [44, chapter 11], [20, chapter 8].

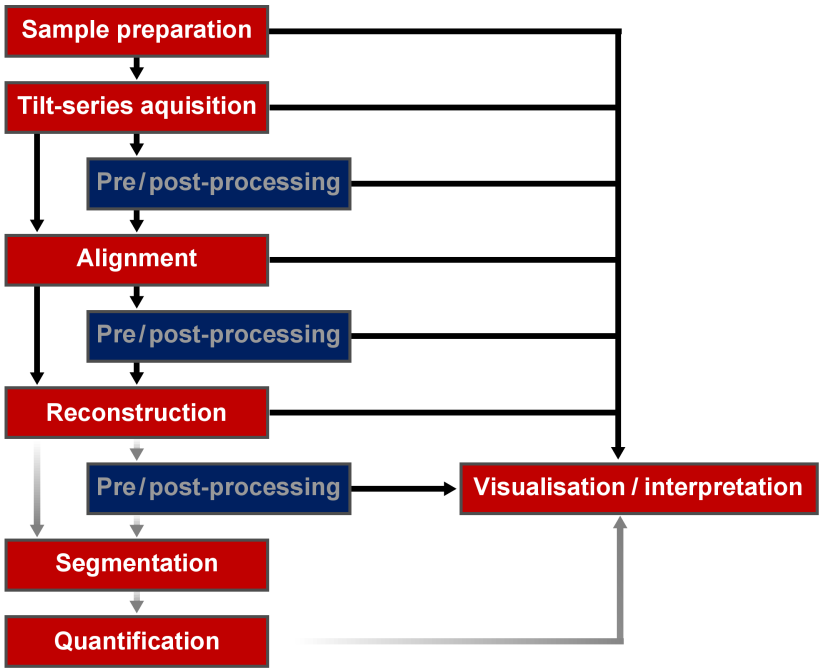

FIGURE 5.6: Principal stages in an ET investigation.

5.3.1 ET acquisition - geometry

5.3.1.1 Finite and limited angular sampling

In an ET experiment, projections at different angles are acquired by tilting the sample in a goniometer, as illustrated for the common single-axis geometry in Figure 5.7a. Collectively, the set of images for all tilt angles is usually referred to as a 'tilt-series'. Together, these also comprise a series of 2D sinograms, as shown in Figure 5.7b.

The sampling theory outlined in section 5.2.2 suggests that the best tomographic reconstructions are achieved by acquiring as many projections over as large an angular range as possible. However, several factors in ET always restrict the actual number of projections obtained to less than ideal. Firstly,

in contrast to many other tomographic techniques, ET is performed in a highly restricted working space. Contrary to the simplified diagram of Figure 5.7, the goniometer is actually located between the pole-pieces of an 'immersion' objective lens, as illustrated in Figure 5.8a. In order to achieve high spatial resolution, the pole-piece gap must be kept as small as possible (ca. 2-5 mm) to minimise the effects of spherical and chromatic aberration [76, and references therein]. This limited gap restricts the angular range over which the specimen can be tilted.

ET is thus a limited-angle tomographic problem, with a large unsampled region in Fourier space, known as the 'missing wedge' (Figure 5.9). The design of specialised narrow profile tomography holders has enabled the maximum tilt angle θ_{max} to approach 80°, use of which is now widespread. However, additional limitations may come into play at high tilt angles, due to shadowing from the specimen support grid or holder (Figures 5.8b and c), because the increase in projected specimen thickness (Figure 5.8d) renders the projection unusable through blurring due to chromatic aberration in CTEM or beam broadening in STEM, or, for very large slab-like specimens, due to limited depth-of-field rendering parts of the projection out of focus (Figure 5.8e).

To minimise the missing wedge problem, dual-axis tomography has been proposed [236–239] which, by combining two mutually perpendicular tilt-series, reduces the missing wedge to a 'missing pyramid'. Other tilting schemes are detailed in ref. [10]. Alternatively, a growing trend has been the preparation of needle shaped samples, which, using specialist holders, can be rotated through the full ±90° range, and avoid the aforementioned problems of shadowing or thickness increases [216, 240–243].

Even for samples that can be tilted over the full angular range, undersampling still occurs because of the finite angular increment $\Delta\theta$ over which the sample is tilted between each projection. Automated or semi-automated tilt-series acquisition and low-dose procedures have facilitated the application of ET to beam-sensitive specimens that damage by inelastic processes (viz. heating and radiolysis), and have been critical in the biological sciences [197]. Likewise, operation below the threshold for knock-on damage can open the door to analysis of specimens that damage predominantly by elastic scattering (e.g. [244]). However, ultimately, for most specimens, the tilt-series acquisition is limited by beam damage. The number of projections sought must also be balanced against the potential build-up of contamination, which can be equally problematic.

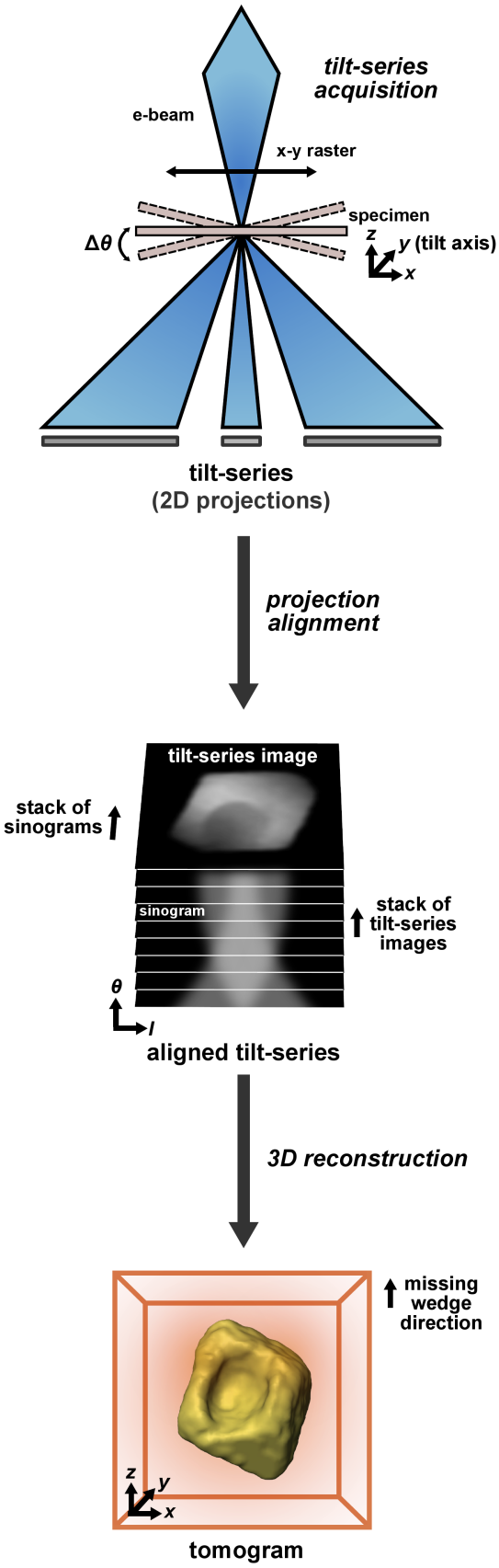

FIGURE 5.7: Overview of single axis ET.

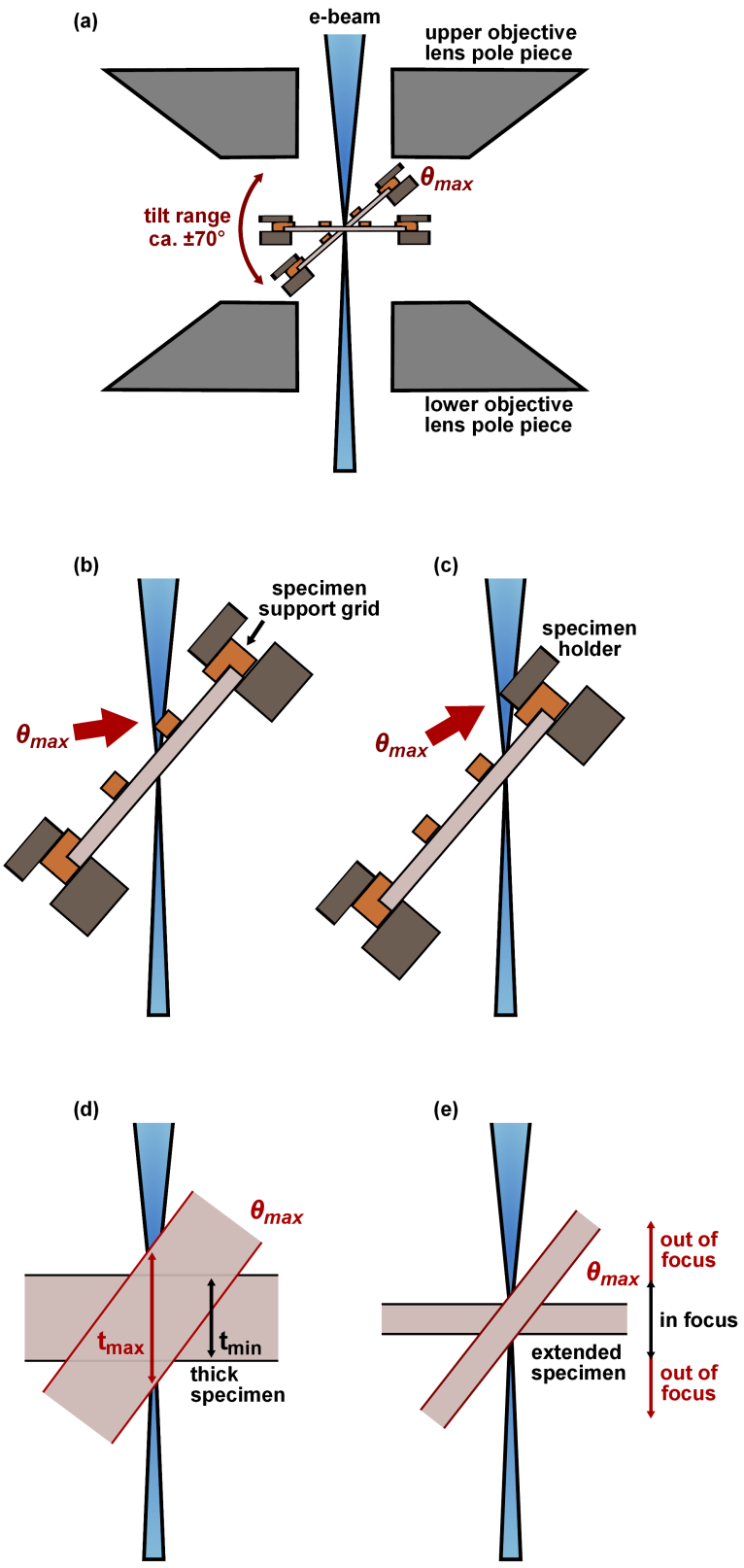

FIGURE 5.8: Reasons for limited angular sampling in ET: (a) restricted pole-piece gap; (b) support grid or (c) holder shadowing; (d) specimen thickness; (e) limited depth-of-field.

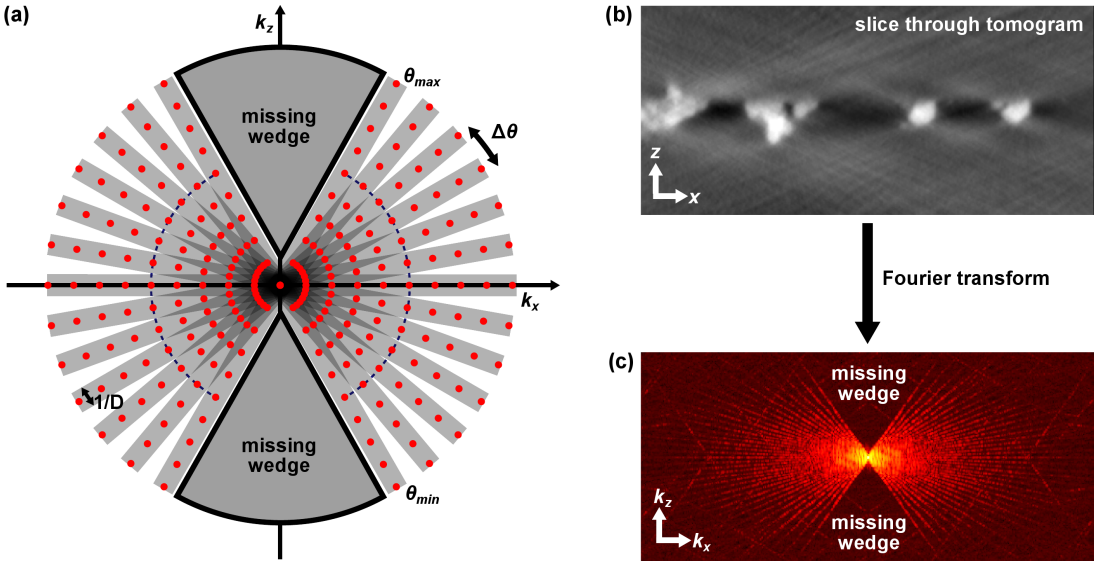

FIGURE 5.9: (a) Illustration of finite and limited angular sampling of Fourier space in ET; (b, c) its manifestation in practice. In (a), each projection, of an object of diameter D, is a central section in Fourier space of thickness $1/D$. The dashed blue line indicates the limit at which the information from adjacent projections just overlaps, corresponding to the Crowther criterion defined in Equation 5.4.

5.3.1.2 Limited sampling: artefacts and reconstruction resolution

The finite and limited angular sampling in ET can lead to serious artefacts in the tomographic reconstructions, which are well documented in the literature [13, 37, 202, 245, 246]. In fact, structures may be partially or entirely absent from the tomogram if they are strongly affected by the missing wedge (e.g. [247]). In general, the missing wedge causes an apparent elongation e in the z-direction, determined by θ_{max} [248]:

$$e_{xz} = \sqrt{\frac{\theta_{max} + \sin\theta_{max} \cdot \cos\theta_{max}}{\theta_{max} - \sin\theta_{max} \cdot \cos\theta_{max}}}, \tag{5.3}$$

as exemplified in Figure 5.10. Experimentally, however, it has been found that the observed elongations can be (considerably) smaller than this, suggesting that specimens may only need to be tilted to ca. $\theta_{max} = \pm 80°$ to enable quantitative ET [202, 249, 250].

Qualitatively, the effect of finite angular sampling is to cause 'streaking' artefacts, the severity of which increases with $\Delta\theta$ (Figure 5.10).

A consequence of the limited angular sampling is that the reconstruction resolution will vary with direction, the determining variables for which in the context of ET were first considered by Crowther [251] (see earlier, Bracewell and

Riddle [252]). The resolution parallel to the tilt axis d_y should, in principle, be equal to that of the input projections. Perpendicular to the tilt axis, the 'Crowther criterion' (which assumes $\theta_{max} = \pm 90°$) gives the resolution d_x as being determined by the number of projections N_p and the diameter of the region to be reconstructed D:

$$d_x = \frac{\pi D}{N_p}, \tag{5.4}$$

the geometry of which is illustrated in Figure 5.9a. Due to the missing wedge, the reconstruction in the direction of the electron beam d_z is further degraded by the elongation factor e_{xz}:

$$d_z = d_x \cdot e_{xz}. \tag{5.5}$$

Although often cited as useful guides, when constrained reconstruction techniques are used these formulae do not strictly apply. Empirically measured resolution (see e.g. [10, chapter 10], or [250, 253] for methods) is often found to differ from their predictions. As summarised by Midgley and Weyland [13], the actual reconstruction resolution is likely to depend on a combination of the effects of the sampling regime, the noise characteristics, the shape of the object to be reconstructed and the nature of the reconstruction routine.

5.3.2 ET acquisition - signal modes

5.3.2.1 The projection requirement

In the most basic sense, the transmission of the electron beam through the specimen allows the TEM to be described as a 'structure projector.' However, as exemplified by Hawkes [10, chapter 3], it is critically important to consider the extent to which the signals obtained in TEM constitute a projection that is valid, or at least useful, for tomographic reconstruction.

While the ideal projection involves a sum integral of some physical property, as defined by the Radon transform (Equation 5.1), practically this is rarely achieved in TEM. Instead, it is generally regarded as sufficient that a TEM signal is a monotonic function of a projected physical quantity. It is this more relaxed stipulation that is generally referred to as the 'projection requirement' in ET.

It was discussed in chapter 2 and exemplified in chapter 3, that a monotonically varying signal is, in general, desirable for facile interpretation. Thus, much of the discussion in chapter 2 regarding direct interpretability applies here. It

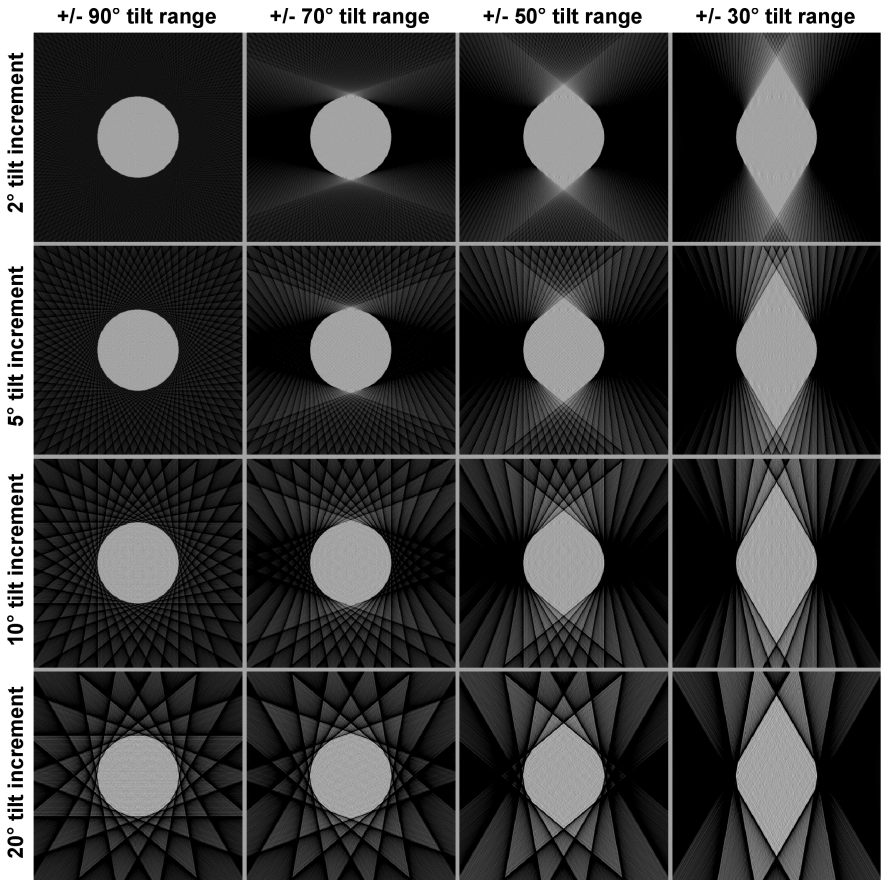

FIGURE 5.10: The effect of finite tilt increment and limited angular tilt range on tomographic reconstruction of a spherical phantom (weighted back-projection reconstructions). The maximum tilt angle and tilt increment of the projections used for each reconstruction is denoted by the column and row headings, respectively.

is clear from ET studies to date that directly interpretable signals satisfying the projection requirement are significantly easier to process, and the ET reconstructions more readily interpreted than those which do not. Nonetheless, ET is often performed using signals that do not fully satisfy the projection requirement. In those cases especially, careful interpretation of the resulting tomograms may be required to differentiate real structure from artefacts.

Table 5.1, summarises the range of signal modes that have now been used in ET. The most important of these are reviewed in the following sections.

5.3.2.2 CTEM for ET

Although it has been the development of alternative imaging modes that has led to the explosion of interest in ET within the physical sciences, BF-CTEM continues to be widely practiced; and it is by far the dominant mode in the biological sciences. A primary advantage is the speed of acquisition compared to STEM. The potential difficulties in BF-CTEM for obtaining a monotonically varying signal were outlined in section 2.1, and the suitability specifically with regards to the tomographic projection requirement (reiterating the potential challenges) has been extensively discussed in the foundational [51, 52], [10, chapter 3] and review literature [9, 13, 37, 40–42, 199, 200, 202, 203, 207], [44, chapter 11], [20, chapter 8]. Especially, domination of images by diffraction contrast, which will change markedly and in a complicated manner as the specimen is tilted, can severely invalidate the projection requirement.

Despite the possible challenges, previous reviews have emphasised that there have been many cases in the physical sciences where important information has been revealed using BF-CTEM, provided that due consideration is given to possible violation of the projection requirement or the effects are insignificant at the level of interest in the tomogram. This continues to be the case, e.g. [272]. Polymers, as relatively weakly scattering specimens, have been a particularly exploited area of application [42, 200]. Coupling beam precession with ET can also be used to minimise deleterious diffraction contrast [267]. There seems to be a consensus in the literature that BF-CTEM is capable of approximately reconstructing the exterior shape of convex homogeneous crystalline objects, while the intensity of the interior may be subject to erroneous non-linearity due to diffraction effects [203, 218, 245].

Alternatively, to profitably use the diffraction contrast that arises in CTEM, DF images can be formed by using the objective aperture in the back focal plane of the objective lens to select a particular Bragg reflection to contribute

TABLE 5.1: Established (E), advanced (A) and niche (N) signal modes used for ET.

Signal mode	Early/selected studies	Selected reviews	Status	Comments
BF-CTEM	DeRosier and Klug [194] Spontak et al. [254, 255] Koster et al. [254, 255]	[42]	E	WPOs, biological specimens, amorphous materials
ADF-STEM	Midgley & Weyland [51, 52]	[13, 42]	E	Crystalline specimens, Z-contrast
EF-TEM	Weyland & Midgley [256] Möbus & Inkson [257]	[13, 42]	E	Chemical segregation, optical properties, bonding variations
EELS	Jarausch et al. [216]	-	A	Chemical segregation, optical properties, bonding variations; new fast spectrometers
EDXS	Möbus et al. [258] Lepinay et al. [217]	- -	A	Chemical segregation; new large area detectors
AC-CTEM	Bar Sadan et al. [47]	[208]	A	Atomic-scale; WPOs
AC-STEM	Van Aert et al. [60] Goris et al. [259]	[225]	A	Atomic-scale; heavy metal nanoparticles
Holography	Twitchett-Harrison et al. [260]	[214]	A	Mean inner potential, electrostatic and magnetic fields
Diffraction	Kolb et al. [261]	[262]	A	Crystalline materials
Time resolved	Kwon & Zewail [263]	-	A	New commercial TEMs
cAC-TEM[1]	Baudoin et al. [264]	-	A	Thick biological specimens
DF-TEM	Barnard et al. [265] Bals et al. [266]	- -	N	Lattice defects, low contrast soft matter
Precession BF-CTEM	Rebled et al. [267]	-	N	Crystalline specimens
BF-STEM	Sousa et al. [268]	[201]	N	Thick specimens, polymers, biological sections
IBF-STEM	Ercius et al. [269]	-	N	Thick specimens
MAADF-STEM	Sharp et al. [270]	-	N	Dislocations
STEM in ESEM[2]	Jornsanoh et al. [271]	-	N	Non-conductive or hydrated specimens

[1] chromatic aberration-corrected (cAC)
[2] Environmental scanning electron microscopy (ESEM)

to the image. By ensuring that the diffraction conditions remain at least nearly constant at each angle, it has been shown that the projection requirement can be approximately satisfied. Although the acquisition is challenging, this technique can be highly sensitive to small changes in crystalline orientation, and has been used for imaging of defects such as precipitates [273] and dislocations (using the weak-beam dark-field technique) [265], or buried structures such as quantum dots [274]. Another alternative, ADF-CTEM, can be implemented using an annular aperture in the back focal plane. This can yield chemically sensitive tomograms in a manner similar to ADF-STEM, and may have particular merits for fast acquisition and low contrast soft matter [266, 275].

5.3.2.3 STEM for ET

As for CTEM, the suitability of ADF-STEM for ET has been well discussed in the review literature. The generally monotonically varying signal and 'direct interpretability' of ADF-STEM was outlined in section 2.2, and accounts for its successful use in ET [13, 51, 52]. Thus it is has often been concluded that ADF-STEM is the most suitable technique for ET nano-metrology (e.g. [29, 203, 276], to cite just a few). A clear example can be found in a study by Lu et al. [276], who found that BF-CTEM substantially overestimated the constituent volume fraction of carbon-black in polymer composites compared to ADF-STEM, which provided acceptable accuracy.

The high contrast between materials of differing atomic number is one of the principal strengths of ADF-STEM for ET. This has been extensively exploited, for instance, in ET of high-Z catalyst nanoparticles on low-Z supports (see reviews by Friedrich et al. [37], and Midgley, Weyland and co-workers [9, 13, 38–42], [44, chapter 12], [20, chapter 8]). However, caution should be noted in that very large differences in atomic number may lead to signals exceeding the dynamic range of the ADF detector, and consequently low contrast of the low-Z component(s), or contrast saturation of those of high Z, which would violate the projection requirement. Detector saturation or contrast reversal can also result from very thick samples, the latter due to scattering to high angles beyond the outer radius of the detector. These can lead to artefacts such as voids or erroneous core-shell structures in ET reconstructions [39, 269], the nature of which are examined in detail in [218].

While ADF-STEM at high-angle is currently the imaging mode that, arguably, is likely to best satisfy the projection requirement for the widest range of specimens, there may be certain scenarios when other variants of

STEM become more suitable. For example, Barnard et al. [277] have found that MAADF-STEM can be the most effective detection range for dislocation tomography; MAADF provides sufficient elastic signal to reveal the dislocation, but also shows minimal coherent contrast because of the presence of multiple beams. Another example is the use of BF-STEM imaging for particularly thick specimens that would produce contrast reversals in ADF-STEM. Ercius et al. [269] have shown that coherence artefacts can be minimised by using a large bright field detector, whose broad integration area effectively suppresses diffraction contrast, providing an 'incoherent bright-field' (IBF) image that satisfies the projection requirement.

5.3.2.4 Spectroscopic ET

The first to be developed [256, 257] and now most widely implemented spectroscopic mode in ET is EFTEM. Although by no means an easy signal mode to acquire over a full tilt-series, and to post-process, and far less frequently utilised than BF-TEM and ADF-STEM, EFTEM ET has now been performed using a number of different regions of the EEL spectrum: from zero-loss [278, 279] and low-loss [212, 213, 279, 280], to a host of core-loss transitions (e.g. [281, 282], reviewed in [42]); and using a variety of different acquisition or processing methods, including established jump-ratio or three-window methods (e.g. [42, and references therein]), or more novel single-window [283], thickness mapping [280] and image spectroscopy [212] techniques. A more recent development, made possible by hardware advances (see section 2.3), is ET based on STEM-EELS [216, 284]. Recent critical discussion of EFTEM and STEM-EELS ET can be found in [216, 280–282, 284].

A similar situation has occurred with EDXS ET. Early attempts suffered from low count rates and unwanted absorption from the specimen grid or holder, but large solid angle detectors (see again section 2.3) mean that EDXS ET is now becoming feasible [217, 285]. However, the acquisition in both STEM-EELS and EDXS ET is still considerably challenging to achieve within a reasonable electron dose and/or time. The acquisition in [217] for example, using a 2° tilt increment typical of current ET practice, took 7.5 hours. Methods that enable robust reconstruction from fewer images may be the only way to open up these imaging modes to less beam resistant specimens.

5.3.2.5 Exotic signal modes in ET

As well as the spectroscopic signals, the past 4-5 years has seen the inception, or progression, of a number of other advanced signal modes for ET. While remaining primarily the practice of a select number of groups, holographic and diffraction techniques have now been firmly confirmed as fruitful ET signal modes (reviewed in [9, 214] and [262], respectively). Indeed, automated acquisition has been developed for both techniques.

Reconstruction in the established mode of diffraction ET typically [262] differs from the back-projection type approaches addressed in this thesis, involving crystallographic structure solution routines. Additionally though, recent work combining precession electron diffraction with beam scanning and tilt-series acquisition is providing new opportunities in diffraction ET. The 'six-dimensional' datasets obtained can be interrogated to extract local 3D crystal orientation, including generation of 'virtual dark-field' images or Euler angle maps amenable to conventional back-projection type ET reconstruction [A.S. Eggeman, personal communication].

Holographic ET, which has now reached a quantitative status, has enabled 3D mapping of electrostatic potentials, including the mean inner potential of materials or the diffusion potential across p-n junctions in semiconductors (see [9, 214] and references therein). In their recent review, Wolf et al. [214] also identify latent scope for holographic ET of magnetostatic fields, as well as electric crystal potentials at atomic resolution. In both cases, ability to achieve reconstruction from limited data will likely be key to practical realisation.

Paucity of data is also inherently faced in atomic-scale ET studies, either because of radiation damage or, in cases where zone axis projections are sought, inherent difficulties on tilting to a sufficient number low index zone axes. In spite of these challenges, ET is now pushing beyond the long standing 1 nm^3 mark [51, 52, 286], helped significantly by AC optics. Atomic-scale ET has been reported using AC-STEM [60, 63, 66, 259] and AC-CTEM [47, 244]. The studies of Scott et al. [287] at 2.4 Å resolution, and Chen et al. [155] revealing (in combination with 3D Fourier filtering) the 3D structure of dislocations in a Pt nanoparticle though, are notable in using aberration uncorrected STEM.

Time-resolved ET has been reported by Kwon and Zewail [263]. Using their stroboscopic pump-probe technique enables dynamic imaging of repeatable changes, and recent commercialisation of the TEM hardware now opens this technique up to the wider community. However, a challenge may again be faced in acquiring tilt-series at sufficiently low dose for many materials. Requiring

a separate tilt-series for each time delay, the data set in [263], where a 1° tilt increment was used, consisted of ca. 4000 images. This suggests, once again, that the ability to perform ET reconstruction from few images would be of great benefit. It is also plausible to see how unique *in situ* changes could be analysed in 3D via ET, if the tilt-series of images can be recorded sufficiently rapidly with respect to the change. This is clearly another aspect in which few-image reconstruction could help. Moreover, many sample holders used for *in situ* TEM (e.g. with heating elements or gaseous chambers) have a significantly restricted tilt range.

5.3.3 Tilt-series alignment

Automated feature tracking during acquisition, computer control of goniometers and improvements in stage design have greatly facilitated the successful acquisition of ET tilt-series (ensuring that the specimen remains close to the centre of the field of view in each image). Nonetheless, post-acquisition alignment of the projections to a common tilt axis is invariably required. This should, ideally, be done to sub-pixel accuracy.

Where specimens have distinctive features, common in the physical sciences, the alignment is usually carried out using cross-correlation [13, 42]; see [10, chapter 6]. An alternative is to place high contrast markers on the specimen or support film, usually gold nanoparticles, and to track these in each image to determine the required shifts [10, chapter 5]. This approach is more common in biological applications, where the specimens often show lower contrast and, often being more sporadically distributed throughout the reconstruction volume, may suffer less from obstruction by the markers. A number of software packages also provide facilities for manual adjustments to be made.

Since only standard cross-correlation methods are used in this thesis, the reader is referred to the cited literature for details of alignment (Weyland and Midgley [42] in particular provide a concise overview). However, it is important to bear in mind that accurate alignment is critical for high-fidelity ET reconstructions to be obtained. Moreover, the growing trend of carrying out ET investigations using very few projections can make alignment considerably more challenging. Similarly, as ET addresses finer details or length scales, such as atomically resolved reconstruction, the accuracy of alignment must be correspondingly higher. New strategies may be required in these contexts, and some specific alignment procedures have already been proposed [287, 288]. Pertinently also, Fernandez [224] has noted that some alignment procedures

applied in the biological sciences, such as 'patch tracking' [10, chapter 6], have barely been explored in the physical sciences. It is likely that advanced alignment procedures will become increasingly important in coming years.

5.3.4 ET reconstruction

Various classifications have been used to differentiate or group tomographic reconstruction algorithms. Considering the established algorithms in contemporary ET, they are classed here as falling into two groups:

1. *Direct transform methods,* including back-projection & Fourier techniques;
2. *Algebraic iterative methods,* including the ART- & SIRT-type classes.

Comprehensive mathematical description of the methods discussed can be found in [10, 228–235], [44, chapter 2]. A notable concise summary of the many different forms of ART and SIRT algorithms is given in [289].

5.3.4.1 Back-projection

The reconstruction method favoured by the ET community has for many years been the weighted back-projection (WBP) algorithm, owing mainly to its speed of execution and because the algorithm is well-understood. In the most basic description [42], [20, chapter 8], back-projection consists of 'smearing' each projection from a tilt-series back into space at the angle at which it was originally formed. By back-projecting a sufficient number of projections, the summation of the back-projected 'rays' in the space will generate the original object; such direct back-projection is illustrated schematically in Figure 5.11.

However, ET reconstructions from simple back-projection appear blurred because the radial sampling regime of ET (cf. Figure 5.9) leads to relative undersampling of higher spatial frequencies (Figure 5.12b). This can be corrected using a ramp-like weighting filter, usually applied to the projections in Fourier space. The result is a weighted back-projection (WBP)[3] [15], [10, chapter 8], as shown in Figure 5.12c. While this filtering process has the benefit of enhancing edges, it can complicate true quantitative analysis of the voxel intensities in the tomogram.

[3] A very closely related variant is the filtered back-projection (FBP). The differences between WBP and FBP are discussed by Carazo [10, chapter 7].

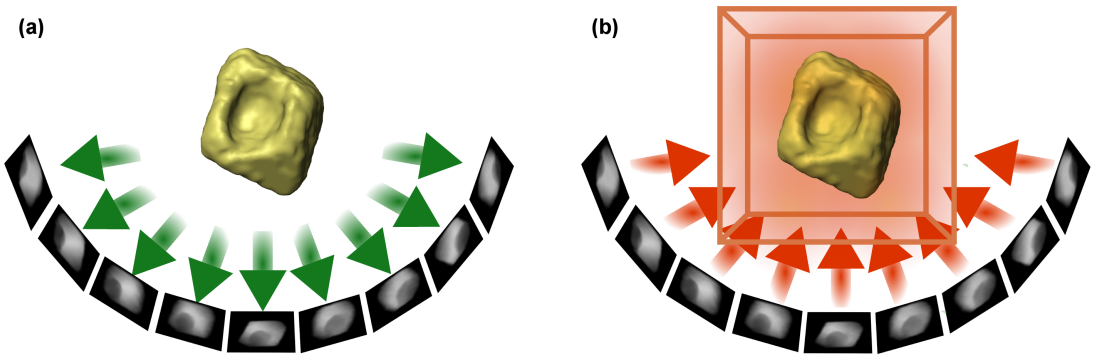

FIGURE 5.11: (a) Acquisition of an angular series of 2D projections of an object, and (b) back-projection of these images into a 3D space to obtain a reconstruction of the object.

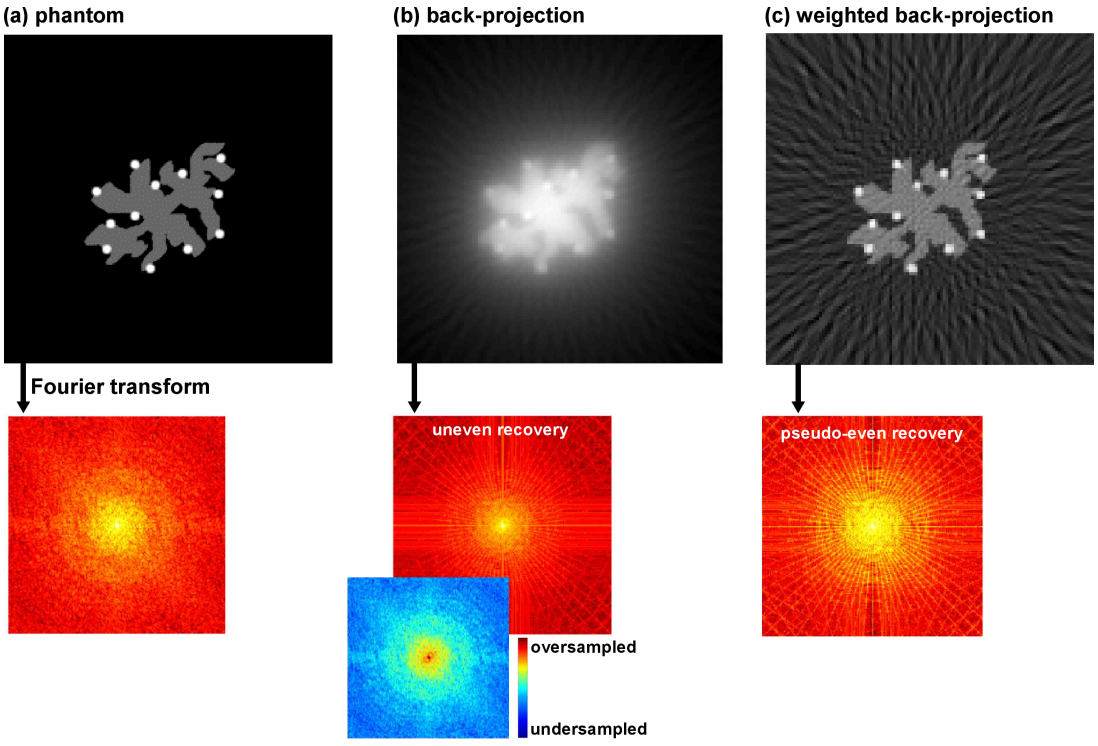

FIGURE 5.12: Back-projection (b) and weighted back-projection (c) from the (discrete) Radon transform of (a), and corresponding Fourier transforms, illustrating the role of the weighting filter for recovering high spatial frequencies.

5.3.4.2 Direct Fourier inversion

Fourier-based reconstruction methods exploit the Fourier slice theorem outlined in section 5.2.2. Essentially, for an N-dimensional reconstruction, Fourier reconstruction entails application of an (N-1)-dimensional discrete Fourier transform across the spatial dimension of the projections, to obtain radial Fourier data. An N-dimensional inverse Fourier transform is then applied to this data to recover the function in real space. However, as was indicated in Figure 5.5, and is shown explicitly in Figure 5.13, the data in the Fourier domain of the function lies on Cartesian co-ordinates, whereas the radial Fourier data is on a polar grid. To convert the data between the two co-ordinate systems requires some form of interpolation or 'gridding' process, illustrated schematically in Figure 5.13c. This step is challenging, and can result in poor quality reconstructions if simple interpolation (such as bilinear) is used. As such, direct Fourier inversion methods have generally been disregarded in ET.

Nonetheless, several Fourier-based reconstruction methods using sophisticated non-uniform Fourier transform, or 'gridding', procedures have been proposed recently in the biological ET and SPM context, with potential performance enhancements; reviewed by, for example, Penczek [235]. A more recent approach, in both biological [290, 291] and physical [155, 210, 287, 292–295] sciences ET, has been to combine sophisticated Fourier based operators with iterative reconstruction. These algorithms are described subsequently in section 5.3.4.6.

5.3.4.3 Algebraic iterative reconstruction

In a qualitative description, algebraic iterative reconstruction (AIR) techniques in ET operate by constraining the reconstruction to match the original projections, with the match being improved at successive iterations (Figure 5.14). A difference reconstruction is obtained via a comparison of projections of the reconstruction with the original projections, either by division in multiplicative techniques or subtraction in additive techniques. The current reconstruction is then updated via multiplication or addition of the difference, respectively. This kind of iterative refinement by projection and re-projection can also be described mathematically in terms of 'projection onto convex sets' [296].

Formally, AIR is based on the discretisation of the projection process into a finite number of basis functions (n in total), as illustrated in Figure 5.15. The projection system is represented by the matrix Φ and the vector $\mathbf{x}$ contains the function in n discrete points in space. The vector $\mathbf{b}$ contains the ray-sums,

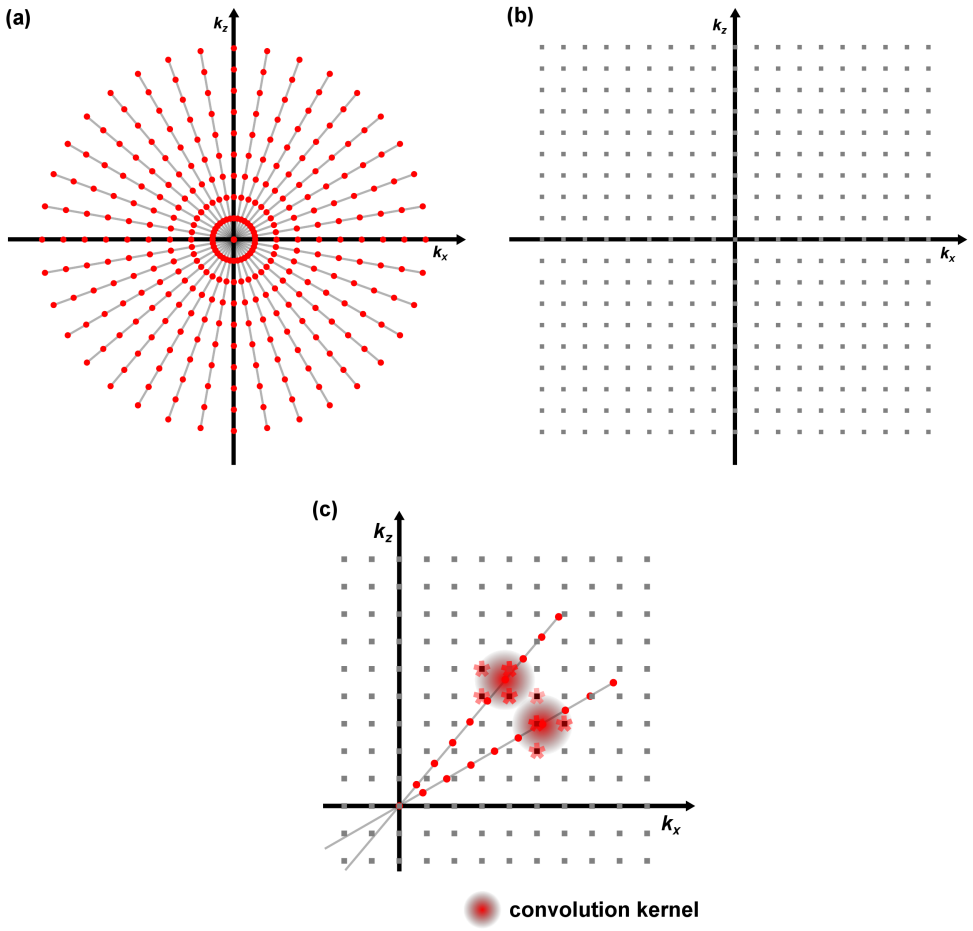

FIGURE 5.13: (a) Radial and (b) Cartesian data points; and (c) an interpolation ('gridding') process to convert between the two.

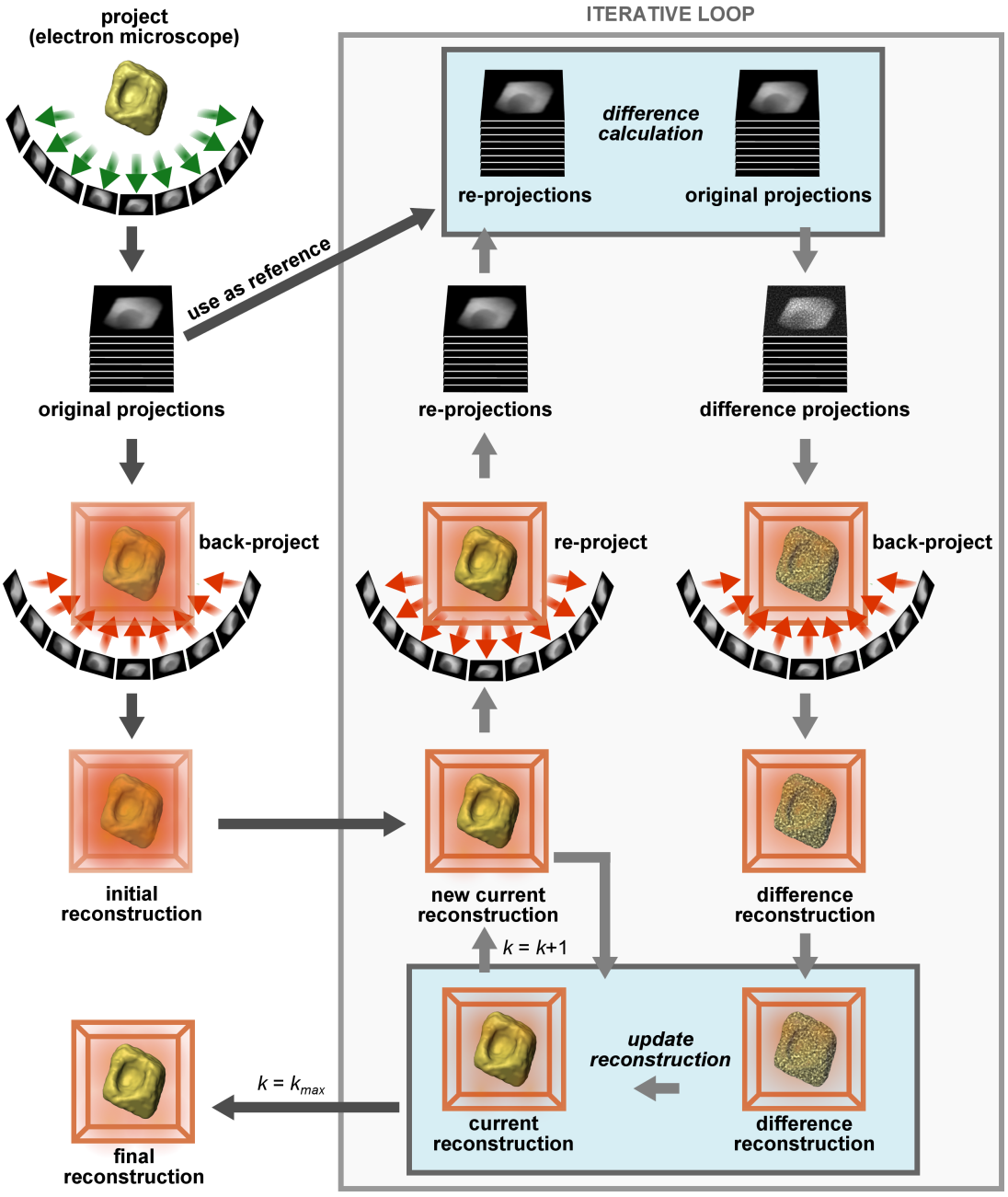

FIGURE 5.14: Principle of iterative tomographic reconstruction. (Shown specifically for a SIRT-type algorithm; based on the diagram of Weyland and co-workers [42])

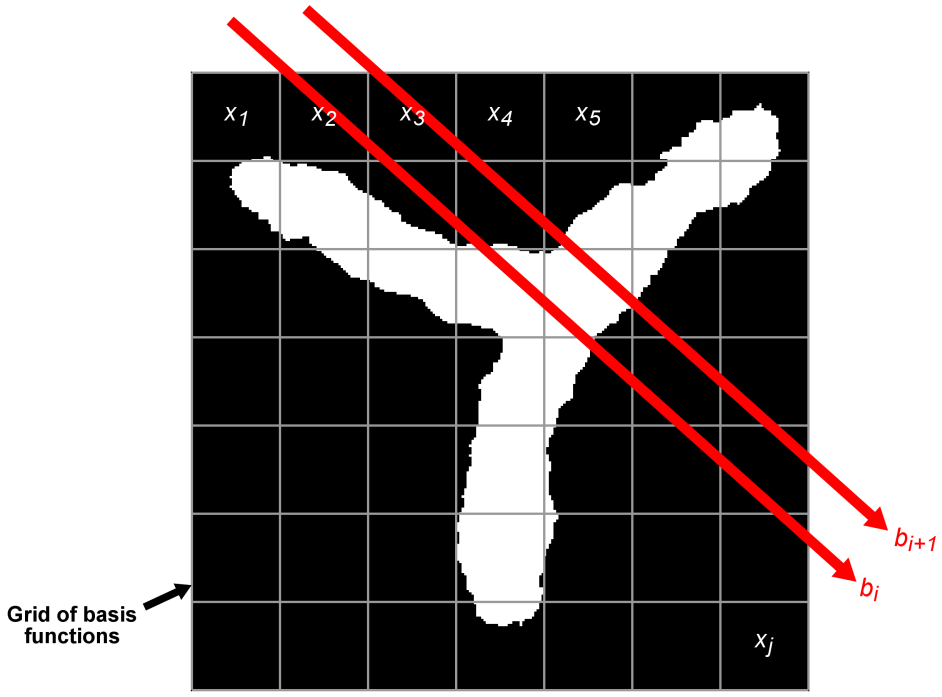

FIGURE 5.15: Discrete representation of a tomographic experiment. The function f is represented by n discrete basis functions, which can be written as a vector $\mathbf{x}$. Each ray-sum is denoted by b_i, with the set of ray-sums forming the vector $\mathbf{b}$. Linking $\mathbf{b}$ and $\mathbf{x}$ is the projection matrix Φ, where each element $\varphi_{i,j}$ describes the contribution of the j'th basis function x_j to the i'th projection ray b_i.

corresponding to a discretised sinogram, with m entries in total. The tomography reconstruction process can then be formulated as a system of linear equations:

$$b_i = \sum_{j=1}^{n} \varphi_{i,j} x_j \qquad \text{for } i = 1, ..., m, \tag{5.6}$$

where each $\varphi_{i,j}$ is often calculated as the fraction of the j'th basis function intersected by the i'th projection ray, implying $0 \leq \varphi_{i,j} \leq 1$. Equation 5.6 can be abbreviated as:

$$\mathbf{b} = \Phi\mathbf{x}. \tag{5.7}$$

Equations 5.6 and 5.7 represent an 'inverse problem', where the task is to estimate $\mathbf{x}$ given the data $\mathbf{b}$ and the projection matrix Φ. In ET the limited number of tilt-series projections means that there are far fewer equations than unknowns (i.e. $m \ll n$), and the system of equations is underdetermined, implying there are an infinite number of solutions consistent with the projection data. This is compounded by the 'ill-posedness' arising from data imperfections, such as noise, projection misalignment or diffraction contrast.

AIR techniques such as the algebraic reconstruction technique (ART) [14] and

the simultaneous iterative reconstruction technique (SIRT) [16] were proposed in the context of ET in the 1970s. With advances in computational power and efficient algorithmic implementations e.g. [297], they are gaining increasing popularity. Due primarily to greater stability when the projections are noisy, the SIRT algorithm has usually been preferred to ART in ET and, in the physical sciences, is generally seen as the established standard.

5.3.4.4 Algebraic Reconstruction Technique (ART)

The classic AIR technique to solve Equation 5.7 is that of Kaczmarz [298]. In the literature, this is often referred to simply as ART, but it is important to realise that ART also refers to a class of AIR techniques. Kaczmarz's method can be expressed with the additive update scheme:

$$\hat{\mathbf{x}}^{k+1} = \hat{\mathbf{x}}^{k} + \rho_k \cdot \frac{b_i - \langle \boldsymbol{\varphi}_i, \hat{\mathbf{x}}^{k} \rangle}{\|\boldsymbol{\varphi}_i\|_{\ell_2}^2} \cdot \boldsymbol{\varphi}_i, \tag{5.8}$$

where each $\boldsymbol{\varphi}_i$ represents a row of Φ in Equation 5.7, and hence $\langle \boldsymbol{\varphi}_i, \hat{\mathbf{x}}^{k} \rangle$ denotes the standard inner product of the vectors $\boldsymbol{\varphi}_i$ and $\hat{\mathbf{x}}^{k}$ (as written explicitly in Equation 5.6). The index i addressed at the k'th iteration is given by $i = (k \mathrm{mod} m) + 1$. ρ is the relaxation parameter, which influences the sensitivity of the update to noise, and may be fixed (ρ) or vary at each iteration (ρ_k).

ART was introduced to the ET community by Gordon et al. [14], who also presented a multiplicative form (sometimes referred to as MART). An update scheme can be written as:

$$\hat{x}_j^{k+1} = \left(\frac{b_i}{\langle \boldsymbol{\varphi}_i, \hat{\mathbf{x}}^{k} \rangle} \right)^{\rho_k \cdot \varphi_{i,j}} \cdot \hat{x}_j^{k}, \tag{5.9}$$

where the significance of $0 \leq \varphi_{i,j} \leq 1$ deserves explicit statement here, and again $i = (k \mathrm{mod} m) + 1$.

Another form of ART that has been extensively discussed in the ET literature is block-ART, first introduced by Eggermont et al. [299], which for O blocks of P equations (where $O \cdot P = m$) may be written as [44, chapter 2], [10, chapter 7]:

$$\hat{\mathbf{x}}^{k+1} = \hat{\mathbf{x}}^{k} + \rho_k \cdot \sum_{i=o_k \cdot P+1}^{(o_k+1)P} \frac{b_i - \langle \boldsymbol{\varphi}_i, \hat{\mathbf{x}}^{k} \rangle}{\|\boldsymbol{\varphi}_i\|_{\ell_2}^2} \cdot \boldsymbol{\varphi}_i, \tag{5.10}$$

where o_k ($0 \leq o_k \leq O$) is the index of the block to be used in the k'th iterative step.

As outlined by Kuba and Herman [44, chapter 2], the essential difference between block-ART and the more conventional ART methods is that in the former the update proceeds by taking into account groups ('blocks') of measurements that come from a particular projection, compared to the latter dealing with only one measurement at a time (i.e. one ray integral). If $P = m$ (and hence $O = 1$), then the method is said to be 'fully simultaneous' [300, p100] and is closely related to SIRT-type methods. An intermediate case is when the blocks are formed by all the equations associated with a single projection, an example of which is the simultaneous algebraic reconstruction technique (SART) [301].

5.3.4.5 Simultaneous Iterative Reconstruction Technique (SIRT)

The other major class of AIR algorithms in ET are SIRT-type methods. As the name suggests, information from all the equations (projections) is used at the same time for the update process. This accounts for SIRT often being less sensitive to noise than ART.

SIRT methods can be written in the general additive form:

$$\hat{\mathbf{x}}^{k+1} = \hat{\mathbf{x}}^{k} + \rho_k \cdot \Upsilon\Phi^{*}\Omega(\mathbf{b} - \Phi\hat{\mathbf{x}}^{k}), \tag{5.11}$$

where Φ^{*} is the (conjugate) transpose of Φ. The matrices Ω and Υ are symmetric and positive definite, and for most implementations Υ is the identity transform (see e.g. [289] for examples of functional roles played by these matrices). The most common variant is the Landweber method [302]:

$$\hat{\mathbf{x}}^{k+1} = \hat{\mathbf{x}}^{k} + \rho_k \cdot \Phi^{*}(\mathbf{b} - \Phi\hat{\mathbf{x}}^{k}), \tag{5.12}$$

which corresponds to setting $\Omega = \Upsilon =$ identity transform in Equation 5.11. It is well-known that in overdetermined cases (i.e. $m > n$) for which there is a unique solution, SIRT effectively solves a (weighted) least-squares problem of the form [303]:

$$\hat{\mathbf{x}} = \arg\min_{\hat{\mathbf{x}}} \|\Phi\hat{\mathbf{x}} - \mathbf{b}\|_{\ell_2}^{2}. \tag{5.13}$$

However, in underdetermined problems (typical of ET) an infinite number of proposed solutions may exist that yield minimal discrepancy in Equation 5.13 (or other AIR algorithms). As will be discussed in the following section, in such cases it can be distinctly advantageous to apply additional constraints during the iterative reconstruction that help to select from the possible solutions.

Further, in highly ill-posed scenarios, the standard AIR algorithms can exhibit marked 'semi-convergence', whereby initial iterations tend towards better approximations of the solution, but at some point may start to deteriorate to a poorer approximation (Figure 5.16) [289, 304, and references therein]. This can be particularly problematic in ET, where semi-convergent type behaviours may occur when there is a high noise level in the projections or other significant inconsistencies such as projection misalignment, which become exacerbated at large iteration numbers. Important aspects that remain to be adequately addressed in this regard are optimal choice of the variables in the basic AIR algorithms, namely the relaxation parameter ρ and the total number of iterations k_{max}, both of which are important parameters influencing the outcome of the algorithm. Determination of the optimal number of iterations in ET often requires reconstruction for different iteration numbers and some form of qualitative or quantitative (e.g. [253]) assessment. Some ET software packages do not even allow ρ to be altered. These parameters have been discussed in the past, but robust automated (i.e. non-empirical) methods for choosing or intelligently varying them (e.g. [289, 303, 304]) are yet to find marked endorsement in ET.

5.3.4.6 Towards advanced reconstruction in ET

It is well-recognised by the ET community that major artefacts are often present in ET reconstructions obtained using the conventional algorithms [13, 42]. While this has been tolerated for qualitative interpretation, efforts towards quantitative ET have shown that the artefacts often cannot be ignored [167, 210, 211, 243, 246, 292, 305, 306]. When very few projections are available, reconstructions obtained from the conventional algorithms degrade substantially. The development of sophisticated ET reconstruction algorithms has therefore become an active area of research.

The highly underdetermined and ill-posed nature of the ET reconstruction process implies that seeking data fidelity alone will be insufficient. In this case it is well-known, from the field of inverse problems, that to improve the fidelity or quality of a tomographic reconstruction, some form of prior knowledge constraints (often called 'regularisation') can be introduced during the reconstruction process. The regularisation selects out of the possible solutions to the underdetermined system of equations those which additionally satisfy the prior knowledge characteristics, and therefore, in principle, should reduce the number of projections required for reconstruction.

In general, as the level of undersampling increases, so must the strength

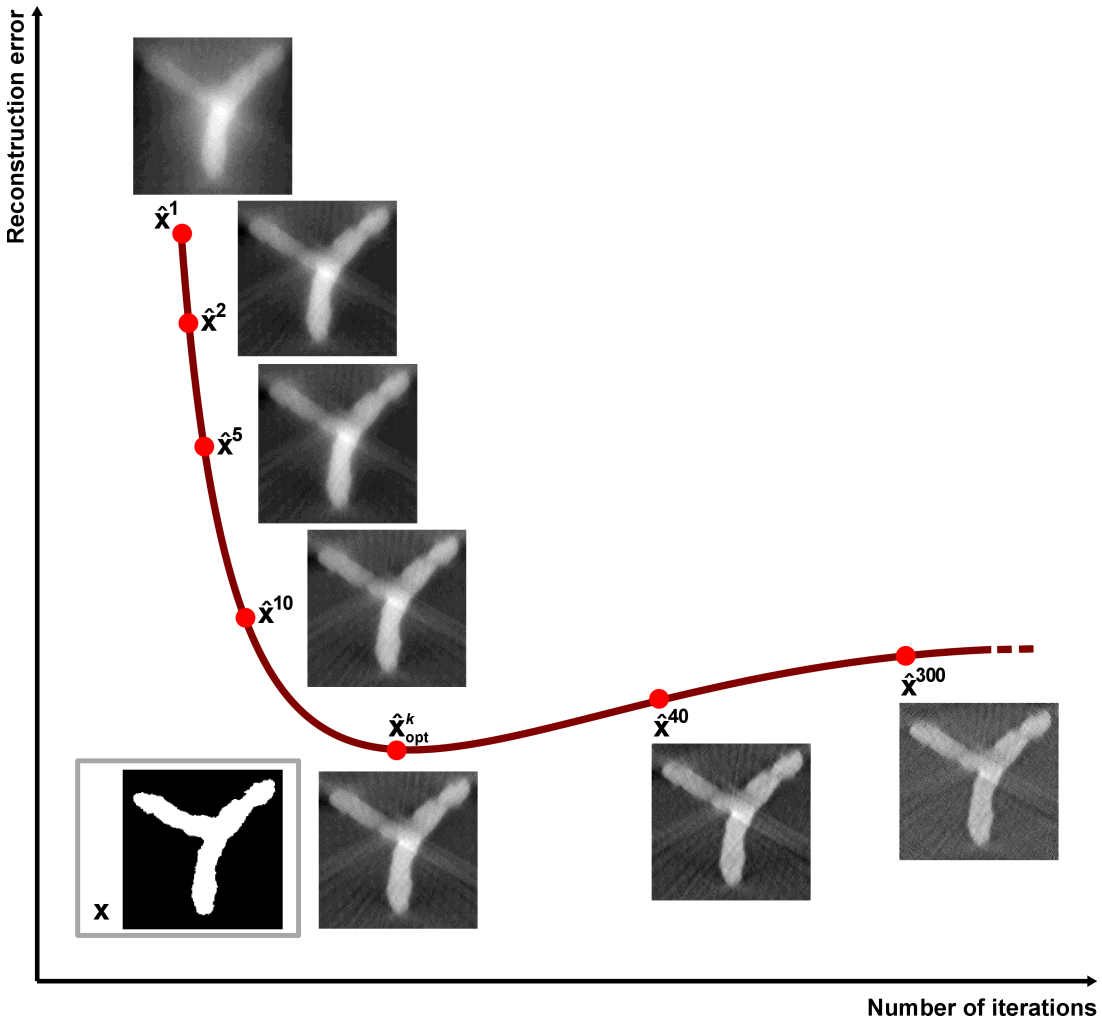

FIGURE 5.16: Principle of semi-convergence in tomographic reconstruction: the initial iterates tend to better approximation of the exact solution, but above a certain number of iterations they begin to deteriorate.

or efficacy of the prior knowledge constraints, if reconstruction fidelity is to be maintained. This is illustrated schematically in Figure 5.17a. Caution should be noted in this regard though, as the fidelity of the outcome depends on validity of any prior knowledge constraints imposed. Stronger constraints can be introduced to bias the results towards a particular outcome, but this outcome will only be of high-fidelity if the constraints are valid. This relationship is illustrated in Figure 5.17b. The ideal scenario is one in which the prior knowledge constraints are relatively liberal but effective during the optimisation process, and accurately describe the object. In some cases though, it may be necessary to sacrifice some degree of reconstruction fidelity, to obtain a reconstruction that possesses other desirable characteristics. For example, a reconstruction that has been biased so that each of its constituent objects possess homogeneous density and sharp boundaries - whether this is true or an approximation of object - may make it easier to identify and analyse those objects.

An established approach of incorporating prior knowledge during tomographic reconstruction is the method of discrete tomography [232, 233], which can be used to provide high-quality and high-fidelity reconstructions if features of the specimen can be considered in discrete terms. A specimen could, for instance, be considered to consist of a discrete number of constituents of uniform density [209], or to consist of discrete elements that lie on a regular grid, such as atomic positions in a (perfect) nanocrystal [60, 307]. The application of such techniques in ET have primarily been pioneered by Batenburg and co-workers, using a class of algorithm known as the discrete algebraic reconstruction technique (DART [209]; see [308] for a more mathematical description). These have shown

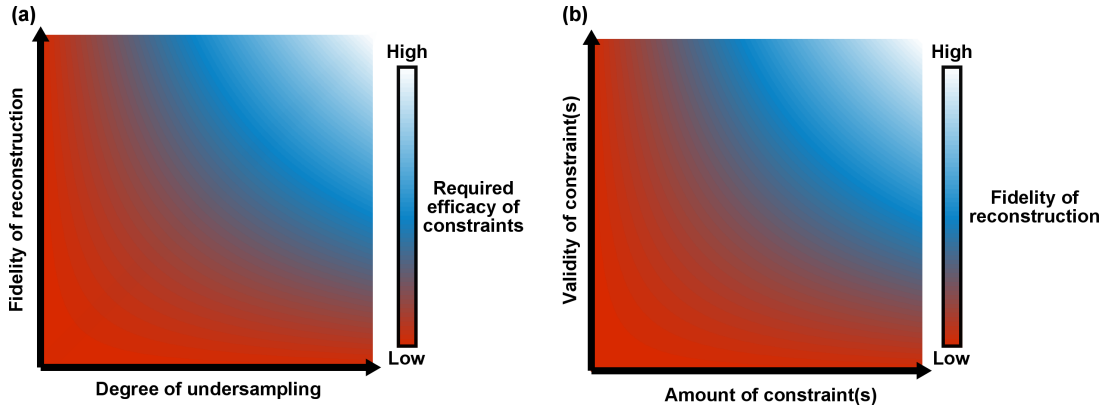

FIGURE 5.17: The influence of prior knowledge constraints on an underdetermined inverse problem such as ET reconstruction. Generally: (a) Greater undersampling necessitates more effective constraints to maintain reconstruction fidelity; and (b) the accuracy with which any imposed constraints describe the object affects the reconstruction fidelity. See text for discussion.

profitable results, including reduction of missing wedge artefacts [209, 243] and reconstruction from few projections [209] in nanoscale ET, as well as enabling atomistic ET studies [60, 63].

DART has received quite wide recognition in the physical sciences, and recently a number of variants have been proposed from the Batenburg group and others [309–312], including a partially discrete approach [313]. At their core, these algorithms harness SIRT, but additionally introduce thresholding and grey level assignment during the iterative refinement. Further variants of discrete tomography advocated for ET include the binary algebraic reconstruction technique (BART, [219]) and the Bayesian approach of Wollgarten and Habeck [314].

A considerable advantage of discrete approaches is that objects are effectively identified ('segmented', see next section) during the reconstruction process, as they are assigned to a particular discrete group. However, the ET practitioner must consider that, even with looser constraints, such as partial discreteness, many real samples do not fully satisfy discrete constraints. Even if a high 'quality' discrete reconstruction of such samples can be obtained, it may not be of high fidelity. Moreover, often such strong prior knowledge is not available (although methods for automatic grey level selection may help in this regard [310]).

Another class of advanced algorithms comes from the field of geometric tomography [315]. These are chiefly concerned with recovering the shape of objects, and mainly incorporate prior knowledge regarding convexity and homogeneity. As shown by Saghi et al. [218], these approaches can be valuable when non-linearities, such as diffraction contrast or detector saturation, are prevalent in the tilt-series projections. In addition to a geometric surface-tangent algorithm proposed by Petersen and Ringer [316], a selection of geometric algorithms from the mathematical literature have recently been explored by Alpers et al. [219], including reconstruction from very few projections when strong geometric prior knowledge is available. Limitations of geometric algorithms are that the mass-density distribution is neglected, i.e. they assume homogeneity and/or recover only external or internal shape or edges, and in a number of cases the object to be reconstructed must be convex.

The past few years have seen a resurgence of Fourier based ET reconstruction, but, crucially, combined with iterative refinement. This includes the methods developed in chapters 7 and 8 [210, 292, 293]. Elsewhere, Miao and co-workers have developed an algorithm known as equally sloped tomography (EST) [287, 294]. A distinct feature of EST is preference for acquisition of projections at equal slope increments, as opposed to conventional equal angular increments (or

other schemes such as the Saxton regime [317]). Equally sloped sampling, in principle, enables high accuracy implementation of a pseudopolar fast Fourier transform (*PPFFT*) to convert between the pseudopolar coordinates of the projections and Cartesian coordinates. The efficacy of the algorithm however, arises primarily because of the combination of a *PPFFT* with oversampling and iterative refinement, during which constraints such as positivity and finite spatial support can be imposed. As outlined by Miao [294], the iterative process in EST can result in filling in some information in the missing wedge due to correlation among Fourier components.

EST has been used in critically acclaimed studies at atomic resolution [155, 287, 295], as well as in low dose imaging of biological structures [290]. Although there has also been criticism of the particular merits and novelty of the algorithm itself [318], the experimental results assert that EST is capable of enabling high-fidelity ET reconstructions, and there is potentially scope for further development with the incorporation of other constraints.

More recently, Chen and Förster have described an iterative non-uniform fast Fourier transform (*NUFFT*) reconstruction ('INFR') algorithm [291]. Proposed in the context of cryo-ET, it is worth highlighting specifically here as the algorithm shares many characteristics with EST and the *NUFFT* based algorithm developed in chapters 7 and 8. Even though the INFR algorithm does not impose any additional prior knowledge constraints, performance improvements over conventional algorithms are reported, including retrieval of some information in the missing wedge, in the low frequency regime in particular. Similar to EST, Chen and Förster suggest that a significant factor in the efficacy of the INFR algorithm is spreading of information in the vicinity of the sampling points during the iterative Fourier based procedure [291]. In contrast to EST though, they also emphasise that the INFR algorithm does not impose prior knowledge of bounded support as a means of information extrapolation. This is particularly important in the biological context, where most specimens constitute large slab-like structures and are therefore unbounded.

Other recently proposed ET reconstruction algorithms include dual-axis SIRT [238, 319], weighted-SIRT (WSIRT) [215], direct iterative reconstruction of computed tomography trajectories (DIRECTT) [320, 321] and model based algorithms directly treating BF-CTEM [322], ADF-STEM [323] or atomic resolution ET [324]. Dual axis SIRT [238] seems not to have caught on, possibly due to the inherent difficulties in aligning dual axis tilt-series and the added computational demands, but has more recently been advocated as yielding

potentially valuable resolution enhancement compared to single-axis ET, even for structures not affected by missing wedge artefacts [319].

WSIRT, recently proposed by Wolf et al. [215], combines WBP and SIRT, showing improved convergence, resolution and reconstruction error compared to SIRT alone, including a reduced point spread in the missing wedge direction. The DIRECTT algorithm of Lange et al. [320, 321] resembles SIRT, but at each iteration only a selected portion of voxels in the reconstruction are updated, based on either their grey level error or local contrast. This favours high density/contrast features, and the gradual introduction of voxel updates acts as a regularising mechanism.

Model based reconstruction procedures such as [322–324] typically differ from conventional ET reconstruction. Often they do not assume applicability of the projection requirement, and concentrate on accurately modelling the imaging process in order to refine an initial reconstruction. While these methods have not yet been widely adopted, they may become more pertinent for ET investigations of advanced or complicated signals.

Finally, it is important to note here the important new class of ET reconstruction algorithms based on 'compressed sensing'. These are addressed in chapters 7 and 8.

5.3.5 Segmentation & quantitative analysis

In order to analyse a tomogram quantitatively, for example to determine surface area, volume fraction, crystallography, or porosity, it must first be 'segmented'. This involves assigning each voxel in the tomogram to a feature of interest, for instance a nanoparticle, the vacuum, or the substrate. The difficulty in achieving segmentation of ET reconstructions has meant that often, they have been treated only in a qualitative manner. Alternatively, in a number of cases where segmentation has been achieved, it has only been through labour intensive manual procedures, in which the identification of features and delineation of their boundaries is open to individual interpretation. Indeed, segmentation can be the most time-consuming part of the ET work flow, and has been described as the 'bottleneck'. A remedy to this situation, however, is the use of image processing techniques. These may facilitate automated or semi-automated segmentation, and recognition of their important role in ET has gradually grown over recent years in both the biological and the physical sciences.

Segmentation is one of the most difficult aspects of ET to review because of the wide variety of different methods employed. The segmentation requirements

will depend on both the nature and the quality of the ET reconstruction, and therefore often need to be developed on a case-by-case basis. However, the key aspects of image processing based segmentation can be generally applicable to many similar data sets with small adjustments.

Several advanced segmentation methods have received attention in previous reviews [224, 325–328], [44, chapter 11], [20, chapter 8], [10, chapters 11-15], mainly originating from the biological ET community. These include denoising by anisotropic non-linear diffusion [329], watershed transformation [330] and gradient vector flows [331]. Examples of more recently proposed advanced segmentation techniques are noise reduction utilising Beltrami flow [332], application of fuzzy set theory [333] and segmentation of thin structures using orientation fields [334].

Segmentation procedures used in physical science ET investigations are sometimes well described in particular studies; see e.g. [167, 222, 335–337] as exemplary cases. Fernandez [224] has recently reviewed computational methods for ET, including a much needed discussion of segmentation techniques in the physical sciences, and a number of the aspects covered are recounted here. Many of the image processing operations that are readily applicable to materials science ET reconstructions can also be found in other tomographic contexts or general reviews of 3D tomographic data analysis (e.g. [44]), as well as in standard image processing texts (e.g. [139]). Often, effective segmentation schemes consist of a number of standard image processing operations strung together.

Broadly, it seems reasonable to identify four stages in the segmentation of ET reconstructions (Figure 5.18). Typically, for most ET reconstructions to date, segmentation must begin with a procedure for denoising and/or enhancing the features of interest. This could involve basic regional averaging such as low-pass [222] or median filtering [272]; histogram equalisation [335]; edge enhancement such as Sobel filtering [338], Difference of Gaussians [167] or unsharp masking [210, 292]; or more sophisticated processes such as anisotropic non-linear diffusion [329]. Denoising or feature enhancement is typically followed by feature extraction based on a similarity metric. One of the most simple yet widely applicable similarity metrics in materials science, where many samples consist of regions of homogeneous density (e.g. nanoparticles), is the voxel intensity [210, 221, 243, 337]. In this case, features can be differentiated by global thresholding on the image grey level histogram or by local spatially aware thresholding, for which a variety of threshold selection methods exist [339].

Optimal threshold selection in tomography is an active area of research

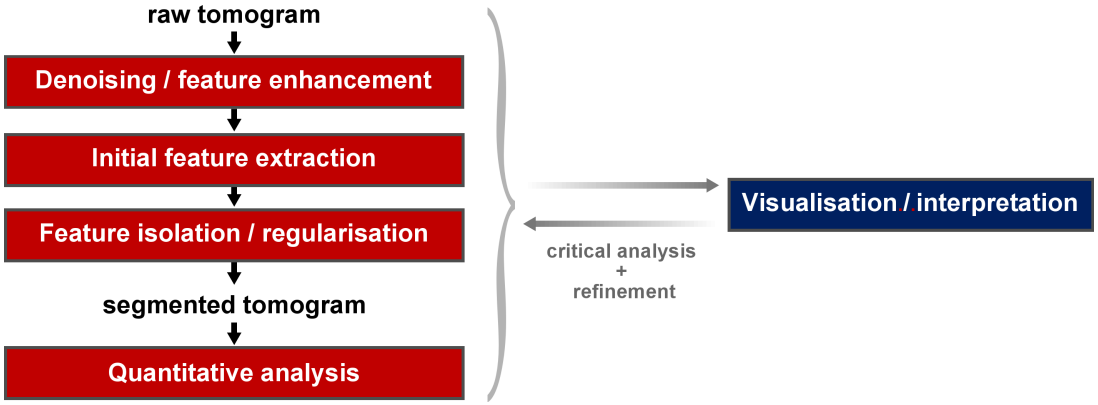

FIGURE 5.18: Primary stages involved in segmentation of ET reconstructions.

(e.g. [340]), and the success will still be dependent on the true complexity of the system under consideration and the quality of the reconstruction. Applicable to sufficiently high quality data where there is a clear intensity difference between features and background, Otsu's method [341] is one of the most well-known automated threshold selection techniques, and seeks the optimal separation based on minimising the intraclass variance in the image histogram. Accordingly, a number of ET studies have used the Otsu or multi-level Otsu method, such as [210, 221, 337]. More sophisticated threshold selection procedures proposed specifically for tomography have involved analysis of edge profiles [336] or projection data error minimisation [342].

Alternative procedures for feature extraction might include detection of specific shapes. Such methods have primarily arisen in the biological field (for extracting membranes and filaments etc., e.g. [343]), but can be equally powerful in materials contexts too; for example, sphere extraction in [222]. Or (recalling section 5.3.4.6), the discrete or partially discrete type reconstruction algorithms [209, 308–314] that incorporate grey level assignment *a priori* as part of the reconstruction process could be classed as a distinct approach to segmentation.

Subsequent to initial feature identification, additional procedures may be used to better delineate or differentiate identified features. These might include, for example, morphological operations to de-noise or regularise the boundaries of objects [210, 292] or the Watershed transform [330, 344] (described in chapter 6) to separate mildly touching objects [167, 222, 337] and/or to locate their centroids [222, 345].

In spite of the challenges, examples of quantitative data obtained from ET are growing in number. Indeed, even early studies enabled parameters such as block co-polymer repeat distances [254, 346] and the curvature of styrene

networks [347, 348] to be determined. More recent examples include fractal analysis of nano-dendritic structures [220], size, shape and local distribution of nanocatalysts [167, 167, 272, 337], local curvature determination of a catalyst support [345], direct measurement of porosity [243, 345], nanoparticle network analysis in polymer solar cells [221, 222], dimensional measurement for input to electrodynamic simulation [349] and thickness mapping combined with crystallographic analysis of gold nanorods [61].

It is important to emphasise that success of segmentation routines and the accuracy of quantitative analysis are often dominated by the quality of the input data. In this regard, appropriate choice of signal mode, acquisition geometry and reconstruction technique can greatly facilitate the segmentation/quantification process. A high quality reconstruction will facilitate simpler segmentation procedures. Despite indications to the contrary in some particular cases [202, 249, 250], the effects of the missing wedge and finite sampling (section 5.3.1) often cannot be ignored in quantitative analysis - this is clearly demonstrated in chapter 6. Methods that overcome or negate these problems, such as the use of needle samples [216, 240–243] or advanced reconstruction algorithms may provide the only routes to truly reliable quantitative ET. The development of more widely applicable methods to tackle these issues is one of the most worthy areas of development in ET.

5.3.6 Visualisation

With advances in computer graphics burgeoning, visualisation of 3D (or higher dimensionality) ET data can reach a high degree of sophistication. It suffices for this thesis to describe the main methods of interrogating ET reconstructions, which are:

- *Slicing:* 2D slices through the reconstruction are shown, usually perpendicular to the primary axes;
- *Surface rendering:* an opaque or semi-transparent surface is placed around voxels of a given intensity;
- *Voxel projection:* a 2D projection of the semi-transparent reconstructed volume is generated, in which properties of interest are emphasised, for example, by assigning colours to voxels in different intensity ranges.

5.4 Other methods for 3D TEM

Several techniques that may be complementary to, or rival, ET should be mentioned briefly. Methods that can yield only partial 3D information in TEM, such as established stereo microscopy techniques or more novel approaches (e.g. [350]), are not discussed. An exception to this is made for quantitative ADF-STEM, owing to its increasing prevalence and often close connection to ET studies.

Very closely related to ET and similarly capable of providing true 3D analysis, is the technique of single particle microscopy (SPM) [351]. In SPM, images of many randomly oriented identical specimens, such as viruses, are classified according to their orientation and input to largely analogous reconstruction procedures. Many of the techniques addressed in this thesis are applicable, with minor adaptation, to SPM and vice versa. While SPM is widely practised in the biological sciences, analogous scenarios in which there are multiple copies of the specimen are less common in the physical sciences. Hence ET has dominated the physical sciences.

Concerning more recent developments that have arisen primarily in the physical sciences, it was noted in chapter 2 (section 2.4) that the reduced depth-of-field possible using AC-optics has given rise to new approaches to 3D TEM [352]. One new method developed for STEM exploits the reduced depth-of-field to 'depth-section' the specimen, producing a stack of images with systematically varied focus position in the z-direction. The image stack constitutes a 3D dataset largely analogous to that obtained by confocal optical microscopy. Indeed, a subtle variant is scanning confocal electron microscopy (SCEM), where a second aberration-corrected lens positioned below the specimen collects transmitted electrons, forming a magnified image of the probe at the image plane, where a pinhole aperture is used to block out-of-focus electrons. These techniques can provide Ångström resolution in the x-y plane, but most suffer from a large missing cone of information and corresponding elongation in the z-direction.

Following the initial exploration of the possible approaches, energy-filtered SCEM has emerged as a promising mode, being the only variant of SCEM offering the prospect of filling the missing cone of information. Energy-filtered SCEM is, however, practically demanding, requiring chromatic as well as spherical aberration-corrected optics. Nellist and Wang [352] have recently reviewed the various different modes of STEM depth-sectioning and SCEM, highlighting that, although the foundations have been established, as the techniques are still

evolving, including availability of the required technology, best applicability to real materials problems where they may offer unique capabilities are only just becoming perceptible.

Concerning depth-sectioning, recent work by Hovden et al. cannot go without particular mention [353]. They have proposed the combination of STEM depth-sectioning with ET to enable high-resolution imaging of extended objects. Such an approach requires fewer tilts to achieve dense sampling of Fourier space, although the acquisition of a through-focal series at each tilt may necessitate a large total electron dose (the data set in [353] comprising 1645 images).

Gaining significant attention over recent years in the physical sciences has been the development of quantitative microscopy, ADF-STEM imaging with respect to 3D analysis in particular. Methods for determining the number of atoms along projected atomic columns [57, 59], the total number of atoms in a nanoparticle [58] or the generation of larger scale thickness maps [61, 62] based on the ADF intensity are emerging as valuable techniques that can provide '$2\frac{1}{2}$D' thickness information that can be used to derive 3D structures. This may be, for example, by comparison to image simulations of known nanoparticle morphologies [58], or as input to atomistic structural simulations [64]. Arguably, these methods do not demonstrate a generalised framework for 3D imaging because they require extensive knowledge specific to the system under consideration. However, for samples that are not amenable to multiple image acquisition, they may provide the only route to 3D structure determination, and are therefore strong competitors to ET for atomic-scale 3D studies.

On the other hand, information from quantitative TEM may be used directly for [60, 63, 66, 307] or in complement to [61, 62], ET. In this vein, Van Aert and co-workers in particular have used statistical atom counting procedures [57] to determine the number of atoms in projected atomic columns for different zone axis projections of nanocrystals, and used the results as input to ET reconstruction [60, 63, 66]. In the first studies [60, 63], discrete tomography was used along with a number of prior knowledge constraints such as assuming that the atoms lie on an FCC lattice. More recently [66], atom counting results have been input to 'compressed sensing' reconstruction for which, as described in chapters 7 and 8, the prior knowledge is less strict.

5.5 Conclusions and discussion

This chapter has shown that ET is now a widely practised technique, capable of yielding many 3D materials insights. However, it has also highlighted a number of inherent deficiencies that need to be overcome to raise the efficacy of ET studies. While alternative 3D TEM methods may rival ET in some aspects, particularly for atomic-scale studies, ET will likely be the method of choice for many current and future 3D investigations in TEM.

The review of the TEM as a 'structure projector' has shown that the primary TEM imaging modes have been relatively well explored for ET, from which it can be concluded that ADF-STEM ET is best suited for seeking quantitative 3D analysis of the Ga-Pd nanocatalysts addressed in this thesis. This is pursued, in the first instance, in chapter 6. An important factor for enabling quantitative ET studies is the development of (semi-)automated segmentation procedures. In chapter 6, a semi-automated image processing based segmentation procedure is devised.

The review of tomographic sampling theory and ET acquisition has emphasised that ET data is always incomplete. The finite and limited angular sampling, viz. few projections and the missing wedge, are frequently the dominant factors limiting the fidelity of ET reconstructions. Since the restrictions on sampling often cannot be improved for reasons of hardware or sample constraints, the development of advanced reconstruction methods takes on particular importance. In this regard, the highly underdetermined nature of the ET reconstruction problem requires incorporation of additional constraints, so called 'prior knowledge' or 'regularisation', in order to produce high-fidelity reconstructions. There is scope for further advances in this direction, and a new approach is developed in chapters 7 and 8.

Additionally, from the review of ET applications and signal modes, it is evident that ET is now being used to address an increasingly wide range of materials, properties or TEM signals, each presenting different characteristics. Advanced ET methods need to be capable of addressing this diversity, especially those that may exploit prior knowledge of the structure. The approaches developed in chapters 7 and 8 seek to address this point by harnessing powerful yet widely applicable 'transform domain sparsity' as prior knowledge.

It has also been highlighted that although use of advanced signal modes in ET is now becoming feasible, in many cases the number of projections that can be acquired is still very stringently limited (even more stringently limited than conventional acquisitions). Alternatively, many of the advanced signal

modes yield higher dimensional data, which may vastly increase the amount of information produced from a tilt-series and become challenging to manage. In either case, the ability to achieve high-fidelity reconstructions from few projections would be of great benefit. This is again a primary aim of chapters 7 and 8.

Chapter 6

Quantitative electron tomography via image processing based segmentation

This chapter describes ET characterisation of the unsupported intermetallic Ga-Pd nanocatalysts that were studied at high resolution in chapter 3. An image processing based routine is devised for segmenting a conventional SIRT reconstruction of the densely-packed nanoparticles. The optimised segmentation routine facilitates otherwise unachievable quantitative morphological analysis of ca. 1800 nanoparticles and agglomerates that possess diverse morphologies and sizes. It is concluded, however, that the fidelity of the segmentation and quantitative analysis is limited ultimately by the fidelity of the tomogram motivating, as a prerequisite, improvement of the tomographic reconstruction process, as addressed in the two subsequent chapters. The contents of this chapter have been published in [167].

6.1 Introduction

As discussed in chapter 5 (section 5.3.5), the segmentation of electron tomograms has often been performed manually, being both laborious and subject to individual bias. However, as an alternative, image processing techniques may be utilised. These may facilitate more facile and robust segmentation, therefore being key in achieving routine and reliable 3D nano-metrological analysis. This is particularly so where nanoparticles or objects are closely spaced. The development of fast yet robust methods for segmenting densely populated nanoparticle tomograms would therefore be of great benefit for the full

exploitation of the 3D data, providing access to valuable quantitative information such as the size, shape, spatial distribution and agglomeration state of the nanoparticles.

Here, quantitative 3D data is obtained via ADF-STEM tomography and the implementation of a step-by-step semi-automated segmentation routine. This approach, combined with effective visualisation and consideration of relevant tomographic theory, enables identification of reconstruction and segmentation artefacts that affect the qualitative and quantitative data obtained, allowing both refinement of the segmentation procedure and more reliable interpretation of the quantitative information. Such analysis could not be obtained easily (if at all) using other characterisation techniques, and the approaches should be readily applicable to other nanoparticle systems beyond those studied here. The ET investigation was complemented by EDXS, BF-CTEM (including high-resolution imaging) and AC-STEM [167] but, largely superseded by the analysis in chapter 3, those results are not shown here.

6.2 ADF-STEM tomography

ADF-STEM tomography was performed on an FEI Tecnai F20 (S)TEM operated at 200 kV, using a Fischione 2020 Advanced Tomography Holder, a probe semi-convergence angle of 11 mrad and an ADF detector inner angle of 45 mrad. The tilt-series was acquired in a semi-automated manner over an angular range of $\pm 76^\circ$ with a 2° tilt increment using FEI Xplore3D. The series of projections was aligned by cross-correlation and the reconstruction performed using 40 iterations of SIRT, implemented in FEI Inspect3D. The resulting tomogram was cropped to the region of interest, yielding dimensions 688 x 941 x 616 voxels, with a voxel size of 0.19 nm^3. Post-processing, including segmentation and visualisation, was carried out using ImageJ and Avizo Fire (Visualisation Sciences Group). As shown in Figure 5.7, the z-direction labelled on the orthoslices is parallel to the optic axis (the missing wedge direction), the y-direction is parallel to the tilt axis and the x-direction perpendicular to these.

Figure 6.1 shows example ADF-STEM images from the tomography tilt-series, where it can be seen that the cluster analysed contains significant numbers of both small (<10 nm) and large (ca. 20 nm) nanoparticles. The full aligned tilt-series can be viewed in Video 1 on the supplementary CD; see Appendix A. A BF-CTEM image of the cluster of nanoparticles, recorded at 0° tilt, is shown in Figure 6.2. Taking 2D slices from the x-y planes of the

tomogram (perpendicular to the optical axis, Figure 6.3) displays this varied size distribution with greater clarity than the original tilt-series images, and reveals a diverse range of nanoparticle morphologies. All x-y slices are shown in Video 2. Consistent with the observations from high-resolution BF-CTEM and AC-STEM (cf. ref. [167] and chapter 3), some nanoparticles show indications of strong faceting (for example, Figures 6.3ci and ii), but many of the nanoparticles in the tomogram appear to be more rounded and irregular in shape.

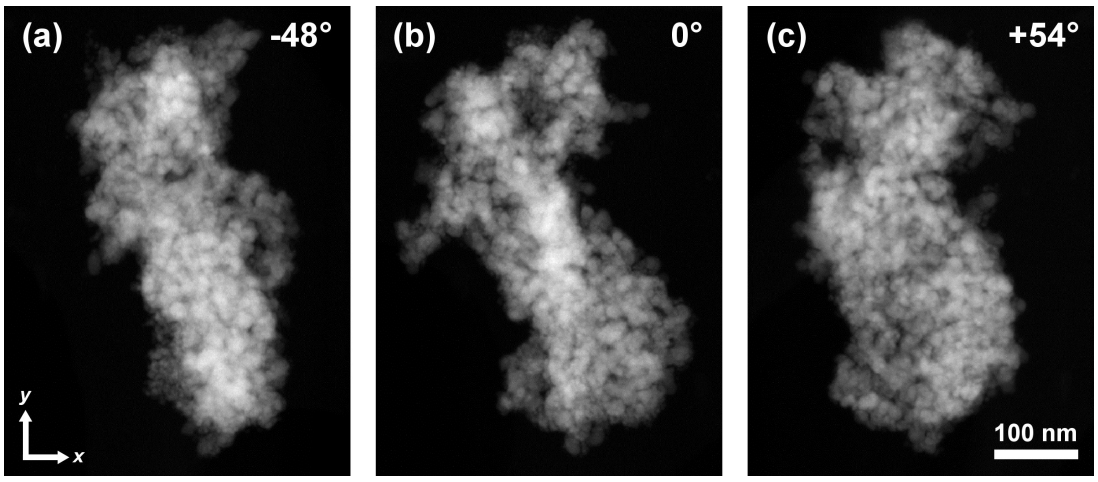

FIGURE 6.1: Example ADF-STEM tomography tilt-series images of a cluster of Ga-Pd nanoparticles. See also Video 1 in Appendix A, where the full aligned tilt-series can be seen.

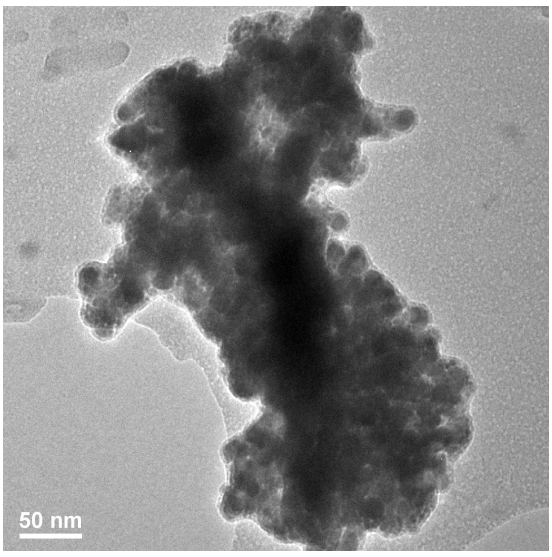

FIGURE 6.2: BF-CTEM image of the cluster of nanoparticles studied by ADF-STEM tomography.

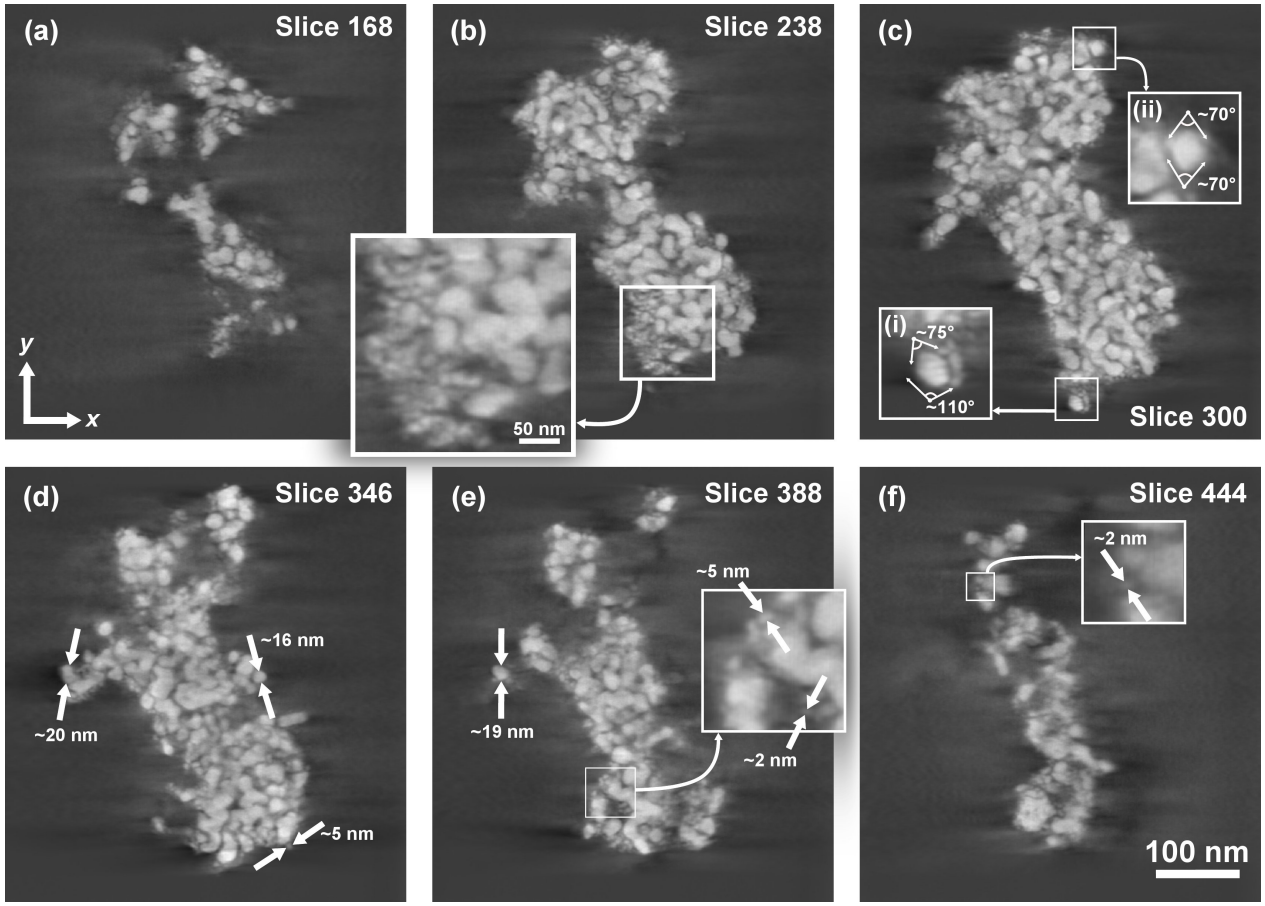

FIGURE 6.3: Selected 2D x-y slices of the tomogram (perpendicular to the optical axis), running sequentially from (a)-(f). Insets (i) and (ii) in (c) highlight example nanoparticles that show indications of a faceted morphology. In (d)-(f) the approximate sizes of selected nanoparticles are indicated, as judged from each single 2D slice. See also Video 2 in Appendix A, where all x-y slices can be seen.

6.3 Segmentation routine

To quantitatively analyse the 3D morphology of the nanoparticles, each voxel in the tomogram must be identified as belonging to a specific nanoparticle, or else to the background, and subsequently assigned an appropriate 'label'. For this nanoparticle tomogram, an appropriate similarity metric is the voxel intensity (grey level). The confirmation of phase identity given by EDXS, high-resolution BF-CTEM and AC-STEM [167] is important as it means that all of the nanoparticles should, in principle, have the same composition and therefore the same voxel intensity in the tomogram.[1]

Hence to achieve segmentation of the entire tomogram in an automated or semi-automated manner, a thresholding operation can be performed, where voxels in a certain intensity range are identified as nanoparticles and assigned a uniform value, while all background voxels are set to zero (yielding a binarised tomogram). Groups of connected non-zero voxels can then be identified as constituting individual nanoparticles or agglomerates of nanoparticles, and assigned a label that is unique to that nanoparticle/agglomerate.

Immediately thresholding without pre-processing may be possible when the nanoparticles are well separated, have a uniform intensity that is distinct from the background, and there is a high SNR, e.g. ref. [336]. However in many cases, including the cluster of nanoparticles considered here, the variation in size and shape and the dense packing of the nanoparticles, as well as the noise in the tomogram, prevents immediate segmentation of individual nanoparticles via thresholding based on the voxel intensity. These factors also mean that manual segmentation would be highly subjective and prohibitively time consuming. Hence a semi-automated segmentation routine is essential, the essence of which is summarised in Figure 6.4.

A Difference of Gaussians (DoG) operation was first applied in the x-y planes of the tomogram (Figures 6.4a-c). The smoothing operation (Gaussian blur, G, Figure 6.4b) suppresses high-frequency information, and the difference between two images smoothed with two different Gaussians (the DoG, Figure 6.4c) retains those features that are in the intermediate size between the two operators [139]. Hence the standard deviations (σ) of the two Gaussians can be chosen according to the size of the features to be detected and the noise characteristics of the data. In this case, using $\sigma_1 = 2$ voxels and $\sigma_2 = 3$ voxels was found to yield

[1] At the magnifications used for this ADF-STEM tomography tilt-series, the disordered overlayer revealed clearly in chapter 3 is not sufficiently distinguishable to constitute another grey level in the tomogram, although its presence does degrade the fidelity of the analysis.

the optimum DoG for highlighting the large nanoparticle boundaries, as well as the smaller nanoparticles. The DoG filtered and original tomograms were then averaged to yield both enhanced boundaries and sufficiently uniform intensity in the interiors of the nanoparticles (Figure 6.4d) to facilitate thresholding and subsequent binarisation, where the individual binarised nanoparticles could be more readily distinguished (Figure 6.4e).

A 3D watershed transform [330, 344] was then applied to separate nanoparticles that were incorrectly joined after thresholding, acting on the contrast inverted Euclidean distance map (EDM) of the binary tomogram (Figures 6.4f-j). The EDM (Figure 6.4f) is a grey-scale image where each voxel constituting a nanoparticle in the binary tomogram (Figure 6.4e) has been assigned an intensity (grey level) according to its distance to the nearest background voxel. Watershed segmentation is capable of separating, in an automated manner, particles that are in contact. A variety of 2D and 3D watershed algorithms are available commercially and in open source software packages. The implementation used in this work (the 'binseparate' command in Avizo Fire) operates on the contrast inverted EDM, and its action can be viewed in terms of an immersion principle: a 'flood' process is initiated from identified intensity minima, which lie at the bottom of 'basins', and separation lines are created where the rising 'water fronts' from adjacent basins come together.

The severity of the watershed separation applied here was tuned by a controlled degree of merging of the intensity minima in the contrast inverted EDM (Figure 6.4g). This measure helps to reduce over-segmentation when the nanoparticles or agglomerates are non-spherical or non-convex. Intimately touching nanoparticles are not separated by the watershed process, and remain in the tomogram as agglomerates. Any holes (isolated black voxels) within the nanoparticles (white voxels) were then filled (Figure 6.4k), as the nanoparticles themselves are not expected to contain substantial voids, while any substantial void space between agglomerated nanoparticles is unlikely to be fully enclosed in 3D following the watershed separation. For nanoparticle tomograms where there may be a greater number of false holes within the nanoparticles in the initial binarised tomogram, and where the spacing of adjacent nanoparticles permits, it may be preferential to perform a hole-filling operation prior to the watershed transform, in order to avoid over-segmentation.

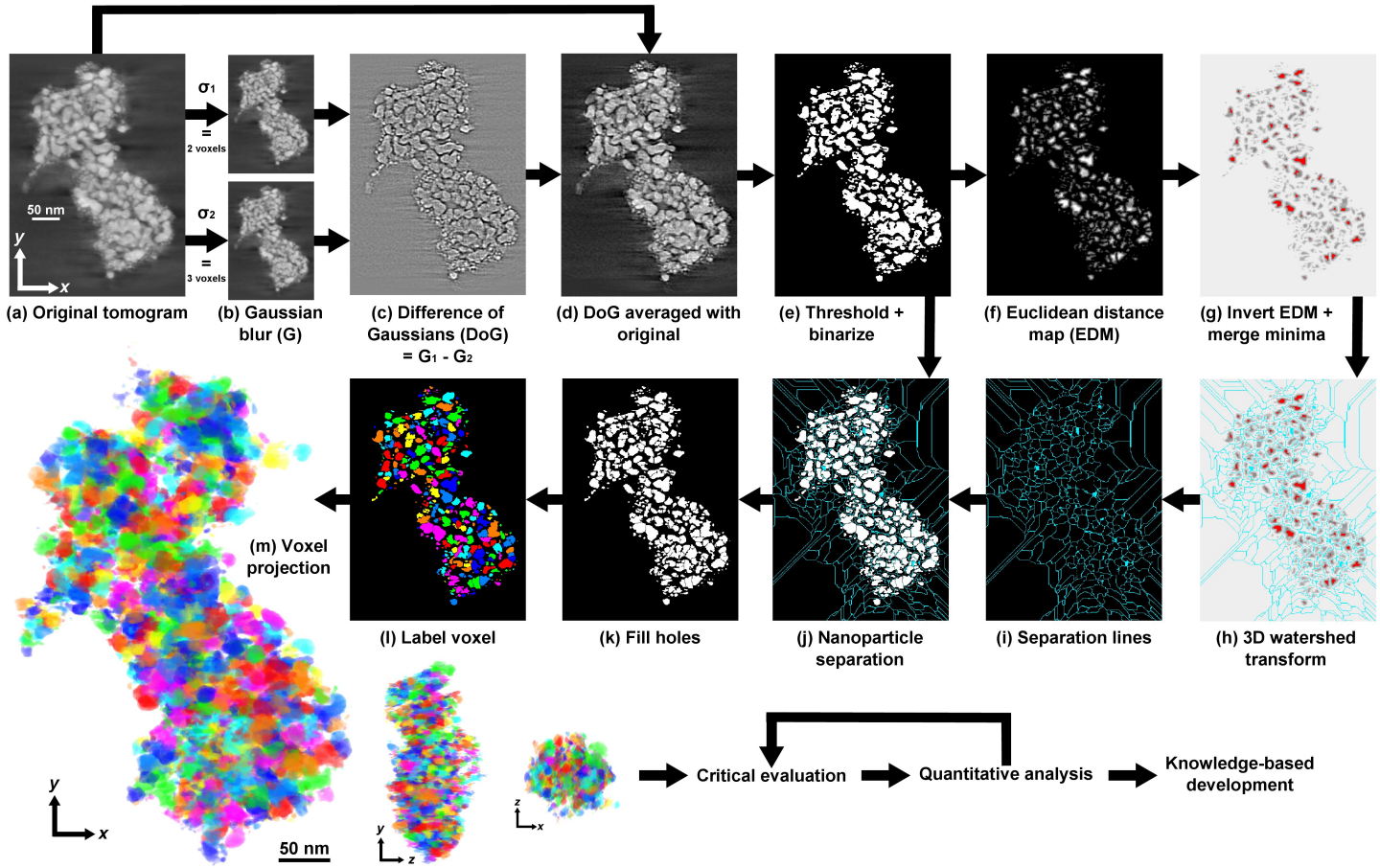

FIGURE 6.4: Semi-automated segmentation routine applied to the tomogram, to enable identification of individual and agglomerated nanoparticles constituting the densely populated cluster. (a)-(l) illustrate the principal stages of the routine on a 2D slice from the x-y plane of the tomogram. For the Gaussian smoothing in (b), σ is the radius of decay to one standard deviation. (m) is a 3D perspective view voxel projection visualisation. (l) and (m) show the final segmented tomogram, where individual voxels have been given a colour according the nanoparticle or group of strongly agglomerated nanoparticles to which they belong, and where the individual nanoparticles or agglomerates have been given a colour that differs from those of their nearest neighbours. See also Video 2 in Appendix A, where a rotating 3D perspective view voxel projection of the colour-coded segmented tomogram is shown.

6.4 Quantitative analysis & critical evaluation

As with any image processing procedures applied to real (noise-corrupted) data, there will be segmentation errors resulting from the methods used here. These were minimised by thorough analysis of the segmented tomogram and the quantitative data obtained, as well as consideration of likely artefacts in the reconstruction based on relevant ET theory. For example, the outcome of the segmentation routine can be represented as shown by the 2D x-y slice in Figure 6.4l, where the voxels have been assigned a colour according to the nanoparticle or group of strongly agglomerated nanoparticles to which they belong, and where the individual nanoparticles or agglomerates have been given a colour that differs from those of their nearest neighbours. Additional 2D x-y slices of the colour-coded segmented tomogram (corresponding to those of the unprocessed tomogram in Figure 6.3), are shown in Figure 6.5, and all x-y slices of the colour-coded segmented tomogram are shown in Video 2. Figure 6.5 and Video 2 also show x-y slices in which the boundaries of the segmented nanoparticles and agglomerates have been overlaid on the unprocessed tomogram.

Figure 6.4m shows 3D perspective view voxel projections of the colour-coded segmented tomogram, confirming that the 3D structure of many of the larger and smaller nanoparticles has been successfully captured by the segmentation routine. A 360° rotating 3D perspective view of the segmented tomogram is shown in Video 3. In addition, to enable reference to the original data itself, orthographic voxel projections of the segmented tomogram (which, to a reasonable approximation, provide a projection view analogous to that obtained in a TEM) have been generated at the same viewing angles as each of the projections in the ADF-STEM tomography tilt-series. Examples, corresponding to the tomography tilt-series images in Figure 6.1, are shown in Figure 6.6, and orthographic projections of the segmented tomogram at all angles matching the tomography tilt-series are shown in Video 1. Visualisation in these ways, combined with more standard techniques, such as viewing orthogonal 2D slices of a region of interest, proved highly effective for judging the appropriate settings of important stages in the segmentation routine, such as the severity of watershed transform, by identifying over- and under-segmented nanoparticles.

A variety of morphological and catalytically relevant properties can be readily determined from segmented nanoparticle data such as that obtained in Figure 6.4m. Two examples are briefly presented for the cluster of nanoparticles considered here, which consists of ca. 1800 nanoparticles. The nanoparticle sizes

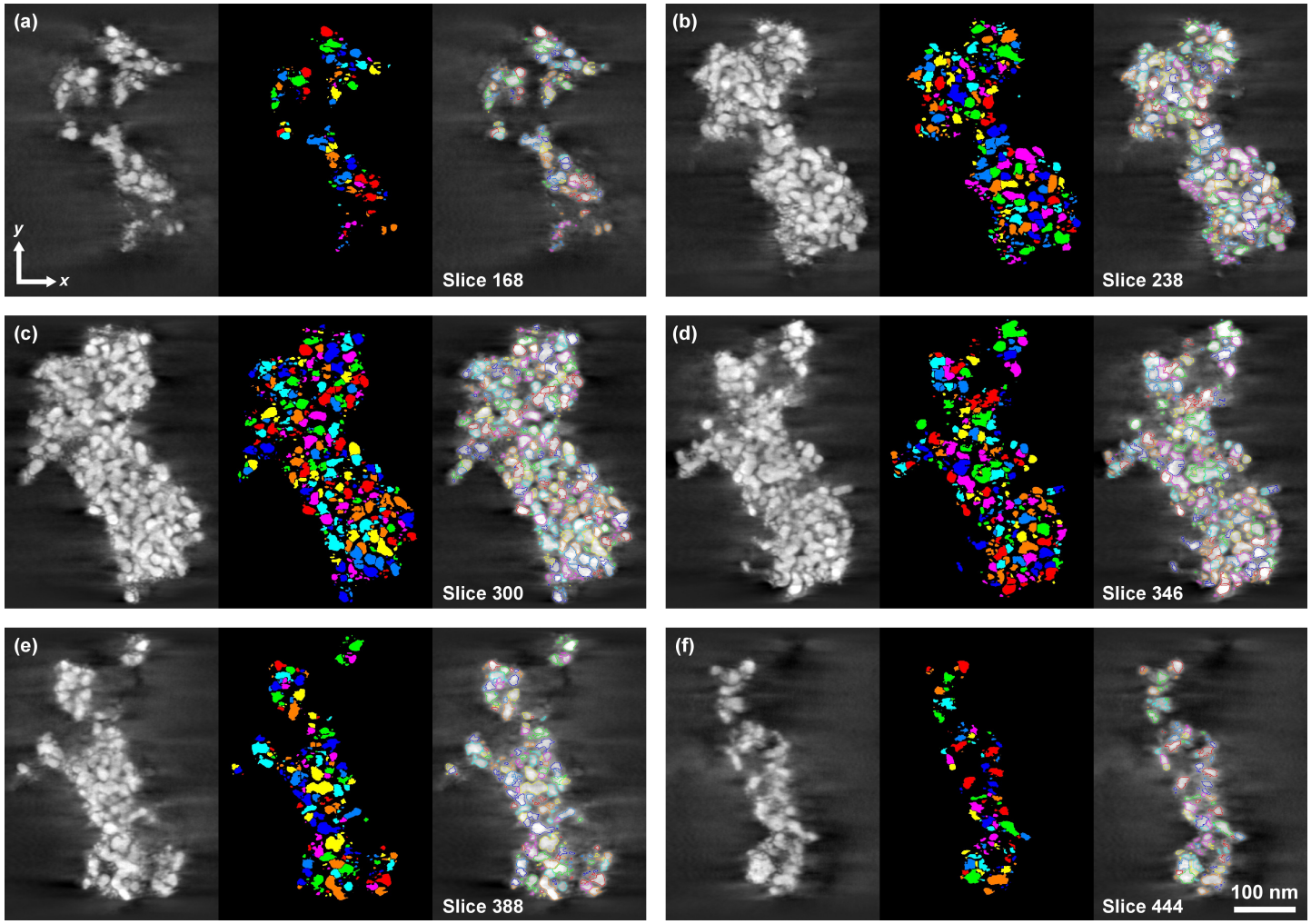

FIGURE 6.5: 2D x-y slices (perpendicular to the optical axis), running sequentially from (a)-(f), displaying the segmentation results. The figure to the left in each panel shows the unprocessed tomogram. The corresponding slice of the segmented tomogram is shown in the centre figure of each panel, with the colour-coding used in Figure 6.4. The figure on the right of each panel shows the boundaries of the segmented nanoparticles and agglomerates overlaid on the unprocessed tomogram. The panels (a)-(f) correspond to those in Figure 6.3. See also Video 2 in Appendix A, where all x-y slices can be viewed.

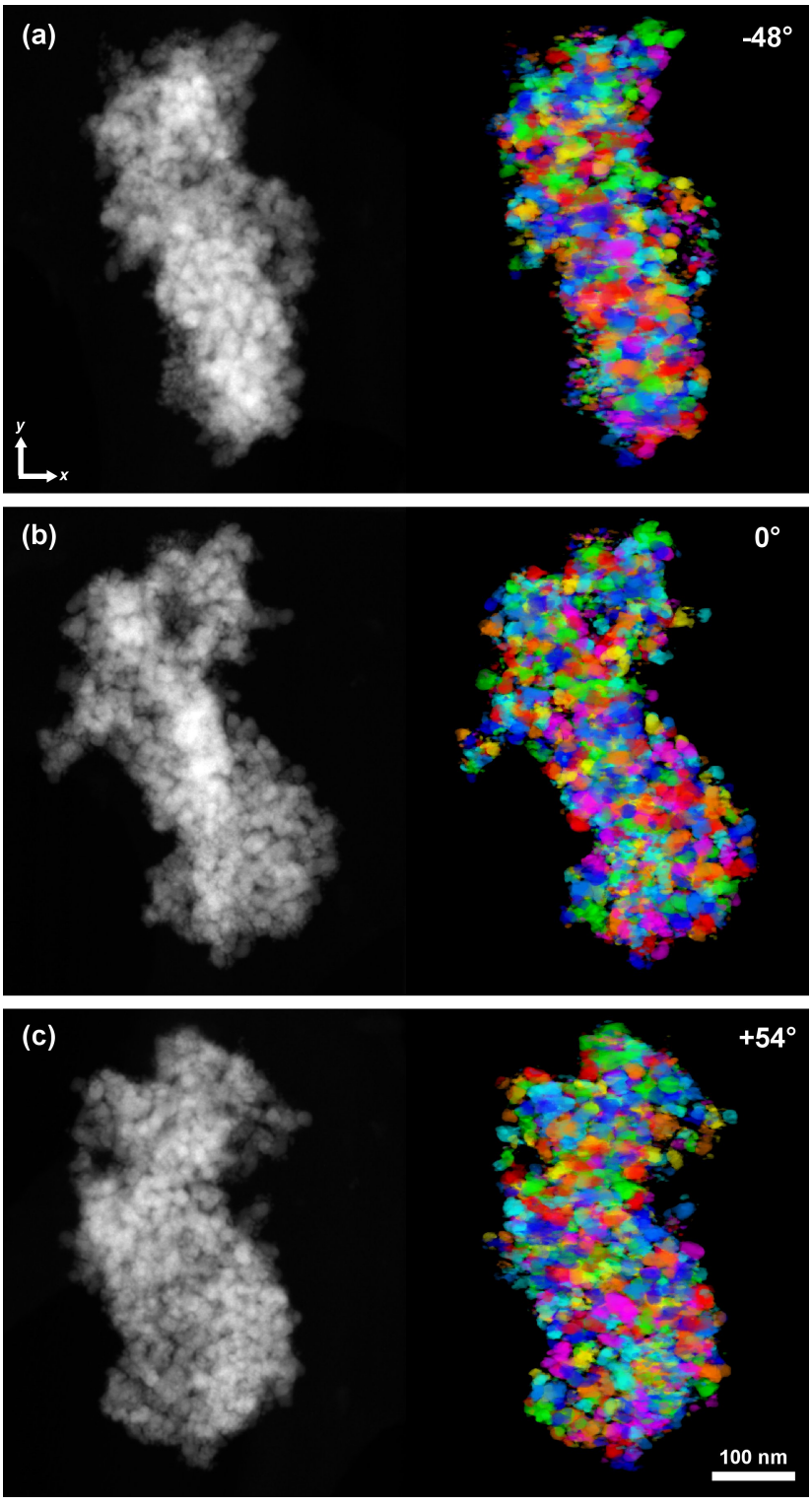

FIGURE 6.6: Orthographic voxel projection views of the colour-coded segmented tomogram, generated at the same viewing angle as the ADF-STEM tomography tilt-series image shown in the left of each panel. See also Video 1 in Appendix A, where corresponding orthographic voxel projection views of the segmented tomogram are shown adjacent to the ADF-STEM images throughout the tomography tilt-series.

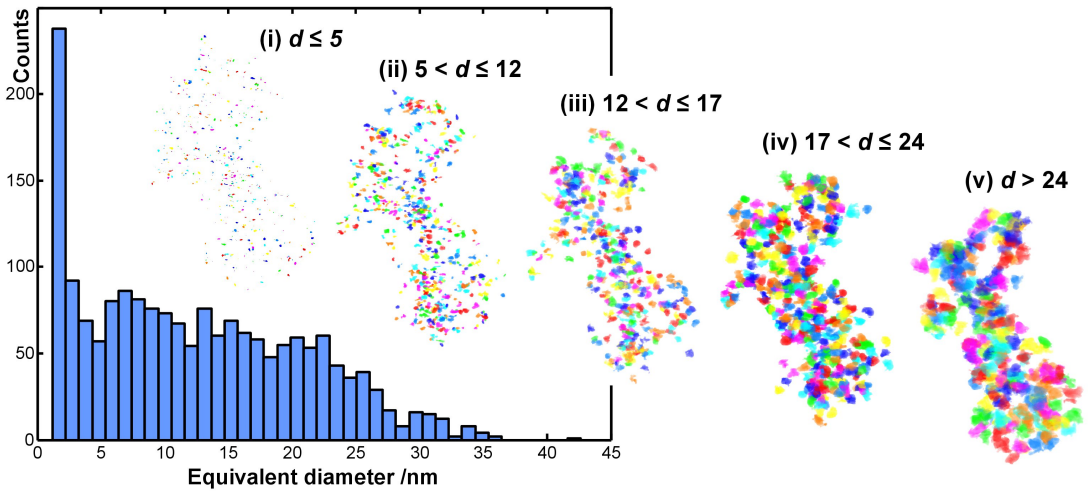

FIGURE 6.7: Statistical distribution and size filtered tomograms according to the equivalent diameter d of the nanoparticles, based on the segmented data. The filtered tomograms are voxel projections shown in the x-y plane (perpendicular to the optical axis), with the colour-coding described in Figure 6.4.

can be gauged by considering their equivalent diameter d, defined as the diameter of a sphere having the same volume as the nanoparticle. This statistical size distribution is shown in Figure 6.7. Given that the unprocessed and segmented tomograms contain a certain amount of noise due to the experimental imaging and tomographic reconstruction process, it was necessary to set a lower limit on the size of groups of connected voxels classed as nanoparticles to be considered in the statistical distribution. Empirically, a threshold of 5 connected voxels was found to yield the best discrimination between isolated noise and groups of voxels constituting genuine small nanoparticles associated with the cluster. With an individual voxel size of 0.19 nm^3, this minimum nanoparticle size is 0.95 nm^3, which is in good agreement with expected maximal attainable resolution in the tomogram of ca. 1 nm^3 [286], although the reliability of the analysis will clearly be lower at this extreme of the size distribution.

A useful indicator of the nanoparticle shape is their 3D Feret ratio (FR), defined as the maximum divided by the minimum Feret diameter, effectively providing a measure of shape anisotropy. Specifically, the Feret diameter may be taken as the distance between two tangent planes on opposite sides of a particle (Figure 6.8a). The maximum and minimum Feret diameters of the nanoparticles in the segmented tomogram were determined in 3D using the Avizo Fire software, by evaluating their Feret diameters over full angular ranges of θ and ϕ at 5° increments, with the coordinate description shown in Figure 6.8b. For analysis of the statistical distribution of the FRs, a threshold of at least 10 connected

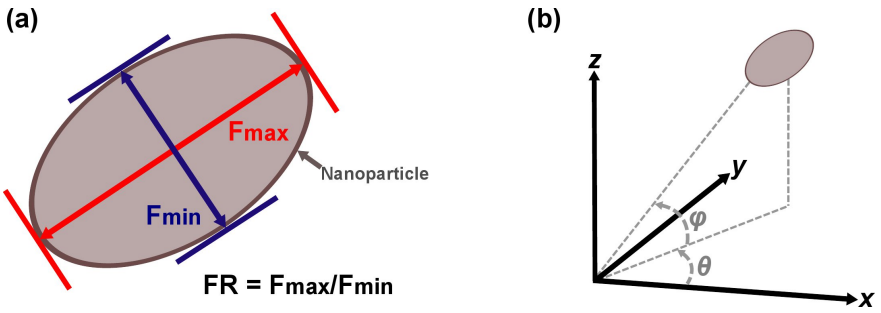

FIGURE 6.8: (a) Schematic illustrating the maximum (F_{max}) and minimum (F_{min}) Feret diameters, and Feret ratio (FR) of a particle (for simplicity drawn in 2D). (b) Coordinate definition for the evaluation of F_{max} and F_{min} in 3D.

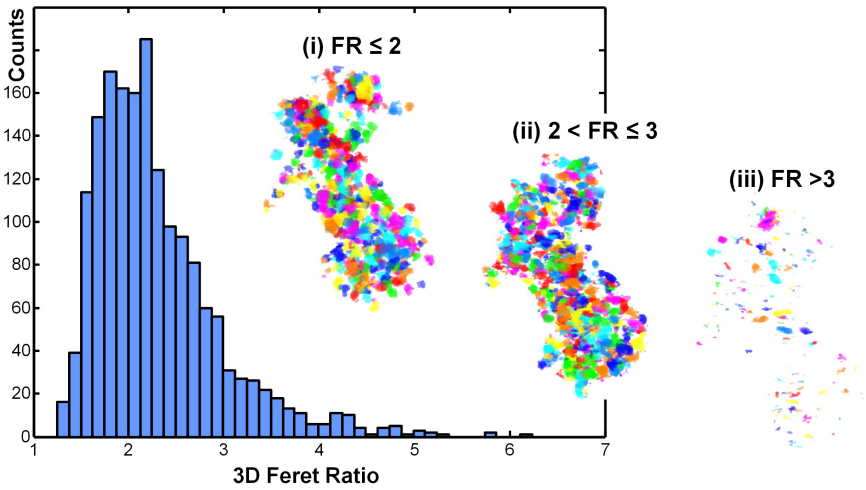

FIGURE 6.9: Statistical distribution and shape filtered tomograms according to the 3D Feret ratio (FR) of the nanoparticles, based on the segmented data. The filtered tomograms are voxel projections shown in the x-y plane (perpendicular to the optical axis), with the colour-coding described in Figure 6.4.

voxels was set for groups of voxels classed as nanoparticles, as the shape of the nanoparticles is unlikely to be faithfully represented by fewer than 10 voxels. The obtained statistical shape distribution is shown in Figure 6.9.

Further insight into the size, shape and spatial distribution of the nanoparticles, and assessment of the fidelity of the segmentation and quantitative analyses, is aided by filtering of the tomogram based on the obtained measures. In Figure 6.7 the tomogram has been split according to nanoparticle sizes, showing that the nanoparticles in each size range are relatively uniformly distributed throughout the cluster. In previous work concerning similarly synthesized Ga-Pd nanoparticles, the nanoparticle size distribution was likewise measured as strongly peaked in the <10 nm range, using disc centrifuge methods [111, 149] (see also chapter 3). However, the investigation here has considered, and is sensitive to, highly agglomerated nanoparticles. The measured size distribution is

therefore characteristic of both nanoparticles and agglomerates of nanoparticles, and the distribution is correspondingly spread to larger sizes. From careful inspection of each size-filtered tomogram, the nanoparticles and agglomerates predominantly making up each of the classes indicated in Figures 6.7(i)-(v) can be described as: (i) fine nanoparticles, (ii) small nanoparticles, (iii) medium nanoparticles and agglomerates of small nanoparticles, (iv) large nanoparticles and medium sized agglomerates, and (v) large agglomerates. The substantial overlap of the nanoparticles when viewed in projection means that this information could not be obtained from 2D TEM images.

The presence of agglomerated nanoparticles in the segmented tomogram reflects true agglomeration visible in the unprocessed data, particularly in BF-CTEM (cf. Figure 6.2), which is contributed to by the disordered over-layer described in chapter 3. However, some degree of false agglomeration will have been introduced into the tomogram by under-segmentation during the binarisation or watershed transform, as well as from the point spread function (PSF) of the ADF-STEM tomography technique.

The overall PSF comprises of the PSF of the ADF-STEM imaging process and a tomographic PSF. The main effect of the ADF-STEM imaging PSF is to cause a blurring of the projected nanoparticle image. In addition to blurring of the reconstructed nanoparticle boundaries, the tomographic PSF also leads to an anisotropic elongation effect. The tomographic PSF is caused primarily by the finite and limited angular sampling of Fourier space in the original tilt-series, and the elongation is most pronounced in the direction parallel to the optical axis (z-direction), due to the missing wedge of un-sampled information (section 5.3.1). These factors can substantially degrade the quality of ET data, and as described in chapter 5, have been considered extensively in the literature, including recent critical analysis specifically in the context of densely-packed nanoparticles [246].

While some of the corrupting effects can be approximately quantified, the cumulative effect of many factors makes estimation of a numerical confidence bound for the quantitative data challenging. Additionally, for the data presented here, the values for the free parameters in the segmentation routine, such as the thresholding step and severity of the watershed transform, have been selected empirically by the user. While the use of image processing techniques has introduced a large degree of objectivity into the segmentation, and the advanced visualisation has enabled refinement of the obtained results to facilitate best choice of the segmentation parameters, there is still some user judgment that can influence the results obtained. This gives further reasoning for it not

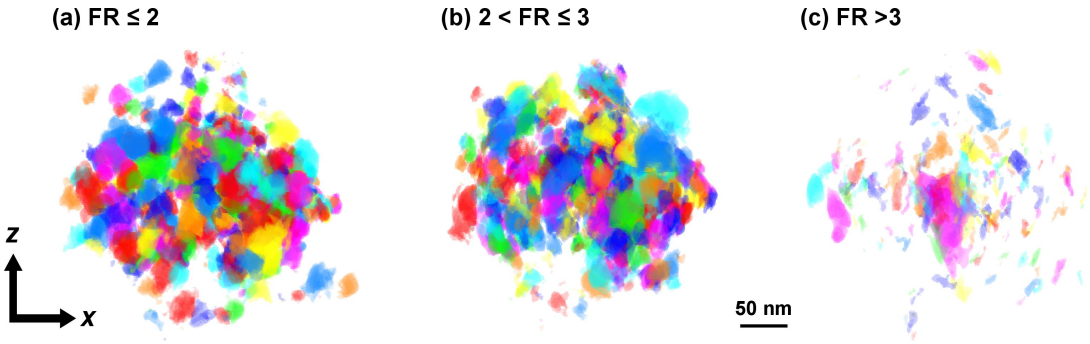

FIGURE 6.10: Shape filtered tomograms according to the 3D Feret ratio (FR) of the nanoparticles, shown as 3D perspective view voxel projections in the x-z plane, with the colour-coding described in Figure 6.4. The z- (missing wedge) direction is parallel to the optical axis. In (c) it can be seen that many of the nanoparticles are actually agglomerates of small/fine nanoparticles that are likely to have been falsely merged by missing wedge artefacts, as their longest dimension is almost exclusively in the z-direction.

being appropriate to express a numerical error bound on the quantitative data, which must be interpreted with knowledge of the limitations of the current ET technique, and with reference to the fidelity, or presence of artefacts, as judged from the rigorous visualisation.

The distribution of FRs (Figure 6.9) suggests that the majority of nanoparticles and agglomerates are mildly anisotropic in their overall shape. Filtered tomograms showing nanoparticles with FRs lying in different ranges are shown in Figures 6.9(i)-(iii). This analysis will be affected to some degree by the limited maximum tilt angle, which leads to a loss of resolution in the missing wedge (z) direction. According to equation 5.3 (section 5.3.1), for the tilt-series considered here, with $\theta_{max} = 76°$, the false elongation is by a factor of ca. 1.2 (although it was noted in section 5.3.1 that the actual elongation can be considerably smaller than this when when constrained reconstruction techniques such as SIRT are used). In particular, it is evident from Figure 6.9 that the measured distribution is skewed to the right of the mean, and the filtered tomogram for FR > 3 (Figure 6.9(iii)) shows that the highly anisotropic nanoparticles are mostly of the small to fine size range. Viewing this filtered tomogram in the x-z plane (Figure 6.10) reveals that many of these nanoparticles are actually agglomerates of small nanoparticles that are likely to have been falsely merged by missing wedge artefacts, as their longest dimension is almost exclusively in the z-direction.

It must also be noted that recent detailed analysis of both WBP and SIRT reconstructed experimental and simulated nanoparticle tomograms has suggested that the intensity (grey level) of reconstructed nanoparticles can be dependent on the nanoparticle size, which has implications for threshold based nanoparticle detection and segmentation [305, 354]. In this work, the use of an image gradient

(DoG) operation in the segmentation routine has provided an objective means of enhancing the smaller nanoparticle intensities and large nanoparticle boundary intensities, facilitating a subsequent thresholding operation where small, large and densely-packed nanoparticles could be simultaneously segmented. However, this step in the routine is not optimal and does not entirely compensate for the shortcomings of the SIRT reconstruction.

Accounting for the reconstruction artefacts, the genuine shape anisotropy of the nanoparticles and agglomerates reinforces the notion that their sizes and shapes cannot be accurately gauged from 2D TEM images. It also means that they possess a greater surface-area-to-volume ratio than a perfect sphere, and so consideration of their equivalent diameter alone would be an insufficient nano-metric analysis. Such insight into the size and spatial distributions of the nanoparticles is, ultimately, key to determining the most catalytically efficacious sizes and the degree to which their active surface area may be restricted due to agglomeration. The shape anisotropy means that, relative to a perfect sphere, more surface area is available for catalysis, potentially increasing the activity per unit of the noble metal catalyst. It may also have implications on stability and selectivity during catalysis, according primarily to the nature of the exposed surfaces in particular morphologies. Fundamentally, these morphologies are determined by the crystallography in Ga-Pd nanoparticles, new insight into which was given in chapters 3 and 4. The resolution in the present tomogram is insufficient to characterize these aspects in detail (cf. Figures 6.3ci and ii), but a higher magnification ET tilt-series of less agglomerated nanoparticles could be insightful.

6.5 Discussion

Primarily, it is clear that the quality of the analysis in this study is limited by artefacts related to the finite tilt increment and the missing wedge. Methods that overcome or negate the effects of limited angular sampling may provide the only routes to truly quantitative ET. Given that the tilt increment often cannot be decreased, and the tilt range not be extended, for reasons of sample or hardware constraints, advanced reconstruction techniques take on particular importance. These advanced reconstruction algorithms must be able to address the particularities of challenging nanoparticle systems of the type considered here. In this case, since the material of interest is known to be near homogeneous single phase, improved reconstruction may be achievable using discrete [209]

or partially discrete algorithms [313]. Another method shown to enhance the quality of nanoparticle catalyst tomograms is the DIRECTT algorithm [320]. Alternatively, in chapters 7 and 8, a 'compressed sensing' approach to ET reconstruction is developed, including specific application to the Ga-Pd catalysts in section 8.3.3.

With higher quality reconstructions, in which the intensity of the reconstructed nanoparticles more accurately reflects their true densities, regardless of the nanoparticle size, and the blurring of the nanoparticle boundaries reduced, it should become increasingly possible to simplify, further automate and raise the overall fidelity of segmentation routines, including use of thresholding methods directly on the unprocessed (or minimally pre-processed) nanoparticle tomogram. This is indeed directly confirmed in chapter 8, section 8.3.3. Alternatively, using discrete algorithms, some form of binarisation or multiple grey level assignment can be incorporated into the reconstruction process itself [209, 308–314].

Automating selection of the appropriate settings for the watershed transform is perhaps a more challenging task. However, by obtaining more robust segmentation in the previous stages, the sensitivity of the outcome to changes in the parameter settings may be reduced in many instances.

Finally, advances in reconstruction algorithms should lead not only to higher quality tomograms, but also to greater understanding, and quantification, of the artefacts that may still be present. When this is the case, an important goal is to quantify not only properties of interest associated with the segmented data, but also the uncertainty in the obtained measures.

Considering the study of other nanoparticle systems, each experimental dataset will have unique characteristics, and therefore demand slightly different segmentation steps, with varying complexity and degree of automation that can be afforded to each step. However, the principal aspects of the routine demonstrated here are generic and widely applicable. Indeed, during the course of this work a complementary study was reported by Grothausmann et al. [337], where similar image processing techniques were used to facilitate segmentation of carbon black-supported Ru fuel cell catalyst nanoparticles from BF-CTEM tomography data. Colour-coded visualisation was also used to enhance the study, and quantitative nano-metrological analysis based on the segmented data was reported.

6.6 Conclusions

Overall, while the approaches employed in this work still require user interaction and careful interpretation of the reconstructions and quantitative data, they have provided access to otherwise unobtainable quantitative nanometrological and spatially-resolved information from statistically relevant numbers of morphologically-diverse and densely-packed nanoparticles. This chapter has shown that ET, and use of an image processing methodology for segmentation, can provide a widely applicable and powerful approach for the morphological characterisation of advanced nanoparticle systems. Further, it has shown where there is greatest scope for improvement, namely improving the tomographic reconstruction itself before segmentation is attempted.

Chapter 7

Compressed sensing electron tomography: theory

The recent mathematical concept of compressed sensing asserts that a small number of well-chosen measurements can suffice to reconstruct signals that are amenable to sparse or compressible representation. In addition to powerful theoretical results, the principles of CS are being exploited increasingly across a range of experiments to yield substantial performance gains relative to conventional approaches.

This chapter introduces the salient aspects of CS theory and its application to electron tomography (ET) reconstruction. Particular effort has been made to provide an accessible overview of what can, at times, appear to be daunting mathematical theory. The technical paper [292] (on which this chapter is primarily based) was written in this vein, to disseminate CS principles to the electron microscopy community. Similarly, sections in a number of review articles [32, 355–357] have been written to address a wide audience.

7.1 Introduction

Concepts of theoretical and practical signal recovery from undersampled data, pertinent throughout science and engineering, have recently undergone a paradigm shift with the development of a new sensing and recovery strategy known as 'compressed sensing' (CS, also referred to as compressive sensing or compressive sampling) [17, 18]. CS entails exploiting sparsity implicit in many signals and rigorous mathematical foundations have shown that, under certain circumstances, exact signal recovery, or recovery with bounded discrepancy, may be possible from far fewer measurements than traditional theories dictate

should be necessary.

The key prior knowledge harnessed in CS is that the signal is sparse or compressible in some known transform domain, meaning that it can be represented or well-approximated, respectively, in a more compact form. A wide variety of transforms are available for this task, making the applicability of CS wide-reaching. A simple, illustrative, example is shown in Figure 7.1.

Many challenging inverse problems, such as tomographic image reconstruction, can be approached as a CS problem. Indeed, the application of CS is growing rapidly, including in areas very closely related to ET such as X-ray computed tomography [358], magnetic resonance imaging (MRI) [359, 360] and single particle microscopy (SPM) [361, 362]. In this chapter, CS theory and its application in the context of ET is described.

7.2 Compressed sensing

CS harnesses principles of transform coding and sparse approximation that are well established from their use in image compression algorithms. Forming the foundation of the ubiquitous JPEG and JPEG-2000 image compression standards, for example, are the discrete cosine transform (DCT) and discrete wavelet transform (DWT), respectively, to provide sparse representation [363].

In the image compression framework, an image is first fully sampled and the transform coefficients calculated. The small, insignificant coefficients in the transform domain are then discarded, leaving only the largest to be stored. With the appropriate choice of transform, the large coefficients will be few in number, meaning that when the small coefficients are discarded, the amount of information representing the image is reduced or 'compressed'. In spite of this data reduction, when the inverse transform is applied to the compressed representation, the image can be recovered with minimal loss of information.

Figure 7.2 demonstrates the efficacy of sparse approximation of 'natural' image content (in this case the well-known 'cameraman' test image) using a DWT. In Figure 7.3 the principal stages in image compression and CS are set side-by-side.

More explicitly, to compress an image or other signal of interest $\mathbf{x}$ (written as a column vector with n entries or values), the aim is to describe $\mathbf{x}$ using only a small number of coefficients. This can be achieved by considering that $\mathbf{x}$ can be expressed using a linear combination of basis functions $\boldsymbol{\psi}_i$ (for example, sinusoids

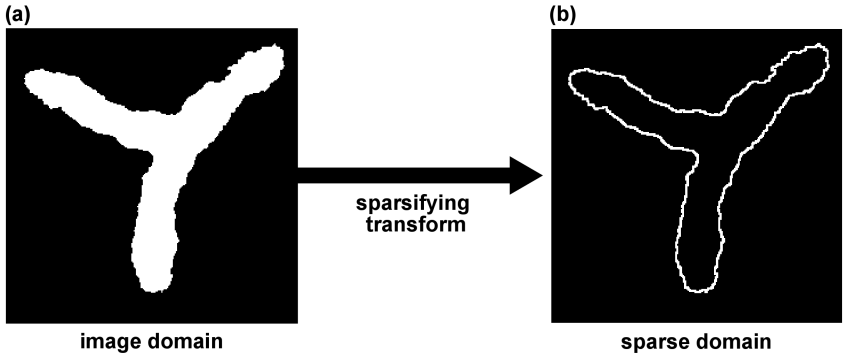

FIGURE 7.1: The concept of sparse representation: a sparse representation (b) of the image (a) is obtained by the application of an appropriate 'sparsifying transform'. In this example, the information in the simple cartoon-like image (a) can be captured by a small number of non-zero pixels in the gradient domain (b). The sparsifying transform, is a spatial finite differences operator.

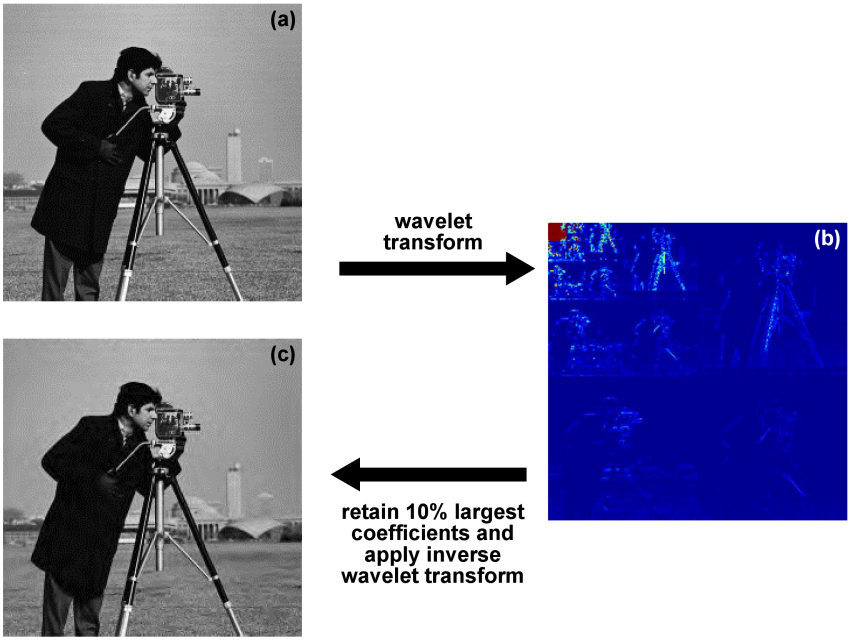

FIGURE 7.2: The efficacy of sparse approximation of 'natural' image content using wavelets. The original image (a) can be well-approximated in a wavelet domain (b) using only a small number of coefficients: there are many small (negligible) wavelet coefficients, but few large (important) coefficients. The small coefficients can be discarded and the image can be recovered from just the large coefficients with minimal loss of information (c). (The wavelet domain representation (b) consists of 'approximation coefficients' in the upper left hand corner and, in the other sectors, 'detail coefficients' at different resolution levels, in the horizontal, vertical and diagonal directions.)

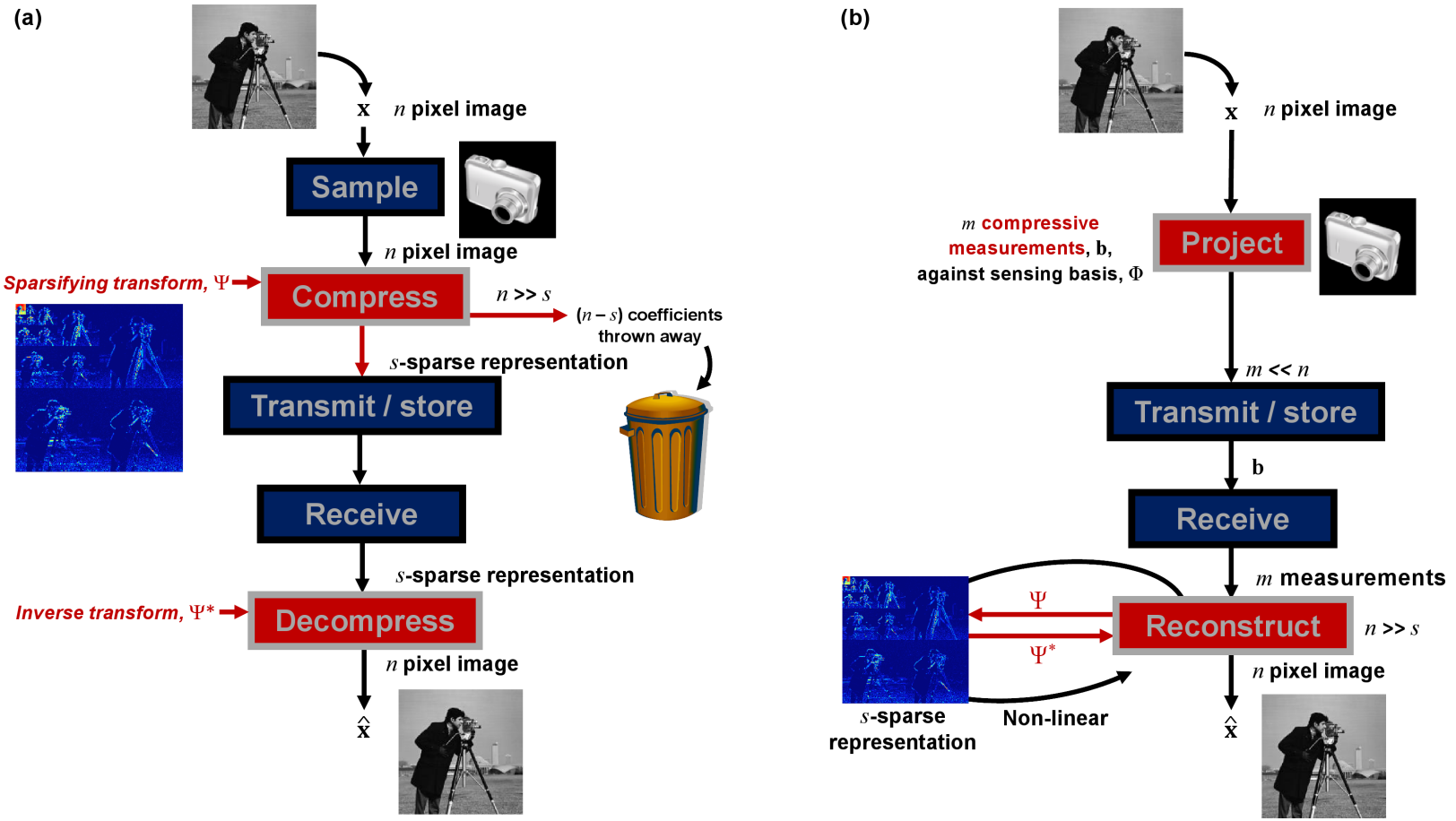

FIGURE 7.3: Comparison of post-acquisition signal compression (a) and compressed sensing (b). See text for description.

in the case of the DCT), so it is possible to obtain a representation:

$$c_i = \sum_{j=1}^{n} \psi_{i,j} x_j, \tag{7.1}$$

where $\psi_{i,j}$ is the j'th element of the row vector $\boldsymbol{\psi}_i$. The set of basis functions is chosen such that only a small number (s in total) of the coefficients of $\mathbf{c}$ are non-zero. This expression can be written more compactly in matrix form as:

$$\mathbf{c} = \Psi \mathbf{x}, \tag{7.2}$$

where each $\boldsymbol{\psi}_i$ is a row of the matrix Ψ.

The representation of $\mathbf{x}$ in the basis Ψ is said to be sparse if $s \ll n$. In this case only s coefficients in the basis Ψ contain all the information about $\mathbf{x}$. If $\mathbf{x}$ can be well approximated by $s \ll n$ non-zero coefficients, $\mathbf{x}$ is said to be compressible in Ψ; here, there may be many small negligible coefficients in $\mathbf{c}$, which can be set to zero, and only s significant coefficients. A compressible representation of $\mathbf{x}$ in the basis Ψ captures only the most important information about $\mathbf{x}$ in s coefficients.

In the CS framework, these concepts of transform sparsity and compressibility are harnessed during the *initial* acquisition. The aim is to record a small number of well-chosen samples that suffice to capture the important information in the signal - just enough for the information content to be recovered. Put simply, the goal in CS is to record the signal directly in compressed form.

Rather than recording values of the signal of interest $\mathbf{x}$ directly, in a CS approach, the measurements are made against some test function or sensing waveform $\boldsymbol{\varphi}_i$, and should comprise a sampling of many of the elements of $\mathbf{x}$. The measurements that are acquired are not dependent on the information content of the signal, or in other words do not need to be adaptive. This form of acquisition is inherent in many standard procedures. For example, in a standard imaging process, where the measurements are the intensities at each pixel of the detector, the sensing waveforms are controlled by the manner in which the lens transfers the scene onto each pixel. In MRI, where the measured data are Fourier coefficients, the sensing waveforms are sinusoids. In a tomographic experiment, the measurements are line integrals, and the sensing waveforms are the projected lines through the sample. Mathematically, m correlations are measured between

the signal of interest $\mathbf{x}$ and sensing waveforms $\boldsymbol{\varphi}_i$ from another basis:

$$b_i = \sum_{j=1}^{n} \varphi_{i,j} x_j, \qquad \text{for } i = 1, ..., m, \tag{7.3}$$

which can be abbreviated as:

$$\mathbf{b} = \Phi \mathbf{x}, \tag{7.4}$$

where each $\boldsymbol{\varphi}_i$ represents a row of Φ. Incorporating the sparse basis Ψ, Equation 7.4 can be re-written as:

$$\mathbf{b} = \Phi \mathbf{x} = \Phi \Psi^* \mathbf{c} = \Theta \mathbf{c}, \tag{7.5}$$

where Ψ^* is the inverse transform converting from the sparse basis to the native domain of the signal and in most cases is equal to the transpose of Ψ (which is assumed here), and Θ is also an $m \times n$ matrix.

In many practical applications it is commonly the case that $m \ll n$, that is, there are far fewer equations than unknowns, and the system of equations is underdetermined, implying there are an infinite number of solutions consistent with the measured data. CS theory, however, asserts that $\mathbf{x}$ may be recoverable in the underdetermined case, subject to the prerequisites that (i) $\mathbf{x}$ can be represented sparsely in the basis Ψ, and (ii) Φ and Ψ are incoherent.

Incoherence expresses the level of dissimilarity between two bases, and hence the key requirement in CS is that the sensing basis is not easily represented in the sparse basis. Formally, the mutual coherence, μ, between a sensing basis, Φ, and the representation basis, Ψ, is given by:

$$\mu(\Psi, \Phi) = \sqrt{n} \cdot \max_{1 \leq i,j \leq n} \left| \langle \boldsymbol{\psi}_i, \boldsymbol{\varphi}_j \rangle \right|, \tag{7.6}$$

where $\boldsymbol{\psi}_i$ is the i'th row of Ψ and $\boldsymbol{\varphi}_j$ is the j'th row of Φ, and if Ψ and Φ are orthonormal bases $\mu(\Psi, \Phi) \in [1, \sqrt{n}]$.

The Dirac $\psi_{i,t} = \delta(t - i)$ and Fourier $\varphi_{j,t} = n^{-1/2} e^{2\pi i j t/n}$ bases, for example, are in this regard maximally incoherent ($\mu = 1$), since many delta functions are required to represent a sinusoid and vice versa; the Fourier basis should therefore also be largely incoherent with any representation basis that has localised support. This incoherence ensures that each measurement b_i provides information about many of the coefficients of the signal $\mathbf{x}$. It also ensures that in each measurement the encoding of the coefficients of $\mathbf{x}$ is different.

An alternative approach to interpreting the incoherence requirement is to

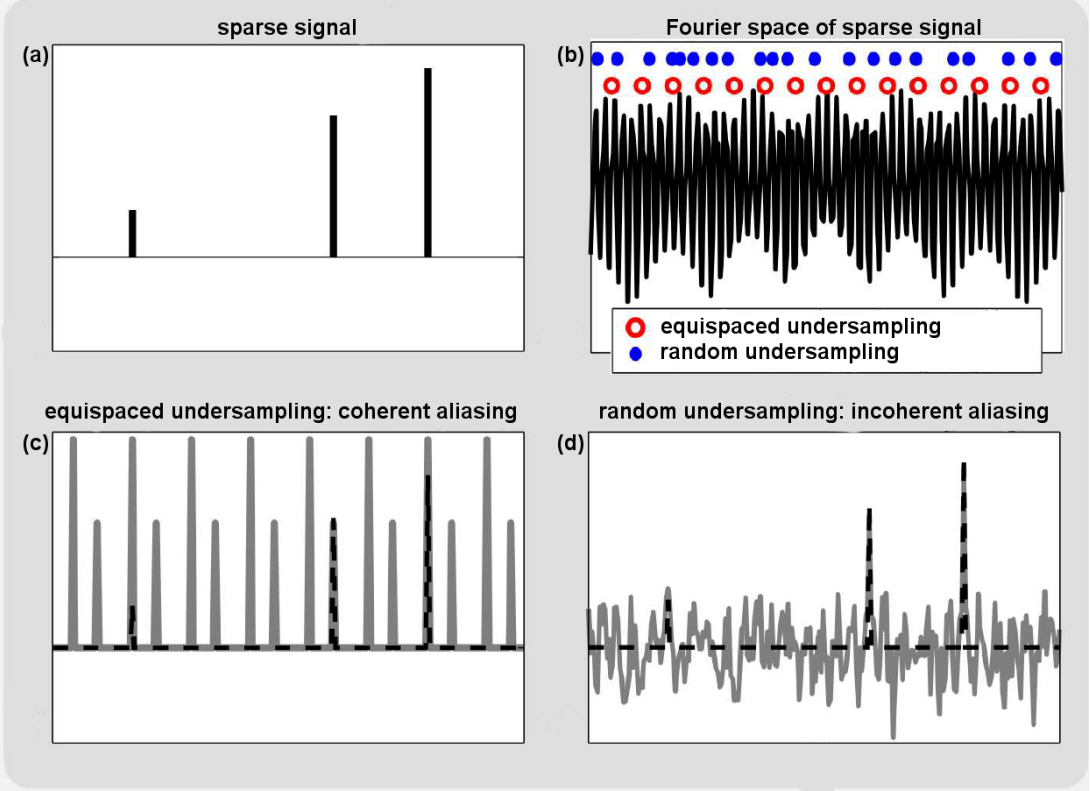

FIGURE 7.4: Illustration of sparse signal recovery from undersampled data in terms of incoherent interference of undersampling artefacts. A sparse signal (a) is eight-fold undersampled in the Fourier domain (b). Equispaced undersampling results in coherent aliasing (c), preventing recovery. With pseudo-random undersampling on the other hand, the undersampling artefacts spread throughout the sparse domain and interfere incoherently, resulting in a noise-like background (d). The true signal coefficients then stand out above the noise-like interferences, allowing them to be recovered by a non-linear sparsity promoting optimisation process. Re-drawn in part from [360].

consider the manner in which the artefacts arising from undersampling become manifest [360, 364]. In an incoherent sampling regime, the undersampling artefacts spread throughout the sparse domain such that they add as noise-like interference. This results in the significant coefficients standing out above the interferences, enabling them to be recovered by a non-linear optimisation process. A simple, intuitive illustration of this principle is given in Figure 7.4 [360, 364].

The mutual coherence also defines the number of measurements that are required to reconstruct a signal. Since it is mathematically easier to analyse and ensures very high incoherence, randomised sampling has played a prominent role in the development of CS. For random undersampling (i.e., where the small number of measurements that are acquired are chosen at random from the possible set), CS theory shows that m measurements are required to recover

an s-sparse signal of length n, where m is defined by [365]:

$$m \geq C \cdot \mu^2(\Phi, \Psi) \cdot s \cdot \log n, \tag{7.7}$$

where C is some small positive constant.

Equation 7.7 shows that the number of measurements required to reconstruct the signal in CS is determined primarily by the information content of the signal, that is the number of non-zeros in the sparse domain, rather than the size of the domain in which the signal resides.

While sparse signals play an important role in the theoretical aspects of CS, consideration of signals that are compressible is often more pertinent to its practical application; most signals in empirical contexts are compressible in some basis, rather than strictly sparse. Importantly, CS theory also applies to compressible signals, asserting that it is possible to recover an s-sparse approximation of $\mathbf{x}$ in a chosen basis. In this case, the accuracy of the recovery is bounded by the error involved in the sparse approximation. This more relaxed framework makes CS a widely applicable technique. Additionally, by controlling the nature of the information that is captured in a compressive representation, through the particular choice of Ψ, it is possible to effect recovery of the signal at a desired level of complexity. With a slight abuse of the terminology, from herein both sparse and compressible signals are referred to as sparse, unless a distinction between the two is important.

Whereas in the context of image compression the sparse coefficients are known, and the image can be retrieved simply by applying the inverse transform, in CS, an optimisation process must be employed to recover the sparse coefficients from the measurements. This can be accomplished using a non-linear algorithm that promotes sparsity by minimising the number of non-zero coefficients in the sparse domain, whilst also ensuring consistency with the measured data.

Since directly minimising the number of non-zeros in the sparse domain is intractable for most real problems, a key part of CS theory has been to show that the minimisation can instead be performed over the sum of the absolute values, known as the ℓ_1-norm, $\|\mathbf{c}\|_{\ell_1} := \sum_i |c_i|$. As outlined in [360], the more established approach of using the ℓ_2-norm ($\|\mathbf{c}\|_{\ell_2} := (\sum_i |c_i|^2)^{1/2}$) as the regularising term (as in Tikhonov regularisation) is inappropriate in this case, because the ℓ_2-norm penalises large coefficients, resulting in globally smooth solutions with many small coefficients. Conversely, CS theory shows that in many scenarios ℓ_1-norm minimisation yields sparse solutions; in this case many small coefficients carry a greater penalty than a few larger coefficients, and the

important larger coefficients carrying information about the signal in the sparse domain are therefore preserved, while the smaller coefficients are suppressed.

The minimum ℓ_1-norm reconstruction can be obtained by solving the convex optimisation:

$$\text{minimise } \|\Psi\hat{\mathbf{x}}\|_{\ell_1} \quad \text{subject to} \quad \Phi\hat{\mathbf{x}} = \mathbf{b}, \tag{7.8}$$

where $\hat{\mathbf{x}}$ is the reconstruction of the true signal $\mathbf{x}$ from the measured data $\mathbf{b}$. Equation 7.8 is often known as basis pursuit [366]. In words, Equation 7.8 seeks the sparsest signal in the transform domain that is consistent with the measured data. For the case of noise corrupted measurements, a tolerance on the data fidelity term can be introduced:

$$\text{minimise } \|\Psi\hat{\mathbf{x}}\|_{\ell_1} \quad \text{subject to} \quad \|\Phi\hat{\mathbf{x}} - \mathbf{b}\|_{\ell_2} \leq \varepsilon \tag{7.9}$$

where ε controls the allowed level of discrepancy to the measured data, and typically characterises the standard deviation of the noise in the data. Another popular formulation is:

$$\hat{\mathbf{x}}_\lambda = \arg\min_{\hat{\mathbf{x}}} \{\|\Phi\hat{\mathbf{x}} - \mathbf{b}\|_{\ell_2}^2 + \lambda \|\Psi\hat{\mathbf{x}}\|_{\ell_1}\}, \tag{7.10}$$

where λ is a weighting parameter that determines the relative importance of transform domain sparsity and data fidelity in the reconstruction. Standard optimization theory [367] asserts there exist values of ε and λ such that the solutions to Equations 7.9 and 7.10 coincide and the problems are in some sense equivalent; although, except for special cases, the particular values of λ can be hard to compute a priori [368, 369].

A large number of powerful algorithms have been developed to solve the above ℓ_1-norm minimisation problems. In addition, there are also other efficacious methods for seeking sparse solutions that can be employed in CS, such as non-convex minimisation and greedy algorithms. An accessible review of the various computational procedures is given in ref. [370].

Finally, the reader is referred to several other concise summaries of the key aspects of CS [360, 364, 371–375], as well as more comprehensive foundational coverage in [376, 377]. A regularly maintained source of CS resources can also be found at: http://dsp.rice.edu/cs.

7.3 Compressed sensing electron tomography

7.3.1 CS-ET reconstruction

Following the discussion of the Radon transform and the Fourier slice theorem in chapter 5 (section 5.2.2), the system of discrete linear equations $\mathbf{b} = \Phi\mathbf{x}$ addressed in CS is applicable in the context of ET from two perspectives. On the one hand, the sensing matrix Φ can be regarded as a real space projection operator, corresponding in the reconstruction process to a discretised variant of the Radon transform, and the data vector $\mathbf{b}$ as the direct projection images, i.e. a discretised sinogram [211, 378]. As an alternative, the Fourier slice theorem can be exploited, which, to reiterate, permits the Fourier transform of the projection data to be considered as discrete radial samples of the object in the Fourier domain. In this case, the sensing matrix Φ can effectively be regarded as an undersampled discrete Fourier operator [210].

A current challenge in bridging CS theory and practice is that performance-characterising parameters can be difficult to evaluate for many real (structured) sensing matrices. To facilitate mathematical proofs, CS performance guarantees have mostly been based around random sampling. Mathematical characterisation of the CS properties of more structured sampling regimes, which are often imposed by acquisition hardware, is less developed [379]. While the strongest performance guarantees can be provided by the so-called restricted isometry property (RIP), at the present time, RIP analysis of the Radon transform is quite limited [380].

However, it is possible to draw on the findings from the more practical analysis of Lustig et al. in the context of CS-MRI [360, 364]. They used a point spread function or transform point spread function based analysis as a means to characterise the incoherence of undersampling artefacts in different (semi) structured sampling schemes, showing that radial undersampling of Fourier space should result in sufficiently incoherent artefacts to be able to use CS (Figure 7.5). This notion is furthered by recovery results in the theoretical CS literature, including those of Candès et al. [17], where exact recovery of the well-known Shepp-Logan phantom was achieved from 22 radial samples of its discrete Fourier transform. More recent mathematical treatment of sampling regimes in CS can be found in the work of Hansen and co-workers [381]. Empirical findings reported in the literature (although primarily focusing on randomised sampling of Fourier space), have suggested that in practice, the number of Fourier measurements required for a good CS reconstruction should be roughly two to five times the

number of sparse coefficients [360, and references therein]. These results intimate that it is possible to apply CS to ET, although it is prudent to note that recovery expectations from experimental ET data should be to some extent more conservative; a primary reason being the missing wedge of entirely un-sampled information, due to the limited tilt range in ET.

It should also be noted that some studies implementing sparse or ℓ_1-type minimisation during tomographic reconstruction (especially many using TV-minimisation) do not invoke or mention explicitly the CS context and the incoherent (compressive) sampling justified above. Instead they refer more to the regularisation process. Sparse minimisation and the power offered by efficacious sparsifying transforms may indeed often yield high-quality results in general. However, specifically harnessing incoherence and the CS framework would be expected to enhance recovery.

7.3.2 Sparse representation in ET

The various imaging modes available in TEM make ET amenable to capturing a range of different morphologies, resulting in differing image content. This makes consideration of appropriate sparsifying transforms an important aspect in CS-ET. Owing to the now extensive use of sparse image representation, such as in image compression, many effective transforms have been developed [382]. The most important of these for CS-ET are outlined here. CS-ET studies using these transforms are presented or discussed in chapter 8.

Given that many nanoscale objects are restricted in one-, two- or possibly three-dimensions, many TEM images and ET reconstructions may be sparse in the image domain itself. In this case, the sparsifying transform Ψ can be considered as the identity transform. As established in chapter 5, it is well known that the finite and limited angular sampling in ET can lead to prominent aliasing or 'streaking' artefacts in the reconstructions, and blurring of the object boundaries, especially in the missing wedge direction. It is shown in chapter 8 that imposing sparsity in the image domain can provide an effective means for reducing these artefacts. In addition, image domain sparsity can be pertinent to atomic-scale ET reconstruction, if it is considered that each atomic potential is sufficiently localised in space that an atomic-scale ET reconstruction should be inherently sparse [259].

A practical consideration is that for most imaging modes used in ET there is a non-zero background signal in the image, in which case the image is not actually sparse. If object sparsity in the image domain is important, it is necessary to

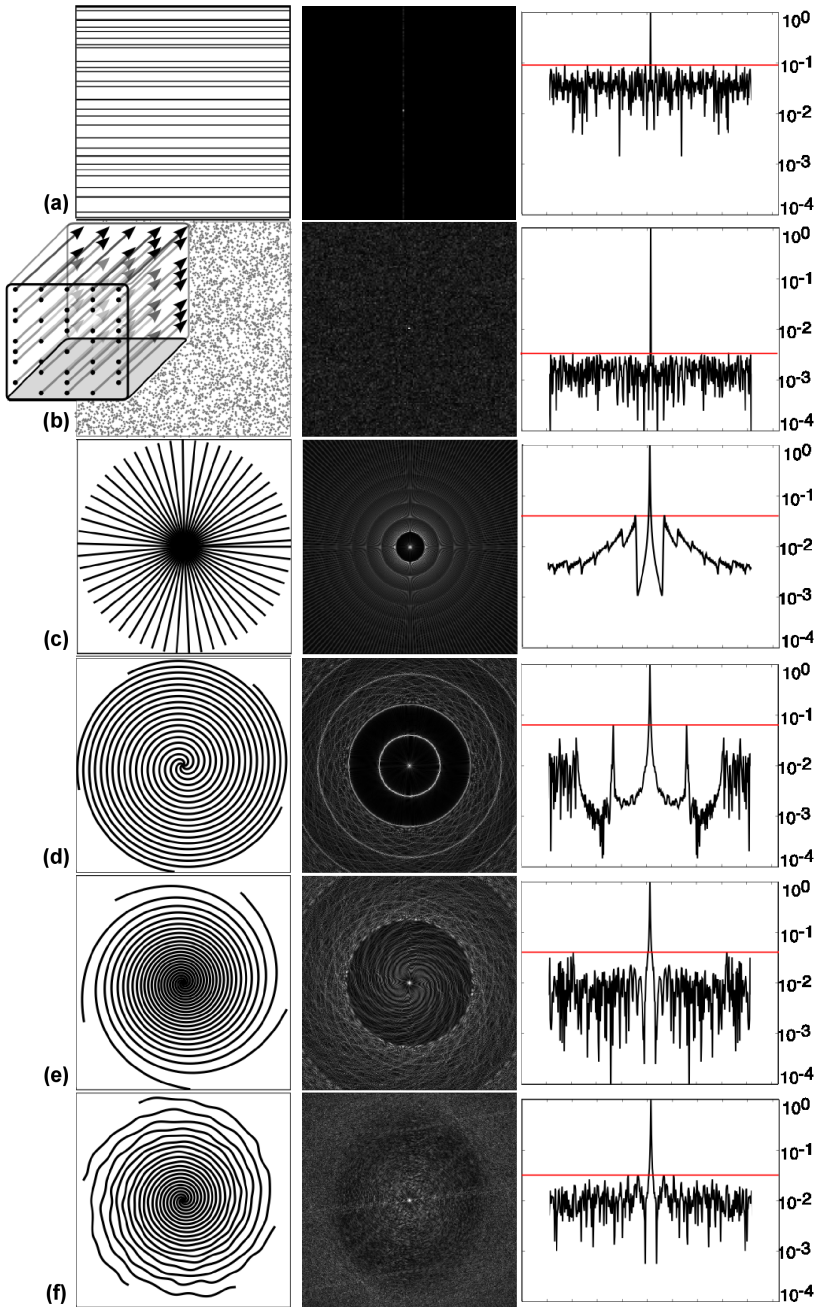

FIGURE 7.5: Point spread functions of various Fourier space sampling regimes. (a) Random lines, (b) random points, (c) radial lines, (d) uniform spirals, (e) variable density spirals and (f) variable density perturbed spirals. Reproduced from [360].

exclude the background during the sparsity promoting reconstruction process so that the image is, or is treated as if it were, sparse. Possible methods for achieving this are given in section 8.2.1. Where the object of interest occupies a large portion of the field of view, or for example if there is a non-uniform background in the projections that is not easily excluded, an image domain sparsity constraint becomes less applicable, and the effective use of other sparsifying transforms takes on increased importance.

A popular sparsifying transform for CS image reconstruction is spatial finite-differences (cf. Figure 7.1). Finite differences sparsity, evaluated as the ℓ_1-norm of the spatial gradients of the image, is often referred to as the 'total variation' (TV)-norm [383]. TV-minimisation entails imposing a constraint on the number of discontinuities in the image and the homogeneity of objects. As an ℓ_1-norm, the TV-norm penalises many small variations in the image intensity, but permits a limited (i.e. sparsely distributed) amount of large gradients. TV-minimisation is therefore suitable for many images that consist of homogeneous regions with sharp boundaries, often referred to as being 'piecewise constant'. A TV constraint would be suitable for ET reconstructions of many specimens in the physical sciences that consist of a small number of homogeneous phases, such as many nanoparticle systems. Even if ET reconstructions of many real systems should often, strictly, not be perfectly piecewise constant, a piecewise constant approximation may still be able to convey the important information, such as the boundaries between different regions (a similar argument was applied to medical images in [360]).

Wavelets are localised functions whose particular form is chosen to satisfy certain desirable properties [384]. In essence, a wavelet basis is derived from a 'mother' wavelet (Figure 7.6), which is dilated and translated. As such wavelets provide a variable time-frequency resolution, and DWTs can focus on localised image structures with a zooming procedure that enables a so-called multiresolution or multiscale analysis [384]. Wavelet coefficients at different scales capture both spatial position and spatial frequency information. Wavelets can therefore very effectively represent smooth and piecewise smooth signal content, including non-periodic point singularities such as jumps and spikes (cf. Figure 7.2). A number of empirical studies, including wavelet-based denoising of biological ET reconstructions [385] and SPM projection images [386], projection image orientation determination in SPM [387] and, more recently, CS-based application to SPM 3D reconstruction [362] have demonstrated the suitability of DWTs for sparsely representing ET data.

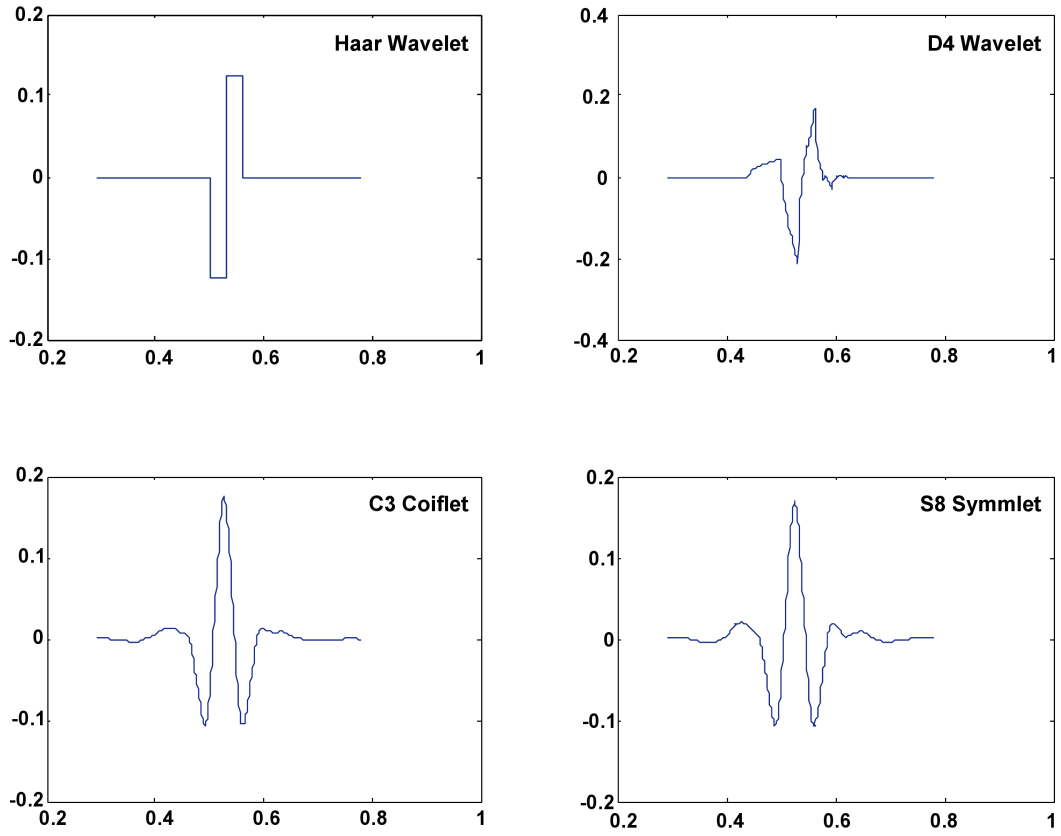

FIGURE 7.6: Examples of well-known mother wavelets. Dilations and translations of these localised waveforms are used to form the respective wavelet bases. (Produced using Wavelab [390]).

Finally, sparse representation of an image containing periodic features (such as a crystal lattice) can be achieved readily using a discrete Fourier transform - yielding a well-known spot diffraction pattern. Many real ordered structures contain defects or are of finite extent, meaning that they possess only short-range order. This will decrease the sparsity of a Fourier representation. However, such structures will still be represented reasonably sparsely in the Fourier domain, because the underlying crystal structure is captured extremely sparsely [388]. Alternatively, the DCT is a variant of the discrete Fourier transform that replaces the complex analysis with real numbers via a symmetric signal extension. Typically, the DCT is applied locally, and has been used to provide sparse representation of locally oscillating textures in natural images [389]. Since the Fourier and DCT domains are not incoherent with the domain in which the signal is acquired in ET (the Radon/sinogram or Fourier domain) it is not expected that these transforms would be suitable for ET reconstruction itself, but they may be exploited in other aspects of pre-/post-processing in ET.

7.4 Discussion

CS has firm mathematical foundations and can provide strong performance guarantees for the recovery of sparse signals in certain contexts, mostly involving randomised sampling. Although this chapter has outlined how it is possible to apply CS to ET, and CS is increasingly being harnessed in other practical applications, the theoretical basis for performance expectations in practical scenarios is much more limited [379]. However, as the interest in CS continues to grow significant progress is being made in this regard [381]. Given the complexity, diversity and challenging nature of ET reconstruction compared to many other problems addressed in the mathematical and signal processing literature, it is likely that a combination of theoretical development and rigorous empirical exploration of CS-ET approaches will be most profitable in identifying the scenarios in, and methods by which, the powerful mathematics can most successfully be applied to experimental ET data.

Also concerning real signals in ET, this chapter has outlined key established sparsifying transforms applicable to ET data. Naturally, as detailed in chapter 8, these have been the first to be explored in CS-ET. However, there are further sophisticated transforms that may provide improved performance, such as 'curvelet', 'contourlet' or 'shearlet' transforms [382, and references therein]. The efficacy of these transforms with respect to ET should be explored in future work, particularly for targeting specific structures in ET reconstructions. Another promising approach is 'dictionary learning', in which the sparse basis is learned empirically [318, 391].

The development of CS recovery algorithms is an active area of research [368, 370, 376, 377, and references therein] and many algorithms are applicable to CS-ET. In particular, there is strong interest in the development of robust algorithms that permit unambiguous determination of regularisation parameters, and exploitation of these will be key in further ensuring the reliability of CS-ET reconstruction. Especially worthy of note are algorithms that aim to robustly solve the constrained optimisation of Equation 7.9, since the ε parameter is in many ways more natural to determine than the λ parameter in Equation 7.10. Alternatively, algorithms that intrinsically seek an optimal ε or λ are particularly attractive - see e.g. [392] for recent promising results applied to X-ray CT - although it is important to note that these too may involve other parameters that need to be wisely chosen, and which may similarly be challenging to select in a fully automated manner. Another potentially beneficial direction for the progression of CS-ET may be to more explicitly address the noise present in

ET projections, for example, by considering CS algorithms that treat Poisson counting statistics [393, 394].

7.5 Conclusions

This chapter has set out the foundations of CS theory and how ET can be pursued within the CS framework. It has introduced mathematical concepts in an accessible manner, covering those most relevant to putting CS-ET into practice. Distilling the salient aspects of the mathematical theory in this manner is important if CS and CS-ET are to be widely adopted by practising communities. Having established the principles, the subject of the next chapter is to explore the practical implementation.

Chapter 8

Compressed sensing electron tomography: applications

The efficacy of a compressed sensing (CS) approach to electron tomography (ET) reconstruction is demonstrated in this chapter, which contains a number of example studies. These comprise both simulated and experimental data. Artefacts present in conventional reconstructions such as streaking, blurring of object boundaries and elongation are markedly reduced, and robust reconstruction is shown to be possible from far fewer projections than are normally used. The CS-ET approach enables more reliable quantitative analysis of the reconstructions as well as novel 3D studies from extremely limited data, including the first 3D imaging of localised surface plasmon resonances. Practical implementation, challenges and key areas for future development are discussed. The results shown in this chapter have been published in [210, 292, 293].

8.1 Proof-of-principle study

Firm proof-of-principle demonstrations of CS-ET were provided by Saghi et al. [210] and Goris et al. [211] in late 2011. The former was carried out as part of this thesis, and involved an ADF-STEM tilt-series of iron oxide nanoparticles possessing a concave surface (Figure 8.1a). The essential details of the study are summarised below, where perhaps the most striking aspect is that the CS-ET reconstruction is robust using just 9 projections - approximately a factor of 10 fewer than usually acquired in ET.

The iron oxide nanoparticles were expected to have homogeneous composition and sharp boundaries, therefore for the CS-ET reconstruction sparsity was enforced in the gradient domain. Additionally, sparsity was enforced in the

image domain, which, as mentioned in section 7.3, can assist greatly in reducing missing wedge and streaking artefacts. Figures 8.1b,c and 8.2 summarise the key aspects of the experimental results [210].[1]

Although relatively little qualitative difference can be seen in the voxel projection visualisations of the conventional SIRT reconstruction and the CS-ET reconstruction (Figures 8.1b and c), the higher fidelity of the CS-ET reconstruction is readily appreciated when viewing orthoslices through the reconstructions in the missing wedge direction (Figures 8.1bi and ci). Blurring of the nanoparticle boundaries and streaking artefacts prevalent in the SIRT reconstruction (bi) are visibly reduced in the CS-ET reconstruction (ci). Similar observations were made for reconstructions from simulated projections of a phantom mimicking the nanoparticles [210].

The real efficacy of CS-ET was revealed when seeking to analyse the reconstructions quantitatively, and further so when reducing the number of projections used for reconstruction. The volume of the concave region of the nanoparticle was used as a morphological feature by which to assess quantitatively the fidelity of the reconstructions,[2] and the quantitative study was repeated for reconstructions obtained using the full 27 projection tilt-series (acquired over the angular range -70° to +60° with a 5° tilt increment), as well as for reconstructions obtained using 13 and 9 projection subsets.

Specifically, the concavity volume of a selected nanoparticle (arrowed in Figure 8.2b) was determined using an image processing based segmentation routine. As a pre-processing step for the SIRT reconstructions, it was necessary to apply an unsharp masking operation to enhance the edges of the nanoparticle. The segmented nanoparticle was then obtained by Otsu thresholding followed by binarisation, and the concavity volume obtained by subtracting the segmented nanoparticle from its convex hull.

Figure 8.2b shows that the volume of the concavity measured from the SIRT reconstruction is lower than that from CS-ET, and decreases substantially as the number of projections used for reconstruction is reduced. These

[1]The iron oxide nanoparticle sample as well as the iron oxide nanoparticles intermixed with cadmium selenide/telluride tetrapods studied in section 8.3.2 were provided by Dr Chandramohan George, Dr Giovanni Bertoni, Professor Adrea Falqui and Professor Liberato Manna (Italian Institute of Technology (IIT), via Morego 30, IT-16163 Genoa, Italy). The ADF-STEM tilt-series of the iron oxide nanoparticles was acquired by Dr Zineb Saghi. CS-ET reconstructions (in this study) were performed by Dr Daniel Holland (Department of Chemical Engineering and Biotechnology, University of Cambridge).

[2]The concavity volume can be critical to their intended applications in drug delivery, catalysis and to effect destabilisation of gold nanoparticles that fit exactly inside the concavity [395].

observations correlate with the poor definition of the nanoparticle boundaries (cf. Figures 8.1bi), and the progressive loss of reconstruction fidelity visible in the isosurface renderings (Figure 8.2a). Conversely, it can be seen from Figures 8.2a and b that the reconstructed morphology and concavity volume measured from the CS-ET reconstruction is remarkably consistent, even when using just 9 projections for reconstruction.

Following this proof-of-principle study, it was felt that two aspects should be addressed to advance CS-ET. The first was to disseminate in greater detail the principles of CS-ET. These aspects were presented in chapter 7 and published as Leary et al. [292]. The second was to explore the application of CS-ET to a range of different specimens. A collection of case studies, published in the same paper, form the bulk of this chapter.

Specifically, in the remainder of this chapter, recounting the results in [292], the CS-ET approach is tested on three very different sets of simulated and experimental ET projection data. The reconstructions are compared qualitatively and quantitatively to those obtained using the established reconstruction algorithm in ET, namely SIRT.

In the first case study, ET reconstruction of concave iron oxide nanoparticles intermixed with cadmium selenide/telluride tetrapods from an ADF-STEM tilt-series is considered, and it is found that with CS-ET it is possible to reconstruct more faithfully the complex morphology and multiple grey levels in the tomogram. The CS-ET reconstruction is found to be robust even when the number of projections used for reconstruction is substantially reduced.

Secondly, CS-ET is used to achieve high quality, more readily segmented reconstructions of densely-packed nanoparticles, which facilitates more accurate quantitative nano-metrological analysis. The experimental data comprised another ADF-STEM tilt-series of the unsupported Ga-Pd nanocatalysts studied in chapters 3, 4 and 6.

In the third case study, it is shown that CS-ET can be applied to signals of very different character to those of the previous examples, entailing the reconstruction of smoothly varying objects. A systematic study is presented, involving ET reconstruction of a smooth phantom from different numbers and angular ranges of tilt-series images.

Additionally, this chapter concludes by describing application of the ability, with CS-ET, to reconstruct smoothly varying signals from very few projections, to enable the first 3D imaging of the localised surface plasmon resonances of a silver nanocube, which has been published as Nicoletti et al. [293].

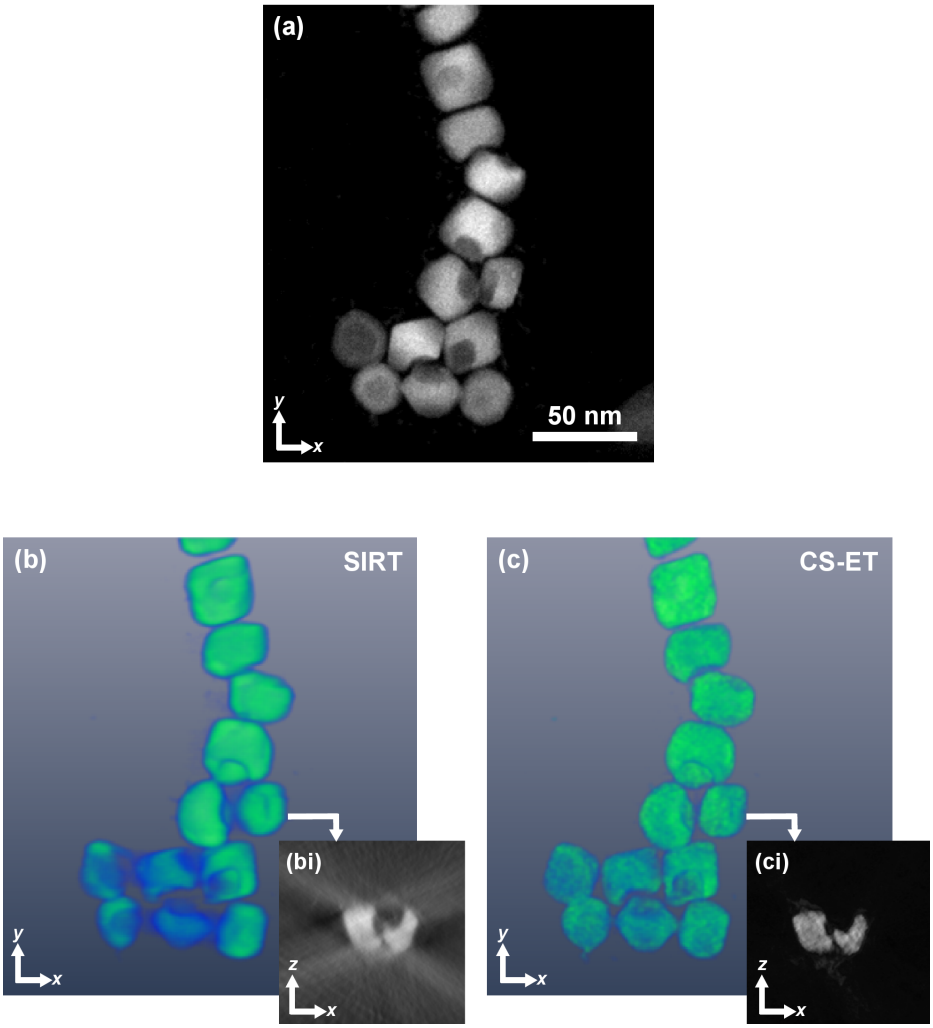

FIGURE 8.1: (a) ADF-STEM image of concave iron oxide nanoparticles from an ET tilt-series. (b, c) 3D voxel projection visualisations of SIRT and CS-ET reconstructions from the tilt-series. The insets (bi, ci) showing two closely spaced nanoparticles are 2D orthoslices taken from the positions indicated by the arrows, in the x-z plane of the 3D reconstructions (where the z-direction is the missing wedge direction and the x-direction is perpendicular to the tilt axis). For objective comparison, each orthoslice is shown with linear mapping between their respective minimum and maximum pixel values.

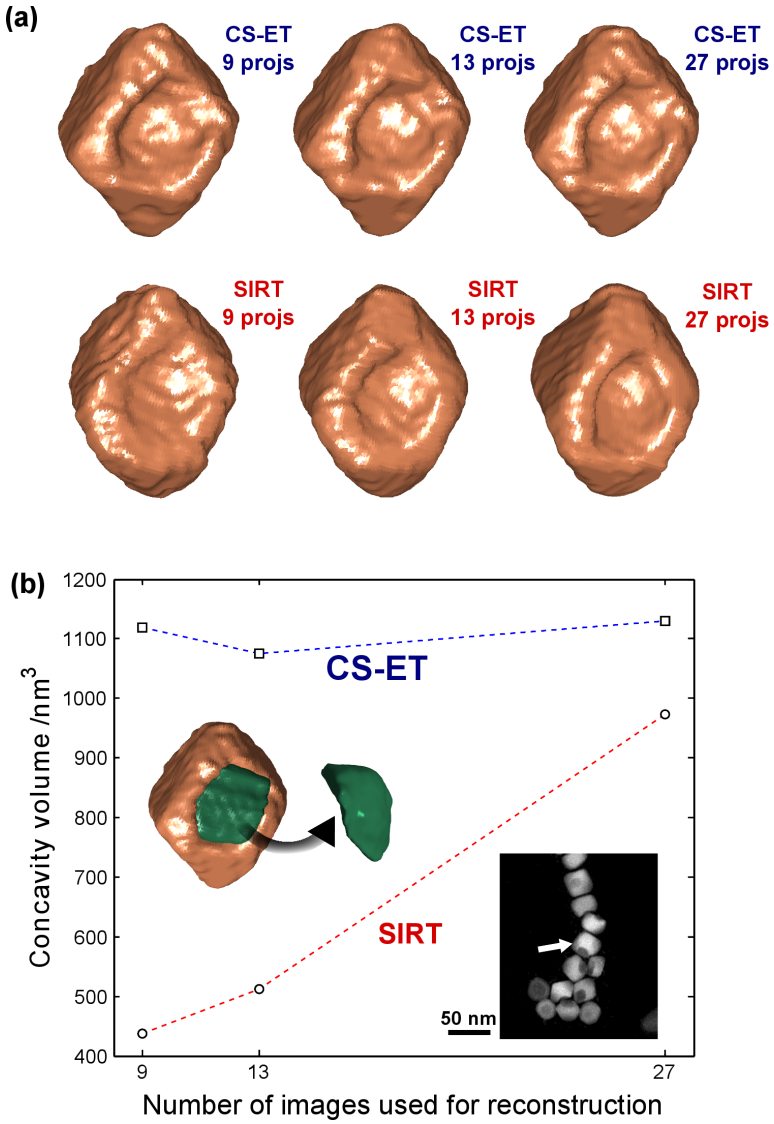

FIGURE 8.2: Surface rendered visualisation of CS-ET and SIRT reconstructions from the ET tilt-series of Figure 8.1a, using the full 27 projection tilt-series, or 13 or 9 projection subsets. (b) Quantification of the concavity volume of the reconstructions. The nanoparticle analysed is indicated by the arrow in the ADF-STEM image inset in (b).

8.2 Methods

8.2.1 CS-ET reconstruction

The practical implementation of CS-ET developed in this work was derived from methods used in CS-MRI. As the data directly acquired in MRI are Fourier coefficients, a Fourier based approach to CS-ET reconstruction was followed. The radial Fourier data obtained in ET is, via the Fourier slice theorem, analogous in many ways to reconstruction of data acquired on radial trajectories in MRI.

The CS-ET reconstruction employed here is implemented in MATLAB (MathWorks, Natick, MA). It was developed by adapting procedures devised for CS-MRI by Lustig and co-workers [360], which are provided in MATLAB code as the SparseMRI package.[3] Their CS-MRI and the CS-ET reconstruction also call upon MATLAB code developed by Fessler and co-workers (Image Reconstruction Toolbox)[4], which stems from the context of X-ray tomography [396, 397]. Primarily, these packages are used to implement the conjugate gradient descent and non-uniform fast Fourier transform (*NUFFT*), respectively (both described below). The WaveLab software package for MATLAB [390][5] may be called upon to implement wavelet transforms when these are used as the sparsifying transform. The programming framework provided by SparseMRI was used to interface to operators in the Image Reconstruction Toolbox and WaveLab.

As noted in section 5.2.2, for the common single axis ET geometry, reconstruction of a 3D tomogram can proceed either via a series of, in principle, independent reconstructions of 2D slices, or as a single 3D volume; the latter being more computationally demanding. The reconstructions shown in sections 8.3.2-8.3.4 were performed in 2D, while that in section 8.4 was performed in 3D.

Specifically, in the Fourier based approach, the projection images are first Fourier transformed to obtain radial samples of the object in the Fourier domain. This corresponds to a 1D Fourier transform of each projection image row in the case of reconstruction by 2D slices, or a 2D Fourier transform of each projection in the case of fully 3D reconstruction. This Fourier transform was performed using the `fft` function in MATLAB. The radial Fourier data (constituting the data vector $\mathbf{b}$, as set out in the context of ET in sections 5.2 and 5.3.4, CS in section 7.2 and CS-ET in section 7.3) is then Fourier transformed in 2D or 3D,

[3] Available at: http://www.stanford.edu/∼mlustig/SparseMRI.html
[4] Available at: http://web.eecs.umich.edu/∼fessler/code/
[5] Available at: http://statweb.stanford.edu/ wavelab/

respectively, into the image domain using the *NUFFT* developed by Fessler and Sutton [396] (the *NUFFT* constitutes the tomographic projection operator or sensing basis Φ described in sections 5.2, 5.3.4, 7.2 and 7.3). The interpolation error of the *NUFFT* is optimised in the min-max sense, making its application in iterative tomographic reconstruction competitive with real space-based forward-/back-projectors [397].[6]

In conjunction with the *NUFFT*, for the sparsity-seeking optimisation process the conjugate gradient descent algorithm of Lustig et al. [360] was used to solve Equation 7.10. Hence the reconstruction proceeds in an iterative manner akin to the AIR methods described in section 5.3.4, using the *NUFFT* as the tomographic forward-/back-projector to enable comparison of the current reconstruction to the original projection data $\mathbf{b}$, with update of the reconstruction based on the difference. Additionally, sparsity of the reconstruction is promoted using the sparsifying transform Ψ and evaluation the ℓ_1-norm of the reconstruction in the sparse domain. The relative importance of these two updates is dictated by the weighting parameter λ. The conjugate gradient descent algorithm used is well-described by Lustig et al. [360], to which the interested reader is referred, and it should also be born in mind that a number of different CS recovery algorithms could be used, as discussed in chapter 7. Further description of the iterative CS-ET reconstruction process, with specific visual overview of the components in Equation 7.10 (or Equation 8.1 below), is given in section 8.3.1 and Figure 8.3.

For application to conventional ET datasets, where the aim is to reconstruct the 3D density of the sample and the sample is expected to be approximately piecewise constant, it has been found in this work, as in ref. [210], that simultaneous enforcement of sparsity in both the image and gradient domains yields the highest fidelity reconstructions. In this case, with Ψ as the identity transform (I), Equation 7.10 can be written as:

$$\hat{\mathbf{x}}_{\lambda_I,\lambda_{TV}} = \arg\min_{\hat{\mathbf{x}}} \{\|\Phi\hat{\mathbf{x}} - \mathbf{b}\|_{\ell_2}^2 + \lambda_I \|\Psi\hat{\mathbf{x}}\|_{\ell_1} + \lambda_{TV} TV(\hat{\mathbf{x}})\}, \tag{8.1}$$

requiring a choice of λ_I and λ_{TV} to determine the weightings of image and gradient domain sparsity, respectively. Similarly, other combinations of transforms can be used for reconstructions involving different morphologies. For clarity regarding the transform domain weightings employed here, λ_I is used to denote the weighting when Ψ is the identity transform, λ_{TV} to refer to a TV

[6]The 3D implementation of the *NUFFT* was developed by Dr Daniel Holland, adapted from the 2D approach of Fessler and Sutton [396].

weighting (Ψ = spatial finite differences) and λ_W to denote the weighting when Ψ is a wavelet transform. The spatial finite differences evaluation of the TV-norm used in this work may be written as:

$$\|\hat{\mathbf{x}}\|_{TV} = TV(\hat{\mathbf{x}}) = \sum_{i,j} |\hat{x}_{i+1,j} - \hat{x}_{i,j}| + |\hat{x}_{i,j+1} - \hat{x}_{i,j}|, \tag{8.2}$$

where the recovered signal $\hat{\mathbf{x}}$ (here constituting a slice of the tomogram in real space) is considered as a two-dimensional (2D) image with spatial coordinates $1 \leq i, j \leq \sqrt{n}$. This definition of the TV-norm is sometimes referred to as 'anisotropic total variation'.[7]

In practice the λ parameter(s) often need to be determined empirically. One method to approach this choice is to solve Equation 7.10 or 8.1 for a number of different λ, and to plot the resulting final data fidelity term against the regularisation term(s). In the case of ℓ_2-regularised solutions this is known to yield an 'L-shaped' curve, where the sharp corner of the curve represents the λ that provides the best trade-off between data fidelity and regularisation [398]. For ℓ_1-regularised solutions such a plot is known as a 'Pareto curve', and is also insightful regarding the data fidelity/regularisation trade-off, although may be challenging to determine and interpret in practice [369]. Such an approach was followed for Equations 7.10 and 8.1, but in general smooth curves were obtained, and it was observed that the most satisfactory reconstructions were obtained at sparsity weightings significantly higher than those near the corner of the curve. This implies promoting sparsity over data fidelity beyond the noise level, and may be related to the need to suppress the significant undersampling artefacts arising from the missing wedge, as well as artefacts caused by other inconsistencies such as projection data misalignment. The λ parameter(s) for the experimental reconstructions were therefore chosen by visually inspecting trial reconstructions on selected slices as well as via simulation studies, and the λ value(s) chosen such that reconstruction artefacts were suppressed with minimal loss of genuine signal.

When image domain sparsity is important, it was found that correcting the non-zero background of the projections, caused by the offset of the ADF detector, can substantially improve the quality of the reconstructions. Bringing the average background intensity in the projections to a nominal value at, or close, to zero allows the image domain in the reconstruction to be made sparse. In practice, the

[7] Another definition often used is the so-called 'isotropic' (direction invariant) TV-norm, defined as: $\|\hat{\mathbf{x}}\|_{TV} = TV(\hat{\mathbf{x}}) = \sum_{i,j} \sqrt{|\hat{x}_{i+1,j} - \hat{x}_{i,j}|^2 + |\hat{x}_{i,j+1} - \hat{x}_{i,j}|^2}$.

background subtraction can be performed via a number of different methods; for example, by simply subtracting the minimum intensity reading in the tilt-series, or by fitting a background to each projection, such as fitting a polynomial to regions of relatively constant background, which is then subtracted. If the latter method is chosen, the background subtraction results in some small negative values in the projections, which could be set to zero. Different approaches have been trialled in this work, and the choice of method was not found to have a significant impact on the reconstructions. An alternative approach to dealing with the non-zero background may be to incorporate a background within the reconstruction model that allows it to be discounted during the sparsity promoting optimisation, as recently employed by Zhu et al. in CS-based stochastic optical reconstruction microscopy (STORM) [399].

For the experimental reconstructions shown here, 150 conjugate gradient iterations were used, with the algorithm being reinitialised every 50 iterations to alleviate possible stagnation at local minima.

8.2.2 SIRT and WBP reconstructions

SIRT reconstructions were implemented via the Tomo3D software package [297]. All reconstructions used 30 iterations without positivity constraint. WBP reconstructions were also implemented in Tomo3D, using the default setting of a ramp filter together with a Hamming filter applied over the full frequency range.

8.2.3 Experimental tilt-series acquisition

ADF-STEM tomography of the iron oxide-cadmium selenide/telluride and Ga-Pd samples was performed on an FEI Tecnai F20 (S)TEM operated at 200 kV, using a Fischione 2020 Advanced Tomography Holder, a probe semi-convergence angle of 11 mrad and an ADF detector inner angle of 45 mrad.[8] Both samples were supported on standard holey carbon TEM grids. The tilt-series were acquired in a semi-automated manner using FEI Xplore3D. The series of projections were aligned by cross-correlation in FEI Inspect3D. The concave iron oxide nanoparticle and cadmium selenide/telluride tetrapod tilt-series was acquired over an angular range of -70° to +60° with a 5° tilt increment, and the Ga-Pd nanoparticle tilt-series over the same angular range with a 2° tilt increment. The size of the images in both tilt-series was 1024 × 1024 pixels. For reconstruction from the concave iron oxide nanoparticle and cadmium selenide/

[8]The Ga-Pd tilt-series was acquired by Dr Zineb Saghi.

telluride tetrapods tilt-series, only the central 512 pixel portion of the images around the tilt axis, containing signal from the nanoparticles and tetrapods, was used. The Ga-Pd tilt-series images were re-binned to 512 × 512 pixels prior to reconstruction.

8.2.4 Simulation studies

Synthetic projections of test phantoms were generated at the same angles as the experimental tilt-series. This was performed using the discrete Radon transform provided in MATLAB, so as to use a different system matrix to create the projections to those used in the reconstruction algorithms. This sufficiently avoided committing the so-called 'inverse crime' [400], wherein the same model or discretisation is used to create a test problem and to solve it. An inverse crime may result in unrealistically optimistic simulations with respect to reconstructions from real data, due to neglecting discretisation errors that occur when seeking to model real systems. Moreover, despite the development of sophisticated alignment procedures, challenging experimental ET projection data will almost always be imperfectly aligned to some extent. Therefore to further ensure realistic simulations, the simulated projections in the case studies were artificially shifted by a randomly determined amount of at most ±1 pixel. Where appropriate, to enable the simulation studies to guide the choice of the λ value(s) in the CS-ET reconstruction of the experimental data, the mean intensity (grey level) of the projected signal from the test object in the simulated projections was scaled to match the intensity evaluated over an object of interest in the background subtracted experimental projections.

Further details of the simulation studies specific to each case study are given along with discussion of the results in section 8.3.

8.2.5 Performance metrics

To evaluate the fidelity of the reconstructions to the test phantom quantitatively, a normalised ℓ_2-error metric has been used, to be referred to as the *phantom error* and defined by: $\|\hat{\mathbf{x}}\beta_{opt} - \mathbf{x}\|_{\ell_2} / \|\mathbf{x}\|_{\ell_2}$, where $\mathbf{x}$ is the true phantom, $\hat{\mathbf{x}}$ is the reconstruction and β_{opt} is a scaling factor. An important consideration in the evaluation of the phantom error is that the simulated reconstructions need to be scaled to bring them back into the same intensity range as the phantom. This is necessary in the simulation studies primarily because of the need to reverse the scaling applied to the simulated projections in order to mimic the magnitude of

the signal in the experimental data. However, it is also known that reconstruction exploiting ℓ_1-norm minimisation can lead to a slight shrinkage in the magnitude of the sparse coefficients, particularly when large λ values are used [360]. Since other effects such as residual artefacts may be present in the reconstructions, it is not adequate to simply normalise the reconstructions to their maximum. Instead, an optimum scaling factor β_{opt} can be determined that minimises the phantom error. This was obtained by solving: $\min_\beta \|\hat{\mathbf{x}}\beta - \mathbf{x}\|_{\ell_2}$ using the derivative-free Nelder-Mead simplex method [401] (implemented via the `fminsearch` function in MATLAB). Seeking an optimum scaling of the reconstructions also negated any differences in reconstructed intensities that may have arisen as a result of the differing computational implementations used in this work, primarily relating to the use of different system matrices for projection data generation and in each of the reconstruction software packages, thereby facilitating fair comparisons between different algorithms.

Another important parameter, to be referred to as the *projection data error*, is the consistency of the reconstruction with the projection data, which can be measured via a normalised ℓ_2-difference between re-projections of the reconstruction and the original projections: $\|\Phi\hat{\mathbf{x}}\gamma_{opt} - \mathbf{b}\|_{\ell_2} / \|\mathbf{b}\|_{\ell_2}$, where Φ denotes a discrete projection operator, $\mathbf{b}$ is the projection data (sinogram) and γ_{opt} is a scaling factor. The different software packages used to implement the reconstruction algorithms in this work each used slightly different measures of data fidelity during their respective iterations. To obtain a common and unbiased projection data error measurement from all the reconstructions, so as to enable comparison, the discrete Radon transform in MATLAB was used to re-project the final reconstructions. For the comparative studies reported here it is also appropriate due to the differing computational implementations, to seek an optimum scaling of the re-projections during this common projection data error evaluation. The optimum scaling factor γ_{opt} was similarly obtained by solving: $\min_\gamma \|\Phi\hat{\mathbf{x}}\gamma - \mathbf{b}\|_{\ell_2}$.

In addition to the phantom and projection data errors as quality measures of the reconstructions, task-oriented assessment has also been performed, based on the ability to obtain desired application-relevant information from the 3D reconstruction. In the case of the concave iron oxide nanoparticles and cadmium selenide/telluride tetrapods, this concerns the ability to resolve the separation between a tetrapod leg and the concave region of an iron oxide nanoparticle, as well as the difference in grey levels between the two species. This has been assessed for the full ET tilt-series data, and using data sets where the

number of projections has been reduced. For the Ga-Pd nanoparticles, the task-oriented performance metric concerns the ability to obtain accurate size and shape distributions, even though the nanoparticles are densely-packed and span a broad size range. The important criterion in the smooth phantom reconstructions is the ability to faithfully reconstruct the morphology of localised smooth objects/ signals, in particular the gradual decay of their intensity.

8.2.6 Visualisation

Orthoslices through reconstructions were generated using ImageJ or MATLAB, and unless otherwise stated are shown with linear mapping between the minimum and maximum pixel values in each image. As shown in Figure 5.7, the z-direction labelled on the orthoslices is parallel to the optic axis (the missing wedge direction), the y-direction is parallel to the tilt axis and the x-direction perpendicular to these. In the 2D simulations, the missing wedge direction runs vertically between the bottom and top of the image.

The voxel projection visualisations of the reconstructions are shown with 3D perspective view and were generated using the volume rendering module in Avizo Fire (Visualization Sciences Group). The voxel projection display windows were restricted and/or overall transparency (alpha value) reduced until the true signal from the object(s) dominated over the background intensity or reconstruction artefacts.

8.3 Case studies: simulations and experimental results

In this section a simple, intuitive, simulation study that illustrates the key principles underlying a CS-ET approach is shown, followed by the specific case studies.

8.3.1 Demonstration of CS-ET

To illustrate the feasibility and key aspects of a CS approach in ET reconstruction, a simple example is shown in Figure 8.3. Figure 8.3a shows a 2D test phantom consisting of 3 ring-shaped objects of uniform density, which can therefore be represented sparsely in the gradient domain (Figure 8.3ai, with Ψ = spatial finite differences transform). An initial reconstruction from simulated projections (Figure 8.3d, in this case obtained following the Fourier based approach), is expectedly quite poor and, as shown in Figure 8.3e, is not sparse in the gradient domain. An iterative non-linear optimisation is therefore undertaken, seeking sparsity in the gradient domain (the ℓ_1-norm minimisation, or specifically in this case TV-minimisation), whilst ensuring that this process does not introduce inconsistency with the measured data in Figure 8.3c. Since the artefacts that have resulted from undersampling appear as noise-like and are distributed throughout the sparse domain (Figure 8.3e), they are gradually suppressed during this process, whilst the true signal components are preserved. The result of the optimisation is shown in Figure 8.3f, the gradient domain sparsity of which is confirmed in Figure 8.3fi. It is clear that the sparsity exploiting optimisation has brought the reconstruction much closer to the original phantom image.

Figures 8.4b-d show the CS-ET as well as SIRT and WBP reconstructions obtained from the projection data in Figure 8.3b. The SIRT and WBP reconstructions show significant streaking and blurring artefacts, which are near absent in the CS-ET reconstruction. Table 8.1 shows the quantitative quality measures for each of the reconstructions in Figures 8.4b-d, where the projection data error has been measured relative to both the clean and noise corrupted sinogram. As expected from a visual analysis, the WBP reconstruction shows the lowest correspondence to both the phantom and the projection data. By minimising the projection data error as its objective, the SIRT algorithm yields a reconstruction with a slightly improved phantom error. However, in the underdetermined and noise corrupted case, data fidelity alone is insufficient as an

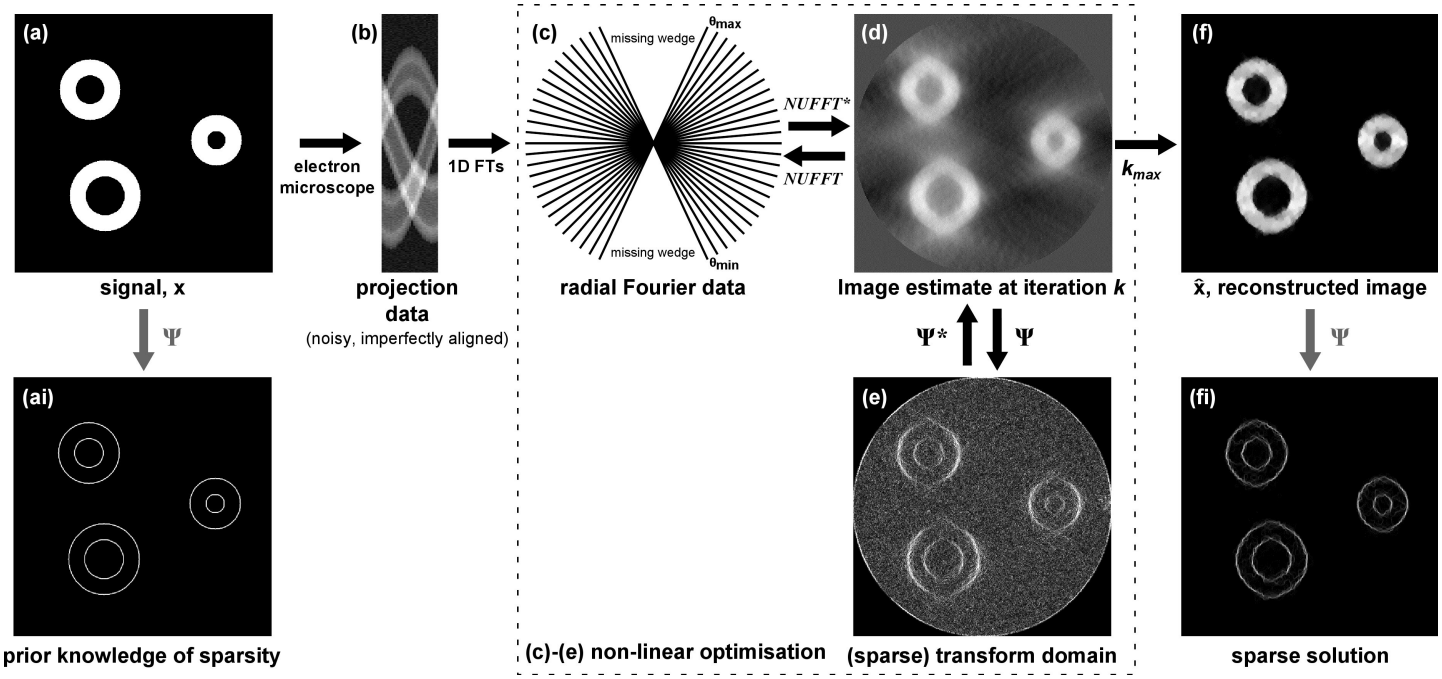

FIGURE 8.3: The key operators, domains and prerequisites in CS-ET. CS requires that it be possible to represent the signal sparsely using an appropriate transform, Ψ; here the image (a) can be represented sparsely in the gradient domain (ai), via a spatial finite differences operator. In the CS framework, linear non-adaptive global measurements of the signal are made against some test function, yielding the undersampled data; in ET a limited number of projection images (b) are acquired in the TEM over a finite tilt range (leaving a missing wedge of un-sampled information). By applying (*N-1*) dimensional Fourier transforms (FTs) (where N is the dimension of the signal), this projection data may also be considered as radial samples of the object's Fourier domain (c), from which an initial reconstruction (d) may be obtained by an N dimensional inverse non-uniform fast Fourier transform (*NUFFT**). CS recovery proceeds via a sparsity promoting non-linear optimisation process (c)-(e), minimising the number of non-zero coefficients in the (sparse) transform domain (e), whilst ensuring consistency with the measured data (c). Incoherent undersampling results in artefacts that appear as noise-like and distributed throughout the transform domain (e), which are suppressed, enabling the larger coefficients corresponding to the signal to be recovered, and hence yielding a reconstruction (f) that is sparse in the transform domain (fi). This simulation used 27 projections of the object in (a), generated over a $\pm 65°$ tilt range. The projections were randomly misaligned by at most ± 1 pixel, and corrupted by Poisson noise and a Gaussian distributed noisy background. The contrast in (e) has been adjusted to increase the visibility of the noise-like undersampling artefacts.

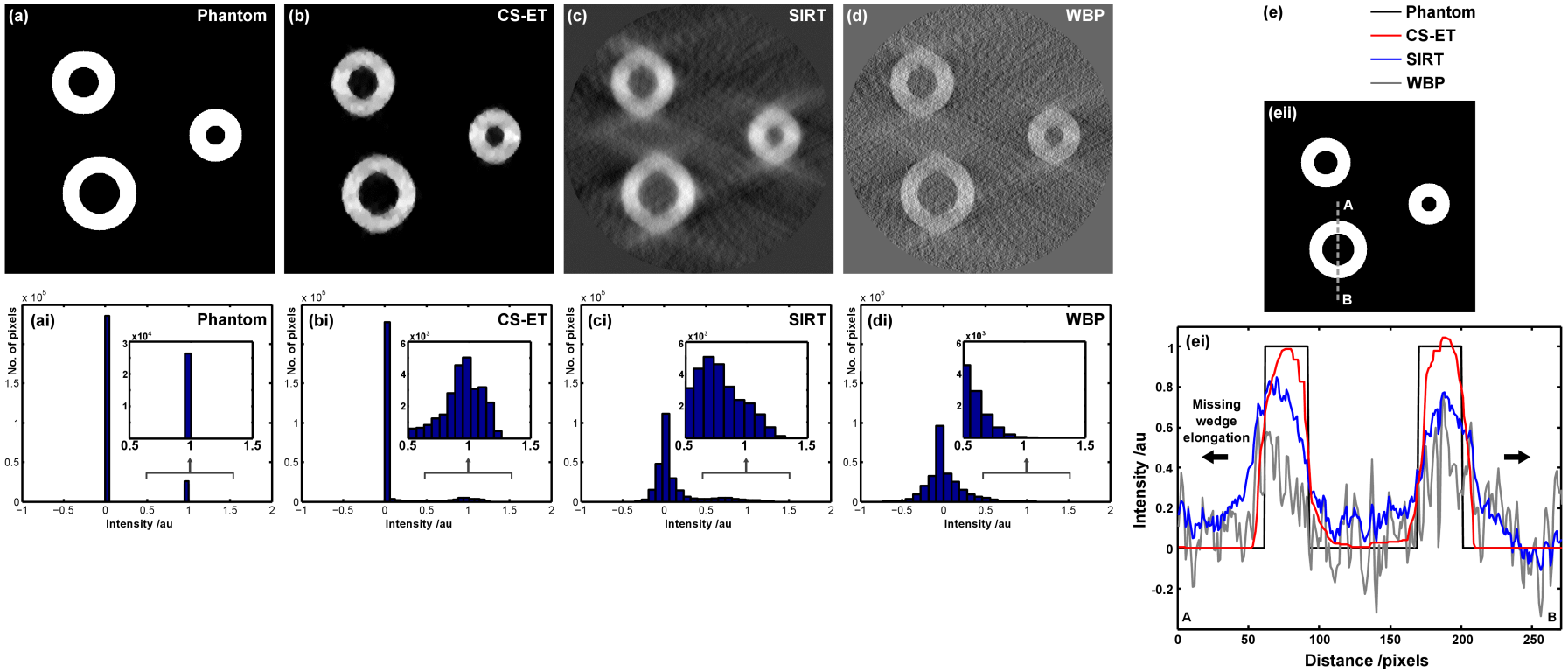

FIGURE 8.4: (a) Test phantom, and (b) CS-ET, (c) SIRT and (d) WBP reconstructions from the simulated projections of the phantom shown in Figure 8.3b. (ai)-(di) Image intensity (grey level) histograms of the phantom and reconstructions, revealing a much greater quantitative correspondence between the CS-ET reconstruction and the phantom compared to the SIRT and WBP reconstructions. (ei) Image intensity profiles from the phantom and reconstructions at the position indicated in (eii). The elongation of the ring-shaped object in the missing wedge (vertical) direction (indicated by the black arrows) visible in the SIRT and WBP intensity profiles is significantly reduced in the case of CS-ET. The line profiles also show that the intensities of the background and test object (in the phantom values of zero and one, respectively) are also recovered more accurately by CS-ET. For SIRT and WBP the reconstructed intensity of the object falls well below its true value, and the intensities of the object and background fluctuate significantly.

TABLE 8.1: Phantom and projection data errors for the reconstructions shown in Figure 8.4.

Reconstruction algorithm	Phantom error	Projection data error (clean sinogram)	Projection data error (noisy sinogram)
CS-ET	0.268	0.0477	0.0995
SIRT	0.477	0.123	0.135
WBP	0.780	0.554	0.527

objective and the phantom error is still relatively large. In the visually improved CS-ET reconstruction, the projection data error relative to the noisy sinogram is of the same order as that of the SIRT reconstruction, but the phantom error and projection data error relative to the clean sinogram are much smaller. By assigning a relative importance to sparsity in the reconstruction, as well as maintaining a sufficient level of fidelity to the noise-corrupted data, CS-ET is able to achieve a more faithful recovery of the phantom that is known to be sparse, and in doing so is also inherently denoising.

The advantages of the higher fidelity CS-ET reconstruction are further reinforced by considering directly the properties that would be important in a quantitative analysis of the reconstructions. Figures 8.4ai-di show the pixel intensity (grey level) histograms of the phantom and reconstructions, where for the CS-ET reconstruction (Figure 8.4bi), the intensity of the ring-shaped objects is recovered to a good degree of accuracy (the true value in the phantom being an intensity of 1) and the pixel intensities belonging to the objects are clearly distinguishable from the background. For the SIRT and WBP reconstruction (Figure 8.4ci and di), the recovered pixel intensities of the objects are primarily below the correct value, and moreover are difficult to distinguish from those of significant artefact-related non-zero intensities. The high noise/artefact levels in the SIRT and WBP reconstructions are also evident in the intensity profiles shown in Figure 8.4e, where the well-known artefact of elongation of the reconstruction in the missing wedge (vertical) direction is also evident. For the CS-ET reconstruction, Figure 8.4e further emphasises that the background artefacts and false elongation are markedly reduced.

This simple example can also be used to illustrate the significant challenge in choosing the λ parameter(s) when seeking a regularised reconstruction, such as that described by Equation 7.10 or 8.1. Primary factors influencing the appropriate λ are the strength of the signal, the number and angular range of the projections (level of undersampling), the noise level and other

inconsistencies such as projection misalignment. Example reconstructions illustrating appropriate and inappropriate choices of λ_I and λ_{TV} in Equation 8.1, for CS-ET reconstruction of the piecewise constant phantom from Figure 8.3, are shown in Figure 8.5. Optimal choice of λ_I and λ_{TV} yields a reconstruction that is sparse in the image domain (Figure 8.5a) and even more sparse in the gradient domain (Figure 8.5ai). With λ_I and λ_{TV} set too low, undersampling artefacts are not suppressed, and the reconstruction is not sparse in either domain (Figures 8.5b,bi). Settingλ_I too high and λ_{TV} relatively low leads to loss of signal in the image domain (Figure 8.5c) and loss of sparsity in the gradient domain (Figure 8.5ci). Setting λ_{TV} too high and λ_I relatively low leads to blurring/ flattening of the objects in the image domain (Figure 8.5d) and only moderate sparsity in the gradient domain (Figure 8.5di). Setting λ_I and λ_{TV} too high (not shown) leads to loss of signal in both domains.

8.3.2 Case study 1: concave iron oxide nanoparticles and cadmium selenide/telluride tetrapods

Compared to the proof-of-principle study (ref. [210], section 8.1), here a system of higher complexity is considered, consisting of concave iron oxide nanoparticles [395] intermixed with cadmium selenide/telluride tetrapods [402]. This tilt-series also has a far lower SNR. An example ADF-STEM projection from the tilt-series is shown in Figure 8.6.

The presence of species with differing atomic number (Z) and the use of ADF-STEM imaging means that the reconstruction should contain multiple grey levels, with significant differences in the reconstructed intensity of the concave iron oxide nanoparticles and cadmium selenide/telluride tetrapods. Since the iron oxide nanoparticles are expected to have uniform composition and sharp boundaries, i.e. they are, to a good approximation, piecewise constant, seeking sparsity in the gradient domain (TV-minimisation) for CS-ET reconstruction is an appropriate approach. In the ideal case, the tetrapods should consist of a cadmium selenide core and cadmium telluride legs. However, the boundary between the core and legs may not be sharp, and there may be some regions of mixed alloy composition [402]. Additionally, some defective nanoparticles, including rods, dipods and tripods, may form through homogeneous nucleation and therefore not contain a core [402]. These factors mean that the grey levels that should be present in a reconstruction of the tetrapods may be variable and non-discrete, the latter implying that tetrapods may not strictly be piecewise constant. However, as noted in chapter 7, a piecewise constant approximation can enable recovery of

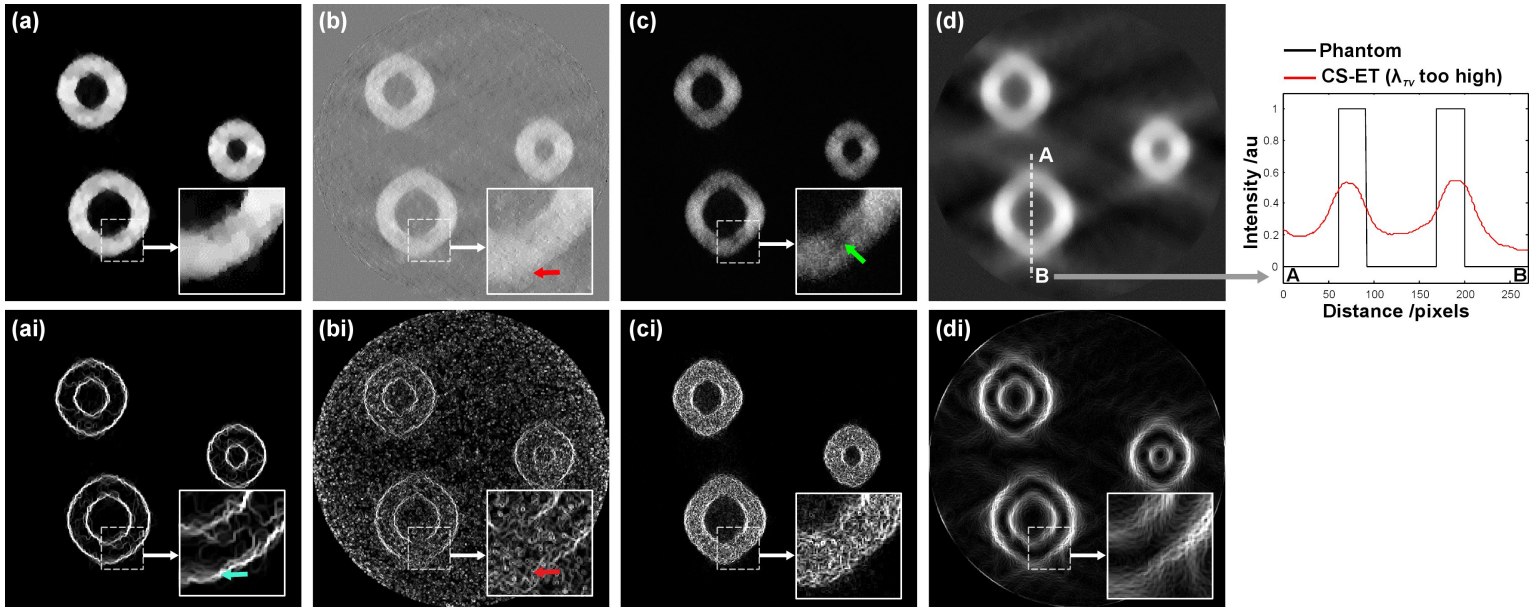

FIGURE 8.5: Influence of the choice of the regularisation parameters λ_I and λ_{TV}, governing the weighting given to image and gradient domain (TV) sparsity, respectively, in Equation 8.1. The top row shows the image domain of the reconstruction and the bottom row the corresponding gradient domain representation. (a, ai) Optimal choice of λ_I and λ_{TV}, yielding a reconstruction that is sparse in the image domain and even sparser in the gradient domain. The sharp boundaries of the objects in the image domain are recovered, which correspond to the highest gradient domain intensity, indicated by the blue arrow in (ai). (b, bi) λ_I and λ_{TV} too low, resulting in insufficient suppression of artefacts, and therefore a reconstruction that is not sparse in the image or gradient domain. The boundaries of the object are difficult to distinguish from undersampling and noise related signals, particularly in the missing wedge (vertical) direction, as indicated by the red arrows in the insets. (c, ci) λ_I too high (and λ_{TV} relatively low), leading to loss of signal in the image domain, as highlighted by the green arrow in the inset in (c), and a general 'speckled' appearance of the objects. This leads to loss of sparsity of the objects in the gradient domain, as highlighted in the corresponding inset in (ci). (d, di) λ_{TV} too high (and λ_I relatively low), leading to blurring and flattening of the objects in the image domain, as shown by the accompanying pixel intensity profile, and only moderate sparsity in the gradient domain, where the boundaries of the objects are broadened and poorly defined in the missing wedge direction, as highlighted in the inset in (di). The contrast in (ai)-(di) has been adjusted to increase the visibility of the image features.

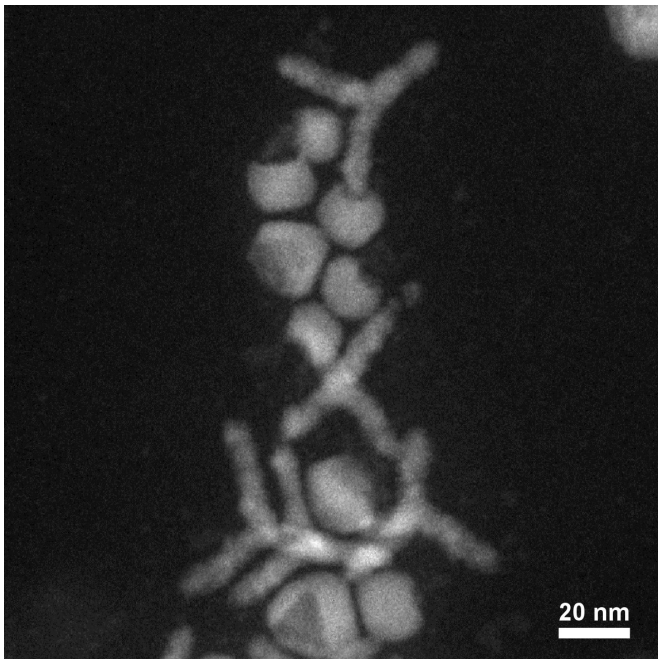

FIGURE 8.6: Example ADF-STEM tomography tilt-series projection of concave iron oxide nanoparticles and cadmium selenide/telluride tetrapods.

the most important information at the desired level of complexity. In other words, a piecewise constant approximation can provide a compressible representation that captures the most important information about the tetrapods. In this case, the key information of interest is the morphology (boundaries) of the tetrapods (or rods, dipods and tripods), the primary difference in grey level with respect to the iron oxide nanoparticles and major regions of substantially different composition in the tetrapods. Notably, a TV-minimisation approach does not impose any prior knowledge of the number or intensity of the image grey levels during the reconstruction process. By using a sufficiently small λ_{TV} value, any regions of differing composition in the tetrapods can be recovered as different grey levels, although regions of gradually varying composition may be approximated as many small uniform regions.

As was the case in ref. [210], in addition to seeking sparsity in the gradient domain, sparsity was also enforced in the image domain to help suppress missing wedge and streaking artefacts. The optimal weightings were found to be $\lambda_I = 40$ and $\lambda_{TV} = 20$ for both the simulated and the experimental reconstructions.

8.3.2.1 Concave iron oxide and cadmium selenide/telluride tetrapods: phantom study

To mimic the experimental data as closely as possible, a 512 × 512 pixel test phantom was generated based on a slice from the SIRT reconstruction, taken from the x-z plane. The phantom (Figure 8.7a) consists of two closely spaced iron oxide nanoparticles, with the tip of a cadmium selenide/telluride tetrapod located in the concave region of the right hand nanoparticle.

The approximate mean image intensities evaluated from the background subtracted experimental projections for the iron oxide nanoparticles and cadmium selenide/telluride tetrapods were ∼5000 and ∼6000, respectively. The simulated nanoparticle/tetrapod projection data was scaled to have a mean equal to the mean of these values (i.e. 5500), and subsequently corrupted by Poisson noise. To obtain a low SNR dataset, approximately mimicking the experimental projections, a noisy Gaussian background of standard deviation 550 was added to the projections, which yielded good qualitative (visual) correspondence to the noise in the experimental images.

To test the limits of the CS-ET approach, reconstructions were also performed using 13 and 9 projection subsets from the full tilt-series. The λ_I and λ_{TV} values for these reconstructions were reduced to one half and one third, respectively, of the weightings used for the full tilt-series.

Figures 8.7b and e show the CS-ET and SIRT reconstructions from the full 27 projection simulated tilt-series of the phantom. Visually, as expected, the SIRT reconstruction clearly suffers from blurring of the nanoparticle boundaries in the missing wedge (vertical) direction, as well as streaking artefacts due to the limited angular sampling. Despite the popularity of the SIRT algorithm in ET studies, it is clear that it does not provide adequate recovery of the piecewise constant image content. These artefacts are markedly reduced in the corresponding CS-ET reconstruction. Horizontal and vertical line profiles through the reconstructions, shown in Figures 8.7h-m, confirm these observations, where it is clear that the CS-ET reconstruction has correctly recovered the boundaries of the nanoparticles. The line profiles through the SIRT reconstruction are distinctly more rounded and it is difficult to locate precisely the nanoparticle edges. The SIRT line profiles oscillate rapidly, indicative of a high background noise level. For the CS-ET reconstruction on the other hand, the denoising effect of the TV constraint has yielded near uniform intensity across the background and the nanoparticles. Additionally, the CS-ET reconstruction has correctly recovered the relative intensities of each component of the phantom,

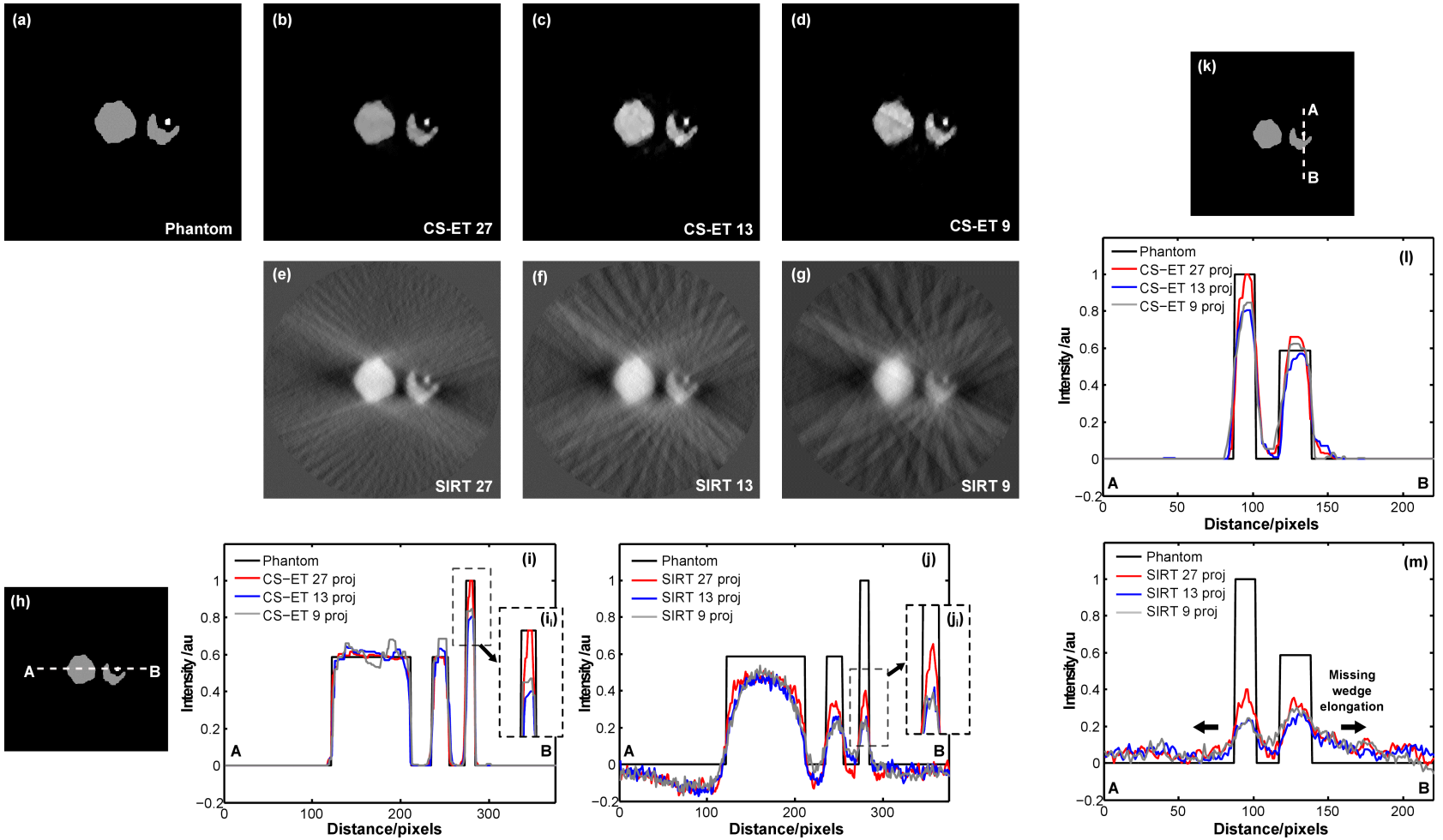

FIGURE 8.7: (a) Concave iron oxide nanoparticle and cadmium selenide/telluride tetrapod test phantom. (b)-(d) CS-ET and (e)-(g) SIRT reconstructions from simulated projections of the phantom. The number of projections used in each reconstruction is indicated in the bottom right hand corner. (i, j) and (l, m) are intensity profiles of the phantom and reconstructions at the positions indicated in (h) and (k), respectively.

whereas in the SIRT reconstruction the reconstructed intensity of the cadmium selenide/telluride tetrapod leg within the iron oxide nanoparticle concavity is actually less than that of the iron oxide nanoparticle. This is likely due to a known deficiency of SIRT reconstructions and the tomographic PSF, where the reconstructed intensity (grey level) of nanoparticles can be dependent on the nanoparticle size [305, 354].

Similar to the simple example shown in section 8.3.1, the phantom and projection data errors for these reconstructions (Table 8.2) confirm the efficacy of the sparsity prior: both the CS-ET and SIRT reconstructions have similar projection data errors with respect to the noisy sinogram, but, in the case of few and noise-corrupted projections, this does not guarantee a solution close to the true object. Incorporating the prior knowledge in CS-ET that the reconstruction should be sparse, in particular in this case that it should have a low TV, yields a solution with a higher SNR that is much closer to the piecewise constant phantom, as measured by the much lower projection data error with respect to the clean sinogram and the lower phantom error.

Table 8.2: Phantom and projection data errors for the concave iron oxide nanoparticle and cadmium selenide/telluride tetrapod reconstructions.

Data	Reconstruction algorithm	Phantom error	Projection data error (clean sinogram)	Projection data error (noisy sinogram)
Simulated				
27 projections	CS-ET	0.236	0.0546	0.171
	SIRT	0.598	0.144	0.177
13 projections	CS-ET	0.273	0.0601	0.168
	SIRT	0.664	0.147	0.157
9 projections	CS-ET	0.263	0.0534	0.163
	SIRT	0.657	0.138	0.141
Experimental				
27 projections	CS-ET	-	-	0.211
	SIRT	-	-	0.218
13 projections	CS-ET	-	-	0.201
	SIRT	-	-	0.213
9 projections	CS-ET	-	-	0.218
	SIRT	-	-	0.222

In the SIRT reconstructions using only 13 and 9 projections (Figures 8.7f and g), the streaking artefacts and blurring of the nanoparticle boundaries become visibly more pronounced and the phantom errors increase correspondingly. The CS-ET reconstructions (Figures 8.7c and d) also suffer some degradation in these cases of significantly reduced data, primarily a greater variation in the intensities within the iron oxide nanoparticles and a slight loss of intensity in the tetrapod leg (see the line profiles in Figures 8.7i and l). However, the overall morphology of the nanoparticles and near absence of streaking artefacts is maintained, which is reflected in the phantom errors remaining relatively low.

8.3.2.2 Concave iron oxide and cadmium selenide/telluride tetrapods: experimental results

The results from the experimental data (Figures 8.8 and 8.9, and Table 8.2) are consistent with many of the features seen in the simulation studies, viz. reduction of streaking and blurring, maintenance of grey level contrast between the nanoparticles and tetrapods, and higher SNR in the CS-ET reconstructions, even when using only 9 projections. Using a sufficiently large λ_I value in CS-ET to suppress the undersampling artefacts has caused some loss of genuine signal, as seen in the slightly 'speckled' appearance of the nanoparticles (Figure 8.8a-c). This could be somewhat reduced by increasing the TV weighting (λ_{TV} value). However, doing so also led to slight loss of sharpness in the nanoparticle boundaries (cf. Figure 8.5d), a 'blocky' appearance (commonly seen in excessive TV regularisation) and an overall loss of high frequency details (including potential compositional variations within the cadmium selenide/ telluride tetrapods), indicating that such a TV weighting was too high. Overall however, the level of artefacts in the CS-ET reconstructions is far lower than for the SIRT reconstructions.

8.3.3 Case study 2: densely-packed Ga-Pd nanoparticles

In chapter 6 it was shown that quantitative 3D information pertaining to the size, shape, spatial distribution and agglomeration state of the unsupported Ga-Pd nanoparticles could be obtained from a sufficiently high-contrast high-tilt range ADF-STEM tomography tilt-series. However, the quality of the analysis was still limited ultimately by the fidelity of the SIRT reconstruction; requiring careful analysis of the reconstruction and segmentation results to interpret the quantitative data correctly. Here, CS-ET has been applied to

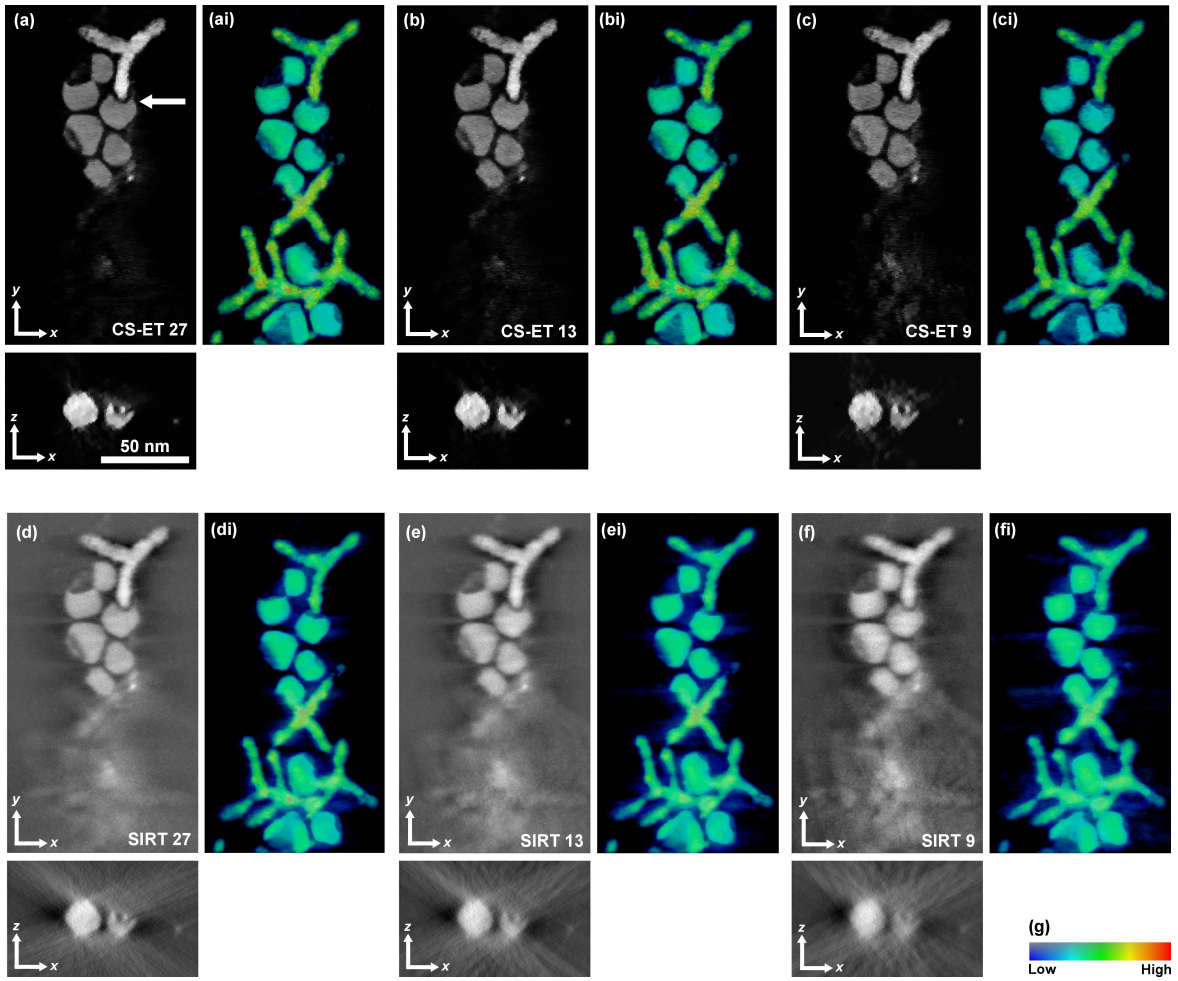

FIGURE 8.8: Reconstructions of concave iron oxide nanoparticles and cadmium selenide/telluride tetrapods from the experimental ADF-STEM tomography tilt-series of Figure 8.6. (a)-(c) and (d)-(f) Orthoslices through CS-ET and SIRT reconstructions, respectively. (g) Colour map of the 3D perspective view voxel projections in (ai)-(fi). The number of projections used in each reconstruction is indicated in the bottom right hand corner of the x-y orthoslice. See Figure 8.9 for additional x-z and y-z orthoslices.

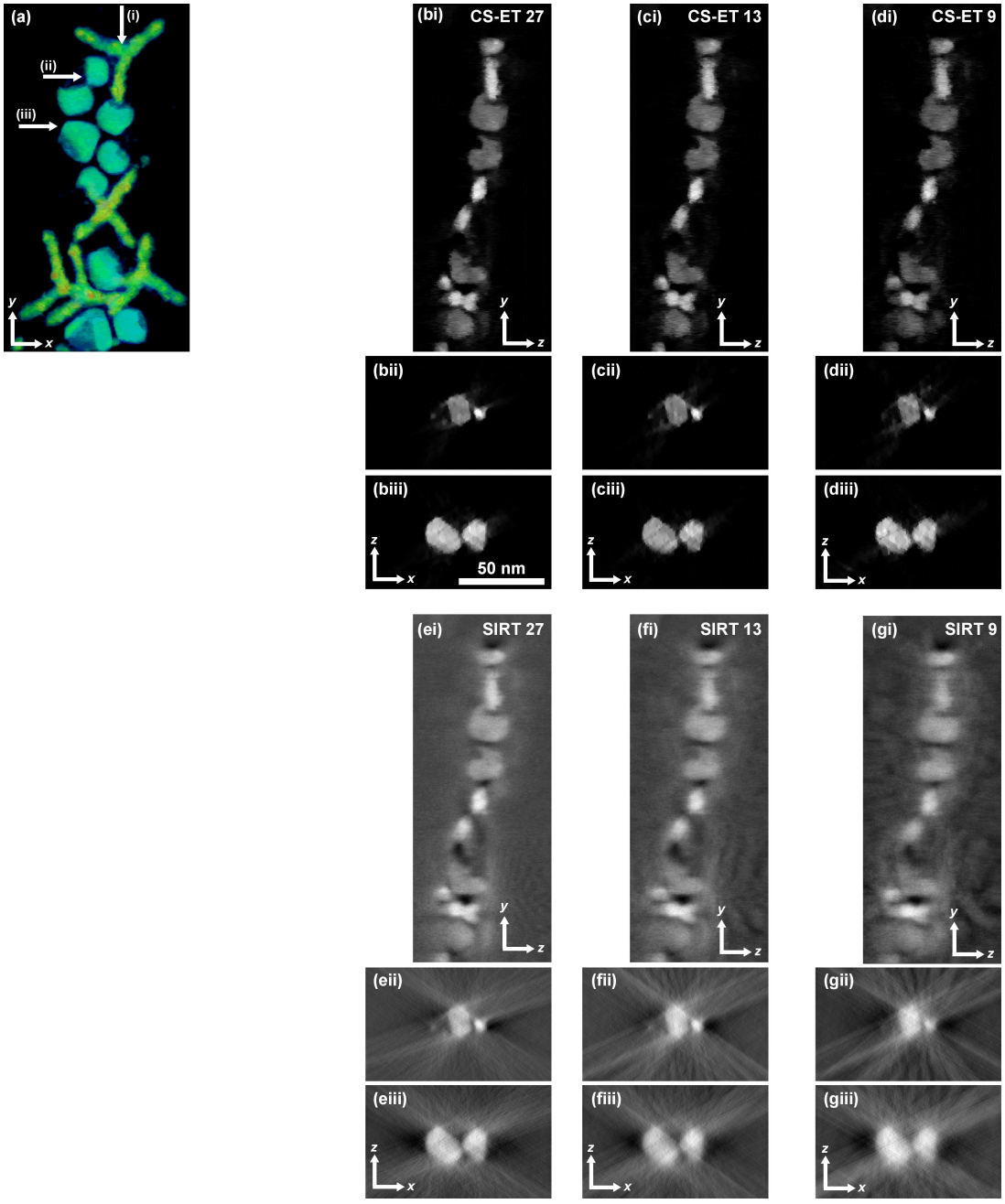

FIGURE 8.9: Additional orthoslices through the reconstructions of concave iron oxide nanoparticles and cadmium selenide/telluride tetrapods shown in Figure 8.8. The positions of the orthoslices in the 3D reconstructions is indicated in (a).

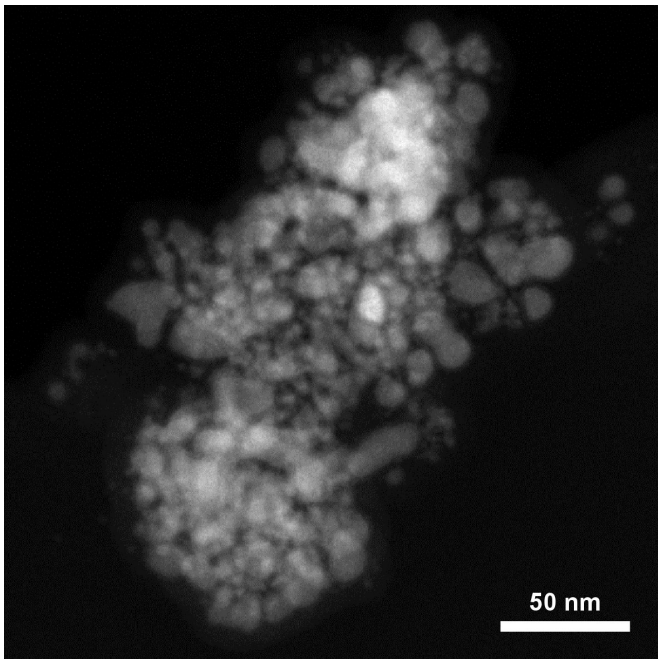

FIGURE 8.10: Example ADF-STEM tomography tilt-series projection of unsupported Ga-Pd nanoparticles.

another ADF-STEM tilt-series of the Ga-Pd nanoparticles (Figure 8.10), seeking a reconstruction that is of higher fidelity than that provided by SIRT, and that can be more readily segmented using (semi-)automated methods.

8.3.3.1 Densely-packed Ga-Pd nanoparticles: phantom study

As per the previous case study (section 8.3.2), a simulation study has been performed to guide the analysis of the experimental data. Test phantoms for this case study were obtained by generating ellipses of random size, aspect ratio and spatial distribution. The ellipses, representing particles, were allowed to overlap to mimic agglomerated particles. All particles and agglomerates were assigned the same intensity value, resulting in binary phantoms. An example phantom, of dimensions 512×512 pixels, is shown in Figure 8.11a.

The approximate image intensity of the Ga-Pd nanoparticles evaluated from the background subtracted experimental projections was $\sim$2000. The simulated projections of the phantoms were scaled to have a mean equal to this value, and subsequently corrupted by Poisson noise. Gaussian distributed noise of standard deviation 150 was then added to mimic background components. For the CS-ET reconstructions, sparsity was enforced in the image and gradient domains. The

optimal λ_I and λ_{TV} parameters in the simulations were determined to be 15 and 5, respectively.

To assess the quality of the reconstructions for enabling accurate quantitative size and shape measurement of the particles and agglomerates, the phantoms and reconstructions were analysed using the same segmentation and quantification procedure. This involved firstly for the reconstructions, thresholding based on the image intensity followed by binarisation. The threshold intensity for each reconstruction was chosen as that which minimises the projection data error of the binarised reconstruction. This method of threshold selection has been shown to be highly effective in the tomographic context [342]. Similar results were also observed in these simulations using Otsu's method [341] (described in section 5.3.5). The binarised reconstructions and the test phantoms were then subjected to the same watershed transform-based particle separation procedure, implemented in MATLAB, to identify individual particles and agglomerates (see again, chapter 6). Intimately touching particles are not separated by the watershed process and remain in the tomogram as an agglomerate, which is considered as a single object. The size and shape of the particles/agglomerates was then quantified in terms of their area and aspect ratio, using features in the MATLAB Image Processing Toolbox. To obtain statistically meaningful size and shape distributions, the simulation and analysis was performed for 512 different phantoms, each with different (randomly selected) distributions of ellipses, and the quantification results combined.

Figure 8.11 shows an example of the results from simulations, in which a number of important artefacts in the SIRT reconstruction can be identified that are overcome using CS-ET. Firstly, the SIRT reconstruction (Figure 8.11c) is visibly elongated in the missing wedge (vertical) direction; some particularly badly affected particles in the thresholded SIRT reconstruction (Figure 8.11e) are indicated by blue arrows. This false elongation is substantially reduced in the CS-ET reconstruction. Secondly, some of the smaller particles are missing in the thresholded SIRT reconstruction, as their intensity is too low. This is likely due to the known deficiency, noted also in the previous case study, where the reconstructed intensity (grey level) of nanoparticles in SIRT reconstructions can be dependent on the nanoparticle size [305]. As indicated by the yellow arrows, these particles are successfully recovered in the CS-ET reconstruction. Finally, following the watershed separation process, some of the particles that were separated in the phantom (Figure 8.11f) are no longer distinguished in the SIRT reconstruction (indicated by white arrows, Figure 8.11h). These were still

successfully distinguished in the CS-ET reconstruction (Figure 8.11g).

The visual observations from Figure 8.11 are reflected in the mean phantom and projection data errors from the 512 simulations (Table 8.3), as well as in the measured size and shape distributions of the particles and agglomerates, shown in Figure 8.12. Many of the SIRT reconstructions were corrupted by noise pixels, which needed to be filtered out of the quantitative data by setting a minimum threshold of at least 5 connected pixels constituting a particle. However, even after the filtering process, the distributions from the SIRT reconstructions in Figure 8.12 show some significant discrepancies to the true distributions measured from the phantoms.

The key characteristics of the size and shape distributions are summarised by the statistics inset in each of the graphs in Figure 8.12. The mean particle size obtained from the segmented SIRT reconstructions is significantly larger than the mean size from the phantoms. This is a result of overestimation of the size of many particles due to poor definition of the particle boundaries and elongation of the particles in the missing wedge direction (cf. Figure 8.11c). It also results from the poor detection of small particles (cf. Figure 8.11e; some partially recovered smaller particles are also lost during the filtering process since they cannot be distinguished from noise), as well as false merging of closely spaced particles (cf. Figure 8.11h). False merging of particles, leading to large agglomerates, is also reflected in the greater skewness of the size distribution to the right of the mean. This is similarly evident in the elevated mean and skewness of the shape distribution measured from the segmented SIRT reconstructions; as shown in chapter 6 (Figure 6.10), the false merging of particles can result in chains of connected particles, particularly in the missing wedge direction, which are then measured as spurious high aspect ratio agglomerates.

The CS-ET reconstructions also suffer from these artefacts in some cases, particularly when the spatial distribution of the simulated particles is unfavourable. However, the much lower mean phantom error (Table 8.3) shows that the CS-ET reconstructions are consistently of higher fidelity than the SIRT reconstructions. In the case of these simulations, no filtering of noise pixels was required for the CS-ET reconstructions. Crucially, the very good correspondence of the size and shape distributions measured from the segmented CS-ET reconstructions to the true distributions measured from the phantoms in Figure 8.12 (see the excellent agreement of the summary statistics inset in the graphs), shows that the consistent higher fidelity, exemplified in Figure 8.11, has enabled much more accurate segmentation and metrological analysis.

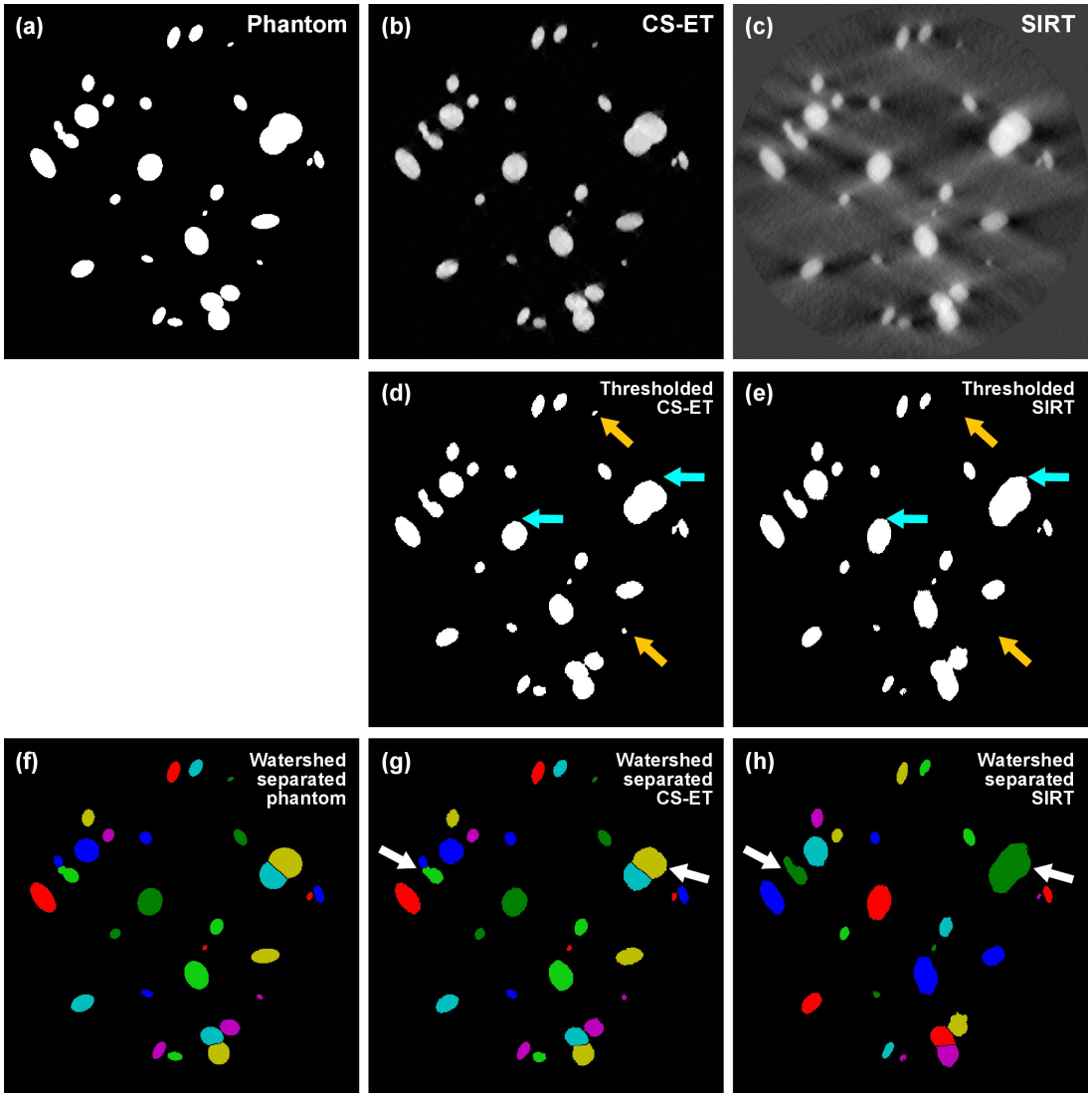

FIGURE 8.11: Example ET simulation involving reconstruction and quantification of densely-packed particles. (a) Test phantom. (b) CS-ET and (c) SIRT reconstructions from simulated projections of the phantom. (d) and (e) thresholded and binarised CS-ET and SIRT reconstructions, respectively. Blue arrows indicate particles that are substantially falsely elongated in the (thresholded) SIRT reconstruction, but much less so in the (thresholded) CS-ET reconstruction. Yellow arrows indicate particles that are missing in the thresholded SIRT reconstruction, but successfully identified in the thresholded CS-ET reconstruction. (f)-(h) Results of applying watershed segmentation to the (f) phantom, (g) thresholded CS-ET reconstruction and (h) thresholded SIRT reconstruction, where each separate identified particle or agglomerate of particles has been assigned a colour that differs from those of its nearest neighbours. White arrows indicate particles that, as per the phantom, are successfully distinguished by the watershed separation process in the CS-ET reconstruction, but are not distinguished in the SIRT reconstruction.

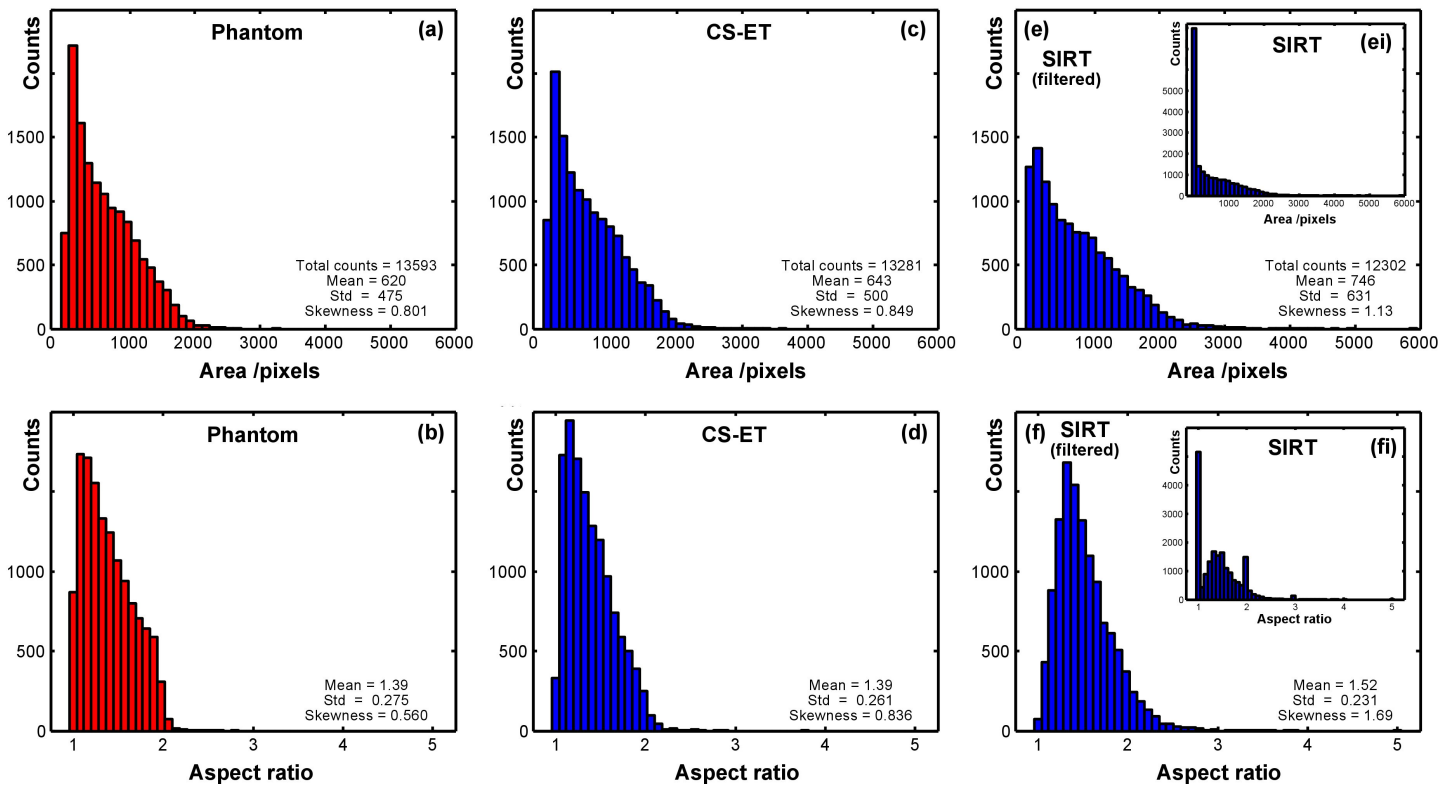

FIGURE 8.12: Statistical size and shape distributions, in terms of area and aspect ratio, respectively, of the identified particles and agglomerates in the (a) and (b) phantoms, (c) and (d) CS-ET reconstructions and (e) and (f) SIRT reconstructions. The distributions are the combined quantification results from 512 simulations, each of which used a phantom with different (randomly selected) distributions of ellipses to mimic particles/agglomerates. The size and shape data in each simulation was obtained by applying the segmentation process illustrated in Figure 8.11. The insets (ei) and (fi) show the distributions for the SIRT reconstruction prior to filtering out noise pixels.

TABLE 8.3: Phantom and projection data errors for the Ga-Pd nanoparticle reconstructions. The quoted values for the simulations are the mean values from the 512 simulations. The standard deviation (std) is also given in square brackets.

Data	Reconstruction algorithm	Phantom error [std]	Projection data error [std] (clean sinogram)	Projection data error [std] (noisy sinogram)
Simulated				
	CS-ET	0.286 [0.0153]	0.0506 [0.00978]	0.0957 [0.00344]
	SIRT	0.568 [0.0218]	0.1634 [0.0111]	0.175 [0.0102]
Experimental				
	CS-ET	-	-	0.239
	SIRT	-	-	0.196

8.3.3.2 Densely-packed Ga-Pd nanoparticles: experimental results

In the experimental CS-ET reconstruction it was necessary to increase λ_I relative to the simulations in order to suppress artefacts, and also reduce λ_{TV} to avoid merging of closely spaced nanoparticles. This was due, in large part, to a progressive build-up of carbonaceous contamination over the nanoparticles during the experimental tilt-series, as well as other experimental imperfections, including diffraction contrast (which occurred in different nanoparticles throughout the tilt-series, prohibiting removal of affected projections), imperfect alignment, and possible movement of nanoparticles during the tilt-series. The best compromise between suppression of artefacts and loss of signal was found to be $\lambda_I = 200$ and $\lambda_{TV} = 1$.

Figure 8.13 shows orthoslices and 3D perspective view voxel projections of the CS-ET and SIRT reconstructions, revealing significantly reduced missing wedge artefacts and clearer definition of the nanoparticle boundaries in the former. Additionally, many of the smaller nanoparticles are not easily seen in the voxel projection of the SIRT reconstruction, whereas they are clearly visible in the CS-ET reconstruction, examples of which are indicated by orange arrows. This difficulty in detecting the small particles is confirmed when seeking to apply global intensity-based thresholding to the reconstructions in order to segment the reconstructed nanoparticles.

Prior to thresholding it was first necessary to apply an unsharp masking operation to both the SIRT and CS-ET reconstructions, to enhance the clarity of nanoparticle boundaries. Additionally, the progressive contamination build-

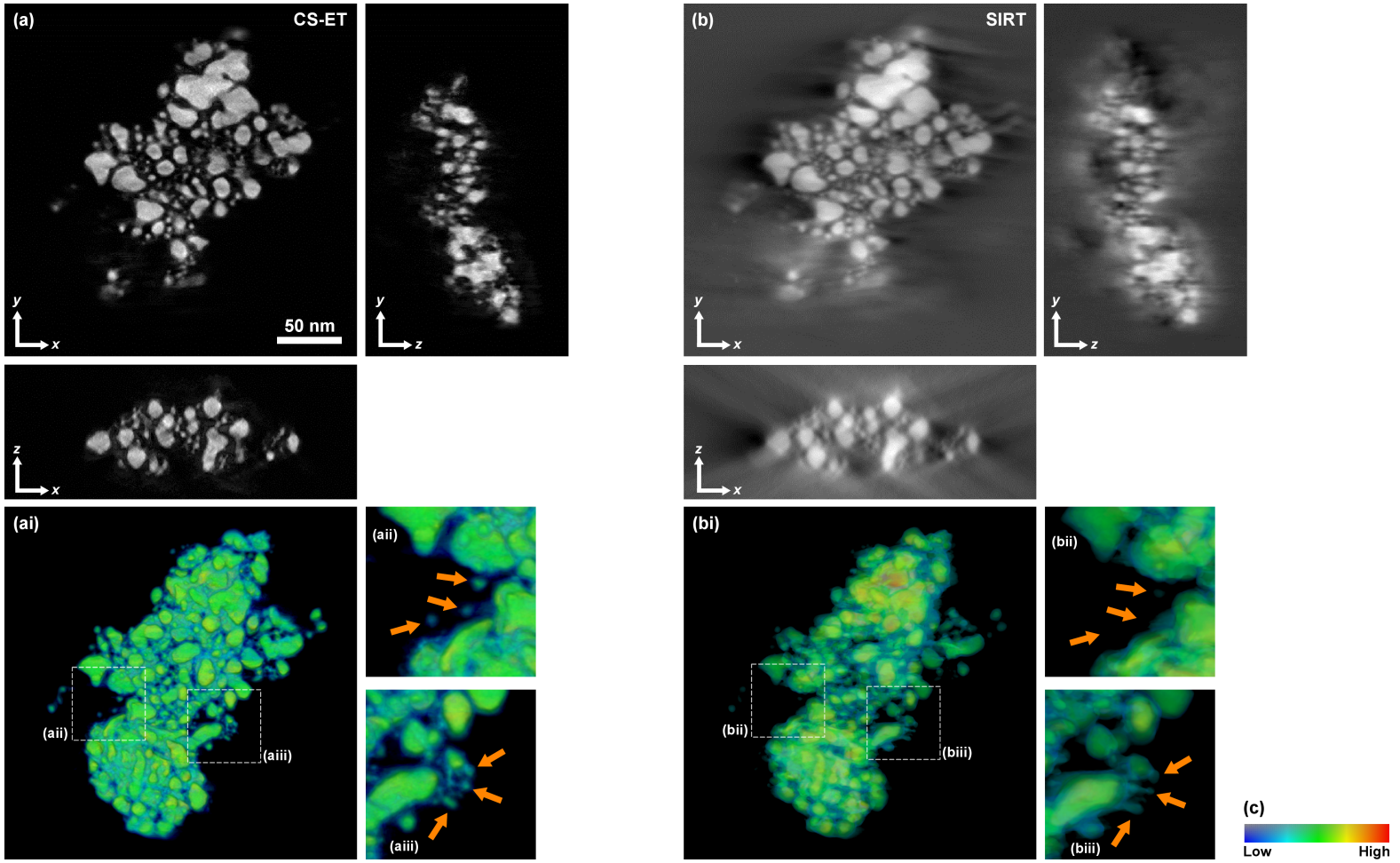

FIGURE 8.13: Reconstructions of unsupported Ga-Pd nanoparticles from the experimental ADF-STEM tomography tilt-series of Figure 8.10. (a) and (b) Orthoslices through CS-ET and SIRT reconstructions, respectively. (c) Colour map of the 3D perspective view voxel projections in (ai) and (bi). Orange arrows indicate small nanoparticles that are clearly visible in the CS-ET reconstruction, but difficult to visualise in the SIRT reconstruction.

up through the tilt-series meant that threshold selection by projection data error minimisation was less suitable for these experimental reconstructions, and so Otsu's method was used. This proved reasonably successful for the CS-ET reconstruction, capturing all of the large, and most of the small, nanoparticles (see example thresholded orthoslices in Figure 8.14a), but for the SIRT reconstruction the nanoparticles were not distinguished from artefacts and background signals (Figure 8.14b). Manually choosing a higher threshold level for the SIRT reconstruction however, leads to a loss of the smaller particles (Figure 8.14c). Indeed, no threshold could be found that captures all the particles in the SIRT reconstruction without incorporation of reconstruction artefacts. The SIRT reconstruction thresholded at the manually-chosen higher threshold level was used in further analysis. Following thresholding, both reconstructions were median filtered to remove noise pixels and obtain more uniform boundaries of the thresholded nanoparticles, and a hole-filling procedure was applied to the SIRT reconstruction to fill voids left within the thresholded nanoparticles. Figures 8.15a and b show voxel projections of the CS-ET and SIRT reconstructions, respectively, following 3D watershed nanoparticle separation (see chapter 6 for details of the procedure). Each identified nanoparticle or agglomerate of nanoparticles is displayed with a colour that differs from those of its nearest neighbours.

As in chapter 6, to reduce the impact of remaining noise pixels on the quantitative data, both reconstructions were filtered to include only nanoparticles consisting of 5 or more connected voxels in the size distributions, and 10 or more connected voxels in the shape distributions. This choice for the size distribution was again found to yield the best distinction between isolated patches of noise and genuine nanoparticles, and again resulted in a minimum nanoparticle size of ca. 1 nm^3, in good agreement with the resolution expected in the tomogram [286]. Similarly, a higher cut-off was imposed for the shape distribution since the shape of the nanoparticles is unlikely to be represented faithfully by fewer than 10 voxels. Once more, the reliability of both analyses though, is clearly reduced at the lower extremes of the distributions. Also as described in chapter 6, the 3D size of the nanoparticles was characterised in terms of their equivalent diameter; and their 3D shape in terms of their 3D Feret ratio, effectively providing a 3D measure of aspect ratio.

Similar to the simulation study, the lower total counts in the SIRT size distribution reflects the poor reconstruction/detection of the smaller nanoparticles; examples of nanoparticles captured in the segmented CS-ET reconstruction but

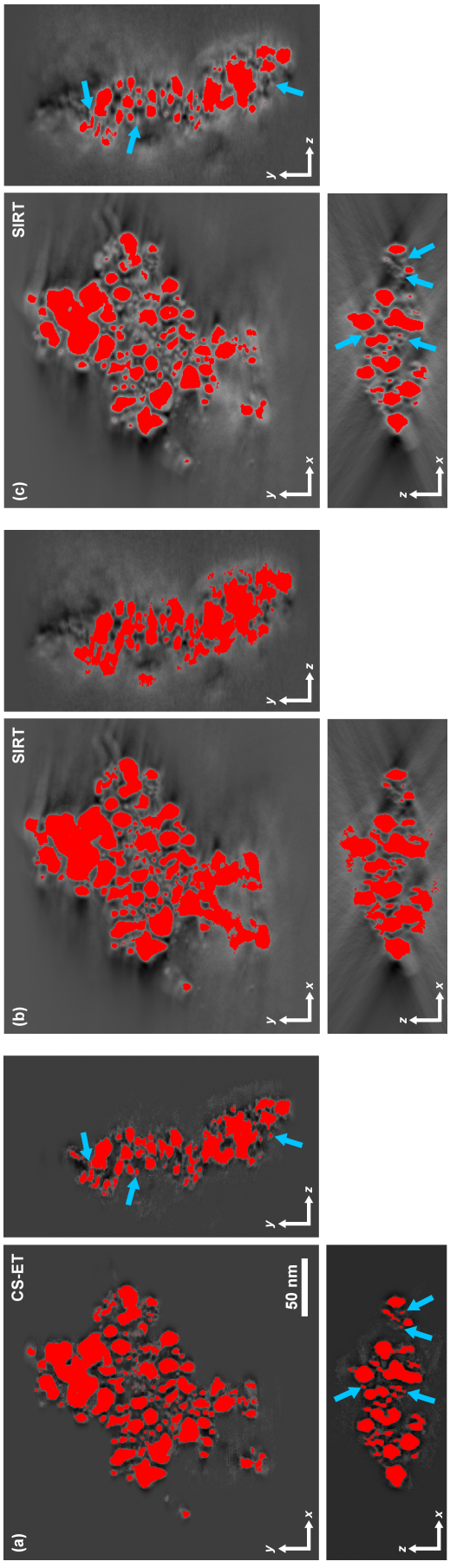

FIGURE 8.14: Image intensity based thresholding of the unsharp masked Ga-Pd nanoparticle reconstructions. (a) Otsu thresholding captures both large and small nanoparticles in the CS-ET reconstruction. (b) Otsu thresholding of the SIRT reconstruction does not distinguish the nanoparticles from artefacts. (c) Setting a manually chosen higher threshold for the SIRT reconstruction to exclude artefacts also leads to exclusion of many small nanoparticles. Examples of small particles successfully captured in the CS-ET reconstruction (a) but not in the SIRT reconstruction (c) are indicated by the blue arrows.

not in the SIRT reconstruction are indicated by grey arrows in Figures 8.15a and b. Both reconstructions likely suffer from some false merging of nanoparticles into agglomerates due to overestimation of the particle sizes caused by contamination build-up during the tilt-series acquisition. A careful visual examination of the colour-coded segmented reconstructions though (Figures 8.15a and b), suggests that this false merging is much more prevalent in the SIRT reconstruction.

Overall, despite the limited quality of this particular tilt-series, the fact that credible segmentation, and thereby valuable quantitative size and shape information, can be obtained from the CS-ET reconstruction using relatively simple image processing steps is a considerable advantage. Obtaining improved segmentation of the SIRT reconstruction in this case would require more sophisticated pre-processing (cf. chapter 6), or else manual segmentation, which is both laborious and subjective.

8.3.4 Case study 3: ET reconstruction of smooth objects

A significant challenge in ET is the faithful reconstruction of signals that show a smooth or piecewise smooth change in the property of interest. Due to their very nature, ET reconstruction of such signals cannot be addressed using discrete algorithms [313]. Smooth and piecewise smooth signals can, however, be dealt with by CS-ET, since they can be sparsely represented; for example, in a wavelet domain. This prospect is significant as it offers the potential to substantially broaden the range of samples or phenomena that are amenable to study by ET. Therefore in this section, a systematic study using CS-ET and SIRT to reconstruct a test phantom consisting of a number of smooth objects is described.

8.3.4.1 Smooth phantom: simulation study

A phantom containing localised regions of smoothly varying intensity was created by superimposing a series of 2D Gaussian functions. Shown in Figure 8.16, the phantom was made challenging by including anisotropic shapes, concavities and regions of differing size and peak intensity. Simulated tilt-series were generated for maximum tilt angles of $\pm 90°$, $\pm 80°$, $\pm 70°$ and $\pm 60°$ and for tilt increments of $2°$, $5°$, $10°$ and $20°$. The maximum intensity of the phantom was 1, and no additional scaling was applied to the simulated projections, which had a mean intensity of 65 and a maximum intensity of approximately 160. The projections were corrupted by Gaussian noise with a standard deviation of 5.

A separable Coiflet DWT with 8 vanishing moments was used as the primary

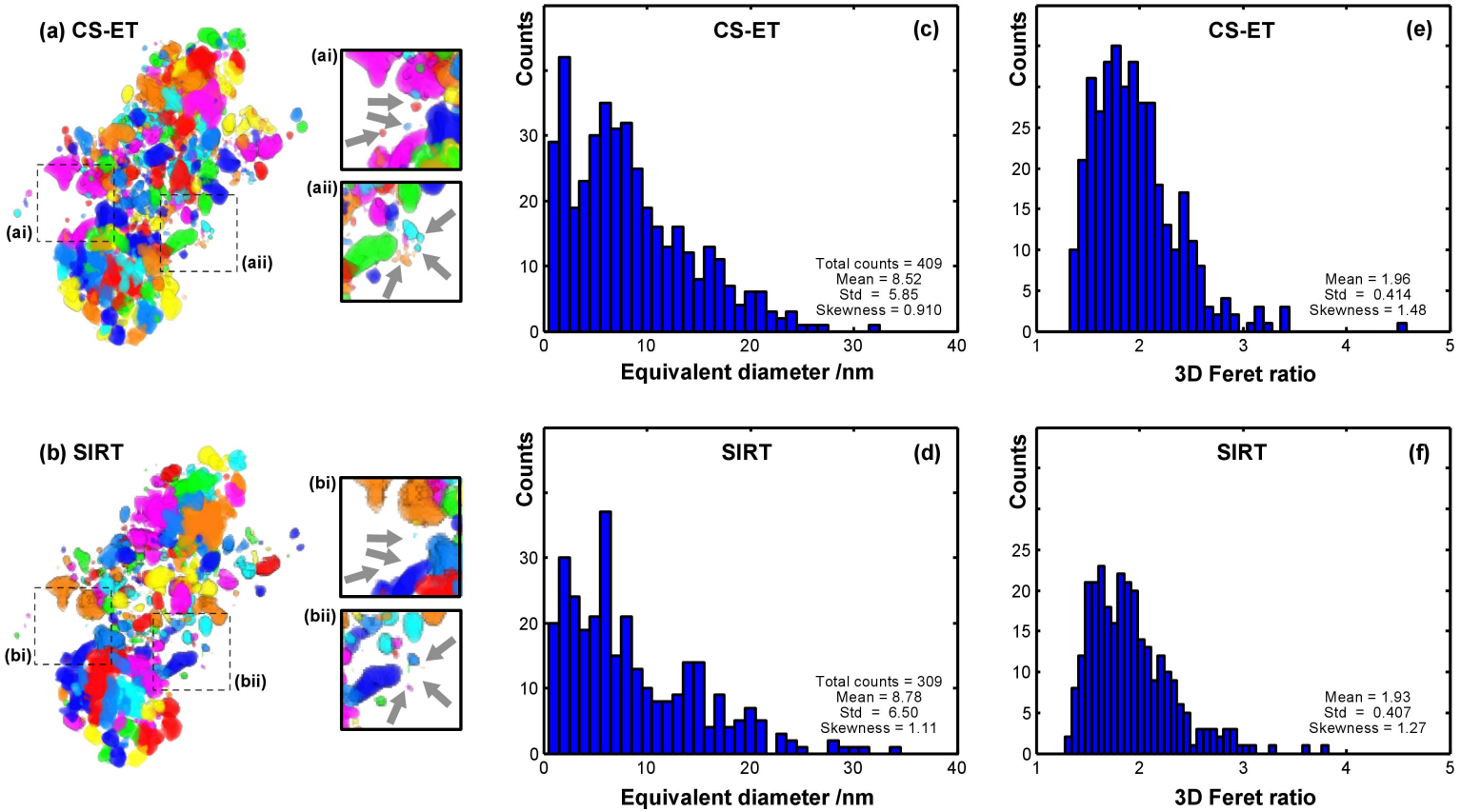

FIGURE 8.15: (a, b) 3D perspective view voxel projection visualisations of the segmented CS-ET and SIRT Ga-Pd nanoparticle reconstructions. Each nanoparticle or agglomerate of nanoparticles is shown with a colour that differs from those of its nearest neighbours. Grey arrows indicate small nanoparticles/agglomerates that are successfully captured in the segmented CS-ET reconstruction but are missing the segmented SIRT reconstruction. (c)-(f) Statistical distributions of the segmented nanoparticles and agglomerates in terms of their (c, d) equivalent diameter and (e, f) 3D Feret ratio.

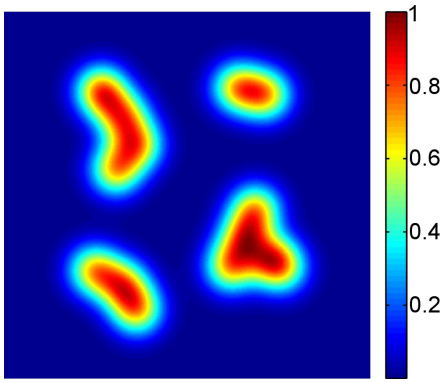

FIGURE 8.16: Test phantom containing regions of smoothly decaying intensity, including anisotropic shapes, concavities and regions of differing size and intensity.

sparsifying transform, implemented via the WaveLab software package for MATLAB [390]. In some CS reconstructions involving wavelets, small oscillatory artefacts may appear in the reconstructions due to false detection of fine-scale wavelet coefficients. To mitigate such artefacts it is suggested to simultaneously apply a small TV penalty during the reconstruction [360]. However, in the reconstructions shown here this was not found to be necessary, and the addition of a small TV weighting was in general detrimental, leading to a false broadening of the smooth objects. Therefore no TV penalty was applied (or equivalently λ_{TV} was set to 0). It was on the other hand, found beneficial to additionally enforce sparsity in the image domain, using a small weighting (i.e. λ_I value) relative to that of the wavelet sparsity weighting (λ_W value). The λ_I and λ_W used ranged between 0.05 and 0.2, and between 0.5 and 1, respectively; the particular values being chosen to provide optimal reconstructions for each simulated tilt-series. The enforcement of sparsity in the image domain helped to reduce missing wedge artefacts, while the imposition of wavelet domain sparsity promoted recovery of the smooth decay of the localised intensities.

The CS-ET and SIRT reconstructions for each of the combinations of maximum tilt angle and tilt increment are shown in Figures 8.17 and 8.18. Qualitatively, it can be seen that at each of the tilt ranges/increments, CS-ET yields a reconstruction that has a much closer resemblance to the phantom than that provided by SIRT. This is confirmed quantitatively by the much smaller phantom errors for the CS-ET reconstructions compared to SIRT, shown in Table 8.4 and plotted in Figure 8.19 (note that different vertical axis ranges have been used in Figures 8.19a and b).

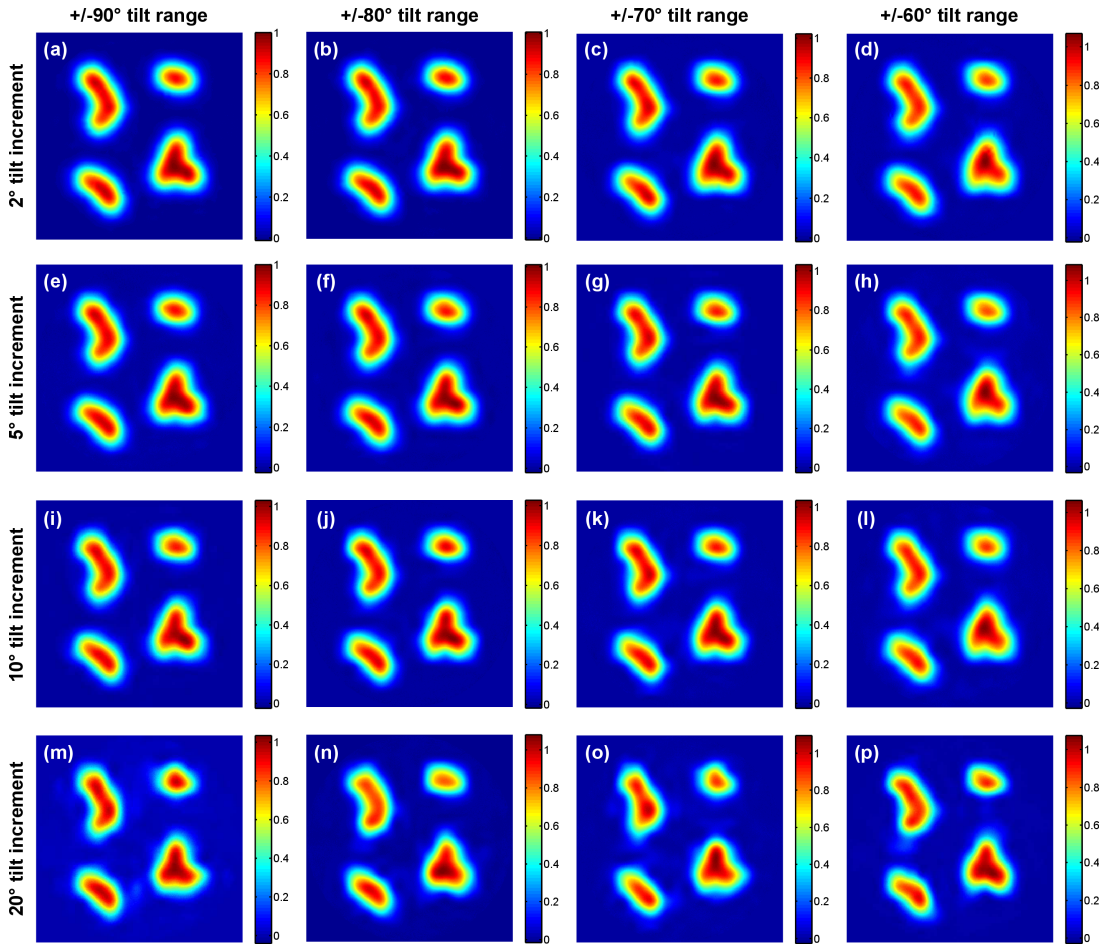

FIGURE 8.17: CS-ET reconstructions from simulated tilt-series projections of the phantom shown in Figure 8.16. The maximum tilt angle and tilt increment of the projections used for each reconstruction is denoted by the column and row headings, respectively. Each reconstruction has been assigned the same colour map across its respective full intensity range.

The projection data errors (Table 8.4) follow a similar trend to those seen in the previous case studies, in that the projection data errors of the CS-ET reconstructions with respect to the clean sinograms are much smaller than those with respect to the noisy sinograms, indicative of the denoising achieved by CS-ET. In this case study, the projection data errors of the CS-ET reconstructions are consistently much lower than those of the SIRT reconstructions, emphasising the substantially higher fidelity of the CS-ET reconstructions in general.

The efficacy of the denoising and successful recovery of the smooth decay of the objects using CS-ET is further reinforced by taking intensity profiles across the objects in the phantom and reconstructions, shown in Figure 8.20 for the $\pm 80°$ and $\pm 60°$ reconstructions as examples. There it is clear that the smooth variations in the phantom are well recovered using CS-ET, while in the SIRT reconstructions the noise level is significant and the intensity profiles oscillate.

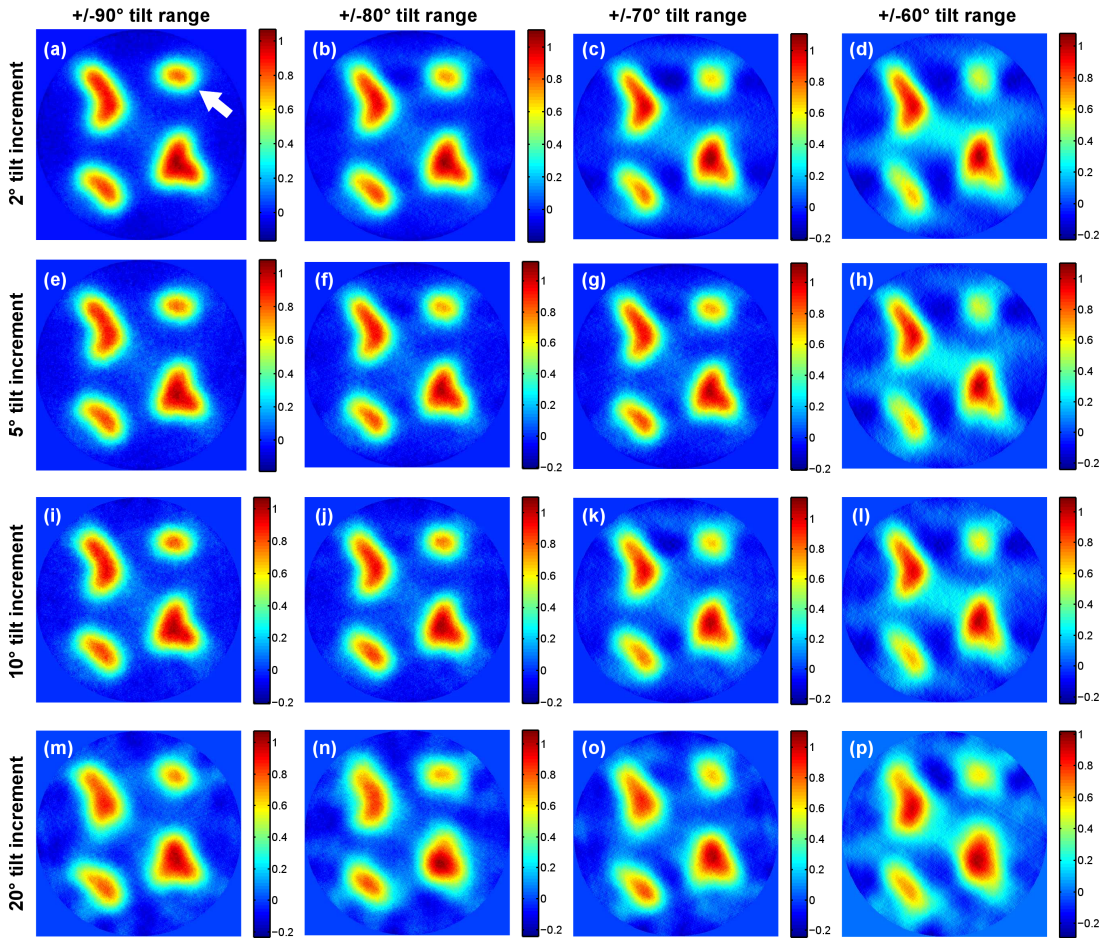

FIGURE 8.18: SIRT reconstructions from simulated tilt-series projections of the phantom shown in Figure 8.16. The maximum tilt angle and tilt increment of the projections used for each reconstruction is denoted by the column and row headings, respectively. Each reconstruction has been assigned the same colour map across its respective full intensity range. The arrow in (a) indicates one of the smooth objects where the false elongation in the missing wedge (vertical) direction, and a decrease in reconstructed intensity as the maximum tilt angle decreases and/or tilt increment increases, is particularly apparent.

Some care must be taken in interpreting trends in the data, especially when considering reconstructions from very few projections. When only a small number of projections are used for reconstruction, the particular angles of the projections in relation to the morphology of the phantom take on greater importance. This explains why the phantom error for the $\pm 60°$ and $20°$ tilt increment CS-ET reconstruction (Figure 8.17p) is slightly lower than that for the $\pm 70°$ and $20°$ tilt increment reconstruction (Figure 8.17o) - and the former is visibly of higher fidelity - as the projections in $\pm 60°$ and $20°$ tilt increment tilt-series capture more favourable information for this particular phantom. Nonetheless, some clear trends can be observed and further key comparisons be made between the CS-ET and SIRT reconstructions. In particular, it is readily

seen that as the tilt range is reduced (for example, by comparing Figures 8.18a-d), the SIRT reconstructions show significantly worsening false elongation in the missing wedge (vertical) direction. By contrast (see for example, Figures 8.17a-d), the false elongation is largely mitigated in the CS-ET reconstructions. This is again confirmed by the trends in the phantom errors and intensity profiles. The SIRT phantom errors (Figure 8.19b) increase sharply as the tilt range is reduced, while those of the CS-ET reconstructions (Figure 8.19a), as well as being consistently much lower, also rise more modestly. In Figure 8.20, the intensity profiles for the CS-ET reconstructions (Figures 8.20 a and b) closely follow those of the phantom, but the false elongation visible in the intensity profiles from the SIRT reconstructions, indicated in Figures 8.20c and d, is clearly significant.

Also visible as the tilt range is reduced, and (to a lesser degree) as the tilt increment is increased, is that the reconstructed intensities of the smooth objects in the SIRT reconstructions degrade, falling below the true value of the phantom. This is particularly evident for the small oval shaped object in the top right hand area, indicated by the arrow in Figure 8.18a. This is also visible in the intensity profiles in Figures 8.20c and d, where the profiles from the SIRT reconstructions fall below that of the phantom, significantly so in the reconstructions from the $\pm 60^\circ$ simulated tilt-series. The poor recovery of the intensity of smaller objects by SIRT was noted in the previous case studies on piecewise constant phantoms and clearly manifests for smooth objects as well. Once again, as highlighted in Figures 8.20b and c, the CS-ET reconstructions show a much more accurate recovery of the intensities, regardless of the size of the object, and even in the case of a large missing wedge and/or large tilt increment.

Even for the most extreme case of a $\pm 60^\circ$ tilt range and a 20° tilt increment, the CS-ET reconstruction (Figure 8.17p) still reveals the morphologies, smooth decay and relative intensities of the objects to a good degree of accuracy, while in the equivalent SIRT reconstruction (Figure 8.18p), or even SIRT reconstructions using many more projections, this information is severely distorted. Overall, this case study shows the feasibility of high-fidelity reconstruction of smooth signals via CS-ET, including from a very small number of well-chosen projections. This opens the door to a range of new investigations via ET, a first example of which is shown in the next section.

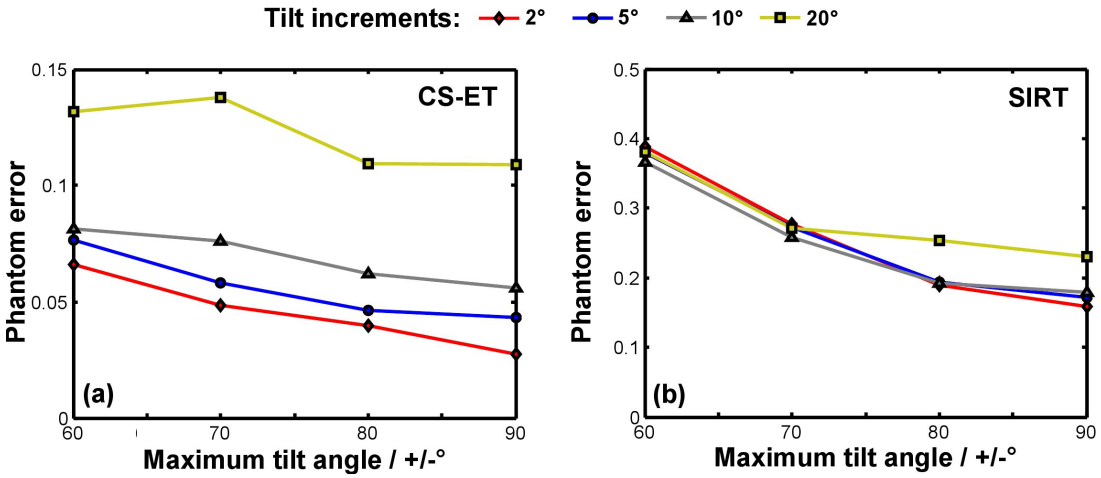

FIGURE 8.19: Phantom errors for the (a) CS-ET and (b) SIRT reconstructions shown in Figures 8.17 and 8.18. Note that different vertical axis ranges have been used for (a) and (b).

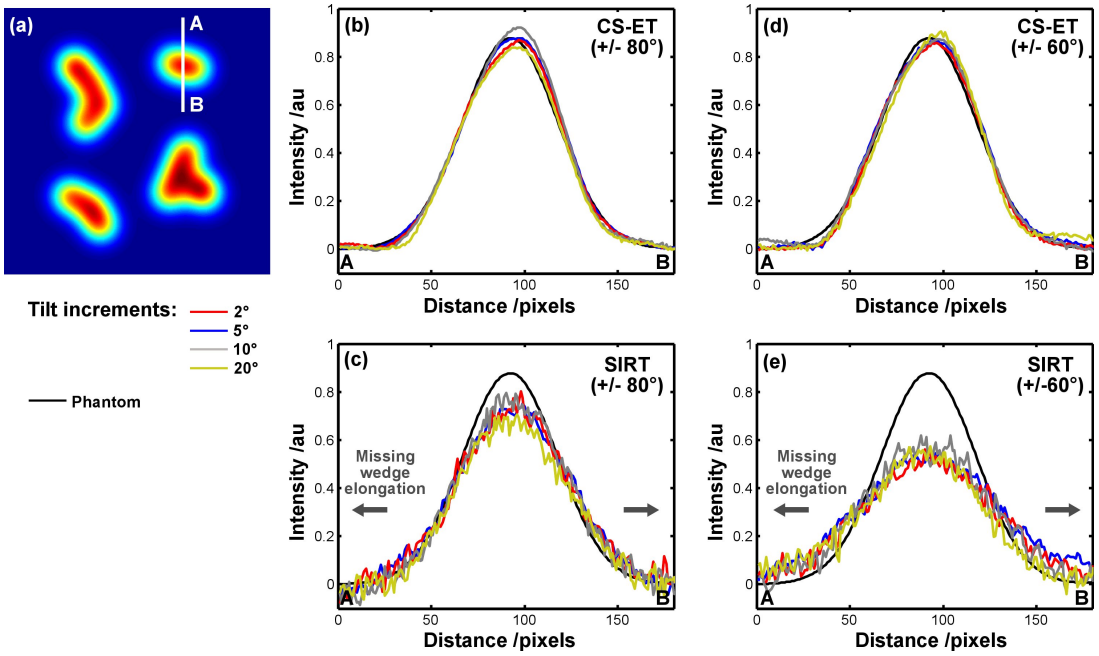

FIGURE 8.20: Intensity profiles from the smooth phantom and corresponding reconstructions from simulated tilt-series projections, taken at the position indicated in (a). Profiles from the (b, d) CS-ET and (c, e) SIRT reconstructions are shown for reconstructions from simulated tilt-series with different tilt increments and maximum tilt angles of $\pm 80°$ and $\pm 60°$.

Table 8.4: Phantom and projection data errors for the smooth phantom reconstructions shown in Figures 8.17 and 8.18. The phantom errors are plotted in Figure 8.19.

Data	Reconstruction algorithm	Phantom error	Projection data error (clean sinogram)	Projection data error (noisy sinogram)
±90° *tilt range*				
2° tilt increment	CS-ET	0.0275	0.0115	0.0631
	SIRT	0.159	0.0973	0.112
5° tilt increment	CS-ET	0.0433	0.0178	0.0631
	SIRT	0.172	0.0983	0.108
10° tilt increment	CS-ET	0.0561	0.0221	0.0637
	SIRT	0.179	0.100	0.106
20° tilt increment	CS-ET	0.109	0.0287	0.0658
	SIRT	0.231	0.106	0.109
±80° *tilt range*				
2° tilt increment	CS-ET	0.0399	0.0152	0.0630
	SIRT	0.190	0.102	0.115
5° tilt increment	CS-ET	0.0462	0.0184	0.0636
	SIRT	0.194	0.102	0.111
10° tilt increment	CS-ET	0.0619	0.0237	0.0643
	SIRT	0.193	0.104	0.108
20° tilt increment	CS-ET	0.109	0.0400	0.0718
	SIRT	0.254	0.107	0.108
±70° *tilt range*				
2° tilt increment	CS-ET	0.0485	0.0135	0.0627
	SIRT	0.277	0.113	0.124
5° tilt increment	CS-ET	0.0580	0.0197	0.0641
	SIRT	0.272	0.114	0.120
10° tilt increment	CS-ET	0.0759	0.0266	0.0667
	SIRT	0.258	0.114	0.116
20° tilt increment	CS-ET	0.138	0.0399	0.0752
	SIRT	0.271	0.114	0.113
±60° *tilt range*				
2° tilt increment	CS-ET	0.0658	0.0156	0.0623
	SIRT	0.389	0.116	0.127
5° tilt increment	CS-ET	0.0765	0.0190	0.0634
	SIRT	0.379	0.118	0.123
10° tilt increment	CS-ET	0.0812	0.0216	0.0625
	SIRT	0.366	0.122	0.122
20° tilt increment	CS-ET	0.132	0.0458	0.0744
	SIRT	0.381	0.124	0.124

8.4 3D imaging of localised surface plasmon resonances via CS-ET

8.4.1 Introduction

The phenomenon of localised surface plasmon resonance (LSPR) gives rise to novel optical properties in metallic nanoparticles [403]. Nanoparticle size, shape, composition and environment are known to dictate the resonant energy and spatial morphology of LSPR modes [404, 405]. The intricate sensitivity to these factors has engendered a great deal of attention towards potential applications; spanning photonics, optoelectronics, catalysis, photovoltaics and sensing [403, 404, 406]. Correspondingly there is a pressing need to better understand LSPR.

Monochromated STEM-EELS in the low-loss region of the EEL spectrum offers a unique combination of spatial and energy resolution to characterise LSPRs [407, 408]. Just as for conventional 2D imaging modes in TEM though, while 2D EELS-LSPR 'maps' have enabled considerable insight, they neglect potentially critical information about the 3D LSPR morphology.

In this section, the results from a collaborative project [293][9] are described, where STEM-EELS, NMF and CS-ET have been used to achieve, for the first time, experimental 3D imaging of LSPR morphology. Aspects of this study directly implicated in the CS-ET reconstruction are described here. First, the salient experimental methods are described, followed by justification that the EELS-LSPR signal is amenable to tomographic reconstruction. The 3D reconstruction results are then presented and discussed. Further specific details relating to the data acquisition, spectral processing and interpretation of the plasmonic response can be found in [293].

8.4.2 Methods

8.4.2.1 Tilt-series acquisition

Using a monochromated FEI Titan 60-300 X-FEG (S)TEM, operated at 300 kV, a tilt-series of STEM-EELS spectrum-images of a 100 nm silver nanocube resting on a 30 nm thick amorphous SiN membrane was acquired at 0° and then at every 15°, from -60° to -15° and +15° to +60°, relative to a [100] cube axis

[9]STEM-EELS acquisition was performed by Dr Olivia Nicoletti, and the simulations and spectral analysis by Dr Francisco de la Peña. CS-ET reconstruction was performed in close collaboration with Dr Daniel Holland, who implemented the reconstructions. All authors interpreted and discussed the experimental results.

perpendicular to the electron beam. Each spectrum-image was 214 nm x 201 nm (152 pixels x 143 pixels) in area, with 2048 channels in the spectral dimension and a dispersion of 0.01 eV per channel. The tilt increment was chosen as a compromise between obtaining sufficient sampling of the 3D object and limiting possible beam damage effects, build-up of carbonaceous contamination, or both. Although spectrum images were acquired across a ±60°tilt range, the C_{4v} $(4mm)$ symmetry of the cube-substrate system means that those on either side of 0° are related by mirror symmetry. Therefore, as a minimum, only the spectrum images on one side of 0° actually need to be considered in the analysis. Here, only the first half of the recorded tilt-series have been used to minimise the effects of damage or contamination on the analysis. Figure 8.21 illustrates the geometry of the experiment, along with representative EEL spectra.

8.4.2.2 Spectral processing

NMF (section 2.3, and justified in section 8.4.3) was used to identify five components related to surface plasmon excitations and hence to obtain EELS-LSPR maps. An example of the NMF spectral components, weighted according to the value for a single pixel from the spatial distribution maps, is shown in Figure 8.22 (coloured areas $\alpha - \varepsilon$). Each component, as shown in Figure 8.23a, is dominated by a single peak, associated with the LSPR mode. The corresponding normalised spatial components, the EELS-LSPR maps, are shown in Figure 8.23b.

8.4.2.3 CS-ET reconstruction (with symmetry constraint)

To obtain a high-fidelity ET reconstruction from the very limited number of EELS maps, CS-ET was used along with imposition of the C_{4v} $(4mm)$ symmetry of the cube-substrate system during reconstruction. As the LSPRs can be considered as localised gradually varying functions, they are amenable to sparse representation using a DWT. Similar to section 8.3.4, a separable Coiflet DWT with 8 vanishing moments was used as the sparsifying transform, although no additional image domain sparsity constraint was used here. The reconstruction was performed in a 'fully 3D' manner, as described in section 8.2.1. This provided consistency of regularisation throughout the 3D volume and enabled imposition of the symmetry constraints.

As a preceding step to the tomographic reconstruction, a normalisation of the EELS maps was performed, to compensate for the variation in the probability of excitation arising from a small amount of contamination in the irradiated area

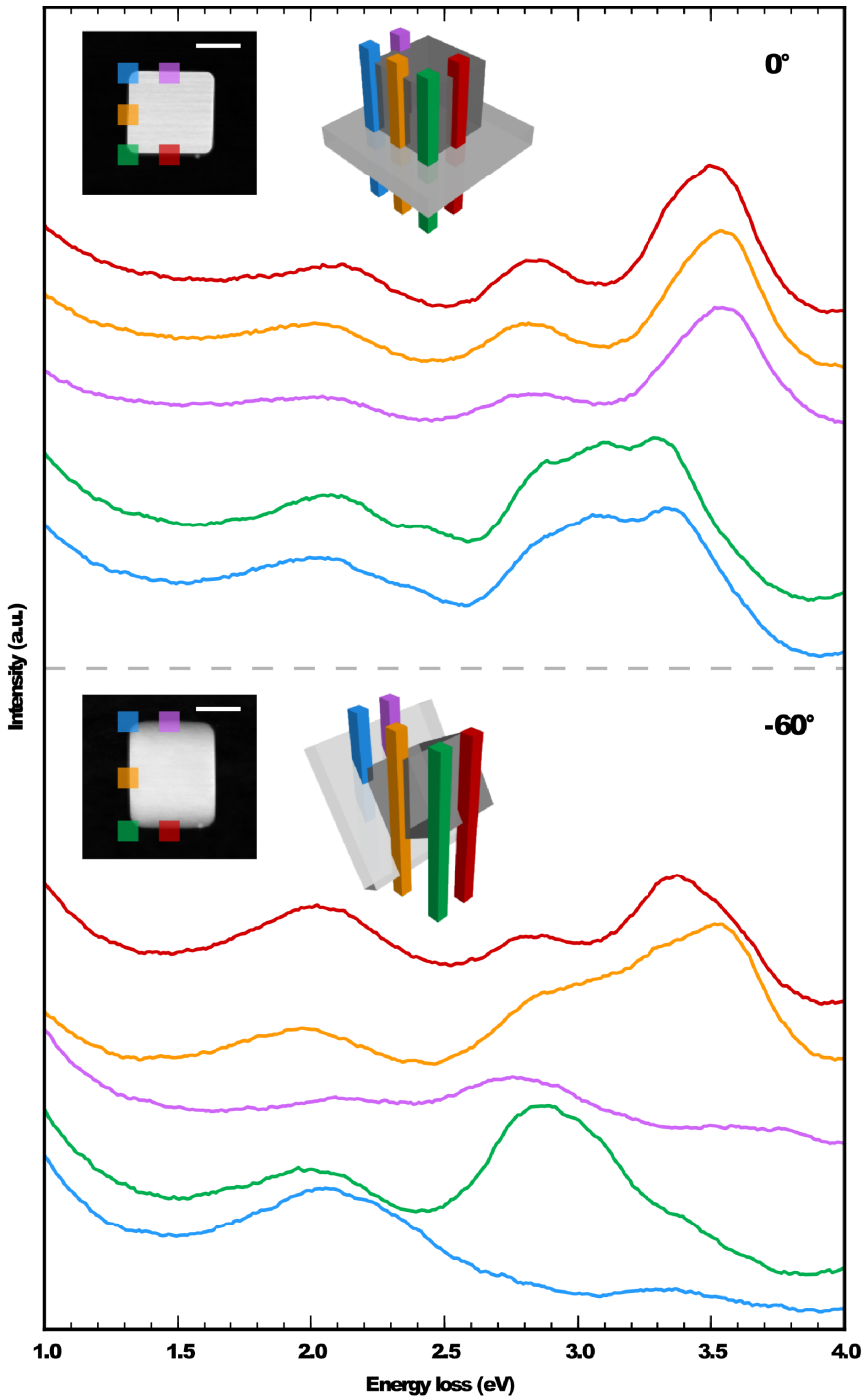

FIGURE 8.21: Selected-area spectra (unprocessed) corresponding to the areas highlighted in the insets, acquired at 0° tilt (top) and at -60° tilt (bottom). The selected-area squares, and square prisms, in the schematics, highlight 25.4 nm x 25.4 nm (18 x 18 pixels) areas from which individual spectra have been extracted and summed. Insets, ADF-STEM images of a silver nanocube resting on a 30 nm-thick SiN membrane at 0° tilt (top) and at -60° tilt (bottom). a.u., arbitrary units. Scale bars: 50 nm.

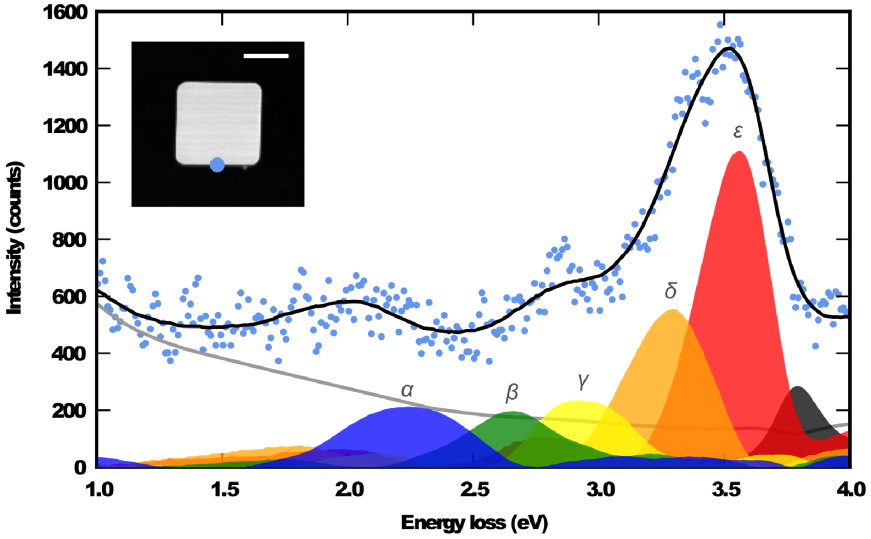

FIGURE 8.22: NMF spectral components weighted according to the value for a single pixel from the spatial distribution maps, at the position indicated by the large blue marker in the inset. The unprocessed spectrum (blue dots) is shown together with five spectral components, labelled $\alpha, \beta, \gamma, \delta$ and ε, related to the LSPRs (areas in blue, green, yellow, orange and red), one spectral component related to the silver volume plasmon at 3.8 eV (black area) and a combination of spectral components related to the zero-loss peak tail, low-energy dipole loss and effects of contamination (grey line). The sum of the eight spectral components is also shown (black line). Scale bar: 50 nm.

increasing through the tilt-series. This was achieved by bringing the respective integrated intensities of the maps for each mode to the same level as the map with the highest integrated intensity among the maps for that mode.

The symmetry of the cube-substrate system was firstly exploited to attain a high-quality sampling of Fourier space over a full $\pm 60°$ tilt range, by using the first half-set of tilt-series EELS maps at their respective angles, as well as the same maps transformed by mirror symmetry in the plane of the tilt axis for the positive angles. Additionally, symmetry-based enhancement was effected during reconstruction by combining, at each iteration in the reconstruction processes, the current reconstructed 3D volume with the same volume rotated by 90° in the plane of the substrate (akin to a dual-axis reconstruction approach [236–239] used in conventional ET), followed by enforcement of symmetry of the wavelet-transformed reconstruction in the {110} planes parallel to the beam direction.

8.4.2.4 3D visualisation

The voxel projection visualisations of the reconstructed 3D volumes, shown in Figure 8.24, were generated using the volume-rendering module in Avizo Fire (Visualization Sciences Group). To exclude false regions of localised intensity that arose primarily at the periphery of some of the reconstruction volumes

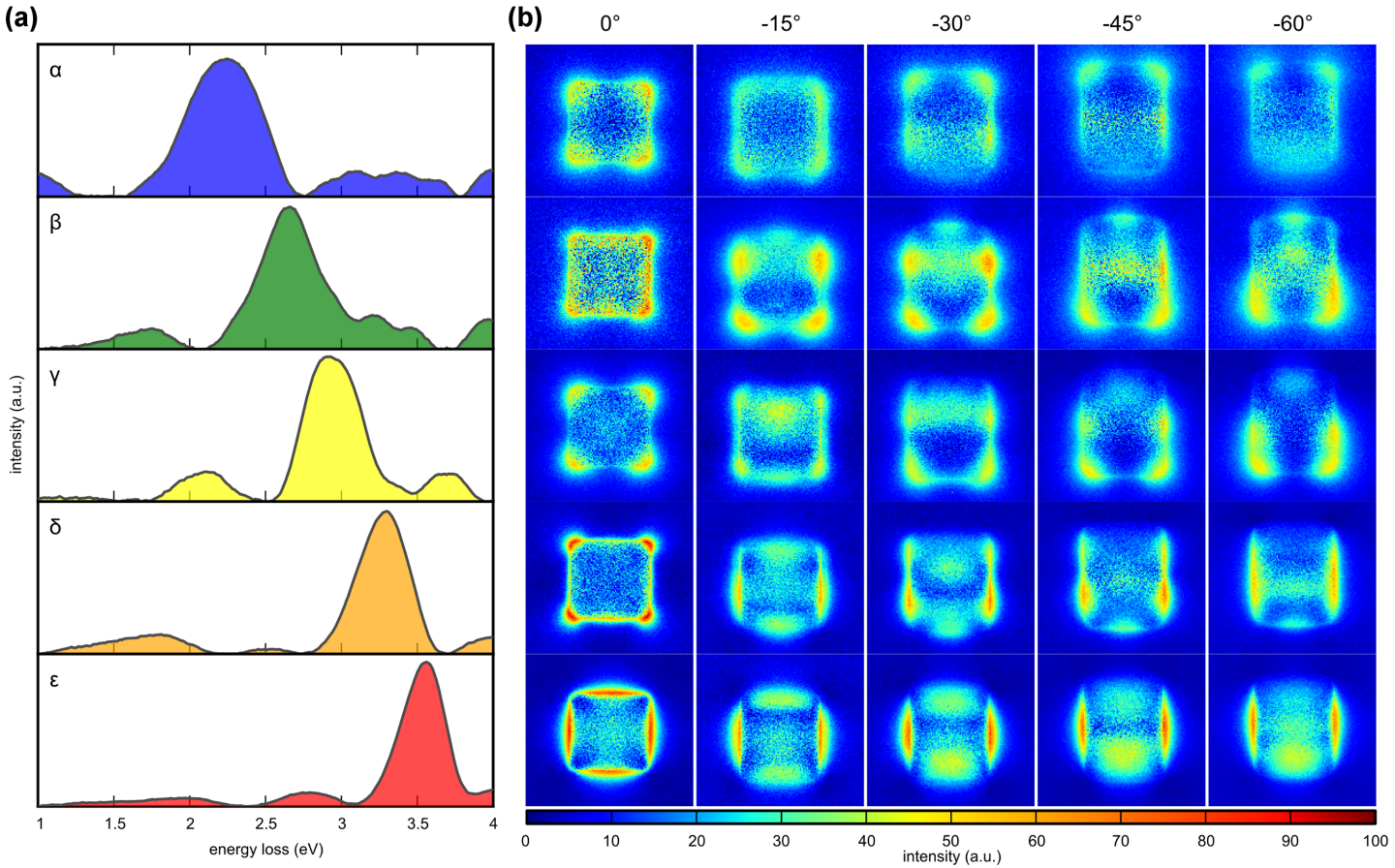

FIGURE 8.23: (a) LSPR spectral components ($\alpha, \beta, \gamma, \delta$ and ε) resulting from applying NMF to the spectrum images at different tilt angles, in order of increasing energy loss. (b) Normalised EELS maps corresponding to the five NMF components shown on the left. In the tilted images, the substrate is closer to the observer in the top half of the image.

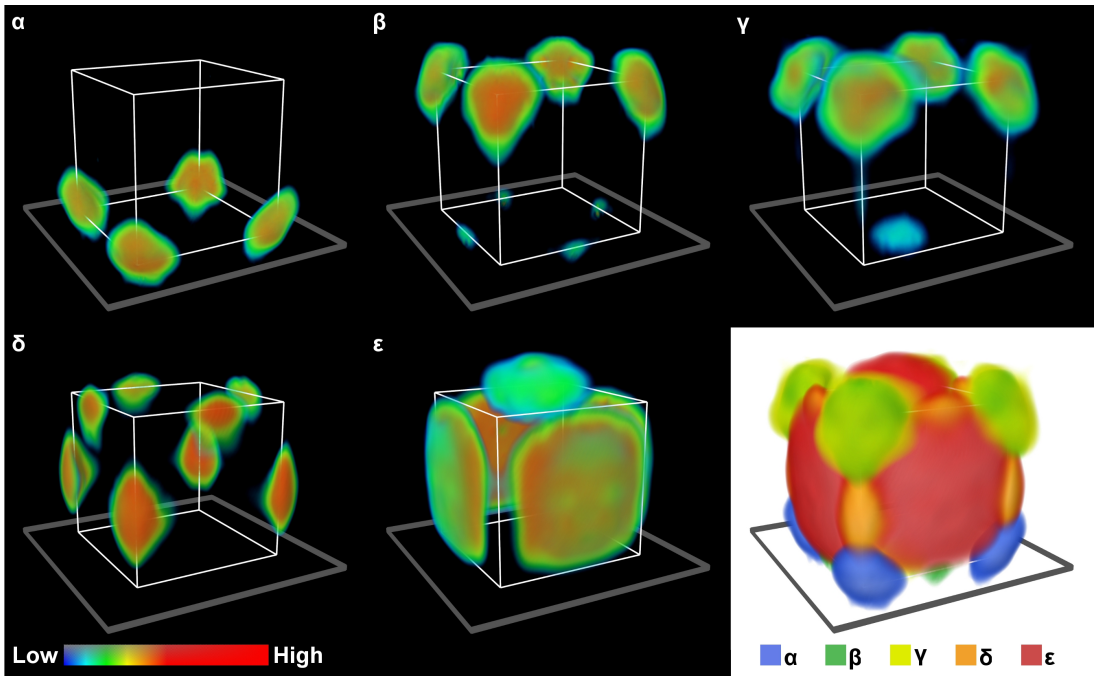

FIGURE 8.24: 3D images ($\alpha - \varepsilon$) obtained by CS-ET reconstruction of the EELS maps of the respective LSPR components in Figure 8.23. The visualisations are voxel projections of the reconstructed 3D volumes. The colour bar indicates the LSPR intensity. The image in the bottom right of the figure shows a combined 3D rendering of all the components. See also Videos 4 and 5 in Appendix A.

(owing to the imperfections involved in seeking a tomographic reconstruction from so few tilt-series images), the voxel projection views have been limited to the volume immediately surrounding the nanocube and LSPRs. Similarly, to enable clear visualisation of the regions of maximal LSPR intensity, each voxel projection shows about the top 40-70% most intense voxels (the particular lower bound being chosen according to the prominence of background intensities, or those due to artefacts, in each reconstruction), with linearly increasing opacity from fully transparent at the minimum to fully opaque at the maximum. Some regions of weaker localised intensity potentially corresponding to weaker LSPR are present in the 3D reconstructions of some components, but because their intensities are appreciably lower than the maximal LSPR intensity, they are not displayed in the visualisations of Figure 8.24. The outline of the cube superimposed on the voxel projections is based on the ADF images.

8.4.3 EELS-LSPR maps and the tomographic 'projection requirement'

At the present time, consideration of the EELS-LSPR signal for ET reconstruction is in its infancy. The signal is considerably more involved than those conventionally used in ET, and it does not trivially, or necessarily universally, satisfy the tomographic 'projection requirement' advocated in section 5.3.2.1.

The manner or scenarios in which assumption of an EELS-LSPR 'projection' may be made has been set out recently by Nicoletti et al. [293], as well as by Hörl et al. [409]. In spite of intricacies, these studies have shown that the EELS-LSPR signal can, under certain experimental conditions or approximations, be regarded as constituting a projection of a scalar quantity, sufficient for a practicable tomographic experiment to be undertaken. Specifically, Nicoletti et al. [293] describe the particularities for the silver nanocube studied here that validate reconstruction via a conventional tomographic approach. The salient assertions from [293] are summarised below in sections 8.4.3.1 and 8.4.3.2. Those of Hörl and Hoenester [409] are discussed along with the results and general discussion in section 8.4.4.

8.4.3.1 The nature of the EELS-LSPR signal

In the most general form, the electron energy-loss probability due to plasmon resonances for a fast electron travelling with constant velocity $\boldsymbol{\nu}$ along a straight-line trajectory $\mathbf{r} = (\mathbf{R}_0, z)$, where $\mathbf{R}_0 = (x_0, y_0)$ defines the impact parameter of the trajectory and z is the direction of travel, can be written as [410]:

$$\Gamma_{\mathrm{EELS}}(\mathbf{R}_0, \omega) = \frac{e}{\pi\hbar\omega|\boldsymbol{\nu}|}\int_{-\infty}^{\infty} \mathrm{d}z\, \mathrm{Re}[e^{-i\omega z/|\boldsymbol{\nu}|}\boldsymbol{\nu}\cdot\mathbf{E}_{\mathrm{ind}}(\mathbf{r},\omega)], \tag{8.3}$$

where $\mathbf{E}_{\mathrm{ind}}(\mathbf{r},\omega)$ represents the induced electric field vector acting back on the electron and $\hbar\omega$ is the energy loss ($\hbar$ is Planck's constant divided by 2π, ω the angular frequency and e the modulus of the electron charge).

It has also been shown recently [411] that, in the quasistatic limit, the LSPR loss probability, $\Gamma^{\mathrm{SP}}(\mathbf{R}_0,\omega)$ can be written as a linear combination of eigenspectra, each corresponding to a mode i composed as a spectral weighting factor $\mathrm{Im}(-g_i(\omega))$ and spatially varying basis functions $|\phi_i(\mathbf{R}_0, q)|^2$:

$$\Gamma^{\mathrm{SP}}(\mathbf{R}_0,\omega) = C\sum_i \mathrm{Im}(-g_i(\omega))|\phi_i(\mathbf{R}_0,q)|^2. \tag{8.4}$$

Here, C is a constant, $q = \omega/|\mathbf{v}|$, $g_i(\omega)$ is the response function, and $\phi_i(\mathbf{R}_0, q)$ is the Fourier transform of the induced potential associated with mode i:

$$\phi_i(\mathbf{R}_0, q) = \int_{-\infty}^{\infty} \mathrm{d}z\, \phi_i(\mathbf{R}_0, z) e^{-iz\omega/|\mathbf{v}|}. \tag{8.5}$$

In either case, that is considering Equation 8.3 or 8.4, it is apparent that the EELS-LSPR signal is more involved than a classical Radon-like integral of a scalar function, as is conventionally considered in ET (cf. Equation 5.1).

8.4.3.2 Circumstances & approximations permitting scalar tomographic reconstruction

Three key aspects need to be addressed with regards to Equations 8.3 and 8.4 to obtain an EELS-LSPR tilt-series of projections that is amenable to a scalar tomographic reconstruction. These concern (i) approximations that apply to a 'thin' particle; (ii) analogies between the modal decomposition and that achieved by NMF; (iii) accounting for the vectorial nature of the excitation.

(i) Thin particle approximation

For localised, low energy modes of isolated, optically isotropic nanoparticles, it is possible to make the approximation that the charge distribution of the electron beam takes the form a of a 'charged wire' [412], and that the change in phase term $e^{-i\omega z/|\mathbf{v}|}$ in Equation 8.3 across the spatial extent of the nanoparticle is small enough that its effect on the reconstruction in minimal.

Formally, further to Equation 8.3, the loss probability $\Gamma_{\mathrm{EELS}}(\mathbf{R}_0, \omega)$ in the quasistatic limit in terms of the screened interaction $W(\mathbf{R}_0, z, \mathbf{R}_0, z', \omega)$ can be written as [410]:

$$\Gamma_{\mathrm{EELS}}(\mathbf{R}_0, \omega) = \frac{e^2}{\pi\hbar\omega|\mathbf{v}|^2} \int_{-\infty}^{\infty} \mathrm{d}z\mathrm{d}z' \cos\Big(\frac{\omega(z-z')}{|\mathbf{v}|}\Big) \mathrm{Im}[-W(\mathbf{R}_0, z, \mathbf{R}_0, z', \omega)], \tag{8.6}$$

where the induced potential ϕ can be expressed in terms of W:

$$\phi(\mathbf{R}_0, z, \omega) = -\frac{e}{|\mathbf{v}|} \int_{-\infty}^{\infty} \mathrm{d}z'\, W(\mathbf{R}_0, z, \mathbf{R}_0, z', \omega) e^{-i\omega z'/|\mathbf{v}|}. \tag{8.7}$$

In the thin particle approximation [411] $z - z' \ll |\mathbf{v}|/\omega$, the loss probability is:

$$\lim_{z-z' \ll |\mathbf{v}|/\omega} \Gamma_{\mathrm{EELS}}(\mathbf{R}_0, \omega) = \frac{e}{\pi\hbar|\mathbf{v}|} \int_{-\infty}^{\infty} \mathrm{d}z\, \mathrm{Im}[\phi(\mathbf{R}_0, z, \omega)]. \tag{8.8}$$

In words, Equation 8.8 shows that, under the thin particle approximation, the loss probability is a projection of the imaginary part of the potential over the electron trajectory.

Given the size of the cube, the very low energy losses and the energy and trajectory of the electrons, the tomographic experiment here on the silver nanocube can be considered to fall within this approximation.

(ii) Modal decomposition

Under the assumption that the quantity $z\omega/|\mathbf{v}|$ is small (the thin particle approximation [411]), the Fourier transform of Equation 8.5 approximates to a simple projection. In this case, the basis functions for each mode in Equation 8.4 are approximately equal to the square modulus of a potential, associated with that mode, projected parallel to the beam trajectory.

There is a strong similarity between the NMF decomposition of the EELS spectra and the modal decomposition of Equation 8.4. It is unlikely that the NMF decomposition will correspond exactly to basis functions of the modal decomposition, but it is possible to consider that the spatial distribution, or EELS-LSPR map, for each NMF component resembles a quantity related to the basis functions in the modal decomposition.

It then follows, in analogy to the modal decomposition, that each EELS-LSPR map can be regarded as if it were the projection of a scalar quantity that is related to the magnitude of the potential as seen by the electron that induces it.

(iii) Vectorial nature of the excitation

From (i) and (ii) it has been established that the EELS-LSPR maps can be related to an induced potential, a scalar quantity, but still one that, in general, depends on the trajectory of the electron because of the anisotropy of the crystalline (atomic) structure or the nanoparticle shape. However, in favourable cases, with careful consideration, a scalar tomographic reconstruction can be valid and interpretable, as exemplified here.

Firstly, in general, the dielectric function of an anisotropic material, $\varepsilon(\mathbf{r})$, is a tensor and so will lead to variation in the induced potential with crystallographic orientation. However, for the cubic crystals of interest here (nanoparticles of silver) the dielectric function is scalar and will thus be invariant with respect to crystal orientation.

Secondly, the geometry of the particle, which determines the geometry of the plasmonic excitation [411], imposes symmetry constraints on the modes for

given trajectories and, in general, mode excitations will therefore show a variation with the angle of incidence similar to that of a dipole or higher multipoles. In principle, this would seem immediately to preclude any valid scalar tomographic reconstruction of modes (or components). However, as shown in a simulation below, and further supported by the experimental results, the energy degeneracy of symmetry-equivalent modes can be exploited to compensate approximately for the effects of the trajectory dependency.

Figure 8.25 shows a series of tomographic reconstructions of five spectral features (C_1, C_2, C_3, E and F) identified in a tilt-series of simulated EELS spectra across the top face of a silver nanocube *in vacuo*. The only component that has reconstructed poorly is C_3, which can be explained using the symmetry of the excited multipolar fields.

The modes strongly excited in the simulations, which correspond to the four major components seen in the simulations, have dipole or quadrupole symmetry, and each is therefore triply degenerate [415, 416]. For each dipole and quadrupole, there are two degenerate modes with dipolar symmetry at the top face in perpendicular directions. As the cube is tilted, the reduction in the contribution to the energy loss from one dipolar field is compensated by an increase in the contribution of a perpendicular dipolar field. The net contribution from the two degenerate (or near-degenerate) dipolar fields, which, experimentally, would be reconstructed as a single component, gives an approximately uniform contribution to the energy loss across all tilt angles, and the component can therefore be reconstructed approximately using conventional scalar tomographic methods.

The top face C_3 component corresponds to a singly degenerate octupole mode [415, 416] that gives rise to a field at the face with quadrupolar symmetry. As the cube is tilted, the quadrupolar field contribution varies sinusoidally but, unlike the dipolar fields described above, there is no other degenerate (or near-degenerate) mode with the same symmetry available to compensate. This leads to a tomographic reconstruction of this mode with some significant negative values (Figure 8.25c), indicating a breakdown in the simple scalar approximation.

The experimental geometry is somewhat intriguing as the substrate breaks the top-bottom (z) symmetry of the cube, and dipole and quadrupole modes will thus not be triply degenerate but will be split into two degenerate (x and y) modes and a singly degenerate (z) mode. Furthermore, substrate-mediated hybridisation of the near-degenerate dipole, quadrupole and octupole modes leads to a more complex situation than in the simulation described above, but the

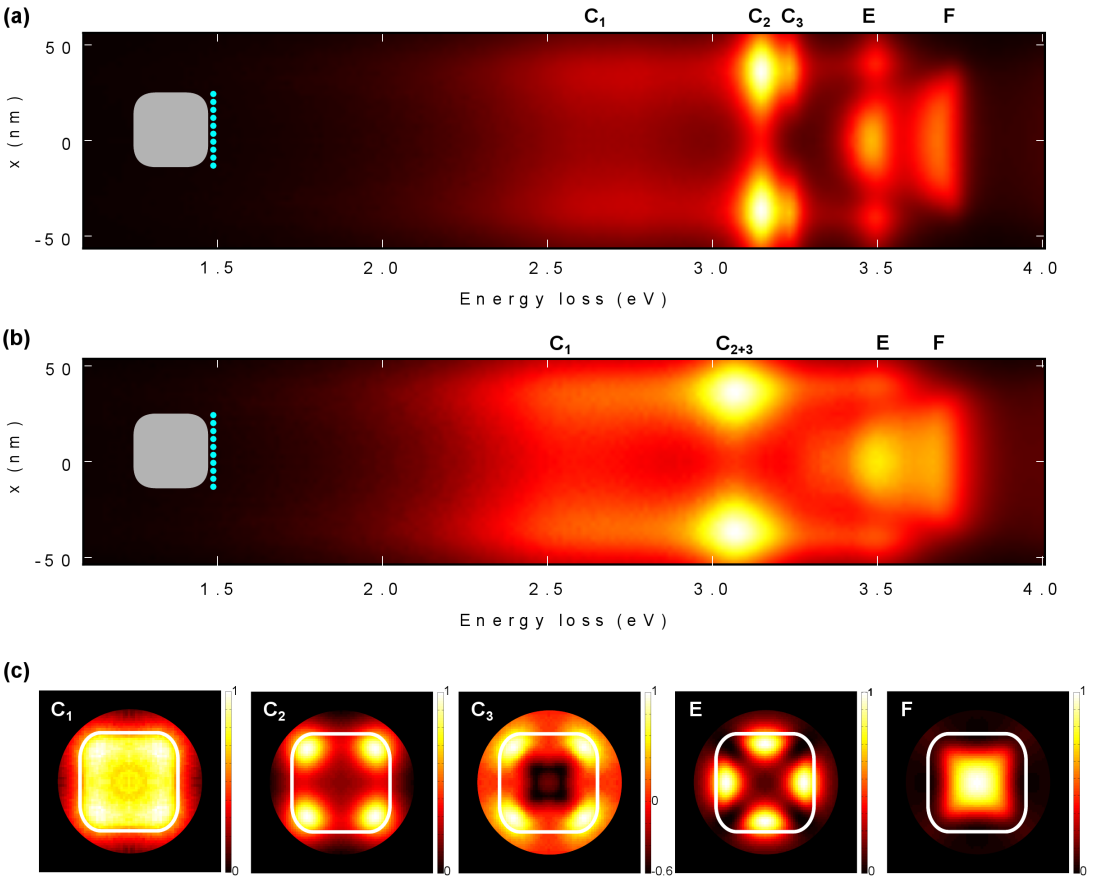

FIGURE 8.25: Discrete dipole approximation (DDA) EELS simulations of a silver nanocube. (a, b) DDA EELS simulated as functions of position (as shown by the blue dotted line) for a 100 nm silver cube with rounded corners in vacuum with dielectric function tabulated in ref. [413] (a), and for a 100-nm silver cube with rounded corners in vacuum with dielectric function tabulated in ref. [414] (b). (c) 2D tomographic reconstructions of the five spectral features identified in (a) and (b) (C_1, C_2, C_3, E and F), made from a tilt-series of simulated spectra in which the cube is rotated about a cube axis perpendicular to the beam. The five spectral features correspond to lowest-energy (dipole) corner (C_1), higher-energy corner (C_2 and C_3), edge (E) and face (F) components. Note that the individual components C_2 and C_3 are not separated if the dielectric tabulation in ref. [414] is used, as in (b). Each reconstruction is scaled independently. There are significant negative values only in the reconstruction of the C_3 component, which corresponds to a singly degenerate octupole mode. Tomographic reconstructions made from this tilt-series were obtained using a conventional SIRT algorithm [16] implemented using the Tomo3D software package [297].

'compensation effect' of degenerate and near-degenerate modes is still applicable, allowing for example what seems to be a valid reconstruction of corner modes from the experimental data.

8.4.4 3D reconstruction: results and discussion

The success of the 3D CS-ET reconstruction, Figure 8.24, for each of the LSPR components from Figure 8.23 supports, empirically, the assertion that the LSPR signal probed in this experiment is amenable to tomographic reconstruction. The fidelity of the reconstructions is further confirmed by re-projecting the reconstructed volumes encompassing the nanocube and LSPRs at the same angles as the experimental data acquisition, as shown in Figure 8.26. While inconsistencies can be seen in the EELS-LSPR maps of Figure 8.23, and these lead to some low intensity artefacts in the 3D reconstructions, the 'consistent' signal through the tilt-series that is valid in the tomographic sense is clearly dominant. However, the mismatches seen between the re-projections of Figure 8.26 and those of the original EELS-LSPR maps in Figure 8.23, which seem to be larger as trajectories become more parallel to the substrate, may, in part, be indicative of a breakdown of the aforementioned compensation effect of degenerate and near-degenerate modes. The spatial resolution in the reconstructions can be estimated as ca. 15 nm. A data set with more images may provide improved resolution, but this will ultimately be limited by the delocalised nature of the surface plasmon excitation.

Although in this case of a cube, the tilt-series of 2D EELS-LSPRS maps alone is instructive regarding the 3D distribution of the LSPRs, the 3D visualisation enables a more powerful interpretation [293]. Further, the investigation serves as valuable proof-of-principle that LSPR morphology is amenable to 3D tomographic reconstruction. This first step into visualising LSPRs in 3D should motivate further 3D imaging studies. Given the inherent empirical challenges in acquiring STEM-EELS tilt-series, it likely that CS-ET reconstruction, which is capable of dealing effectively with the paucity of data and the smoothly varying nature of LSPRs, will play a key role. Incorporating advanced prior knowledge, as has been done here regarding the LSPR mode symmetry, is likely to be important. This could include, for example, in addition to LSPR mode symmetry, imposing further constraint on the nature of the LSPR 'smoothness' (via the sparsifying transform), or very close involvement with simulation, such as model based reconstruction.

The study of Hörl et al. [409] is complementary to that presented here.

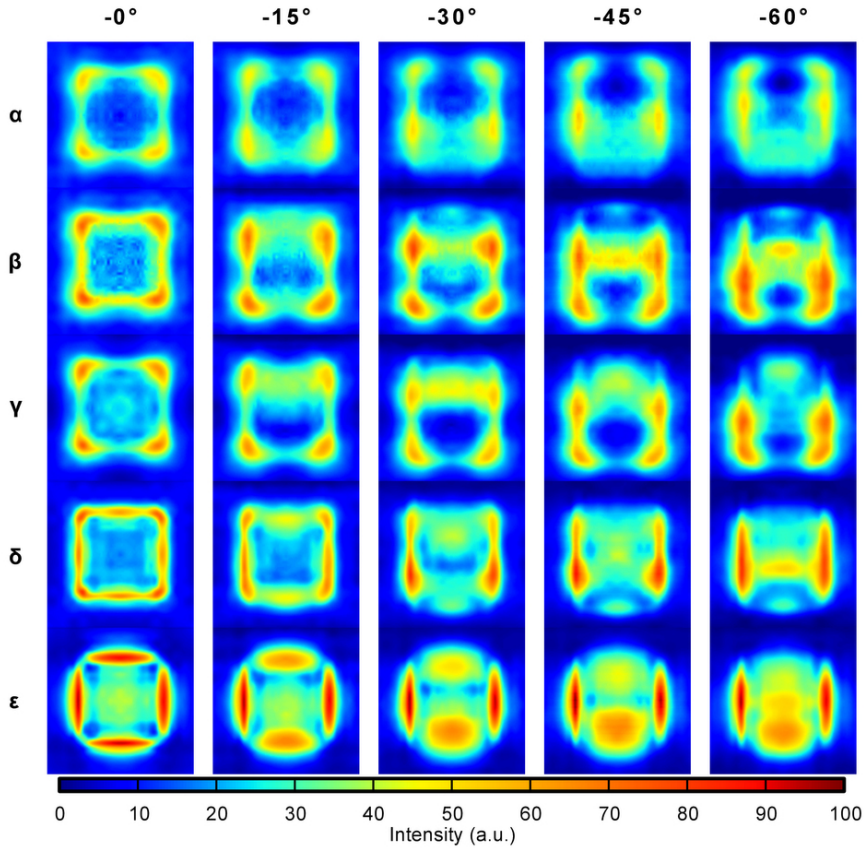

FIGURE 8.26: Re-projections of the reconstructed 3D volumes of the five LSPR components, at the same tilt angles as the experimental data acquisition. Letters $\alpha - \varepsilon$ correspond to those of Figure 8.23. The orientation is as in Figure 8.23, with the substrate-cube interface towards the top of the image at negative tilts. To exclude false regions of localised intensity that arose at the periphery of some of the reconstruction volumes (owing to the imperfections involved in seeking a tomographic reconstruction from so few tilt-series images), the re-projected volume was restricted to that immediately surrounding the nanocube and LSPRs.

Using a quasistatic approximation scheme together with a plasmon eigenmode expansion they similarly rephrase the EELS loss probability in terms of a tomographic projection (viz. a Radon transform) proposing and demonstrating, via simulations, the feasibility of plasmon-field tomography. In addition to classical tomographic reconstruction, via an inverse Radon type method, they also formulate the field extraction in terms of a model based inverse problem solvable by optimisation. This may provide a valuable approach for achieving 3D reconstruction when the conventional tomographic projection requirement is clearly violated.

Challenging yet potentially very rewarding advances would be the inclusion of relativistic effects, and the development of vector ET methods allowing reconstructions from arbitrary-shaped nanoparticles. Although with small modifications the present approach can be adapted to other geometries, for

objects of much lower symmetry a vector tomography method may be needed. Directly reconstructing a (vector) electric field from multiple tilt-series of EELS-LSPR maps may be theoretically possible [417], but it is clearly experimentally demanding.

8.5 Discussion

The rapidly growing exploitation of CS in many different fields is indicative of its efficacy and broad applicability. In this work it has been shown how ET can be pursued via a CS approach, and the merits of CS-ET demonstrated when applied to some very different data sets. Building on initial grounding studies [210, 211], this contribution has, in particular, described and demonstrated the use of different sparsifying transforms in CS-ET. Indeed, CS-ET may be applicable to any reconstruction of a nanoscale object that exhibits transform sparsity. The procedures of sparse image representation are well-developed, making CS-ET both powerful and widely applicable. Moreover, compared to discrete algorithms applied in ET [60, 209, 313], the prior knowledge of transform sparsity and its imposition during CS-ET reconstruction can be less strict, making CS-ET applicable to a range of different specimens, which may have complicated or partially unknown characteristics.

Indeed, as CS-ET is beginning to be embraced, a number of studies have arisen elsewhere. Goris et al. [211, 378] have applied a TV-based CS-ET algorithm to small (1-5 nm) and large (30 nm) gold nanoparticles, lead selenide-cadmium selenide core-shell nanoparticles and a needle-shaped silicon sample containing lead inclusions. Similarly, Monsegue et al. [306] have used an anisotropic TV algorithm that addresses elongation artefacts in the missing wedge direction, obtaining improved reconstruction of porous iron oxide nanoparticles.

Additionally, Goris et al. have recently used an image domain sparsity constraint in atomic-scale ET reconstruction of gold [259] or gold-silver [66] nanorods, using sets of high-resolution ADF-STEM images. Recalling section 7.3.2, this reconstruction strategy is based on the premise that each atomic potential can be considered as sufficiently localised in space, and therefore an atomic scale ET reconstruction that is concerned with recovering each atomic position should be inherently sparse. However, it is worth raising the notion that a more sophisticated transform that better captures the true image content could prove beneficial in future work. In this regard, atomic columns (or single

atoms) are typically approximated as displaying Gaussian profiles (e.g. [57]). Alternatively, Liu et al. [318] have recently used a 'dictionary learning' based CS-ET algorithm to reconstruct simulated atomic resolution images of a gold nanoparticle, in which the sparse basis is generated ('learned') empirically.

As well as ET reconstruction, CS can be used in other aspects of ET, as recently exemplified by Song et al. [388] concerning CS-inpainting of fiducial markers. There, cryo-ET projections of the surface layer of *Bacillus sphaericus*, which show short-range order, were found to be near sparse in the DCT domain, and cryo-ET projections of whole cells of *Caulobactor crescentus* were compressible by DCT. There have also been several reports of TV-based ET reconstruction in a biological context [418–420], although adoption of CS-ET in the biological community seems to be meeting greater resistance. A significant factor in this may be the more intricate image content and often low SNR, which may require use of sophisticated sparsifying transforms and/or pre-processing procedures.

The work in this chapter has, however, highlighted the need for careful consideration of the sparse regularisation imposed during CS-ET reconstruction; in particular, over-regularisation can lead to its own artefacts, such as loss of signal, particularly for low contrast objects, or smoothing of image features. Nevertheless, it has shown qualitatively and quantitatively that the CS-ET reconstructions can be of much higher fidelity than those provided by the current widely adopted SIRT algorithm, making them more readily interpreted and easier to segment. By avoiding the need for time-consuming manual segmentation, which is prone to user bias, CS-ET should facilitate more robust and routine quantitative analysis of ET reconstructions.

Using CS-ET, it has been shown that robust reconstruction may be possible from far fewer projections than are used conventionally. This opens the door to novel ET studies in a number of important areas [9, 32, 355], including 3D mapping of physical properties [293] and 3D atomic-scale analysis [66, 259, 318], and there is clear potential for ET study of electron beam sensitive specimens, as well as application in conjunction with *in-situ* [153, 421] and time-resolved [263] capabilities. Moreover, even for ET study of relatively beam resistant materials, CS-ET may render a full conventional tilt-series acquisition, consisting of typically 70 or more projections, somewhat unnecessary. In these cases, a fewer projection tilt-series would also alleviate other common problems that occur during prolonged acquisition, such as carbonaceous contamination or specimen movement. Such a strategy though, as was noted in section 5.3.3, may also

require sophisticated procedures for alignment of the tilt-series images, which becomes more challenging as the tilt-increment is widened.

In this work a Fourier based approach to CS-ET reconstruction has been pursued, but it has been noted that CS-ET algorithms employing real space based forward-/back-projection are equally possible. While real space based techniques, primarily WBP and SIRT, have been most widely adopted in ET over the last decade, the recent development of accurate and efficient non-uniform or 'pseudopolar' Fourier transforms now also facilitates high fidelity Fourier based ET reconstructions (as noted in section 5.3.4.6, see for example, in addition to the work here, the recent results of Miao and co-workers [155, 287, 290, 294, 295, 422]). It is likely that the future development of both Fourier and real space based CS-ET reconstruction algorithms will prove profitable, as each may offer particular advantages for certain applications. An immediate consideration, for example, is that differing incoherence properties of Fourier and real space based sensing matrices with respect to particular sparse bases may prove significant. One reason, at present, for pursuing the Fourier approach is that there is already a broad base of CS literature that deals with an undersampled Fourier space, including much applied literature from CS-MRI, which can be drawn upon. Alternatively, there are also a growing number of CS approaches being proposed in the context of X-ray CT, where real space based reconstruction is most common. In particular, there are promising approaches being developed to tackle key issues there, such as reconstruction from truncated projections (often known as 'interior' or 'region-of-interest' tomography) [394, 423, 424], which can also be important issues in ET.

Concerning the practical implementation to real ET data, it is clear that many variables may contribute to determining the optimum allowed projection data error - not simply random noise but also other significant restrictions and inconsistencies such as the missing wedge, projection misalignment, diffraction contrast or projection truncation. In this regard, it is important to stress that the ε parameter is not simply a measure of the data inconsistency, but is a parameter of the optimisation problem, and it represents a bound on the error of the estimated data with respect to the available data [358]. These factors make automated selection of parameters in CS-ET (and other) reconstruction algorithms particularly challenging. However, establishing a more comprehensive quantitative estimate of the most dominant of these may facilitate automated or semi-automated selection of key parameters, such as an appropriate ε.

A further profitable endeavour would be the development of computationally

efficient CS-ET algorithms. The CS-ET reconstructions in this work took ca. 5-10 hours computing time, but the code has not yet been optimised for speed of implementation. SIRT reconstructions have now been demonstrated in minutes [297] exploiting modern computing hardware such as multi-core central processing units (CPUs) and graphics processing units (GPUs). CS-ET is amenable to these advances too. The development of CS algorithms that are intrinsically fast and efficient is also an aspect receiving significant attention [368, 370, 376]. Although solving for a regularised solution will ultimately be computationally more costly than for an un-regularised solution, the use of algorithms that are intrinsically fast and that exploit modern computing hardware should facilitate much faster CS-ET implementations than that used here.

8.6 Conclusions

Implicit sparsity is prevalent at the nanoscale and can be exploited in CS-ET, via an appropriate sparsifying transform. Many different sparsifying transforms are applicable to CS-ET, and can be chosen to recover the desired type of information in a reconstruction. This chapter has shown, through simulation and experiment, verification of CS-ET for several different case studies, using different sparsifying transforms. Artefacts present in conventional reconstructions due to the limited sampling were markedly reduced using CS-ET, facilitating more reliable and quantitative analysis of the reconstructions. Using CS-ET, robust reconstruction was possible from very few projections, making it a promising means for the development of ET studies in which acquisition may be stringently restricted, as well as suggesting fewer projection acquisition protocols in general.

Chapter 9

Conclusions and future work

This thesis has addressed TEM characterisation of nanoparticle morphology from a number of perspectives, obtaining specific materials insights and advancing the characterisation capabilities. It has been shown how a variety of nano- and atomic-scale structures important in nanotechnology can be elucidated using contemporary TEM; in particular those that, owing to their length-scale or other intricacies, are inaccessible using alternative characterisation techniques. Insights relevant to target applications have been obtained, contributing directly to knowledge-based development in those areas. Fundamental physico-chemical properties, pertinent to many potential applications, have also been explored.

Using AC-STEM, the atomic-scale morphology of nanoparticulate intermetallic Ga-Pd catalysts has been revealed, providing valuable information for further rational catalyst design and understanding intricacies of nanoparticle crystallography. It is likely that similar challenges to those highlighted here for the Ga-Pd nanocatalysts will be faced in the development of other intermetallic catalysts, which is an active area of research [425]. AC-STEM should make significant contributions to those investigations too, especially the intermetallic compounds produced in nano-sized form. The atomic-scale analysis has been approached qualitatively in this thesis, but quantitative analysis of atomically resolved images in TEM, ADF AC-STEM in particular, should yield significant benefits in such investigations. The analysis of distinctive crystal structures in nanoparticles, as is (nominally) the case with nano-sized intermetallic compounds, should be a particularly fruitful area of investigation.

Concurrently, this thesis has reviewed the rise of ET in materials science, and further extended the characterisation capabilities for high-fidelity and novel nanoscale tomographic analysis. This has been via quantitative image processing to achieve more rapid and reliable segmentation of electron tomograms and

especially in the development of CS-ET reconstruction approaches. Both aspects contribute to the drive towards robust 3D nano-metrology. In additional to 3D structural imaging, this thesis has also involved novel '4D' spectroscopic ET, and the growing trend of multi-dimensional ET has been highlighted. In these aspects, as well as others such as ET of beam-sensitive specimens and atomic-scale ET, the ability to obtain high-fidelity reconstructions from fewer projections, using CS-ET or otherwise, should open up significant new opportunities.

Notably, this thesis has focused on considering TEM signals in the context of the conventional tomographic projection requirement, even when doing so may be distinctly involved, such as for the silver nanocube LSPRs. The broadening use of ET though inevitably leads to the desire to study complicated signals, including those that will not satisfy the projection requirement. 3D reconstruction approaches that circumvent, or otherwise extend beyond, the conventional projection requirement in ET are likely to become increasingly important in future innovative 3D TEM investigations.

An important theme addressed has been the intelligent use of prior knowledge, such as in CS-ET. This can be critical in many aspects of TEM, owing to the frequent paucity, low SNR, or other common deficiencies of data. Specifically, the CS-ET reconstruction capabilities developed should be instrumental in the advancement of ET, but CS methods are also highly pertinent in many other areas of electron microscopy. There has already been proposed application of CS to facilitate low dose imaging [391, 426, 427] and application in other inverse problems arising in various modes of TEM [428]. The application of CS to electron microscopy should be further explored, including possible radical re-thinking of acquisition strategies to best suit the CS approach. As CS offers broadly applicable prior knowledge constraints and the ability to substantially reduce the number of required measurements, it offers significant opportunities in TEM, where beam-induced modification of the sample remains the bane of most investigations. Indeed, it is quite widely expressed that many future opportunities in TEM lie in the broadening of usable signals and analysis regimes, towards the 'laboratory in a microscope' concept, rather than in ultimate spatial resolution. In tandem with hardware advances, smart computational methods and effective exploitation of prior knowledge, such as developed in this thesis, have an extremely important role to play.

A much sought-after goal is union of the two major themes of this thesis - atomic-scale and 3D analysis - to carry out 3D analysis with atomic sensitivity.

This is an increasingly active research area, offering the prospect of fully determining materials structures. It is, however, a challenging task that has been achieved only in favourable circumstances. Seeking feasible investigations that best exploit the unique capabilities of TEM, an area certainly worthy of greater attention is the characterisation of so-called 'atomic clusters'. These are ultra-small aggregates of atoms, and can present quite distinct properties - even compared to nanoparticles of the size addressed in this thesis.

Analysis of atomic clusters has been potent since the early development of STEM, but has advanced in the aberration-corrected era (e.g. [64, 429, 430]). Further advances may be expected as protocols for exploiting the intuitive atomic-scale imaging provided by AC-TEM reach maturity, especially methods for quantitative atomic-scale analysis. Moreover, there should be benefit from a number of the methods addressed in this thesis, such as CS. In the smallest atomic clusters, typically comprising fewer than around twenty atoms, only two or three atoms, at most, will overlap in projection, meaning that direct imaging can enable full atomic-scale 3D structure determination with confidence. Figure 9.1 shows an exemplar ADF AC-STEM image of small bismuth clusters, in which the scope for atom-by-atom analysis is clearly apparent. Indeed, ultra-small cluster catalysts, so-called 'single-site heterogeneous catalysts' [431], have grown in abundance in recent years because of the ability to directly relate the atomic architecture of the active site to catalytic performance. This is an area that can thoroughly exploit the strengths of atomic resolution AC-TEM and enable firm establishment of the link between TEM image, structure and properties.

This thesis has emphasised the diversity of modern nanotechnology research and topics faced by the contemporary electron microscopist. Application and development in this manner demonstrates the important role of TEM and the perpetual demand for its evolution.

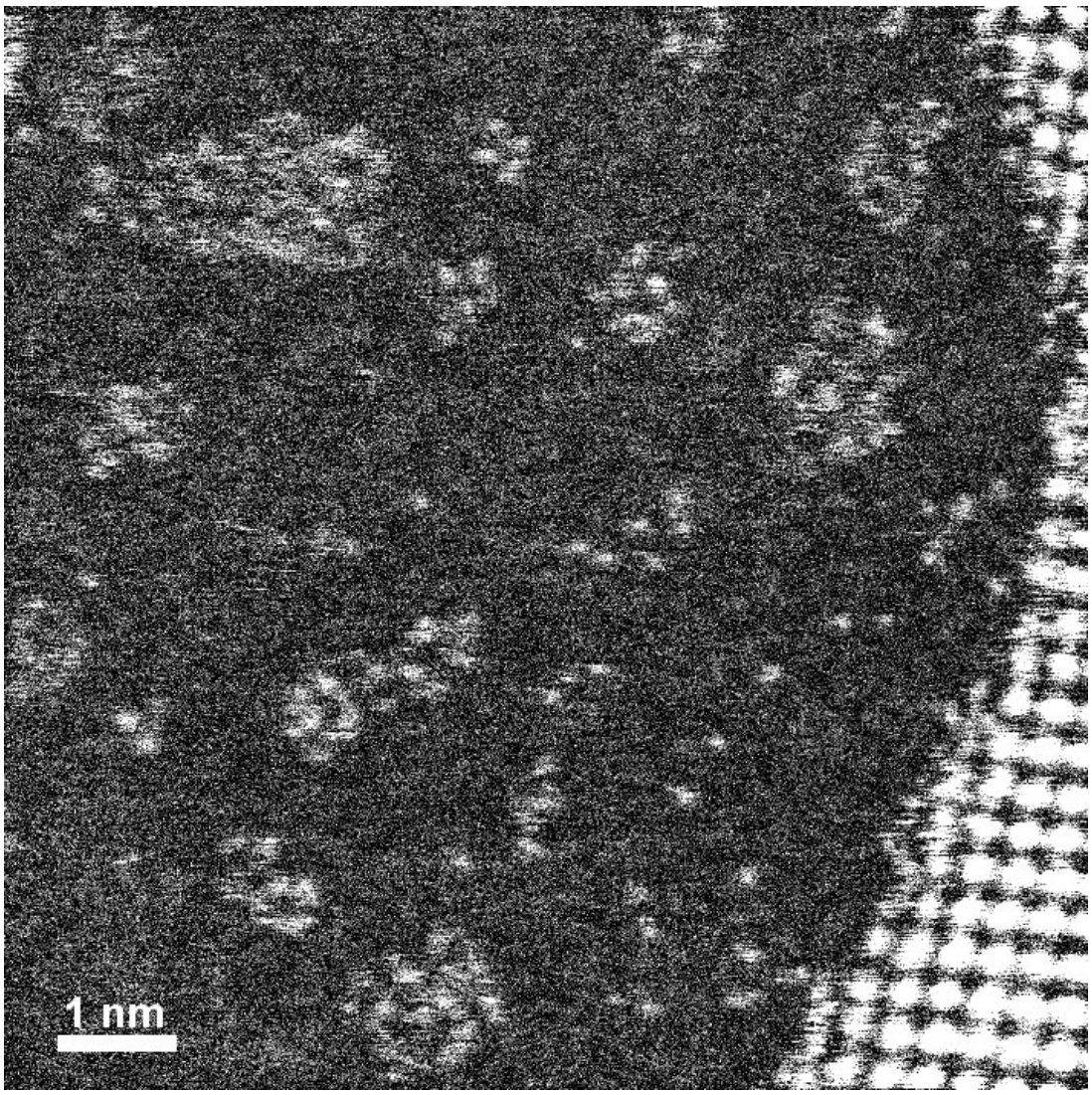

FIGURE 9.1: Atomic resolution ADF AC-STEM image revealing ultra-small bismuth clusters in a pulsed laser deposited alumina/bismuth nanoparticle/alumina thin film. Single bismuth atoms are visible, as is the atom-by-atom structure of few-atom bismuth clusters, and the morphology of some larger branched, rounded and prolate clusters. A crystalline bismuth nanoparticle is visible on the right hand side of the image. A local background subtraction has been applied to remove the non-uniform contrast arising from the alumina matrix. (Sample courtesy of Rosalia Serna, Instituto de Optica, CSIC, Spain).

Appendix A

Supplementary videos

Available on the supplementary CD:

Video 1 The full aligned ADF-STEM tomography tilt-series of Figure 6.1, shown adjacent to corresponding orthographic voxel projections of the colour-coded segmented tomogram.

Video 2 Sequential view of 2D x-y slices of the unprocessed tomogram shown in Figure 6.3, adjacent to corresponding slices from the colour-coded segmented tomogram of Figure 6.4 and slices showing the boundaries of the segmented nanoparticles and agglomerates overlaid on the unprocessed tomogram.

Video 3 Rotating 3D voxel projection (perspective view) of the colour-coded segmented tomogram shown in Figure 6.4.

Video 4 Combined 3D voxel projection rendering of the LSPR components displayed Figure 8.24.

Video 5 3D voxel projection view of each LSPR component, in respective energy order, leading to a combined 3D rendering, as displayed in Figure 8.24.

References

[1] J.M. Thomas and W.J. Thomas. *Principles and Practice of Heterogeneous Catalysis, 2nd edition*. Wiley VCH, Weinheim, 2014 (forthcoming).

[2] M. Haider, S. Uhlemann, E. Schwan, H. Rose, B. Kabius, and K. Urban. Electron microscopy image enhanced. *Nature*, 392(6678):768–769, 1998.

[3] O.L. Krivanek, et al. Aberration correction in the STEM. *Inst. Phys. Conf. Ser. (EMAG 1997)*, 153:35–40, 1997.

[4] O.L. Krivanek, N. Dellby, and A.R. Lupini. Towards sub-Å electron beams. *Ultramicroscopy*, 78(1-4):1–11, 1999.

[5] O.L. Krivanek, P.D. Nellist, N. Dellby, M.F. Murfitt, and Z. Szilagyi. Towards sub-0.5 Å electron beams. *Ultramicroscopy*, 96(3-4):229–237, 2003.

[6] P.W. Hawkes, editor. Aberration-corrected electron microscopy. *Adv. Imag. Elec. Phys.*, 153:3–538, 2008.

[7] D.A. Muller. Structure and bonding at the atomic scale by scanning transmission electron microscopy. *Nat. Mater.*, 8(4):263–270, 2009.

[8] D. Cockayne, A.I. Kirkland, P.D. Nellist, and A. Bleloch, editors. New possibilities with aberration-corrected electron microscopy. *Phil. Trans. Roy. Soc. A*, 367(1903):3633–3870, 2009.

[9] P.A. Midgley and R.E. Dunin-Borkowski. Electron tomography and holography in materials science. *Nat. Mater.*, 8(4):271–280, 2009.

[10] J. Frank. *Electron tomography: methods for three-dimensional visualization of structures in the cell*. Springer, New York; London, 2006.

[11] M. Armbrüster, K. Kovnir, M. Behrens, D. Teschner, Y. Grin, and R. Schlögll. Pd-Ga intermetallic compounds as highly selective

semihydrogenation catalysts. *J. Am. Chem. Soc.*, 132(42):14745–14747, 2010.

[12] W. Baumeister, R. Grimm, and J. Walz. Electron tomography of molecules and cells. *Trends Cell Biol.*, 9(2):81–85, 1999.

[13] P.A. Midgley and M. Weyland. 3D electron microscopy in the physical sciences: the development of Z-contrast and EFTEM tomography. *Ultramicroscopy*, 96(3-4):413–431, 2003.

[14] R. Gordon, R. Bender, and G.T. Herman. Algebraic reconstruction techniques (ART) for three-dimensional electron microscopy and X-ray photography. *J. Theor. Biol.*, 29(3):471–481, 1970.

[15] P.F.C. Gilbert. The reconstruction of a three-dimensional structure from projections and its application to electron microscopy. II. direct methods. *Proc. R. Soc. B*, 182(1066):89–102, 1972.

[16] P. Gilbert. Iterative methods for the three-dimensional reconstruction of an object from projections. *J. Theor. Biol.*, 36(1):105–117, 1972.

[17] E.J. Candès, J. Romberg, and T. Tao. Robust uncertainty principles: exact signal reconstruction from highly incomplete frequency information. *IEEE Trans. Inf. Theory*, 52(2):489–509, 2006.

[18] D.L. Donoho. Compressed sensing. *IEEE Trans. Inf. Theory*, 52(4):1289–1306, 2006.

[19] D.B. Williams and C.B. Carter. *Transmission electron microscopy: a textbook for materials science.* Springer, New York, 2009.

[20] S.J. Pennycook and P.D. Nellist. *Scanning Transmission Electron Microscopy.* Springer, New York, 2011.

[21] L.D. Marks. Experimental studies of small particle structures. *Rep. Prog. Phys.*, 57(6):603–649, 1994.

[22] L.C. Gontard, L.-Y. Chang, C.J.D. Hetherington, A.I. Kirkland, D. Ozkaya, and R.E. Dunin-Borkowski. Aberration-corrected imaging of active sites on industrial catalyst nanoparticles. *Angew. Chem. Int. Edit.*, 46(20):3683–3685, 2007.

[23] C.L. Johnson, E. Snoeck, M. Ezcurdia, B. Rodriguez-Gonzalez, I. Pastoriza-Santos, L.M. Liz-Marzan, and M.J. Hytch. Effects of elastic anisotropy on strain distributions in decahedral gold nanoparticles. *Nat. Mater.*, 7(2):120–124, 2008.

[24] M. Behrens, et al. The active site of methanol synthesis over $Cu/ZnO/Al_2O_3$ industrial catalysts. *Science*, 336(6083):893–897, 2012.

[25] M.J. Walsh, K. Yoshida, A. Kuwabara, M.L. Pay, P.L. Gai, and E.D. Boyes. On the structural origin of the catalytic properties of inherently strained ultrasmall decahedral gold nanoparticles. *Nano Lett.*, 12(4):2027–2031, 2012.

[26] R. Brydson. *Aberration-Corrected Analytical Transmission Electron Microscopy*. RMS-Wiley, Chichester, 2011.

[27] S.J. Pennycook. Z-contrast STEM for materials science. *Ultramicroscopy*, 30(1-2):58–69, 1989.

[28] S.J. Pennycook and P.D. Nellist. Z-contrast scanning transmission electron microscopy. In D. Rickerby, editor, *Impact of electron and scanning probe microscopy on materials research*, pages 161–207. Kluwer, Dordrecht, 1999.

[29] J.M. Thomas, P.A. Midgley, T.J.V. Yates, J.S. Barnard, R. Raja, I. Arslan, and M. Weyland. The chemical application of high-resolution electron tomography: bright field or dark field? *Angew. Chem. Int. Edit.*, 43(48):6745–6747, 2004.

[30] J.M. Thomas and P.A. Midgley. The merits of static and dynamic high-resolution electron microscopy (HREM) for the study of solid catalysts. *ChemCatChem*, 2(7):783–798, 2010.

[31] J.M. Thomas and P.A. Midgley. The modern electron microscope: a cornucopia of chemico-physical insights. *Chem. Phys.*, 385(1-3):1–10, 2011.

[32] R. Leary, P.A. Midgley, and J.M. Thomas. Recent advances in the application of electron tomography to materials chemistry. *Acc. Chem. Res.*, 45(10):1782–1791, 2012.

[33] Z. Li. Scanning transmission electron microscopy studies of mono- and bimetallic nanoclusters. In R. L. Johnston and J. Wilcoxon, editors, *Metal Nanoparticles and Nanoalloys*, pages 213–248. Elsevier, Oxford, 2012.

[34] S.J. Pennycook. Seeing the atoms more clearly: STEM imaging from the Crewe era to today. *Ultramicroscopy*, 123:28–37, 2012.

[35] W. Zhou, I.E. Wachs, and C.J. Kiely. Nanostructural and chemical characterization of supported metal oxide catalysts by aberration corrected analytical electron microscopy. *Curr. Opin. Solid St. M.*, 16(1):10–22, 2012.

[36] S.I. Sanchez, M.W. Small, S. Sivaramakrishnan, J.-g. Wen, J.-M. Zuo, and R.G. Nuzzo. Visualizing materials chemistry at atomic resolution. *Anal. Chem.*, 82(7):2599–2607, 2010.

[37] H. Friedrich, P.E. de Jongh, A.J. Verkleij, and K.P. de Jong. Electron tomography for heterogeneous catalysts and related nanostructured materials. *Chem. Rev.*, 109(5):1613–1629, 2009.

[38] M. Weyland. Electron tomography of catalysts. *Top. Catal.*, 21(4):175–183, 2002.

[39] M. Weyland and P.A. Midgley. Electron tomography. *Mater. Today*, 7(12):32–40, 2004.

[40] P.A. Midgley, M. Weyland, T.J.V. Yates, I. Arslan, R.E. Dunin-Borkowski, and J.M. Thomas. Nanoscale scanning transmission electron tomography. *J. Microsc.*, 223(3):185–190, 2006.

[41] P.A. Midgley, E.P.W. Ward, A.B. Hungria, and J.M. Thomas. Nanotomography in the chemical, biological and materials sciences. *Chem. Soc. Rev.*, 36:1477–1494, 2007.

[42] M. Weyland and P.A. Midgley. Electron tomography. In A. Kirkland and J. L. Hutchinson, editors, *Nanocharacterisation*, pages 184–267. Royal Society of Chemistry, Cambridge, 2007.

[43] J. Zečević, K.P. de Jong, and P.E. de Jongh. Progress in electron tomography to assess the 3D nanostructure of catalysts. *Curr. Opin. Solid St. M.*, 17(3):115–125, 2013.

[44] J. Banhart. *Advanced tomographic methods in materials research and engineering.* Oxford University Press, Oxford, 2008.

[45] J.C.H. Spence. *High-resolution electron microscopy.* Oxford University Press, Oxford, 2003.

[46] A.I. Kirkland and R.R. Meyer. "Indirect" high-resolution transmission electron microscopy: aberration measurement and wavefunction reconstruction. *Microsc. Microanal.*, 10(04):401–413, 2004.

[47] M. Bar Sadan, L. Houben, S.G. Wolf, A. Enyashin, G. Seifert, R. Tenne, and K. Urban. Toward atomic-scale bright-field electron tomography for the study of fullerene-like nanostructures. *Nano Lett.*, 8(3):891–896, 2008.

[48] P.W. Hawkes and J.C.H. Spence. *Science of microscopy*. Springer, New York, 2007.

[49] O.L. Krivanek, M.F. Chisholm, V. Nicolosi, T.J. Pennycook, G.J. Corbin, N. Dellby, M.F. Murfitt, C.S. Own, Z.S. Szilagyi, M.P. Oxley, S.T. Pantelides, and S.J. Pennycook. Atom-by-atom structural and chemical analysis by annular dark-field electron microscopy. *Nature*, 464(7288):571–574, 2010.

[50] M.M.J. Treacy. Z dependence of electron scattering by single atoms into annular dark-field detectors. *Microsc. Microanal.*, 17(06):847–858, 2011.

[51] P.A. Midgley, M. Weyland, J.M. Thomas, and B.F.G. Johnson. Z-contrast tomography: a technique in three-dimensional nanostructural analysis based on Rutherford scattering. *Chem. Commun.*, 18(10):907–908, 2001.

[52] M. Weyland, P.A. Midgley, and J.M. Thomas. Electron tomography of nanoparticle catalysts on porous supports: a new technique based on Rutherford scattering. *J. Phys. Chem. B*, 105(33):7882–7886, 2001.

[53] P. Hartel, H. Rose, and C. Dinges. Conditions and reasons for incoherent imaging in STEM. *Ultramicroscopy*, 63(2):93–114, 1996.

[54] A. Howie. Image contrast and localised selection techniques. *J. Microsc.*, 177(1):11–23, 1979.

[55] P.B. Hirsch, A. Howie, P.B. Nicholson, D.W. Pashley, and W.J. Whelan. *Electron microscopy of thin crystals*. Krieger, New York, 1977.

[56] H. E, K.E. MacArthur, T.J. Pennycook, E. Okunishi, A.J. D'Alfonso, N.R. Lugg, L.J. Allen, and P.D. Nellist. Probe integrated scattering cross sections in the analysis of atomic resolution HAADF STEM images. *Ultramicroscopy*, 133:109–119, 2013.

[57] S. Van Aert, J. Verbeeck, R. Erni, S. Bals, M. Luysberg, D.V. Dyck, and G.V. Tendeloo. Quantitative atomic resolution mapping using high-angle annular dark field scanning transmission electron microscopy. *Ultramicroscopy*, 109(10):1236–1244, 2009.

[58] Z.Y. Li, N.P. Young, M. Di Vece, S. Palomba, R.E. Palmer, A.L. Bleloch, B.C. Curley, R.L. Johnston, J. Jiang, and J. Yuan. Three-dimensional atomic-scale structure of size-selected gold nanoclusters. *Nature*, 451(7174):46–48, 2008.

[59] J.M. LeBeau, S.D. Findlay, L.J. Allen, and S. Stemmer. Standardless atom counting in scanning transmission electron microscopy. *Nano Lett.*, 10(11):4405–4408, 2010.

[60] S. Van Aert, K.J. Batenburg, M.D. Rossell, R. Erni, and G. Van Tendeloo. Three-dimensional atomic imaging of crystalline nanoparticles. *Nature*, 470(7334):374–377, 2011.

[61] H. Katz-Boon, C.J. Rossouw, M. Weyland, A.M. Funston, P. Mulvaney, and J. Etheridge. Three-dimensional morphology and crystallography of gold nanorods. *Nano Lett.*, 11(1):273–278, 2011.

[62] H. Katz-Boon, C.J. Rossouw, C. Dwyer, and J. Etheridge. Rapid measurement of nanoparticle thickness profiles. *Ultramicroscopy*, 124:61–70, 2013.

[63] S. Bals, M. Casavola, M.A. van Huis, S. Van Aert, K.J. Batenburg, G. Van Tendeloo, and D.l. Vanmaekelbergh. Three-dimensional atomic imaging of colloidal core-shell nanocrystals. *Nano Lett.*, 11(8):3420–3424, 2011.

[64] S. Bals, S. Van Aert, C.P. Romero, K. Lauwaet, M.J. Van Bael, B. Schoeters, B. Partoens, E. Yücelen, P. Lievens, and G. Van Tendeloo. Atomic scale dynamics of ultrasmall germanium clusters. *Nat. Commun.*, 3:897, 2012.

[65] S. Van Aert, A. De Backer, G.T. Martinez, B. Goris, S. Bals, G. Van Tendeloo, and A. Rosenauer. Procedure to count atoms with trustworthy single-atom sensitivity. *Phys. Rev. B*, 87(6):064107, 2013.

[66] B. Goris, A. De Backer, S. Van Aert, S. Gómez-Graña, L.M. Liz-Marzán, G. Van Tendeloo, and S. Bals. Three-dimensional elemental mapping at

the atomic scale in bimetallic nanocrystals. *Nano Lett.*, 13(9):4236–4241, 2013.

[67] P. Schlossmacher, D.O. Klenov, B. Freitag, and H.S. von Harrach. Enhanced detection sensitivity with a new windowless XEDS system for AEM based on silicon drift detector technology. *Microscopy Today*, 18(04):14–20, 2010.

[68] R.F. Egerton. *Electron Energy-Loss Spectroscopy in the Electron Microscope*. Springer, New York, 2011.

[69] B. Freitag, G. Knippels, S. Kujawa, P.C. Tiemeijer, M. Van der Stam, D. Hubert, C. Kisielowski, P. Denes, A. Minor, and U. Dahmen. First performance measurements and application results of a new high brightness Schottky field emitter for HR-S/TEM at 80-300kV acceleration voltage. In *EMC 2008, 14th European Microscopy Congress, 1st-5th September, Aachen, Germany*, pages 55–56.

[70] P.C. Tiemeijer. Operation modes of a TEM monochromator. *Inst. Phys. Conf. Ser. (EMAG 1999)*, 161:191–194, 1999.

[71] F. de la Peña, M.H. Berger, J.F. Hochepied, F. Dynys, O. Stephan, and M. Walls. Mapping titanium and tin oxide phases using EELS: an application of independent component analysis. *Ultramicroscopy*, 111(2):169–176, 2011.

[72] D.D. Lee and H.S. Seung. Learning the parts of objects by non-negative matrix factorization. *Nature*, 401(6755):788–791, 1999.

[73] P. Paatero and U. Tapper. Positive matrix factorization: a non-negative factor model with optimal utilization of error estimates of data values. *Environmetrics*, 5(2):111–126, 1994.

[74] C. Jeanguillaume and C. Colliex. Spectrum-image: the next step in EELS digital acquisition and processing. *Ultramicroscopy*, 28(1-4):252–257, 1989.

[75] O. Scherzer. Über einige fehler von elektronenlinsen. *Z. Phys. A-Hadron Nucl.*, 101(9):593–603, 1936.

[76] R. Leary and R. Brydson. Chromatic aberration correction: the next step in electron microscopy. *Adv. Imag. Elec. Phys.*, 165:73–130, 2011.

[77] R. Erni. *Aberration-corrected imaging in transmission electron microscopy: an introduction*. Imperial College Press, London; Singapore, 2010.

[78] R. Erni, M.D. Rossell, C. Kisielowski, and U. Dahmen. Atomic-resolution imaging with a sub-50-pm electron probe. *Phys. Rev. Lett.*, 102(9):096101, 2009.

[79] P.E. Batson, N. Dellby, and O.L. Krivanek. Sub-ångstrom resolution using aberration corrected electron optics. *Nature*, 418(6898):617–620, 2002.

[80] D.A. Muller, L.F. Kourkoutis, M. Murfitt, J.H. Song, H.Y. Hwang, J. Silcox, N. Dellby, and O.L. Krivanek. Atomic-scale chemical imaging of composition and bonding by aberration-corrected microscopy. *Science*, 319(5866):1073–1076, 2008.

[81] R.F. Egerton, P. Li, and M. Malac. Radiation damage in the TEM and SEM. *Micron*, 35:399–409, 2004.

[82] R. Leary, F. de la Peña, J.S. Barnard, Y. Luo, M. Armbrüster, J.M. Thomas, and P.A. Midgley. Revealing the atomic structure of intermetallic $GaPd_2$ nanocatalysts by using aberration-corrected scanning transmission electron microscopy. *ChemCatChem*, 5(9):2599–2609, 2013.

[83] A. Borodziński and G.C. Bond. Selective hydrogenation of ethyne in ethene-rich streams on palladium catalysts. Part 1. Effect of changes to the catalyst during reaction. *Cataly. Rev.*, 48(2):91–144, 2006.

[84] A. Borodziński and G.C. Bond. Selective hydrogenation of ethyne in ethene-rich streams on palladium catalysts, Part 2: Steady-state kinetics and effects of palladium particle size, carbon monoxide, and promoters. *Cataly. Rev.*, 50(3):379–469, 2008.

[85] F. Studt, F. Abild-Pedersen, T. Bligaard, R.Z. Sørensen, C.H. Christensen, and J.K. Nørskov. Identification of non-precious metal alloy catalysts for selective hydrogenation of acetylene. *Science*, 320(5881):1320–1322, 2008.

[86] J.K. Norskov, T. Bligaard, J. Rossmeisl, and C.H. Christensen. Towards the computational design of solid catalysts. *Nat Chem*, 1(1):37–46, 2009.

[87] M. Armbrüster, et al. How to control the selectivity of palladium-based catalysts in hydrogenation reactions: the role of subsurface chemistry. *ChemCatChem*, 4(8):1048–1063, 2012.

[88] M. Crespo-Quesada, F. Cárdenas-Lizana, A.-L. Dessimoz, and L. Kiwi-Minsker. Modern trends in catalyst and process design for alkyne hydrogenations. *ACS Catal.*, 2(8):1773–1786, 2012.

[89] N. Lopez and C. Vargas-Fuentes. Promoters in the hydrogenation of alkynes in mixtures: insights from density functional theory. *Chem. Commun.*, 48(10):1379–1391, 2012.

[90] K. Kovnir, M. Armbrüster, D. Teschner, T.V. Venkov, F.C. Jentoft, A. Knop-Gericke, Y. Grin, and R. Schlögl. A new approach to well-defined, stable and site-isolated catalysts. *Sci. Technol. Adv. Mat.*, 8(5):420–427, 2007.

[91] Á. Molnár, A. Sárkány, and M. Varga. Hydrogenation of carbon-carbon multiple bonds: chemo-, regio- and stereo-selectivity. *J. Mol. Catal.*, 173(1-2):185–221, 2001.

[92] B. Chen, U. Dingerdissen, J.G.E. Krauter, H.G.J. Lansink Rotgerink, K. Möbus, D.J. Ostgard, P. Panster, T.H. Riermeier, S. Seebald, T. Tacke, and H. Trauthwein. New developments in hydrogenation catalysis particularly in synthesis of fine and intermediate chemicals. *Appl. Catal. A-Gen.*, 280(1):17–46, 2005.

[93] H. Zea, K. Lester, A.K. Datye, E. Rightor, R. Gulotty, W. Waterman, and M. Smith. The influence of Pd-Ag catalyst restructuring on the activation energy for ethylene hydrogenation in ethylene-acetylene mixtures. *Appl. Catal. A-Gen.*, 282(1-2):237–245, 2005.

[94] A. Lamberov, S. Egorova, I. Il'yasov, K. Gil'manov, S. Trifonov, V. Shatilov, and A. Ziyatdinov. Changes in the course of reaction and regeneration of a Pd-Ag/Al_2O_3 catalyst for the selective hydrogenation of acetylene. *Kinet. Catal.*, 48(1):136–142, 2007.

[95] M. Behrens and M. Armbrüster. Methanol steam reforming. In L. Guczi and A. Erdôhelyi, editors, *Catalysis for Alternative Energy Generation*, pages 175–235. Springer, New York, 2012.

[96] A. Haghofer, D. Ferri, K. Föttinger, and G. Rupprechter. Who is doing the job? Unraveling the role of Ga_2O_3 in methanol steam reforming on Pd_2Ga/Ga_2O_3. *ACS Catal.*, 2(11):2305–2315, 2012.

[97] A. Haghofer, K. Föttinger, F. Girgsdies, D. Teschner, A. Knop-Gericke, R. Schlögl, and G. Rupprechter. In situ study of the formation and stability of supported Pd_2Ga methanol steam reforming catalysts. *J. Catal.*, 286:13–21, 2012.

[98] N. Iwasa and N. Takezawa. New supported Pd and Pt alloy catalysts for steam reforming and dehydrogenation of methanol. *Top. Catal.*, 22(3):215–224, 2003.

[99] L. Li, B. Zhang, E. Kunkes, K. Föttinger, M. Armbrüster, D.S. Su, W. Wei, R. Schlögl, and M. Behrens. Ga-Pd/Ga_2O_3 catalysts: the role of gallia polymorphs, intermetallic compounds, and pretreatment conditions on selectivity and stability in different reactions. *ChemCatChem*, 4(11):1764–1775, 2012.

[100] H. Lorenz, S. Penner, W. Jochum, C. Rameshan, and B. Klötzer. Pd/Ga_2O_3 methanol steam reforming catalysts: Part II. catalytic selectivity. *Appl. Catal. A-Gen.*, 358(2):203–210, 2009.

[101] H. Lorenz, R. Thalinger, E.-M. Köck, M. Kogler, L. Mayr, D. Schmidmair, T. Bielz, K. Pfaller, B. Klötzer, and S. Penner. Methanol steam reforming: CO_2-selective Pd_2Ga phases supported on α- and γ-Ga_2O_3. *Appl. Catal. A-Gen.*, 453:34–44, 2013.

[102] A. Ota, E.L. Kunkes, I. Kasatkin, E. Groppo, D. Ferri, B. Poceiro, R.M. Navarro Yerga, and M. Behrens. Comparative study of hydrotalcite-derived supported Pd_2Ga and PdZn intermetallic nanoparticles as methanol synthesis and methanol steam reforming catalysts. *J. Catal.*, 293:27–38, 2012.

[103] S. Penner, H. Lorenz, W. Jochum, M. Stöger-Pollach, D. Wang, C. Rameshan, and B. Klötzer. Pd/Ga_2O_3 methanol steam reforming catalysts: Part I. morphology, composition and structural aspects. *Appl. Catal. A-Gen.*, 358(2):193–202, 2009.

[104] C. Rameshan, W. Stadlmayr, S. Penner, H. Lorenz, L. Mayr, M. Hävecker, R. Blume, T. Rocha, D. Teschner, A. Knop-Gericke, R. Schlögl, D. Zemlyanov, N. Memmel, and B. Klötzer. In situ XPS study of methanol reforming on PdGa near-surface intermetallic phases. *J. Catal.*, 290:126–137, 2012.

[105] K. Kovnir, M. Armbrüster, D. Teschner, T.V. Venkov, L. Szentmiklósi, F.C. Jentoft, A. Knop-Gericke, Y. Grin, and R. Schlögl. In situ surface characterization of the intermetallic compound PdGa - a highly selective hydrogenation catalyst. *Surf. Sci.*, 603(10-12):1784–1792, 2009.

[106] K. Kovnir, J. Osswald, M. Armbrüster, D. Teschner, G. Weinberg, U. Wild, A. Knop-Gericke, T. Ressler, Y. Grin, and R. Schlögl. Etching of the intermetallic compounds PdGa and Pd_3Ga_7: an effective way to increase catalytic activity? *J. Catal.*, 264(2):93–103, 2009.

[107] J. Osswald, R. Giedigkeit, R.E. Jentoft, M. Armbrüster, F. Girgsdies, K. Kovnir, T. Ressler, Y. Grin, and R. Schlögl. Palladium-gallium intermetallic compounds for the selective hydrogenation of acetylene. Part I: Preparation and structural investigation under reaction conditions. *J. Catal.*, 258(1):210–218, 2008.

[108] J. Osswald, K. Kovnir, M. Armbrüster, R. Giedigkeit, R.E. Jentoft, U. Wild, Y. Grin, and R. Schlögl. Palladium-gallium intermetallic compounds for the selective hydrogenation of acetylene. Part II: Surface characterization and catalytic performance. *J. Catal.*, 258(1):219–227, 2008.

[109] J. Prinz, R. Gaspari, C.A. Pignedoli, J. Vogt, P. Gille, M. Armbrüster, H. Brune, O. Gröning, D. Passerone, and R. Widmer. Isolated Pd sites on the intermetallic PdGa(111) and PdGa($\bar{1}\bar{1}\bar{1}$) model catalyst surfaces. *Angew. Chem.-Int. Edit.*, 51(37):9339–9343, 2012.

[110] D. Rosenthal, R. Widmer, R. Wagner, P. Gille, M. Armbrüster, Y. Grin, R. Schlögl, and O. Gröning. Surface investigation of intermetallic PdGa($\bar{1}\bar{1}\bar{1}$). *Langmuir*, 28(17):6848–6856, 2012.

[111] M. Armbrüster, G. Wowsnick, M. Friedrich, M. Heggen, and R. Cardoso-Gil. Synthesis and catalytic properties of nanoparticulate intermetallic Ga-Pd compounds. *J. Am. Chem. Soc.*, 133(23):9112–9118, 2011.

[112] S.E. Collins, J.J. Delgado, C. Mira, J.J. Calvino, S. Bernal, D.L. Chiavassa, M.A. Baltanás, and A.L. Bonivardi. The role of Pd-Ga bimetallic particles in the bifunctional mechanism of selective methanol synthesis via CO_2 hydrogenation on a Pd/Ga_2O_3 catalyst. *J. Catal.*, 292:90–98, 2012.

[113] A. Haghofer, K. Föttinger, M. Nachtegaal, M. Armbrüster, and G. Rupprechter. Microstructural changes of supported intermetallic

nanoparticles under reductive and oxidative conditions: an in situ X-ray absorption study of Pd/Ga_2O_3. *J. Phys. Chem. C*, 116(41):21816–21827, 2012.

[114] A. Ota, M. Armbrüster, M. Behrens, D. Rosenthal, M. Friedrich, I. Kasatkin, F. Girgsdies, W. Zhang, R. Wagner, and R. Schlögl. Intermetallic compound Pd_2Ga as a selective catalyst for the semi-hydrogenation of acetylene: from model to high performance systems. *J. Phys. Chem. C*, 115(4):1368–1374, 2011.

[115] L. Shao, W. Zhang, M. Armbrüster, D. Teschner, F. Girgsdies, B. Zhang, O. Timpe, M. Friedrich, R. Schlögl, and D.S. Su. Nanosizing intermetallic compounds onto carbon nanotubes: active and selective hydrogenation catalysts. *Angew. Chem. Int. Edit.*, 50(43):10231–10235, 2011.

[116] F. Baletto and R. Ferrando. Structural properties of nanoclusters: energetic, thermodynamic, and kinetic effects. *Rev. Mod. Phys.*, 77(1):371–423, 2005.

[117] R. Ferrando, J. Jellinek, and R.L. Johnston. Nanoalloys: from theory to applications of alloy clusters and nanoparticles. *Chem. Rev.*, 108(3):845–910, 2008.

[118] A. Mayoral, H. Barron, R. Estrada-Salas, A. Vazquez-Duran, and M. Jose-Yacaman. Nanoparticle stability from the nano to the meso interval. *Nanoscale*, 2(3):335–342, 2010.

[119] J. Wu, P. Li, Y.-T. Pan, S. Warren, X. Yin, and H. Yang. Surface lattice-engineered bimetallic nanoparticles and their catalytic properties. *Chem. Soc. Rev.*, 41(24):8066–8074, 2012.

[120] H. Okamoto. Ga-Pd (Gallium-Palladium). *J. Phase Equilib. Diff.*, 29(5):466–467, 2008.

[121] S. Geller and V.M. Wolontis. The crystal structure of Co_2Si. *Acta Crystallogr.*, 8(2):83–87, 1955.

[122] K. Kovnir, M. Schmidt, C. Waurisch, M. Armbrüster, Y. Prots, and Y. Grin. Refinement of the crystal structure of dipalladium gallium, Pd_2Ga. *Z. Krist.-New Cryst. Struct.*, 223(1):7–8, 2008.

[123] M. Boudart. Catalysis by supported metals. *Adv. Catal.*, 20:153–166, 1969.

[124] R. Van Hardeveld and F. Hartog. The statistics of surface atoms and surface sites on metal crystals. *Surf. Sci.*, 15(2):189–230, 1969.

[125] J.P. Boitiaux, J. Cosyns, and S. Vasudevan. Hydrogenation of highly unsaturated hydrocarbons over highly dispersed palladium catalyst: Part I: behaviour of small metal particles. *Appl. Catal.*, 6(1):41–51, 1983.

[126] N. Semagina and L. Kiwi-Minsker. Recent advances in the liquid-phase synthesis of metal nanostructures with controlled shape and size for catalysis. *Catal. Rev.*, 51(2):147–217, 2009.

[127] M. Crespo-Quesada, A. Yarulin, M. Jin, Y. Xia, and L. Kiwi-Minsker. Structure sensitivity of alkynol hydrogenation on shape- and size-controlled palladium nanocrystals: which sites are most active and selective? *J. Am. Chem. Soc.*, 133(32):12787–12794, 2011.

[128] C.-J. Jia and F. Schuth. Colloidal metal nanoparticles as a component of designed catalyst. *Phys. Chem. Chem. Phys.*, 13(7):2457–2487, 2011.

[129] B. Roldan Cuenya. Metal nanoparticle catalysts beginning to shape-up. *Acc. Chem. Res.*, 46(8):1682–1691, 2012.

[130] H. Zhang, M. Jin, Y. Xiong, B. Lim, and Y. Xia. Shape-controlled synthesis of Pd nanocrystals and their catalytic applications. *Acc. Chem. Res.*, 46(8):1783–1794, 2012.

[131] F. Zaera. Shape-controlled nanostructures in heterogeneous catalysis. *ChemSusChem*, 6(10):1797–1820, 2013.

[132] F. Zaera. Probing catalytic reactions at surfaces. *Prog. Surf. Sci.*, 69(1-3):1–98, 2001.

[133] D. Teschner, et al. Alkyne hydrogenation over Pd catalysts: a new paradigm. *J. Catal.*, 242(1):26–37, 2006.

[134] M. Crespo-Quesada, S. Yoon, M. Jin, Y. Xia, A. Weidenkaff, and L. Kiwi-Minsker. Size and shape-controlled Pd nanocrystals on ZnO and SiO_2: when the nature of the support determines the active phase. *ChemCatChem*, 6(3):767–771, 2014.

[135] A.S. Barnard. Mapping the shape and phase of palladium nanocatalysts. *Catal. Sci. Technol.*, 2(7):1485–1492, 2012.

[136] V.G. Gryaznov, J. Heydenreich, A.M. Kaprelov, S.A. Nepijko, A.E. Romanov, and J. Urban. Pentagonal symmetry and disclinations in small particles. *Cryst. Res. Technol.*, 34(9):1091–1119, 1999.

[137] H. Hofmeister. Forty years study of fivefold twinned structures in small particles and thin films. *Cryst. Res. Technol.*, 33(1):3–25, 1998.

[138] E. Ringe, R.P. Van Duyne, and L.D. Marks. Kinetic and thermodynamic modified Wulff constructions for twinned nanoparticles. *J. Phys. Chem. C*, 117(31):15859–15870, 2013.

[139] J.C. Russ. *The Image Processing Handbook*. CRC Press, Boca Raton, Fla., 2002.

[140] C. Ahn and O.L. Krivanek. *EELS Atlas*. Gatan Inc., Pleasanton, CA, 1983.

[141] T. Manoubi, M. Tencé, M.G. Walls, and C. Colliex. Curve fitting methods for quantitative analysis in electron energy loss spectroscopy. *Microsc. Microanal. Microstruct.*, 1(1):23–39, 1990.

[142] J. Verbeeck and S. Van Aert. Model based quantification of EELS spectra. *Ultramicroscopy*, 101(2-4):207–224, 2004.

[143] C.J. Lin. Projected gradient methods for nonnegative matrix factorization. *Neural Comput.*, 19(10):2756–2779, 2007.

[144] F. Pedregosa, et al. Scikit-learn: machine learning in python. *J. Mach. Learn. Res.*, 12:2825–2830, 2011.

[145] C. Wannek and B. Harbrecht. Die kristallstruktur von Ga_5Pd_{13} - eine niedersymmetrische ordnungsvariante der kubisch dichtesten kugelpackung. *Z. Anorg. Allg. Chem.*, 626(7):1540–1544, 2000.

[146] K. Khalaff and K. Schubert. Kristallstruktur von Pd_5Ga_2. *J. Less-Common Met.*, 37(1):129–140, 1974.

[147] C. Wannek and B. Harbrecht. Phase equilibria in the palladium-rich part of the gallium-palladium system. The crystal structures of Ga_3Pd_7 and $Ga_{1-x}Pd_{2+x}$. *J. Alloy. Compd.*, 316(1-2):99–106, 2001.

[148] K. Schubert, H.L. Lukas, H.G. Meissner, and S. Bhan. Zum aufbau der systeme kobalt-gallium, palladium-gallium, palladium-zinn und verwandter legierungen. *Z. Metallk.*, 50(9):534–540, 1959.

[149] M. Armbrüster, H. Borrmann, M. Wedel, Y. Prots, R. Giedigkeit, and P. Gille. Refinement of the crystal structure of palladium gallium (1:1), PdGa. *Z. Kristallogr. NCS*, 225:617–618, 2010.

[150] Y. Grin, K. Peters, and H.G. von Schnering. Refinement of the crystal structure of palladium pentagallide, $PdGa_5$. *Z. Kristallogr.*, 212(s1):6, 1997.

[151] G. Wowsnick, D. Teschner, I. Kasatkin, F. Girgsdies, M. Armbrüster, A. Zhang, Y. Grin, R. Schlögl, and M. Behrens. Surface dynamics of the intermetallic catalyst Pd_2Ga, Part I - structural stability in UHV and different gas atmospheres. *J. Catal.*, 309:209–220, 2014.

[152] G. Wowsnick, D. Teschner, M. Armbrüster, I. Kasatkin, F. Girgsdies, Y. Grin, R. Schlögl, and M. Behrens. Surface dynamics of the intermetallic catalyst Pd_2Ga, part II - reactivity and stability in liquid-phase hydrogenation of phenylacetylene. *J. Catal.*, 309:221–230, 2014.

[153] P.L. Gai and E.D. Boyes. Atomic-resolution environmental transmission electron microscopy. In G. van Tendeloo, D. van Dyck, and S.J. Pennycook, editors, *Handbook of Nanoscopy*, pages 375–403. Wiley-VCH, Weinheim, 2012.

[154] H. Hofmeister. Fivefold twinned nanoparticles. In H.S. Nalwa, editor, *Encyclopedia of Nanoscience and Nanotechnology*, volume 3, pages 431–452. American Scientific Publishers, Los Angeles, 2004.

[155] C.-C. Chen, C. Zhu, E.R. White, C.-Y. Chiu, M.C. Scott, B.C. Regan, L.D. Marks, Y. Huang, and J. Miao. Three-dimensional imaging of dislocations in a nanoparticle at atomic resolution. *Nature*, 496(7443):74–77, 2013.

[156] Y. Sun, Y. Ren, Y. Liu, J. Wen, J.S. Okasinski, and D.J. Miller. Ambient-stable tetragonal phase in silver nanostructures. *Nat. Commun.*, 3:971, 2012.

[157] M.J. Walsh, K. Yoshida, M.L. Pay, P.L. Gai, and E.D. Boyes. On the effect of atomic structure on the activity and deactivation of catalytic gold nanoparticles. *ChemCatChem*, 4(10):1638–1644, 2012.

[158] Zi-An Li, M. Spasova, Q. M. Ramasse, M. E. Gruner, C. Kisielowski, and M. Farle. Chemically ordered decahedral FePt nanocrystals observed by electron microscopy. *Phys. Rev. B*, 89:161406, 2014.

[159] D. Belic, R.L. Chantry, Z.Y. Li, and S.A. Brown. Ag-Au nanoclusters: structure and phase segregation. *Appl. Phys. Lett.*, 99(17):171914, 2011.

[160] D.K. Saha, K. Koga, and H. Takeo. Stable icosahedral nanoparticles in an as-grown Au-Fe alloy. *Eur. Phys. J. D*, 9(1):539–542, 1999.

[161] J. L. Rodríguez-López, J. M. Montejano-Carrizales, U. Pal, J. F. Sánchez-Ramírez, H. E. Troiani, D. García, M. Miki-Yoshida, and M. José-Yacamán. Surface reconstruction and decahedral structure of bimetallic nanoparticles. *Phys. Rev. Lett.*, 92:196102, 2004.

[162] B. Zhu and M. Hou. On the role of mechanical stress in the chemical ordering of nanoalloys. *Eur. Phys. J. D*, 66(3):1–8, 2012.

[163] J. Yang, L.L. Chng, X. Yang, X. Chen, and J.Y. Ying. Multiply-twinned intermetallic AuCu pentagonal nanorods. *Chem. Commun.*, 50(9):1141–1143, 2014.

[164] M.E. Gruner and A. Dannenberg. Structure and magnetism of near-stoichiometric FePd nanoparticles. *J. Magn. Magn. Mater.*, 321(7):861–864, 2009.

[165] F. Tournus, K. Sato, T. Epicier, T. J. Konno, and V. Dupuis. Multi-$l1_0$ domain CoPt and FePt nanoparticles revealed by electron microscopy. *Phys. Rev. Lett.*, 110:055501, 2013.

[166] S. Stappert, B. Rellinghaus, M. Acet, and E.F. Wassermann. Multiply twinned structures in gas-phase sintered stoichiometric FePt nanoparticles. *MRS Proceedings*, 704, doi:10.1557/PROC-704-W5.7.1, 2001.

[167] R. Leary, Z. Saghi, M. Armbrüster, G. Wowsnick, R. Schlögl, J.M. Thomas, and P.A. Midgley. Quantitative high-angle annular dark-field scanning transmission electron microscope (HAADF-STEM) tomography and high-resolution electron microscopy of unsupported intermetallic $GaPd_2$ catalysts. *J. Phys. Chem. C*, 116(24):13343–13352, 2012.

[168] B.G. Bagley. A dense packing of hard spheres with five-fold symmetry. *Nature*, 208(5011):674–675, 1965.

[169] A. Mackay. A dense non-crystallographic packing of equal spheres. *Acta Crystallogr.*, 15(9):916–918, 1962.

[170] C. Hammond. *The Basics of Crystallography and Diffraction*. Oxford University Press, Oxford, 2009.

[171] R.W. Cahn. Twinned crystals. *Adv. Phys.*, 3(12):363–445, 1954.

[172] E. Koch. Twinning. In E. Prince, editor, *International Tables for Crystallography, Vol. C*, pages 10–14. Kluwer Academic Publishers, Dordrecht, 2006.

[173] H. Grimmer and M. Nespolo. Geminography - the crystallography of twins. *Z. Kristallogr.*, 221:28–50, 2006.

[174] A. Howie and L.D. Marks. Elastic strains and the energy balance for multiply twinned particles. *Phil. Mag. A*, 49(1):95–109, 1984.

[175] C.Y. Yang. Crystallography of decahedral and icosahedral particles: I. geometry of twinning. *J. Cryst. Growth*, 47(2):274–282, 1979.

[176] K. Heinemann, M.J. Yacamán, C.Y. Yang, and H. Poppa. The structure of small, vapor-deposited particles: I. experimental study of single crystals and particles with pentagonal profiles. *J. Cryst. Growth*, 47(2):177–186, 1979.

[177] M.J. Yacamán, K. Heinemann, C.Y. Yang, and H. Poppa. The structure of small, vapor-deposited particles: II. experimental study of particles with hexagonal profile. *J. Cryst. Growth*, 47(2):187–195, 1979.

[178] B.G. Bagley. Five-fold pseudosymmetry. *Nature*, 225(5237):1040–1041, 1970.

[179] L.D. Marks. Inhomogeneous strains in small particles. *Surf. Sci.*, 150(2):302–318, 1985.

[180] S. Ino. Stability of multiply-twinned particles. *J. Phys. Soc. Jpn.*, 27(4):941–953, 1969.

[181] R. de Wit. Partial disclinations. *J. Phys. C Solid State*, 5(5):529, 1972.

[182] A.E. Romanov and A.L. Kolesnikova. Application of disclination concept to solid structures. *Prog. Mater. Sci.*, 54(6):740–769, 2009.

[183] Q. Chen, M. Tanaka, and K. Furuya. Unusual crystallographic structure and its fluctuation of indium nanoparticles as-deposited and observed with

HRTEM using the UHV-DC-TEM system. *Surf. Sci.*, 440(3):398–406, 1999.

[184] Y. Wu, Q. Chen, M. Takeguchi, and K. Furuya. High-resolution transmission electron microscopy study on the anomalous structure of lead nanoparticles with UHV-MBE-TEM system. *Surf. Sci.*, 462(1-3):203–210, 2000.

[185] L.D. Marks. Surface structure and energetics of multiply twinned particles. *Phil. Mag. A*, 49(1):81–93, 1984.

[186] H. Hofmeister, S.A. Nepijko, D.N. Ievlev, W. Schulze, and G. Ertl. Composition and lattice structure of fivefold twinned nanorods of silver. *J. Cryst. Growth*, 234(4):773–781, 2002.

[187] G. Casillas, J.J. Velázquez-Salazar, and M. Jose-Yacaman. A new mechanism of stabilization of large decahedral nanoparticles. *J. Phys. Chem. C*, 116(15):8844–8848, 2012.

[188] A. Richter, A.E. Romanov, W. Pompe, and V.I. Vladimirov. On the screening length of disclinations in amorphous structures. *Phys. Status Solidi B*, 143(1):43–53, 1987.

[189] Z.W. Wang and R.E. Palmer. Determination of the ground-state atomic structures of size-selected Au nanoclusters by electron-beam-induced transformation. *Phys. Rev. Lett.*, 108:245502, 2012.

[190] B.G. Hyde, M. O'Keeffe, W.M. Lyttle, and N.E. Brese. Alternative descriptions of the C23 ($PbCl_2$), C37 (Co_2Si), B8b (Ni_2In) and related structure types. *Acta Chem. Scand.*, 46:216–223, 1992.

[191] U. Müller. *Symmetry relationships between crystal structures*. Oxford University Press, Oxford, 2013.

[192] L. Jones and P.D. Nellist. Identifying and correcting scan noise and drift in the scanning transmission electron microscope. *Microsc. Microanal.*, 19(04):1050–1060, 2013.

[193] A.S. Barnard, N.P. Young, A.I. Kirkland, M.A. van Huis, and H. Xu. Nanogold: a quantitative phase map. *ACS Nano*, 3(6):1431–1436, 2009.

[194] D.J. De Rosier and A. Klug. Reconstruction of three dimensional structures from electron micrographs. *Nature*, 217(5124):130–134, 1968.

[195] R.G. Hart. Electron microscopy of unstained biological material: the polytropic montage. *Science*, 159(3822):1464–1467, 1968.

[196] W. Hoppe, R. Langer, G. Knesch, and C. Poppe. Protein-kristallstrukturanalyse mit elektronenstrahlen. *Naturwissenschaften*, 55(7):333–336, 1968.

[197] A.J. Koster, R. Grimm, D. Typke, R. Hegerl, A. Stoschek, J. Walz, and W. Baumeister. Perspectives of molecular and cellular electron tomography. *J. Struct. Biol.*, 120(3):276–308, 1997.

[198] K.P. de Jong and A.J. Koster. Three-dimensional electron microscopy of mesoporous materials - recent strides towards spatial imaging at the nanometer scale. *ChemPhysChem*, 3(9):776–780, 2002.

[199] H. Jinnai and R.J. Spontak. Transmission electron microtomography in polymer research. *Polymer*, 50(5):1067–1087, 2009.

[200] H. Jinnai, R.J. Spontak, and T. Nishi. Transmission electron microtomography and polymer nanostructures. *Macromolecules*, 43(4):1675–1688, 2010.

[201] H. Jinnai and X. Jiang. Electron tomography in soft materials. *Curr. Opin. Solid St. M.*, 17(3):135–142, 2013.

[202] S.S. van Bavel and J. Loos. Volume organization of polymer and hybrid solar cells as revealed by electron tomography. *Adv. Funct. Mater.*, 20:3217–3234, 2010.

[203] C. Kübel, A. Voigt, R. Schoenmakers, M. Otten, D. Su, T.-C. Lee, A. Carlsson, and J. Bradley. Recent advances in electron tomography: TEM and HAADF-STEM tomography for materials science and semiconductor applications. *Microsc. Microanal.*, 11:378–400, 2005.

[204] G.S. Liu, S.D. House, J. Kacher, M. Tanaka, K. Higashida, and I.M. Robertson. Electron tomography of dislocation structures. *Mater. Charact.*, 87:1–11, 2014.

[205] P.A. Midgley. Tomography using the transmission electron microscope. In N. Yao and Z.L. Wang, editors, *Handbook of Microscopy for Nanotechnology*, pages 601–627. Springer US, 2005.

[206] O. Ersen, C. Hirlimann, M. Drillon, J. Werckmann, F. Tihay, C. Pham-Huu, C. Crucifix, and P. Schultz. 3D-TEM characterization of nanometric objects. *Solid State Sci.*, 9(12):1088–1098, 2007.

[207] G. Möbus and B.J. Inkson. Nanoscale tomography in materials science. *Mater. Today*, 10(12):18–25, 2007.

[208] Z. Saghi and P.A. Midgley. Electron tomography in the (S)TEM: from nanoscale morphological analysis to 3D atomic imaging. *Annu. Rev. Mater. Res.*, 42(1):59–79, 2012.

[209] K.J. Batenburg, S. Bals, J. Sijbers, C. Kübel, P.A. Midgley, J.C. Hernandez, U. Kaiser, E.R. Encina, E.A. Coronado, and G. Van Tendeloo. 3D imaging of nanomaterials by discrete tomography. *Ultramicroscopy*, 109(6):730–740, 2009.

[210] Z. Saghi, D.J. Holland, R. Leary, A. Falqui, G. Bertoni, A.J. Sederman, L.F. Gladden, and P.A. Midgley. Three-dimensional morphology of iron oxide nanoparticles with reactive concave surfaces. a compressed sensing-electron tomography (CS-ET) approach. *Nano Lett.*, 11(11):4666–4673, 2011.

[211] B. Goris, W. Van den Broek, K.J. Batenburg, H. Heidari Mezerji, and S. Bals. Electron tomography based on a total variation minimization reconstruction technique. *Ultramicroscopy*, 113:120–130, 2012.

[212] M.H. Gass, K.K.K. Koziol, A.H. Windle, and P.A. Midgley. Four-dimensional spectral tomography of carbonaceous nanocomposites. *Nano Lett.*, 6(3):376–379, 2006.

[213] A. Yurtsever, M. Weyland, and D.A. Muller. Three-dimensional imaging of nonspherical silicon nanoparticles embedded in silicon oxide by plasmon tomography. *Appl. Phys. Lett.*, 89(15):151920, 2006.

[214] D. Wolf, A. Lubk, F. Röder, and H. Lichte. Electron holographic tomography. *Curr. Opin. Solid St. M.*, 17(3):126–134, 2013.

[215] D. Wolf, A. Lubk, and H. Lichte. Weighted simultaneous iterative reconstruction technique for single-axis tomography. *Ultramicroscopy*, 136:15–25, 2014.

[216] K. Jarausch, P. Thomas, D.N. Leonard, R. Twesten, and C.R. Booth. Four-dimensional STEM-EELS: enabling nano-scale chemical tomography. *Ultramicroscopy*, 109(4):326–337, 2009.

[217] K. Lepinay, F. Lorut, R. Pantel, and T. Epicier. Chemical 3D tomography of 28nm high K metal gate transistor: STEM XEDS experimental method and results. *Micron*, 47:43–49, 2013.

[218] Z. Saghi, X. Xu, and G. Mobus. Electron tomography of regularly shaped nanostructures under non-linear image acquisition. *J. Microsc.-Oxford*, 232(1):186–195, 2008.

[219] A. Alpers, R.J. Gardner, S. König, R.S. Pennington, C.B. Boothroyd, L. Houben, R.E. Dunin-Borkowski, and K.J. Batenburg. Geometric reconstruction methods for electron tomography. *Ultramicroscopy*, 128:42–54, 2013.

[220] Z. Saghi, X. Xu, and G. Mobus. Three-dimensional metrology and fractal analysis of dendritic nanostructures. *Phys. Rev. B*, 78(20):205428, 2008.

[221] J.C. Hindson, Z. Saghi, J.-C. Hernandez-Garrido, P.A. Midgley, and N.C. Greenham. Morphological study of nanoparticle-polymer solar cells using high-angle annular dark-field electron tomography. *Nano Lett.*, 11(2):904–909, 2011.

[222] R. Thiedmann, A. Spettl, O. Stenzel, T. Zeibig, J.C. Hindson, Z. Saghi, N.C. Greenham, P.A. Midgley, and V. Schmidt. Networks of nanoparticles in organic-inorganic composites: algorithmic extraction and statistical analysis. *Image Anal. Stereol.*, 31(1):27–42, 2011.

[223] P.A. Midgley and Z. Saghi. Electron tomography in solid state and materials science - an introduction. *Curr. Opin. Solid St. M.*, 17(3):89–92, 2013.

[224] J.-J. Fernandez. Computational methods for materials characterization by electron tomography. *Curr. Opin. Solid St. M.*, 17(3):93–106, 2013.

[225] S. Bals, S. Van Aert, and G. Van Tendeloo. High resolution electron tomography. *Curr. Opin. Solid St. M.*, 17(3):107–114, 2013.

[226] J. Radon. Über die bestimmung von funktionen durch ihre integralwerte langs gewisser mannigfaltigkeiten. *Ber. Verh. K. Sachs. Ges. Wiss. Leipzig Math.-Phys. Kl.*, 69:262–277, 1917.

[227] R.N. Bracewell. Two-dimensional aerial smoothing in radio astronomy. *Aust. J. Phys.*, 9:297–314, 1956.

[228] S.R. Deans. *The Radon transform and some of its applications.* Wiley, New York; Chichester, 1983.

[229] A.C. Kak and M. Slaney. *Principles of computerized tomographic imaging.* IEEE Press, New York, 1988.

[230] F. Natterer. *The mathematics of computerized tomography.* Teubner; Wiley, Stuttgart; Chichester, 1986.

[231] F. Natterer and F. Wübbeling. *Mathematical methods in image reconstruction.* SIAM, Philadelphia, 2001.

[232] G.T. Herman and A. Kuba. *Discrete Tomography: Foundations, Algorithms and Applications.* Birkhauser, Boston, 1999.

[233] G.T. Herman and A. Kuba. *Advances in Discrete Tomography and Its Applications.* Birkhauser, Boston, 2007.

[234] G.T. Herman. *Fundamentals of computerized tomography: image reconstruction from projections.* Springer, Dordrecht; Heidelberg; London; New York, 2009.

[235] P.A. Penczek and J.J. Grant. Fundamentals of three-dimensional reconstruction from projections. *Method. Enzymol.*, 482:1–33, 2010.

[236] D.N. Mastronarde. Dual-axis tomography: an approach with alignment methods that preserve resolution. *J. Struct. Biol.*, 120(3):343–352, 1997.

[237] P. Penczek, M. Marko, K. Buttle, and J. Frank. Double-tilt electron tomography. *Ultramicroscopy*, 60(3):393–410, 1995.

[238] J. Tong, I. Arslan, and P. Midgley. A novel dual-axis iterative algorithm for electron tomography. *J. Struct. Biol.*, 153(1):55–63, 2006.

[239] I. Arslan, J.R. Tong, and P.A. Midgley. Reducing the missing wedge: high-resolution dual axis tomography of inorganic materials. *Ultramicroscopy*, 106(11-12):994–1000, 2006.

[240] M. Koguchi, H. Kakibayashi, R. Tsuneta, M. Yamaoka, T. Niino, N. Tanaka, K. Kase, and M. Iwaki. Three-dimensional STEM for observing nanostructures. *J. Electron Microsc.*, 50(3):235–241, 2001.

[241] M. Kato, N. Kawase, T. Kaneko, S. Toh, S. Matsumura, and H. Jinnai. Maximum diameter of the rod-shaped specimen for transmission electron microtomography without the "missing wedge". *Ultramicroscopy*, 108(3):221–229, 2008.

[242] K. Jarausch and D.N. Leonard. Three-dimensional electron microscopy of individual nanoparticles. *J. Electron Microsc.*, 58(3):175–183, 2009.

[243] E. Biermans, L. Molina, K.J. Batenburg, S. Bals, and G. Van Tendeloo. Measuring porosity at the nanoscale by quantitative electron tomography. *Nano Lett.*, 10(12):5014–5019, 2010.

[244] J. Leschner, J. Biskupek, A. Chuvilin, and U. Kaiser. Accessing the local three-dimensional structure of carbon materials sensitive to an electron beam. *Carbon*, 48(14):4042–4048, 2010.

[245] H. Friedrich, M.R. McCartney, and P.R. Buseck. Comparison of intensity distributions in tomograms from BF TEM, ADF STEM, HAADF STEM, and calculated tilt series. *Ultramicroscopy*, 106(1):18–27, 2005.

[246] X.Y. Wang, R. Lockwood, M. Malac, H. Furukawa, P. Li, and A. Meldrum. Reconstruction and visualization of nanoparticle composites by transmission electron tomography. *Ultramicroscopy*, 113:96–105, 2012.

[247] H. Sugimori, T. Nishi, and H. Jinnai. Dual-axis electron tomography for three-dimensional observations of polymeric nanostructures. *Macromolecules*, 38(24):10226–10233, 2005.

[248] M. Radermacher and W. Hoppe. Properties of 3-D reconstruction from projections by conical tilting compared to single-axis tilting. In P. Brederoo and G. Boom, editors, *7th European Congress on Electron Microscopy*, pages 132–133. Den Haag, Leiden, The Netherlands, 1980.

[249] N. Kawase, M. Kato, H. Nishioka, and H. Jinnai. Transmission electron microtomography without the "missing wedge" for quantitative structural analysis. *Ultramicroscopy*, 107(1):8–15, 2007.

[250] D. Chen, H. Friedrich, and G. de With. On resolution in electron tomography of beam sensitive materials. *J. Phys. Chem. C*, 118(2):1248–1257, 2013.

[251] R.A. Crowther, D.J. DeRosier, and A. Klug. The reconstruction of a three-dimensional structure from projections and its application to electron microscopy. *Proc. R. Soc. A*, 317(1530):319–340, 1970.

[252] R.N. Bracewell and A.C. Riddle. Inversion of fan-beam scans in radio astronomy. *Astrophys. J.*, 150:427–434, 1967.

[253] H. Heidari Mezerji, W. Van den Broek, and S. Bals. A practical method to determine the effective resolution in incoherent experimental electron tomography. *Ultramicroscopy*, 111(5):330–336, 2011.

[254] R.J. Spontak, M.C. Williams, and D.A. Agard. Three-dimensional study of cylindrical morphology in a styrene-butadiene-styrene block copolymer. *Polymer*, 29(3):387–395, 1988.

[255] A.J. Koster, U. Ziese, A.J. Verkleij, A.H. Janssen, and K.P. de Jong. Three-dimensional transmission electron microscopy: a novel imaging and characterization technique with nanometer scale resolution for materials science. *J. Phys. Chem. B*, 104(40):9368–9370, 2000.

[256] M. Weyland and P.A. Midgley. 3D-EFTEM: tomographic reconstruction from tilt series of energy loss images. *Inst. Phys. Conf. Ser. (EMAG 2001)*, 161:239–242, 2001.

[257] G. Mobus and B.J. Inkson. Three-dimensional reconstruction of buried nanoparticles by element-sensitive tomography based on inelastically scattered electrons. *Appl. Phys. Lett.*, 79(9):1369–1371, 2001.

[258] G. Möbus, R.C. Doole, and B.J. Inkson. Spectroscopic electron tomography. *Ultramicroscopy*, 96(3-4):433–451, 2003.

[259] B. Goris, S. Bals, W. Van den Broek, E. Carbó-Argibay, S. Gómez-Graña, L.M. Liz-Marzán, and G. Van Tendeloo. Atomic-scale determination of surface facets in gold nanorods. *Nat. Mater.*, 11(11):930–935, 2012.

[260] A.C. Twitchett-Harrison, T.J.V. Yates, S.B. Newcomb, R.E. Dunin-Borkowski, and P.A. Midgley. High-resolution three-dimensional mapping of semiconductor dopant potentials. *Nano Lett.*, 7(7):2020–2023, 2007.

[261] U. Kolb, T. Gorelik, C. Kübel, M.T. Otten, and D. Hubert. Towards automated diffraction tomography: part I-data acquisition. *Ultramicroscopy*, 107(6-7):507–513, 2007.

[262] U. Kolb, E. Mugnaioli, and T.E. Gorelik. Automated electron diffraction tomography - a new tool for nano crystal structure analysis. *Cryst. Res. Technol.*, 46(6):542–554, 2011.

[263] O.-H. Kwon and A.H. Zewail. 4D electron tomography. *Science*, 328(5986):1668–1673, 2010.

[264] J.-P. Baudoin, J.R. Jinschek, C.B. Boothroyd, R.E. Dunin-Borkowski, and N. de Jonge. Chromatic aberration-corrected tilt series transmission electron microscopy of nanoparticles in a whole mount macrophage cell. *Microsc. Microanal.*, 19(04):814–820, 2013.

[265] J.S. Barnard, J. Sharp, J.R. Tong, and P.A. Midgley. High-resolution three-dimensional imaging of dislocations. *Science*, 313(5785):319, 2006.

[266] S. Bals, G. Van Tendeloo, and C. Kisielowski. A new approach for electron tomography: annular dark-field transmission electron microscopy. *Adv. Mater.*, 18(7):892–895, 2006.

[267] J.M. Rebled, L. Yedra, S. Estradé, J. Portillo, and F. Peiró. A new approach for 3D reconstruction from bright field TEM imaging: beam precession assisted electron tomography. *Ultramicroscopy*, 111(9-10):1504–1511, 2011.

[268] A.A. Sousa, A.A. Azari, G. Zhang, and R.D. Leapman. Dual-axis electron tomography of biological specimens: extending the limits of specimen thickness with bright-field STEM imaging. *J. Struct. Biol.*, 174(1):107–114, 2011.

[269] P. Ercius, M. Weyland, D.A. Muller, and L.M. Gignac. Three-dimensional imaging of nanovoids in copper interconnects using incoherent bright field tomography. *Appl. Phys. Lett.*, 88(24):243116, 2006.

[270] J.H. Sharp, et al. Dislocation tomography made easy: a reconstruction from ADF STEM images obtained using automated image shift correction. *J. Phys.: Conf. Ser.*, 126(1):012013, 2008.

[271] P. Jornsanoh, G. Thollet, J. Ferreira, K. Masenelli-Varlot, C. Gauthier, and A. Bogner. Electron tomography combining ESEM and STEM: a new 3D imaging technique. *Ultramicroscopy*, 111(8):1247–1254, 2011.

[272] G. Prieto, J. Zečević, H. Friedrich, K.P. de Jong, and P.E. de Jongh. Towards stable catalysts by controlling collective properties of supported metal nanoparticles. *Nat. Mater.*, 12(1):34–39, 2013.

[273] K. Kimura, S. Hata, S. Matsumura, and T. Horiuchi. Dark-field transmission electron microscopy for a tilt series of ordering alloys: toward electron tomography. *J. Electron Microsc.*, 54(4):373–377, 2005.

[274] R. Beanland, A. Sánchez, J. Hernandez-Garrido, D. Wolf, and P. Midgley. Electron tomography of III-V quantum dots using dark field 002 imaging conditions. *J. Microsc.*, 237(2):148–154, 2010.

[275] F. Leroux, E. Bladt, J.-P. Timmermans, G. Van Tendeloo, and S. Bals. Annular dark-field transmission electron microscopy for low contrast materials. *Microsc. Microanal.*, 19(03):629–634, 2013.

[276] K. Lu, E. Sourty, R. Guerra, G. Bar, and J. Loos. Critical comparison of volume data obtained by different electron tomography techniques. *Macromolecules*, 43(3):1444–1448, 2010.

[277] J.S. Barnard, A.S. Eggeman, J. Sharp, T.A. White, and P.A. Midgley. Dislocation electron tomography and precession electron diffraction - minimising the effects of dynamical interactions in real and reciprocal space. *Phil. Mag.*, 90(35):4711–4730, 2010.

[278] R. Grimm, D. Typke, and W. Baumeister. Improving image quality by zero-loss energy filtering: quantitative assessment by means of image cross-correlation. *J. Microsc.-Oxford*, 190:339–349, 1998.

[279] A.A. Herzing, L.J. Richter, and I.M. Anderson. 3D nanoscale characterization of thin-film organic photovoltaic device structures via spectroscopic contrast in the TEM. *J. Phys. Chem. C*, 114(41):17501–17508, 2010.

[280] B. Goris, S. Bals, W. Van den Broek, J. Verbeeck, and G. Van Tendeloo. Exploring different inelastic projection mechanisms for electron tomography. *Ultramicroscopy*, 111(8):1262–1267, 2011.

[281] N.Y. Jin-Phillipp, C.T. Koch, and P.A. van Aken. Toward quantitative core-loss EFTEM tomography. *Ultramicroscopy*, 111(8):1255–1261, 2011.

[282] I. Florea, O. Ersen, C. Hirlimann, L. Roiban, A. Deneuve, M. Houlle, I. Janowska, P. Nguyen, C. Pham, and C. Pham-Huu. Analytical electron tomography mapping of the SiC pore oxidation at the nanoscale. *Nanoscale*, 2:2668–2678, 2010.

[283] X. Xu, Z. Saghi, R. Gay, and G. Mobus. Reconstruction of 3D morphology of polyhedral nanoparticles. *Nanotechnology*, 18(22):225501, 2007.

[284] L. Yedra, A. Eljarrat, R. Arenal, E. Pellicer, M. Cabo, A. López-Ortega, M. Estrader, J. Sort, M.D. Baró, S. Estradé, and F. Peiró. EEL spectroscopic tomography: towards a new dimension in nanomaterials analysis. *Ultramicroscopy*, 122:12–18, 2012.

[285] A. Genc, L. Kovarik, M. Gu, H. Cheng, P. Plachinda, L. Pullan, B. Freitag, and C. Wang. XEDS STEM tomography for 3D chemical characterization of nanoscale particles. *Ultramicroscopy*, 131:24–32, 2013.

[286] I. Arslan, T.J.V. Yates, N.D. Browning, and P.A. Midgley. Embedded nanostructures revealed in three dimensions. *Science*, 309(5744):2195–2198, 2005.

[287] M.C. Scott, C.-C. Chen, M. Mecklenburg, C. Zhu, R. Xu, P. Ercius, U. Dahmen, B.C. Regan, and J. Miao. Electron tomography at 2.4-ångström resolution. *Nature*, 483(7390):444–447, 2012.

[288] L. Houben and M. Bar Sadan. Refinement procedure for the image alignment in high-resolution electron tomography. *Ultramicroscopy*, 111(9-10):1512–1520, 2011.

[289] P.C. Hansen and M. Saxild-Hansen. AIR Tools - a MATLAB package of algebraic iterative reconstruction methods. *J. Comput. Appl. Math.*, 236(8):2167–2178, 2012.

[290] E. Lee, B.P. Fahimian, C.V. Iancu, C. Suloway, G.E. Murphy, E.R. Wright, D. Castaño Díez, G.J. Jensen, and J. Miao. Radiation dose reduction and image enhancement in biological imaging through equally-sloped tomography. *J. Struct. Biol.*, 164(2):221–227, 2008.

[291] Y. Chen and F. Förster. Iterative reconstruction of cryo-electron tomograms using nonuniform fast Fourier transforms. *J. Struct. Biol.*, 185(3):309–316, 2014.

[292] R. Leary, Z. Saghi, P.A. Midgley, and D.J. Holland. Compressed sensing electron tomography. *Ultramicroscopy*, 131:70–91, 2013.

[293] O. Nicoletti, F. de la Pena, R.K. Leary, D.J. Holland, C. Ducati, and P.A. Midgley. Three-dimensional imaging of localized surface plasmon resonances of metal nanoparticles. *Nature*, 502(7469):80–84, 2013.

[294] J. Miao, F. Förster, and O. Levi. Equally sloped tomography with oversampling reconstruction. *Phys. Rev. B*, 72(5):052103, 2005.

[295] C. Zhu, C.-C. Chen, J. Du, M.R. Sawaya, M.C. Scott, P. Ercius, J. Ciston, and J. Miao. Towards three-dimensional structural determination of amorphous materials at atomic resolution. *Phys. Rev. B*, 88:100201, 2013.

[296] M.I. Sezan. An overview of convex projections theory and its application to image recovery problems. *Ultramicroscopy*, 40(1):55–67, 1992.

[297] J.I. Agulleiro and J.J. Fernandez. Fast tomographic reconstruction on multicore computers. *Bioinformatics*, 27(4):582–583, 2011.

[298] S. Kaczmarz. Angenäherte auflösung von systemen linearer gleichungen. *Bull. Int. Acad. Pol. Sci. Lett.*, A35:355–357, 1937.

[299] P.P.B. Eggermont, G.T. Herman, and A. Lent. Iterative algorithms for large partitioned linear systems, with applications to image reconstruction. *Linear Algebra Appl.*, 40:37–67, 1981.

[300] Y. Censor and S.A. Zenios. *Parallel optimization: theory and algorithms*. Oxford University Press, New York, 1997.

[301] A.H. Andersen and A.C. Kak. Simultaneous algebraic reconstruction technique (SART): a superior implementation of the ART algorithm. *Ultrasonic Imaging*, 6(1):81–94, 1984.

[302] L. Landweber. An iteration formula for Fredholm integral equations of the first kind. *Am. J. Math.*, 73(3):615–624, 1951.

[303] J. Gregor and T. Benson. Computational analysis and improvement of SIRT. *IEEE Trans. Med. Imaging*, 27(7):918–924, 2008.

[304] E. Elfving, T. Nikazad, and P.C. Hansen. Semi-convergence and relaxation parameters for a class of SIRT algorithms. *Electron. T. Numer. Ana.*, 37:321–336, 2010.

[305] C. Kübel, M. Godehardt, R. Cieslinski, and S. Rozeveld. Towards a quantitative understanding in electron tomography. *Microsc. Microanal.*, 15(SupplementS2):602–603, 2009.

[306] N. Monsegue, X. Jin, T. Echigo, G. Wang, and M. Murayama. Three-dimensional characterization of iron oxide (α-Fe_2O_3) nanoparticles: application of a compressed sensing inspired reconstruction algorithm to electron tomography. *Microsc. Microanal.*, 18(06):1362–1367, 2012.

[307] J.R. Jinschek, K.J. Batenburg, H.A. Calderon, R. Kilaas, V. Radmilovic, and C. Kisielowski. 3-D reconstruction of the atomic positions in a simulated gold nanocrystal based on discrete tomography: prospects of atomic resolution electron tomography. *Ultramicroscopy*, 108(6):589–604, 2008.

[308] K. Batenburg and J. Sijbers. DART: a practical reconstruction algorithm for discrete tomography. *IEEE Trans. Image Proc.*, 20(9):2542–2553, 2011.

[309] F.J. Maestre-Deusto, G. Scavello, J. Pizarro, and P.L. Galindo. ADART: an adaptive algebraic reconstruction algorithm for discrete tomography. *IEEE Trans. Image Proc.*, 20(8):2146–2152, 2011.

[310] K.J. Batenburg, W. van Aarle, and J. Sijbers. A semi-automatic algorithm for grey level estimation in tomography. *Pattern Recogn. Lett.*, 32(9):1395–1405, 2011.

[311] A. Zürner, M. Döblinger, V. Cauda, R. Wei, and T. Bein. Discrete tomography of demanding samples based on a modified SIRT algorithm. *Ultramicroscopy*, 115:41–49, 2012.

[312] W. Van Aarle, K.J. Batenburg, and J. Sijbers. Automatic parameter estimation for the discrete algebraic reconstruction technique (DART). *IEEE Trans. Imag. Proc.*, 21(11):4608–4621, 2012.

[313] T. Roelandts, K.J. Batenburg, E. Biermans, C. Kübel, S. Bals, and J. Sijbers. Accurate segmentation of dense nanoparticles by partially discrete electron tomography. *Ultramicroscopy*, 114:96–105, 2012.

[314] M. Wollgarten and M. Habeck. Autonomous reconstruction and segmentation of tomographic data. *Micron*, 63:20–27, 2014.

[315] R.J. Gardner. *Geometric Tomography*. Cambridge University Press, Cambridge, 2006.

[316] T.C. Petersen and S.P. Ringer. Electron tomography using a geometric surface-tangent algorithm: application to atom probe specimen morphology. *J. Appl. Phys.*, 105(10):103518, 2009.

[317] W.O. Saxton, W. Baumeister, and M. Hahn. Three-dimensional reconstruction of imperfect two-dimensional crystals. *Ultramicroscopy*, 13(1-2):57–70, 1984.

[318] B. Liu, H. Yu, S.S. Verbridge, L. Sun, and G. Wang. Dictionary-learning-based reconstruction method for electron tomography. *Scanning*, doi:10.1002/sca.21127, 2013.

[319] G. Haberfehlner, R. Serra, D. Cooper, S. Barraud, and P. Bleuet. 3D spatial resolution improvement by dual-axis electron tomography: application to tri-gate transistors. *Ultramicroscopy*, 136:144–153, 2014.

[320] A. Lange, A. Kupsch, M.P. Hentschel, I. Manke, N. Kardjilov, T. Arlt, and R. Grothausmann. Reconstruction of limited computed tomography data of fuel cell components using direct iterative reconstruction of computed tomography trajectories. *J. Power Sources*, 196(12):5293–5298, 2011.

[321] S. Lück, A. Kupsch, A. Lange, M.P. Hentschel, and V. Schmidt. Statistical analysis of tomographic reconstruction algorithms by morphological image characteristics. *Image Anal. Stereol.*, 29(2):61–77, 2010.

[322] S.V. Venkatakrishnan, et al. Model based iterative reconstruction for bright field electron tomography. *Proc. SPIE, Computational Imaging XI*, 8657, 2013.

[323] S.V. Venkatakrishnan, L.F. Drummy, M.A. Jackson, M. De Graef, J. Simmons, and C.A. Bouman. A model based iterative reconstruction algorithm for high angle annular dark field-scanning transmission electron microscope (HAADF-STEM) tomography. *IEEE Trans. Image Proc.*, 22(11):4532–4544, 2013.

[324] W. Van den Broek, S. Van Aert, and D. Van Dyck. A model based atomic resolution tomographic algorithm. *Ultramicroscopy*, 109(12):1485–1490, 2009.

[325] K. Sandberg and J.R. McIntosh. Methods for image segmentation in cellular tomography. *Method. Cell Biol.*, 79:769–798, 2007.

[326] R. Narasimha, I. Aganj, A.E. Bennett, M.J. Borgnia, D. Zabransky, G. Sapiro, S.W. McLaughlin, J.L.S. Milne, and S. Subramaniam. Evaluation of denoising algorithms for biological electron tomography. *J. Struct. Biol.*, 164(1):7–17, 2008.

[327] N. Volkmann and J.J. Grant. Methods for segmentation and interpretation of electron tomographic reconstructions. *Method. Enzymol.*, 483:31–46, 2010.

[328] J.-J. Fernandez. Computational methods for electron tomography. *Micron*, 43(10):1010–1030, 2012.

[329] J.-J. Fernández and S. Li. An improved algorithm for anisotropic nonlinear diffusion for denoising cryo-tomograms. *J. Struct. Biol.*, 144(1-2):152–161, 2003.

[330] N. Volkmann. A novel three-dimensional variant of the watershed transform for segmentation of electron density maps. *J. Struct. Biol.*, 138(1-2):123–129, 2002.

[331] C. Bajaj, Z. Yu, and M. Auer. Volumetric feature extraction and visualization of tomographic molecular imaging. *J. Struct. Biol.*, 144(1-2):132–143, 2003.

[332] J.-J. Fernandez. TOMOBFLOW: feature-preserving noise filtering for electron tomography. *BMC Bioinformatics*, 10(178), 2009.

[333] E. Garduño, M. Wong-Barnum, N. Volkmann, and M.H. Ellisman. Segmentation of electron tomographic data sets using fuzzy set theory principles. *J. Struct. Biol.*, 162(3):368–379, 2008.

[334] K. Sandberg and M. Brega. Segmentation of thin structures in electron micrographs using orientation fields. *J. Struct. Biol.*, 157(2):403–415, 2007.

[335] C.d.J. Gommes, K. de Jong, J.-P. Pirard, and S. Blacher. Assessment of the 3D localization of metallic nanoparticles in Pd/SiO_2 cogelled catalysts by electron tomography. *Langmuir*, 21(26):12378–12385, 2005.

[336] H. Friedrich, S. Guo, P.E. de Jongh, X. Pan, X. Bao, and K.P. de Jong. A quantitative electron tomography study of ruthenium particles on the interior and exterior surfaces of carbon nanotubes. *ChemSusChem*, 4(7):957–963, 2011.

[337] R. Grothausmann, G. Zehl, I. Manke, S. Fiechter, P. Bogdanoff, I. Dorbandt, A. Kupsch, A. Lange, M.P. Hentschel, G. Schumacher, and J. Banhart. Quantitative structural assessment of heterogeneous catalysts by electron tomography. *J. Am. Chem. Soc.*, 133(45):18161–18171, 2011.

[338] H. Li, H.L. Xin, D.A. Muller, and L.A. Estroff. Visualizing the 3D internal structure of calcite single crystals grown in agarose hydrogels. *Science*, 326(5957):1244–1247, 2009.

[339] M. Sezgin and B. Sankur. Survey over image thresholding techniques and quantitative performance evaluation. *J. Electron. Imaging*, 13(1):146–168, 2004.

[340] W. van Aarle, K.J. Batenburg, and J. Sijbers. Optimal threshold selection for segmentation of dense homogeneous objects in tomographic reconstructions. *IEEE Trans. Med. Imaging*, 30(4):980–989, 2011.

[341] N. Otsu. A threshold selection method from gray-level histograms. *IEEE Trans. Syst. Man Cyb.*, SMC-9(1):62–66, 1979.

[342] K.J. Batenburg and J. Sijbers. Optimal threshold selection for tomogram segmentation by projection distance minimization. *IEEE Trans. Med. Imaging*, 28(5):676–686, 2009.

[343] M.N. Lebbink, W.J.C. Geerts, T.P. van der Krift, M. Bouwhuis, L.O. Hertzberger, A.J. Verkleij, and A.J. Koster. Template matching as a tool for annotation of tomograms of stained biological structures. *J. Struct. Biol.*, 158(3):327–335, 2007.

[344] J. Ohser and K. Schladitz. *3D Images of Materials Structures: Processing and Analysis*. Wiley-VCH, Weinheim, 2009.

[345] E.P.W. Ward, T.J.V. Yates, J.-J. FernÃ¡ndez, D.E.W. Vaughan, and P.A. Midgley. Three-dimensional nanoparticle distribution and local curvature of heterogeneous catalysts revealed by electron tomography. *J. Phys. Chem. C*, 111(31):11501–11505, 2007.

[346] J.H. Laurer, D.A. Hajduk, J.C. Fung, J.W. Sedat, S.D. Smith, S.M. Gruner, D.A. Agard, and R.J. Spontak. Microstructural analysis of a cubic bicontinuous morphology in a neat SIS triblock copolymer. *Macromolecules*, 30(13):3938–3941, 1997.

[347] H. Jinnai, T. Koga, Y. Nishikawa, T. Hashimoto, and S.T. Hyde. Curvature determination of spinodal interface in a condensed matter system. *Phys. Rev. Lett.*, 78(11):2248–2251, 1997.

[348] H. Jinnai, Y. Nishikawa, R.J. Spontak, S.D. Smith, D.A. Agard, and T. Hashimoto. Direct measurement of interfacial curvature distributions in a bicontinuous block copolymer morphology. *Phys. Rev. Lett.*, 84(3):518–521, 2000.

[349] E.M. Perassi, J.C. Hernandez-Garrido, M.S. Moreno, E.R. Encina, E.A. Coronado, and P.A. Midgley. Using highly accurate 3D nanometrology to model the optical properties of highly irregular nanoparticles: a powerful tool for rational design of plasmonic devices. *Nano Lett.*, 10(6):2097–2104, 2010.

[350] D. Van Dyck and F.-R. Chen. 'Big Bang' tomography as a new route to atomic-resolution electron tomography. *Nature*, 486(7402):243–246, 2012.

[351] J. Frank. *Three-Dimensional Electron Microscopy of Macromolecular Assemblies: Visualization of Biological Molecules in Their Native State.* Oxford University Press, New York, 2006.

[352] P.D. Nellist and P. Wang. Optical sectioning and confocal imaging and analysis in the transmission electron microscope. *Annu. Rev. Mater. Res.*, 42(1):125–143, 2012.

[353] R. Hovden, P. Ercius, Y. Jiang, D. Wang, Y. Yu, H.D. Abruña, V. Elser, and D.A. Muller. Breaking the Crowther limit: combining depth-sectioning and tilt tomography for high-resolution, wide-field 3D reconstructions. *Ultramicroscopy*, 140:26–31, 2014.

[354] H. Heidari, W. Van den Broek, and S. Bals. Quantitative electron tomography: the effect of the three-dimensional point spread function. *Ultramicroscopy*, 135:1–5, 2013.

[355] J.M. Thomas, R. Leary, P.A. Midgley, and D.J. Holland. A new approach to the investigation of nanoparticles: electron tomography with compressed sensing. *J. Colloid Interface Sci.*, 392:7–14, 2013.

[356] J.M. Thomas, C. Ducati, R. Leary, and P.A. Midgley. Some turning points in the chemical electron microscopic study of heterogeneous catalysts. *ChemCatChem*, 5(9):2560–2579, 2013.

[357] J.M. Thomas, P.A. Midgley, C. Ducati, and R.K. Leary. Nanoscale electron tomography and atomic scale high-resolution electron microscopy of nanoparticles and nanoclusters: a short survey. *Prog. Nat. Sci.*, 23(3):222–234, 2013.

[358] E.Y. Sidky and X.C. Pan. Image reconstruction in circular cone-beam computed tomography by constrained, total-variation minimization. *Phys. Med. Biol.*, 53(17):4777–4807, 2008.

[359] D.J. Holland, D.M. Malioutov, A. Blake, A.J. Sederman, and L.F. Gladden. Reducing data acquisition times in phase-encoded velocity imaging using compressed sensing. *J. Magn. Reson.*, 203(2):236–246, 2010.

[360] M. Lustig, D. Donoho, and J.M. Pauly. Sparse MRI: the application of compressed sensing for rapid MR imaging. *Magn. Reson. Med.*, 58(6):1182–1195, 2007.

[361] M.W. Kim, et al. Cryo-electron microscopy single particle reconstruction of virus particles using compressed sensing theory. *Proc. SPIE 6498, Computational Imaging V, 64981G*, (February 28^{th}, 2007):doi:10.1117/12.705008.

[362] C. Vonesch, W. Lanhui, Y. Shkolnisky, and A. Singer. Fast wavelet-based single-particle reconstruction in cryo-EM. In *IEEE International Symposium on Biomedical Imaging: From Nano to Macro*, pages 1950–1953, March 2011.

[363] D.S. Taubman and M.W. Marcellin. JPEG2000: standard for interactive imaging. *Proc. IEEE*, 90(8):1336–1357, 2002.

[364] M. Lustig, D.L. Donoho, J.M. Santos, and J.M. Pauly. Compressed sensing MRI. *IEEE Signal Proc. Mag.*, 25(2):72–82, 2008.

[365] E. Candès and J. Romberg. Sparsity and incoherence in compressive sampling. *Inverse Probl.*, 23(3):969–985, 2007.

[366] S.S. Chen, D.L. Donoho, and M.A. Saunders. Atomic decomposition by basis pursuit. *SIAM J. Sci. Comput.*, 20(1):33–61, 1998.

[367] R.T. Rockafellar. *Convex Analysis*. Princeton University Press, Princeton, NJ, 1970.

[368] S. Becker, J. Bobin, and E.J. Candes. NESTA: a fast and accurate first-order method for sparse recovery. *SIAM J. Imaging Sciences*, 4(1):1–39, 2011.

[369] E. van den Berg and M.P. Friedlander. Probing the Pareto frontier for basis pursuit solutions. *SIAM J. Sci. Comput.*, 31(2):890–912, 2008.

[370] J.A. Tropp and S.J. Wright. Computational methods for sparse solution of linear inverse problems. *Proc. IEEE*, 98(6):948–958, 2010.

[371] R.G. Baraniuk. Compressive sensing [lecture notes]. *IEEE Signal Proc. Mag.*, 24(4):118–121, 2007.

[372] E.J. Candès and M.B. Wakin. An introduction to compressive sampling. *IEEE Signal Proc. Mag.*, 25(2):21–30, 2008.

[373] M.F. Duarte, M.A. Davenport, D. Takhar, J.N. Laska, S. Ting, K.F. Kelly, and R.G. Baraniuk. Single-pixel imaging via compressive sampling. *IEEE Signal Proc. Mag.*, 25(2):83–91, 2008.

[374] J. Romberg. Imaging via compressive sampling. *IEEE Signal Proc. Mag.*, 25(2):14–20, 2008.

[375] R.M. Willett, R.F. Marcia, and J.M. Nichols. Compressed sensing for practical optical imaging systems: a tutorial. *Opt. Eng.*, 50(7):072601, 2011.

[376] M. Davenport, M. Duarte, Y.C. Eldar, and G. Kutynoik. Introduction to compressed sensing. In Y. C. Eldar and G. Kutynoik, editors, *Compressed Sensing: Theory and Applications*, pages 1–64. Cambridge University Press, Cambridge, 2012.

[377] S. Foucart and H. Rauhut. *A Mathematical Introduction to Compressive Sensing*. Applied and Numerical Harmonic Analysis, Springer, 2013.

[378] B. Goris, T. Roelandts, K.J. Batenburg, H. Heidari Mezerji, and S. Bals. Advanced reconstruction algorithms for electron tomography: from comparison to combination. *Ultramicroscopy*, 127:40–47, 2013.

[379] M.F. Duarte and Y.C. Eldar. Structured compressed sensing: from theory to applications. *IEEE Trans. Signal. Proc.*, 59(9):4053–4085, 2011.

[380] X. Pan, E.Y. Sidky, and M. Vannier. Why do commercial CT scanners still employ traditional, filtered back-projection for image reconstruction? *Inverse Probl.*, 25(12):123009, 2009.

[381] B. Adcock, A. Hansen, B. Roman, and G. Teschke. Breaking the coherence barrier: A new theory for compressed sensing. *arXiv:1302.0561 [cs.IT]*, 2014.

[382] J.L. Starck, F. Murtagh, and J.M. Fadili. *Sparse image and signal processing: wavelets, curvelets, morphological diversity.* Cambridge University Press, Cambridge, 2010.

[383] L. Rudin, S. Osher, and E. Fatemi. Non-linear total variation noise removal algorithm. *Physica D*, 60:259–268, 1992.

[384] S. Mallat. *A Wavelet Tour of Signal Processing.* Academic Press, Burlington, MA, 2008.

[385] A. Stoschek and R. Hegerl. Denoising of electron tomographic reconstructions using multiscale transformations. *J. Struct. Biol.*, 120(3):257–265, 1997.

[386] C.O.S. Sorzano, E. Ortiz, M. López, and J. Rodrigo. Improved Bayesian image denoising based on wavelets with applications to electron microscopy. *Pattern Recogn.*, 39(6):1205–1213, 2006.

[387] C.O.S. Sorzano, S. Jonić, C. El-Bez, J.M. Carazo, S. De Carlo, P. Thévenaz, and M. Unser. A multiresolution approach to orientation assignment in 3D electron microscopy of single particles. *J. Struct. Biol.*, 146(3):381–392, 2004.

[388] K. Song, L.R. Comolli, and M. Horowitz. Removing high contrast artifacts via digital inpainting in cryo-electron tomography: an application of compressed sensing. *J. Struct. Biol.*, 178(2):108–120, 2012.

[389] J.L. Starck, M. Elad, and D.L. Donoho. Image decomposition via the combination of sparse representations and a variational approach. *IEEE Trans. Image Proc.*, 14(10):1570–1582, 2005.

[390] J. Buckheit and D.L. Donoho. Wavelab and reproducible research. In A. Antoniadis and G. Oppenheim, editors, *Wavelets and Statistics*, pages 55–81. Springer-Verlag, Berlin, New York, 1995.

[391] A. Stevens, H. Yang, L. Carin, I. Arslan, and N.D. Browning. The potential for Bayesian compressive sensing to significantly reduce electron dose in high-resolution STEM images. *Microscopy*, 63(1):41–51, 2014.

[392] L. Ritschl, F. Bergner, C. Fleischmann, and M. Kachelriess. Improved total variation-based CT image reconstruction applied to clinical data. *Phys. Med. Biol.*, 56(6):1545–1561, 2011.

[393] Z.T. Harmany, R.F. Marcia, and R.M. Willett. This is SPIRAL-TAP: Sparse Poisson Intensity Reconstruction ALgorithms-theory and practice. *IEEE Trans. Image Proc.*, 21(3):1084–1096, 2012.

[394] Q. Xu, X. Mou, G. Wang, J. Sieren, E.A. Hoffman, and H. Yu. Statistical interior tomography. *IEEE Trans. Med. Imaging*, 30(5):1116–1128, 2011.

[395] C. George, D. Dorfs, G. Bertoni, A. Falqui, A. Genovese, T. Pellegrino, A. Roig, A. Quarta, R. Comparelli, M.L. Curri, R. Cingolani, and L. Manna. A cast-mold approach to iron oxide and Pt/Iron oxide nanocontainers and nanoparticles with a reactive concave surface. *J. Am. Chem. Soc.*, 133(7):2205–2217, 2011.

[396] J.A. Fessler and B.P. Sutton. Nonuniform fast Fourier transforms using min-max interpolation. *IEEE Trans. Signal. Proc.*, 51(2):560–574, 2003.

[397] S. Matej, J.A. Fessler, and I.G. Kazantsev. Iterative tomographic image reconstruction using Fourier-based forward and back-projectors. *IEEE Trans. Med. Imaging*, 23(4):401–412, 2004.

[398] P.C. Hansen and D.P. O'Leary. The use of the L-curve in the regularization of discrete ill-posed problems. *SIAM J. Sci. Comput.*, 14(6):1487–1503, 1993.

[399] L. Zhu, W. Zhang, D. Elnatan, and B. Huang. Faster STORM using compressed sensing. *Nat. Methods*, 9(7):721–723, 2012.

[400] J. Kaipio and E. Somersalo. Statistical inverse problems: discretization, model reduction and inverse crimes. *J. Comput. Appl. Math.*, 198(2):493–504, 2007.

[401] J.C. Lagarias, J.A. Reeds, M.H. Wright, and P.E. Wright. Convergence properties of the Nelder-Mead simplex method in low dimensions. *SIAM J. Optimiz.*, 9(1):112–147, 1998.

[402] A. Fiore, R. Mastria, M.G. Lupo, G. Lanzani, C. Giannini, E. Carlino, G. Morello, M. De Giorgi, Y. Li, R. Cingolani, and L. Manna. Tetrapod-shaped colloidal nanocrystals of II-VI semiconductors prepared by seeded growth. *J. Am. Chem. Soc.*, 131(6):2274–2282, 2009.

[403] S.A. Maier and H.A. Atwater. Plasmonics: localization and guiding of electromagnetic energy in metal/dielectric structures. *J. Appl. Phys.*, 98:011101, 2005.

[404] J.N. Anker, W.P. Hall, O. Lyandres, N.C. Shah, J. Zhao, and R.P. Van Duyne. Biosensing with plasmonic nanosensors. *Nat. Mater.*, 7(6):442–453, 2008.

[405] S. Zhang, K. Bao, N.J. Halas, H. Xu, and P. Nordlander. Substrate-induced Fano resonances of a plasmonic nanocube: a route to increased-sensitivity localized surface plasmon resonance sensors revealed. *Nano Lett.*, 11(4):1657–1663, 2011.

[406] J.A. Schuller, E.S. Barnard, W. Cai, Y.C. Jun, J.S. White, and M.L. Brongersma. Plasmonics for extreme light concentration and manipulation. *Nat. Mater.*, 9(3):193–204, 2010.

[407] J. Nelayah, M. Kociak, O. Stephan, F.J. Garcia de Abajo, M. Tence, L. Henrard, D. Taverna, I. Pastoriza-Santos, L.M. Liz-Marzan, and C. Colliex. Mapping surface plasmons on a single metallic nanoparticle. *Nat. Phys.*, 3(5):348–353, 2007.

[408] A. Yurtsever, R.M. van der Veen, and A.H. Zewail. Subparticle ultrafast spectrum imaging in 4D electron microscopy. *Science*, 335(6064):59–64, 2012.

[409] A. Hörl, A. Trügler, and U. Hohenester. Tomography of particle plasmon fields from electron energy loss spectroscopy. *Phys. Rev. Lett.*, 111:076801, 2013.

[410] F.J. García de Abajo. Optical excitations in electron microscopy. *Rev. Mod. Phys.*, 82:209–275, 2010.

[411] G. Boudarham and M. Kociak. Modal decompositions of the local electromagnetic density of states and spatially resolved electron energy loss probability in terms of geometric modes. *Phys. Rev. B*, 85:245447, 2012.

[412] U. Hohenester, H. Ditlbacher, and J.R. Krenn. Electron-energy-loss spectra of plasmonic nanoparticles. *Phys. Rev. Lett.*, 103:106801, 2009.

[413] P.B. Johnson and R.W. Christy. Optical constants of the noble metals. *Phys. Rev. B*, 6:4370–4379, 1972.

[414] E.D. Palik. *Handbook of Optical Constants of Solids Vol. 1, pp. 350-357.* Academic, San Diego, 1998.

[415] D. Langbein. Normal modes at small cubes and rectangular particles. *J. Phys. A: Math. Gen.*, 9(4):627, 1976.

[416] R. Fuchs. Theory of the optical properties of ionic crystal cubes. *Phys. Rev. B*, 11:1732–1740, 1975.

[417] S.J. Lade, D. Paganin, and M.J. Morgan. Electron tomography of electromagnetic fields, potentials and sources. *Opt. Commun.*, 253(4-6):392–400, 2005.

[418] I. Aganj, A. Bartesaghi, M. Borgnia, H.Y. Liao, G. Sapiro, and S. Subramaniam. Regularization for inverting the radon transform with wedge consideration. In *IEEE International Symposium on Biomedical Imaging: From Nano to Macro*, pages 217–220, April 2007.

[419] H. Rullgård. A new principle for choosing regularization parameter in certain inverse problems. *arXiv:0803.3713 [math.NA]*, 2008.

[420] G.L. Xu, M. Li, A. Gopinath, and C.L. Bajaj. Inversion of electron tomography images using L2-gradient flows. *J. Comput. Math.*, 29(5):501–525, 2011.

[421] S.K. Malladi, Q. Xu, M.A. van Huis, F.D. Tichelaar, K.J. Batenburg, E. Yücelen, B. Dubiel, A. Czyrska-Filemonowicz, and H.W. Zandbergen. Real-time atomic scale imaging of nanostructural evolution in aluminum alloys. *Nano Lett.*, 14(1):384–389, 2013.

[422] Y. Mao, B.P. Fahimian, S.J. Osher, and J. Miao. Development and optimization of regularized tomographic reconstruction algorithms utilizing equally-sloped tomography. *IEEE Trans. Image Proc.*, 19(5):1259–68, 2010.

[423] J.C. Yang, H. Yu, M. Jiang, and G. Wang. High-order total variation minimization for interior tomography. *Inverse Probl.*, 26:035013, 2010.

[424] H. Yu and G. Wang. Compressed sensing based interior tomography. *Phys. Med. Biol.*, 54(9):2791, 2009.

[425] M. Armbrüster, et al. $Al_{13}Fe_4$ as a low-cost alternative for palladium in heterogeneous hydrogenation. *Nat. Mater.*, 11(8):690–693, 2012.

[426] P. Binev, W. Dahmen, R. DeVore, P. Lamby, D. Savu, and R. Sharpley. Compressed sensing and electron microscopy. In T. Vogt, W. Dahmen, and P. Binev, editors, *Modeling Nanoscale Imaging in Electron Microscopy*, pages 73–126. Springer US, 2012.

[427] H.S. Anderson, J. Ilic-Helms, B. Rohrer, J. Wheeler, and K. Larson. Sparse imaging for fast electron microscopy. *Proc. SPIE 8657, Computational Imaging XI, 86570C*, (February 14, 2013):doi:10.1117/12.2008313.

[428] W. Van den Broek and C.T. Koch. General framework for quantitative three-dimensional reconstruction from arbitrary detection geometries in TEM. *Phys. Rev. B*, 87(18):184108, 2013.

[429] J. Lee, W. Zhou, S.J. Pennycook, J.-C. Idrobo, and S.T. Pantelides. Direct visualization of reversible dynamics in a Si_6 cluster embedded in a graphene pore. *Nat. Commun.*, 4:1650, 2013.

[430] N.D. Browning, C. Aydin, J. Lu, A. Kulkarni, N.L. Okamoto, V. Ortalan, B.W. Reed, A. Uzun, and B.C. Gates. Quantitative Z-contrast imaging of supported metal complexes and clusters - a gateway to understanding catalysis on the atomic scale. *ChemCatChem*, 5(9):2673–2683, 2013.

[431] J.M. Thomas. *Design and Applications of Single-Site Heterogeneous Catalysts: Contributions to Green Chemistry, Clean Technology and Sustainability.* Imperial College Press, London, 2012.